Investigating the Androgen Metabolizing Enzymes HSD17B6 & DHRS7 in Prostate Cancer

Inauguraldissertation
zur
Erlangung der Würde eines Doktors der Philosophie
vorgelegt der
Philosophisch-Naturwissenschaftlichen Fakultät
der Universität Basel

von

Simon Stücheli

2022

Genehmigt von der Philosophisch-Naturwissenschaftlichen Fakultät

auf Antrag von

Prof. Dr. Alex Odermatt, Prof. Dr. Henriette E. Meyer zu Schwabedissen, Prof. Dr. Didier Picard

Basel, den 14.12.2021

_____

Dekan

Prof. Dr. Marcel Mayor

TABLE OF CONTENTS

LIST OF ABBREVIATIONS 4
1 SUMMARY 7
2 INTRODUCTION 9
2.1 Steroid Hormones 9
2.1.1 Steroidogenesis of Androgens 9
2.2 The Short-Chain Dehydrogenase/Reductase Superfamily 12
2.2.1 3α-Hydroxysteroid Dehydrogenases 12
2.2.2 The Orphan Enzyme DHRS7 15
2.3 Prostate Cancer 18
2.3.1 Anatomy of the Prostate 18
2.3.2 Epidemiology 19
2.3.3 Diagnosis & Treatment 20
2.3.4 Late Stage Prostate Cancer 24
3 AIMS OF THE THESIS 28
4 PROJECT 1 – HSD17B6 29
4.1 Materials & Methods 29
4.2 Results 33
4.2 Discussion & Outlook 38
5 PROJECT 2 – DHRS7 44
5.1 The Expression of DHRS7 Correlates Negatively with EGFR Expression and Positively with Survival Rate in Prostate Cancer 44
5.2 Discussion & Outlook 74
6 OTHER CONTRIBUTIONS 84
6.1 Summary 84
6.2 The ratio of ursodeoxycholyltaurine to 7-oxolithocholyltaurine serves as a biomarker of decreased 11β-hydroxysteroid dehydrogenase 1 activity in mouse. 86
6.3 Development and Validation of a Highly Sensitive LC-MS/MS Method for the Analysis of Bile Acids in Serum, Plasma, and Liver Tissue Samples 105
6.4 Impact on Bile Acid Concentrations by Alveolar Echinococcosis and Treatment with Albendazole in Mice 123
6.5 Albendazole reduces hepatic inflammation and endo-plasmic reticulum-stress in a mouse model of chronic Echinococcus multilocularis infection 141
7 ACKNOWLEDGEMENTS 165
8 SUPPLEMENTARY INFORMATION 166
9 REFERENCES 172
10 CURRICULUM VITAE 183

LIST OF ABBREVIATIONS

17OH-Allopregnanolone	17β-hydroxyallopregnanolone
17OH-Dihydroprogesterone	17β-hydroxydihydroprogesterone
17OH-Pregnenolone	17β-hydroxypregnenolone
17OH-Progesterone	17β-hydroxyprogesterone
3α-Adiol	3α-androstanediol
3α-ADT	3α-androsterone
3β-Adiol	3β-androstanediol
3β-ADT	3β-epiandrosterone
3α-HSD	3α-hydroxysteroid dehydrogenase
5α-DHT	5α-dihydrotestosterone
ABHD2	Abhydrolase domain containing 2
ABZ	Albendazole
ACTH	Adrenocorticotropic hormone
AE	Alveolar echinococcosis
AKR	Aldo-keto reductase
Akt	AKT serine/threonine kinase
AR(v7)	Androgen receptor (splice variant 7)
AS	Active site
CB2	Cannabinoid receptor type 2
CDK2	Cyclin dependent kinase 2
CRH	Corticotropin-releasing hormone
CRPC	Castration resistant prostate cancer
CTNNB1	β-Catenin
CYB5A	Cytochrome b_5 type A
CYP	Cytochrome P450
DHEA	Dehydroepiandrosterone
DHRS	Dehydrogenase/reductase
EGF(R)	Epidermal growth factor (receptor)
EMT	Epithelial-to-mesenchymal transition
Epim.	Epimerization
ER(S)	Endoplasmic reticulum (stress)
ERα/β	Estrogen Receptor α/β
Erk	Extracellular signal-regulated kinase
FBS	Fetal bovine serum
FDX1	Ferredoxin

FDXR	Ferredoxin reductase
FKBP5	FK506 binding protein 5; FKBP prolyl isomerase 5
GnRH	Gonadotropin-releasing hormone
GR	Glucocorticoid receptor
HCC	Hepatocellular carcinoma
HSD11B	11β-Hydroxysteroid dehydrogenase
HSD17B	17β-Hydroxysteroid dehydrogenase
HSD3B	3β-Hydroxysteroid dehydrogenase
HSP90	Heat shock protein 90
IRE1(α)	Inositol-requiring enzyme 1(α)
KLK3	Kallikrein related peptidase 3
LC-MS	Liquid chromatography-mass spectrometry
LH	Luteinizing hormone
MAPK	Mitogen-activated protein kinase
MR	Mineralocorticoid receptor
NAD(P)(H)	Nicotinamide adenine dinucleotide (phosphate)
NNK	Nicotine-derived nitrosamine ketone
Oxid.	Oxidation
PCa	Prostate cancer (adenocarcinoma of the prostate)
PD-L1	Programmed death-ligand 1
PEI	Polyethylenimine
PI3K	Phosphatidylinositol 3-kinase
PIK3CB	Phosphatidylinositol-4,5-bisphosphate 3-kinase catalytic subunit β
PIP_3	Phosphatidylinositol 3,4,5-triphosphate
POR	CYP oxidoreductase
PSA	Prostate-specific antigen
PTEN	Phosphatase and tensin homolog
RB1	Retinoblastoma protein transcriptional corepressor 1
RDH	Retinol dehydrogenase
Red.	Reduction
RF	Rossmann fold
RTK	Receptor tyrosine kinase
SDR	Short-chain dehydrogenase/reductase
SRD5A	Steroid 5α-reductase
STAT	Signal transducer and activator of transcription
Strep	Twin-Strep-tag
TCGA	The Cancer Genome Atlas

TMA	Tissue microarray
TMPRSS2	Transmembrane serine protease 2
UGT	UDP-glucuronosyltransferase
UPR	Unfolded protein response
αPD-L1	PD-L1 targeting antibody

1 SUMMARY

Prostate cancer (adenocarcinoma of the prostate, PCa) is one of the most common cancers in the world. Several treatment options exist, including surgery and radiotherapy with curative intention, hormonal therapy, and chemotherapy. The etiology of PCa is heavily dependent on androgens activating the androgen receptor (AR) with most drugs and therapy approaches focusing on this aspect. Unfortunately, cancer progression to a state that is characterized by therapy resistance and metastases is common and this late stage of PCa is considered incurable. Therefore, there is a need to further understand the underlying biology of this malignancy in order to discover new therapeutic approaches.

The first project addressed the 17β-hydroxysteroid dehydrogenase (HSD17B) 6. This enzyme performs the oxidation of 3α-androstanediol (3α-Adiol) to 5α-dihydrotestosterone (5α-DHT), thereby providing the AR with its main ligand. This reaction is an essential step in the so-called “backdoor” pathway of androgen synthesis and is suspected to play a role in PCa. Other enzymes were reported to perform the same reaction and together with HSD17B6 they are referred to as 3α-hydroxysteroid dehydrogenases (3α-HSDs). It was the goal to compare the enzymes’ ability to oxidize not only 3α-Adiol, but also 3β-Adiol as well as a potential reverse reaction by reducing 5α-DHT. For that purpose, a reporter gene assay (transactivation assay) was used in intact CV-1 cells. This revealed that several enzymes were able to cause an AR activation by oxidation of 3α-Adiol, but HSD17B6 was uniquely able to oxidize 3β-Adiol as well. Oxidation of 3α-androsterone (3α-ADT) leads to the formation of 5α-DHT as well (*via* the intermediate product 5α-androstanedione or 3α-Adiol). A preliminary experiment showed that HSD17B6 was again the only enzyme to use not only 3α-ADT as substrate, but also its isomer 3β-epiandrosterone (3β-ADT). Based on the finding that HSD17B6 has a wider range of substrates that can lead to AR activation, we were interested in finding potential inhibitors for HSD17B6. While colleagues of the Computational Pharmacy group of the University of Basel generated a homology model of HSD17B6 to perform a virtual screening, I generated different expression constructs that can be used to establish an enzymatic assay for testing any hits obtained from the screening. Discovery of an inhibitor can help to further understand the importance of androgen synthesis in PCa and ideally may even find clinical application.

The main project investigated the role of the “orphan” enzyme dehydrogenase/reductase (DHRS) 7 in PCa. This enzyme has so far no assigned physiological substrate but it appears to be a tumor suppressor in the prostate. This is based on publications that showed decreased expression of DHRS7 in clinical PCa samples and that reduced expression in the PCa cell line LNCaP leads to increased proliferation. In addition, it was shown that DHRS7 is capable of reducing, and therefore inactivating, the AR ligand 5α-DHT to 3α-Adiol. The goal of this project was to further understand the role of DHRS7 in PCa. Experiments indicated that the function of DHRS7 in PCa cells is surprisingly unrelated to AR signaling. In order to discover other potentially related molecular pathways, an siRNA-mediated knock-down of *DHRS7* in LNCaP cells was performed and followed by proteomic analysis. We discovered an increased expression of the epidermal growth factor (EGF) receptor (EGFR), a well known drug target in other cancers with both antibodies and small molecule inhibitors used to treat patients. Our findings were confirmed by molecular biology techniques in the LNCaP cells and in two additional PCa cell lines. Treating the cells with EGF after knock-down of *DHRS7* led to increased activation of the EGFR by phosphorylation. Trends of increased phosphorylation of downstream signaling proteins were observed as well. By using data obtained from clinical samples of PCa, we were able to show a negative correlation of DHRS7 and EGFR expression and finally, analysis of patient survival rates showed a positive correlation between high expression of DHRS7 and better survival rates while high expression of EGFR correlated negatively with survival rates. These results support the hypothesis that DHRS7 is a tumor suppressor in the prostate but future studies are required to further describe the relationship between DHRS7 and EGFR and to identify the substrate of DHRS7.

2 INTRODUCTION

2.1 Steroid Hormones

Steroid hormones regulate various physiological functions and participate in the development [1-3]. They can be separated into glucocorticoids, mineralocorticoids, progestogens, estrogens, and androgens. Androgens are sex hormones that play a pivotal role in male sexual differentiation, maturation, and spermatogenesis [4-7]. The importance of androgens in health and development comes together with a substantial role in the development of diseases, including PCa [5, 6, 8].

In essence, steroid hormones act by binding to their corresponding receptor that leads to conformational changes, dimerization, translocation into the nucleus, and gene expression control by binding to DNA elements of genes harboring the corresponding response elements [1, 2]. For androgens, the target receptor is the AR and 5α-DHT the primary ligand [6, 9, 10].

2.1.1 Steroidogenesis of Androgens

Androgen production is controlled by the hypothalamus through the secretion of gonadotropin-releasing hormone (GnRH), which stimulates the anterior pituitary gland to secrete follicle-stimulating hormone and luteinizing hormone (LH) [11-13]. The latter stimulates the Leydig cells of the testes to produce testosterone, which is converted to 5α-DHT in the prostate and other target tissues. Testosterone also participates in the negative feedback loop thus limiting its own production (Figure 1).

Of note is also corticotropin-releasing hormone (CRH) that is released by the hypothalamus [3, 11, 12]. It stimulates the anterior pituitary gland to release adrenocorticotropic hormone (ACTH). The adrenals, stimulated by ACTH, produce androgens in the *Zona reticularis*, particularly dehydroepiandrosterone (DHEA) (Figure 1). This is important in the context of PCa because this provides an alternative source of androgens other than the testes after castration [13].

The common precursor of all steroid hormones is cholesterol which is converted to pregnenolone by cytochrome P450 (CYP) 11A1 with ferredoxin reductase (FDXR) and ferredoxin (FDX1) participating in the electron transfer [3, 5].

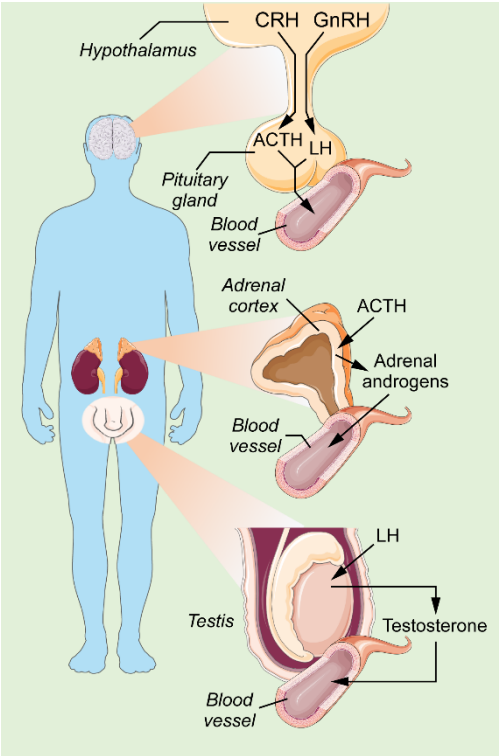

Figure 1 Hormonal regulation of androgen synthesis. Corticotropin- and gonadotropin-releasing hormone (CRH and GnRH, respectively), produced by the hypothalamus, stimulate the pituitary gland to secrete adrenocorticotropic hormone (ACTH) and luteinizing hormone (LH). ACTH stimulates the adrenal *Zona reticularis* to produce adrenal androgens and LH stimulates the production of testosterone in the testes.

Conventionally, through the 17β-hydroxylation and 17,20-lyase reaction, both mediated by CYP17A1 (with participation of CYP oxidoreductase [POR] and cytochrome b_5 type A [CYB5A]), pregnenolone is first converted to 17β-hydroxypregnenolone (17OH-pregnenolone) and then to DHEA (Δ^5-route) [3, 5, 14]. Alternatively, pregnenolone is first converted to progesterone by the 3β-hydroxysteroid dehydrogenase (HSD3B) 1 or 2, followed by the actions of CYP17A1, leading to 17β-hydroxyprogesterone (17OH-progesterone) and then to androstenedione through the Δ^4-route, although the Δ^5-route is preferred. To produce testosterone, DHEA is either A) first converted to androstenedione *via* HSD3B1/2 and then reduced by HSD17B3 or aldo-keto reductase (AKR) 1C3 to testosterone or B) first reduced by HSD17B3 or AKR1C3 to androstenediol and secondly converted by HSD3B1/2 to testosterone [3, 5, 8, 15]. Finally, testosterone is converted to 5α-DHT by the steroid 5α-reductase (SRD5A) 1 or 2, primarily in the target tissue [3-5, 8]. The production of 5α-DHT *via* DHEA and testosterone describes the conventional pathway and is indicated by orange color with the preferred Δ^5-pathway in Figure 2.

In the backdoor pathway, 5α-DHT is formed without testosterone as precursor. Instead, progesterone is hydroxylated by CYP17A1 to 17OH-progesterone, reduced to 17β-hydroxydihydroprogesterone (17OH-dihydroprogesterone) by SRD5A1, and further to 17β-hydroxyallopregnanolone (17OH-allopregnanolone) by AKR1C2/4 [3, 5, 8]. The 17,20-lyase activity of CYP17A1 will then lead to 3α-ADT and by the activity of AKR1C3 or HSD17B3 to 3α-Adiol [14]. This acts as the precursor to 5α-DHT, which is generated by the oxidative activity of a 3α-HSD, *e.g.* HSD17B6 [10]. Depending on the sequence of reactions performed, other intermediate products may occur. For example, progesterone may be reduced by SRD5A1 before 17β-hydroxylation or 3α-ADT is first oxidized to 5α-androstanedione [3, 5]. In Figure 2, the backdoor pathway is indicated with green color. The backdoor pathway is suspected to play a role in disorders of sexual development and other pathologies, including prostate cancer [3, 16-18].

A second alternative pathway converts androstenedione to 5α-androstanedione *via* SRD5A1, which is then reduced to 5α-DHT, thus skipping testosterone as precursor, and may play a role in PCa as well [5, 18, 19].

Inactivation of 5α-DHT occurs through reduction, by AKR1C2 to 3α-Adiol or by AKR1C1 to 3β-Adiol [20], and by glucuronidation [21, 22]. Glucuronidation of 3α-Adiol at the 3α-hydroxyl group is mediated by UDP-glucuronosyltransferase (UGT) 2B7 or at the 17β-hydroxyl group by UGT2B15/17. UGT2B17 can also glucuronidate 5α-DHT.

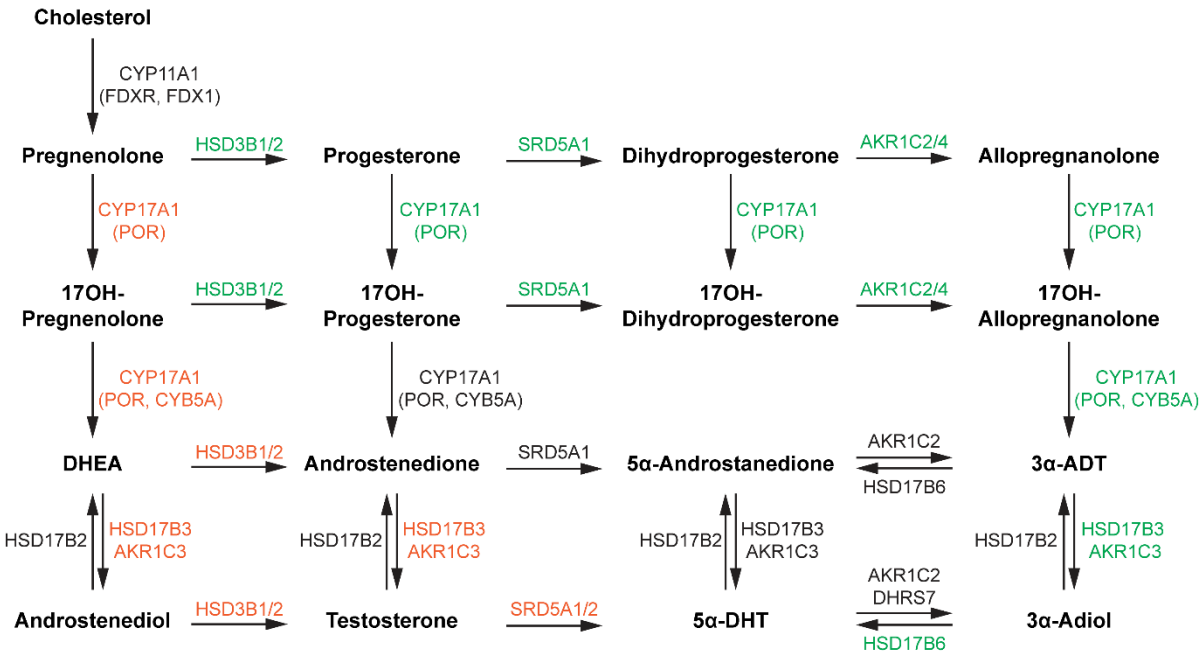

Figure 2 Androgen synthesis. Orange color indicates the conventional pathway with the preferred Δ^5-route and testosterone as precursor to 5α-DHT. Green color indicates the backdoor pathway with 3α-ADT and 3α-Adiol as precursors. The nomenclature of the different steroids is adressed in Table S1 in the supplementary information for an unambigous identification.

2.2 The Short-Chain Dehydrogenase/Reductase Superfamily

The enzyme superfamily of short-chain dehydrogenases/reductases (SDRs) consists of over 80 members in humans, subdivided into five clusters [23]. Most are localized in either the endoplasmic reticulum (ER), mitochondria, or cytoplasm, and fewer members in the peroxisomes, nucleus, and Golgi apparatus [23]. With one another they share only around 10-30% sequence identity but the Rossmann fold, the binding site of the cofactor nicotinamide adenine dinucleotide (phosphate) NAD(P)(H), is common to all SDRs and the majority of the members share the catalytic tetrad Asn-Ser-Tyr-Lys [23-26]. SDRs use a plethora of different substrates, including retinoids, lipids, xenobiotics, and steroids, including androgens [10, 15, 27], and are therefore involved in various physiological processes [23, 26, 28].

2.2.1 3α-Hydroxysteroid Dehydrogenases

A number of SDRs – DHRS9 (SDR9C4), retinol dehydrogenase (RDH) 5 (SDR9C5), RDH16 (SDR9C8), HSD17B10 (SDR5C1), and HSD17B6 (SDR9C6) – have been described to perform an oxidative reaction towards the 3α-hydroxyl group of steroidal substrates and are therefore referred to as 3α-HSDs [10, 29, 30]. This reaction is central to the backdoor pathway in androgen synthesis and for that matter these enzymes are suspected to play a role in PCa. Figure 3 schematically shows the cluster of 5α-reduced androgens of the backdoor pathway and the enzymatic activities required for their interconversions. Within the SDR superfamily the 3α-HSDs are phylogenetically closely related and located in the ER, except for HSD17B10 [23, 28, 31].

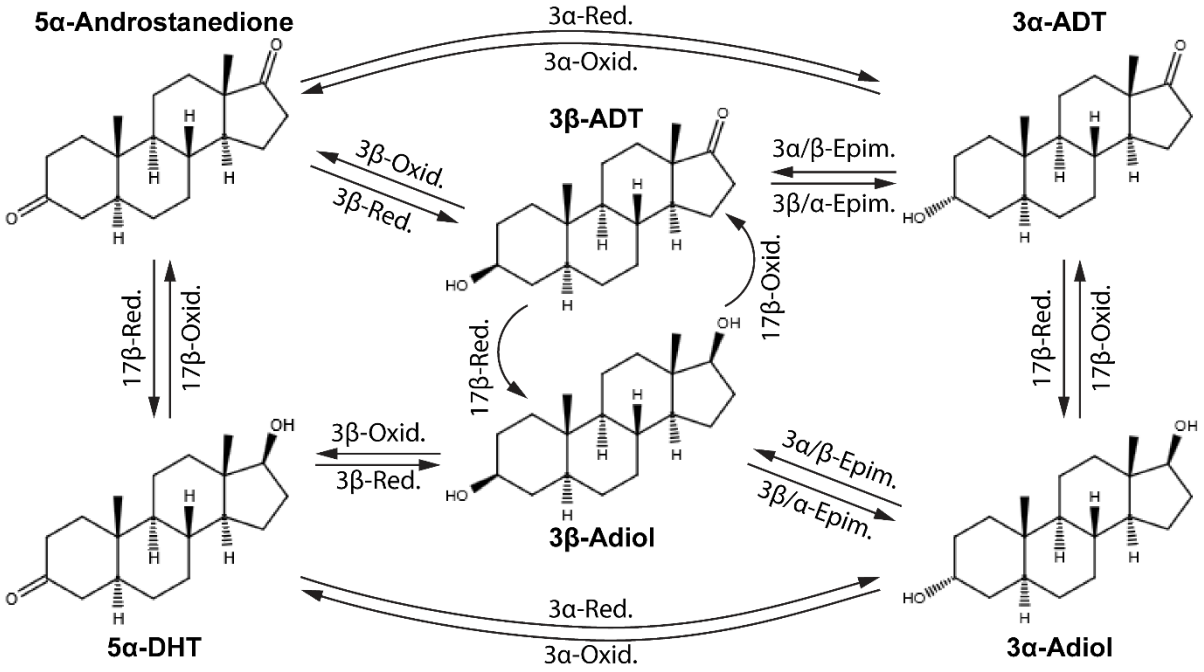

Figure 3. The cluster of 5α-reduced androgens in the backdoor pathway. The arrows indicate the interconversions of the androgens with the required enzymatic activity to perform the conversion by either epimerization (Epim.), oxidation (Oxid.), or reduction (Red.).

2.2.1.1 DHRS9

DHRS9 harbors an oxidative activity towards 3α-Adiol, allopregnanolone, and 3α-ADT but also on the 17β-hydroxyl position of 5α-DHT [32]. Interestingly, a weak isomerase activity was shown as well, converting allopregnanolone to the 3β-isomer isopregnanolone *via* 5α-dihydroprogesterone [32]. Oxidation of retinoids was also described for all-*trans* retinol [33]. *In vitro* experiments providing NADH as cofactor allows DHRS9 to perform reductive activities towards 3α-ADT and 5α-DHT [32]. Overall, it was claimed that the 3α-oxidation worked most efficiently and that the enzyme is abundantly expressed in the trachea [32]. The expression of DHRS9 is decreased in colorectal cancer compared to matched non-tumor tissue which was associated with higher chance of lymph node metastasis, tumor stage, disease recurrence, and lower survival rates [34]. Conversely, in pancreatic cancer, the expression of DHRS9 was shown to be increased and associated with lower survival rates [35, 36].

2.2.1.2 RDH5

Oxidative activity was observed towards 9-, 11-, and 13-*cis* retinol, but not all-*trans* retinol [37, 38]. Among steroids, 3α-Adiol and 3α-ADT are substrates for oxidation ([38]). RDH5 is expressed in retinal pigment epithelium, the mammary gland, liver, prostate, and other tissues [37-39]. In hepatocellular carcinoma (HCC), decreased expression was associated with lower overall survival rates and a higher frequency of metastases [40, 41]. Additionally, knock-down using siRNA led to faster cell growth, whereas overexpression slowed down proliferation and migration as well as a loss of the epithelial-to-mesenchymal transition (EMT) marker vimentin, but an increase of E-cadherin [40].

2.2.1.3 RDH16

Substrates for oxidation by RDH16 are 3α-Adiol, 3α-ADT, 13-*cis*, and all-*trans* retinol and reductive activity converting 5α-DHT into 3α-Adiol was shown as well [42, 43]. RDH16 is highly expressed in the liver but decreased in HCC [42-46], which was associated with lower survival rates [46]. This is supported by reduced cell migration and tumor formation in xenografts when cells overexpressed RDH16 [46].

2.2.1.4 HSD17B10

Of the five described 3α-HSDs, HSD17B10 is the only one not located in the ER, but in mitochondria instead [23, 47]. It is largely expressed in the brain but was detected in the prostate as well [48, 49]. Different catalytic activities have been shown, including a 3α-HSD activity towards allopregnanolone, 3α-ADT, and 3α-Adiol and an oxoreduction of 5α-DHT and 5α-androstanedione [48-51]. HSD17B10 was associated with various neurological diseases and intellectual disabilities, particularly Alzheimer's disease and Down's syndrome [48]. Additionally, elevated expression was observed in PCa epithelium and in osteosarcoma patients with poor response to therapy [49, 52].

2.2.1.6 HSD17B6

The tissue with the highest expression of HSD17B6 is the liver, with lower expression in the prostate, adrenals, spleen, lung, and other organs [53-57].

HSD17B6 was shown to perform oxidative reactions on the 3α-hydroxyl group of 3α-Adiol, 3α-ADT, and allopregnanolone and a weak oxidative activity towards 3β-ADT and all-*trans* retinol [53, 54, 56]. A reductive activity was detected as well, converting 5α-androstanedione to both 3α-ADT and 3β-ADT, with a preference for the latter (one third versus two thirds), and 5α-DHT to 3α- and 3β-Adiol [54, 56-58]. More interestingly, an epimerase activity was observed, interconverting 3α-ADT and 3β-ADT, with a preference for the 3α- to 3β-conversion both in microsomes and intact cells overexpressing HSD17B6 and a weaker 3α- to 3β-conversion of allopregnanolone to isopregnanolone [54].

While HSD17B6 is generally discussed in the literature as a 3α-HSD that leads to the formation of 5α-DHT [30, 59], one publication suggested a protective role of HSD17B6 in PCa instead through reduction and epimerization of 5α-DHT and 3α-Adiol, respectively, to 3β-Adiol, leading to increased activation of the estrogen receptor β (ERβ) [57]. In regards to other diseases, HSD17B6 was shown to be less expressed in HCC and the lower expression correlating with higher tumor stages [45, 60]. The lower expression of HSD17B6 was also associated with worse disease outlooks and overexpression of HSD17B6 in HepG2 cells led to decreased proliferation and migration [55, 60]. Besides PCa and HCC, a lower expression was also observed in lung and other cancers, but an increase in head and neck squamous cell carcinoma and breast cancer [55, 61]. Single nucleotide polymorphisms of HSD17B6 might be associated with hyperandrogenism in patients with polycystic ovarian syndrome [62].

2.2.2 The Orphan Enzyme DHRS7

DHRS7 (SDR34C1) is closely related to DHRS7B and -C, as well as to the better known 11β-hydroxysteroid dehydrogenase 1 (HSD11B1) [23, 28, 31] (Figure 4). It was first isolated from retinal tissue, but it is also expressed in the skeletal muscle, heart, kidney, pancreas, and the prostate [63-66].

It was shown that DHRS7 has a reductive activity towards the steroid hormones estrone, cortisone, and androstenedione, as well as towards several xenobiotics (*e.g.*

1,2-naphtoquinone, 9,10-phenanthrenequinone, and nicotine-derived nitrosamine ketone [NNK]), and all-*trans* retinal [64, 67, 68]. NADPH is the preferred cofactor and DHRS7 is bound to the ER membrane with the catalytic site facing the cytosol [27, 67] (Figure 4).

Cortisone was proposed to be converted to cortisol by DHRS7, but the product was identified as 20β-dihydrocortisone instead, revealing a 20β-reductase activity [27, 64, 67]. Although androstenedione was also reported to be a substrate in Sf9 cells, a conversion to testosterone could not be confirmed in DHRS7 overexpressing HEK-293 cells [27, 64, 67]. Instead, a time and concentration dependent conversion of 5α-DHT to 3α-Adiol was observed, which was further supported by a decreased AR-mediated luciferase activity when DHRS7-expressing HEK-293 cells were treated with 5α-DHT at concentrations of 1 nM and higher [27]. An *in silico* approach also predicted 5α-DHT to be a substrate, which was then confirmed experimentally [69]. The ability of DHRS7 to perform 20β- and 3α-reductions in the case of cortisone and 5α-DHT, respectively, was suggested to be due to the rotational symmetry of steroid hormones [27, 70].

The study of Araya *et al.* showing that DHRS7 is capable of reducing the AR ligand 5α-DHT to 3α-Adiol is of great interest [27]. It may help explain the previous observation that the expression of DHRS7 in PCa tissue is gradually decreased with

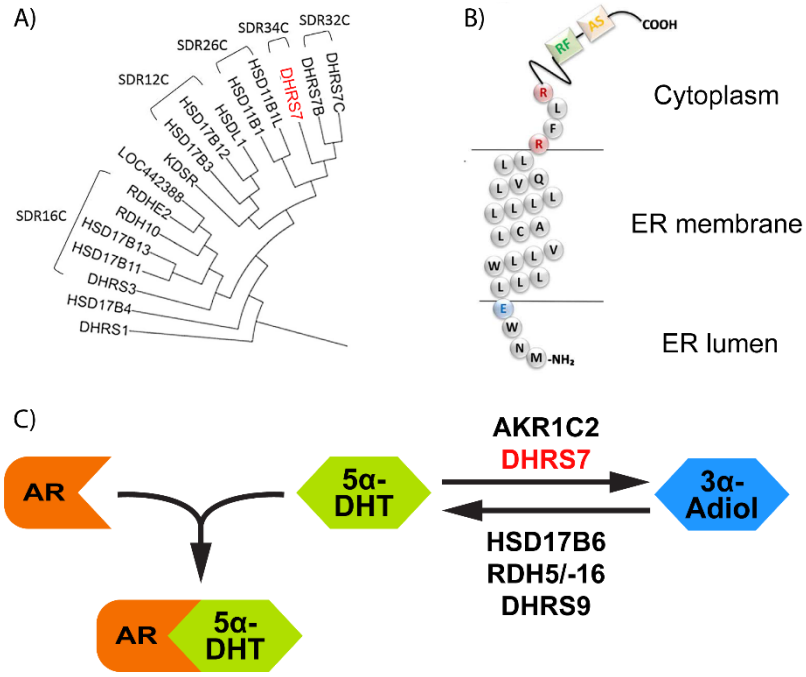

Figure 4. The orphan enzyme DHRS7. A) Cluster 3 of the phylogenetic tree of the SDR superfamily showing the close relationship of DHRS7 to DHRS7B, -C, and HSD11B1. B) Topology of DHRS7 in the ER membrane with the active site (AS) and the Rossmann fold (RF) on the cytoplasmic site. C) Proposed role of DHRS7 in the metabolism of 5α-DHT, preventing activation of the AR by 5α-DHT. Pictures taken from Štambergová H. *et al.* [64], Bray J. E. *et al.* [31], and Araya S. *et al.* [27] and adapted.

increasing Gleason score [63]. Furthermore, by performing siRNA-mediated knock-down of *DHRS7* an increase of cell proliferation and migration as well as a decreased adhesion of the LNCaP cells was observed. The changes of migration and adhesion were also seen in PC-3 and BPH1 cells, but no increase of proliferation. A microarray experiment followed by RT-qPCR of selected differentially expressed genes showed expression changes of genes related to cell adhesion, cell cycle, and apoptosis [63]. The loss of DHRS7 expression in PCa is supported by another publication that showed primary PCa to express higher levels of DHRS7 than metastatic, androgen independent bone marrow metastases [71]. Conversely, Romanuik *et al.*, using an LNCaP hollow fiber model, observed an increase of DHRS7 expression in LNCaP cells when transitioning from an androgen-sensitive towards a castration resistant phenotype. However, these experiments were performed in three mice only [72].

Taking together the loss of DHRS7 in higher grade PCa and metastatic samples, the increased aggressive phenotype of LNCaP cells after knock-down of *DHRS7*, and the ability of DHRS7 to convert the AR ligand 5α-DHT to 3α-Adiol raised the suspicion that loss of DHRS7 leads to higher intratumoral concentrations of 5α-DHT and thus promoting cancer progression. Figure 4 schematically displays the suggested role of DHRS7 in PCa.

2.3 Prostate Cancer

2.3.1 Anatomy of the Prostate

The prostate is part of the male reproductive system and located under the urinary bladder, in front of the rectum, and surrounds part of the urethra (prostatic urethra). The glandular part is divided into three major zones. The transitional zone (ca. 5% of the volume) surrounds part of the prostatic urethra and is typically the origin of benign prostatic hyperplasia. The central zone (ca. 25% of the volume) is behind the transitional zone and surrounds the ejaculatory ducts of the seminal vesicles. The peripheral zone (ca. 70% of the volume) is the most common origin of PCa and surrounds the transitional and central zones, except anteriorly, where the anterior fibromuscular stroma lays (Figure 5) [12, 73-75].

The prostate is made of two tissue types. The supporting stroma contains smooth muscle fibers and fibrous tissue. Embedded within the fibromuscular stroma are the acinar glands that transition into canals, which run together to form 12 - 20 main ducts that reach into the prostatic urethra [12, 74].

The glands are largely composed of luminal and basal epithelial cells. The secretory luminal cells are dependent on androgens and express AR whereas the basal cell layer maintains contact with the stromal tissue and houses prostatic stem cells [12, 74-76]. Scattered within the epithelium are neuroendocrine cells. They do not express AR and their function is unclear, but they are suspected to play a role in the growth regulation of the surrounding cells through a paracrine way [12, 75, 77-80]. The various epithelial and stromal cells can be identified based on their protein expression pattern [81].

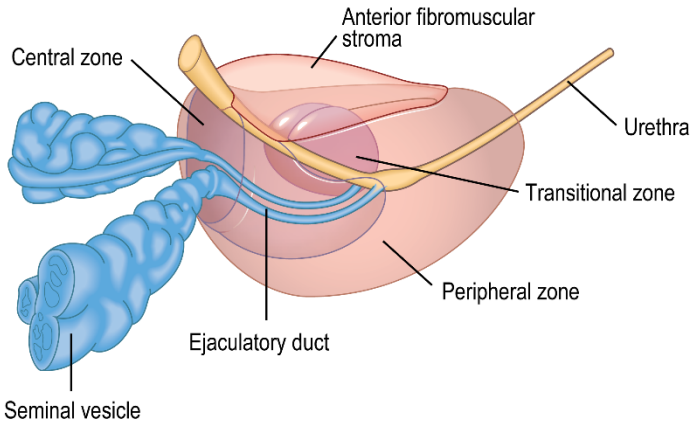

Figure 5 Anatomy of the prostate. The prostate is composed of three major zones and the anterior fibromuscular stroma. Picture taken from Gray's Anatomy and adapted [12].

2.3.2 Epidemiology

2.3.2.1 Incidence & Mortality

The Global Cancer Statistics 2018 estimated PCa to be the second most commonly diagnosed cancer (13.5%) and the 5th most common cause of cancer related deaths (6.7%) in males. The highest incidence rates can be found in Australia/New Zealand and Northern and Western Europe, whereas the Caribbean and South and Middle Africa show the highest mortality rates. The lowest rates for both incidence and mortality are generally observed in different Asian regions [82].

In Switzerland, based on the latest Swiss Cancer Report [83], during 2008 to 2012, there were on average about 6200 PCa new cases and ca. 1300 PCa related deaths per year. With that, it was the most common one (30%) and second most common cause of cancer related deaths (15%) after lung cancer in males. With an overall life-time risk of 16.4%, ca. every 6th male will be diagnosed with PCa at some point in his life.

2.3.2.2 Risk Factors

There are three major risk factors for PCa – older age, being of black ethnicity, and a positive family history of PCa [84].

Diagnosis of PCa at a young age (*i.e.* younger than 50 years) is uncommon, but incidence rates increase sharply after the age of 50 years [83, 85]. Accordingly, autopsy studies showed increased prevalence of undiagnosed PCa with older age [86].

Prevalence of PCa in autopsy studies was also different for various ethnicities. Asian males had a lower prevalence of PCa than males of European descent and black males had the highest [86, 87]. African American males show the highest incidence and mortality rates compared to other population groups and are more likely to present a more advanced type of PCa at the time of diagnosis [88-91].

Not only is a positive history of PCa in the family a risk factor, the risk is even higher when the family member was diagnosed at a younger age, was of first degree, and with the number of cases in the family. In addition, some studies have hinted at higher PCa risk when there were cases of breast cancer in the family [92-96].

2.3.3 Diagnosis & Treatment

2.3.3.1 Screening

Screening for PCa, in hope of detecting it in an early, potentially curable state, is performed by digital rectal examination and by measuring blood levels of prostate-specific antigen (PSA). Tumors that are palpable tend to be rather large already and not necessarily confined to the primary organ anymore and increased PSA levels are not necessarily related to cancerous tissue [75, 97-99]. While one patient can benefit from an early PCa detection and earlier treatment due to a PSA test [100-102], a patient with a less aggressive form is in danger of being "overdiagnosed" and suffer more from the unnecessary treatment rather than from the asymptomatic PCa itself [97, 103, 104]. Some studies indicated a link of PSA screening to reduced incidence of higher grade or late stage PCa or a lower mortality rate but others have failed to do so [100, 101, 105-107]. Thus, population wide PSA screening is somewhat controversial. In light of these inconclusive observations regarding the benefit of PSA screening and the danger of overdiagnosis and overtreatment, PSA testing should be performed on a case by case basis that weighs the benefits against the risks, incorporates patient-related factors (*e.g.* life expectancy and comorbidities), and the patient's own preferences (a process termed informed decision making) [75, 98, 99, 103, 108].

2.3.3.2 Tumor Staging

In a suspected PCa case, a prostate biopsy should be performed, not only to confirm PCa as the cause of elevated PSA levels and/or an odd finding during digital rectal examination, but also for PCa staging purposes [98, 109, 110]. Traditionally, PCa is graded according to the Gleason grading system, a histological assessment of the biopsies with originally five architectural patters (Gleason grades 1 to 5; the higher the less differentiated) [109, 111, 112]. The grades of the two most common patterns in one sample are added, leading to a Gleason score of 2 to 10 – for example, a biopsy with grades 3 and 4 results in a Gleason score of 7. Over time, because of modifications to the grading system and a lack of reported grades 1 and 2, the scores nowadays range from 6 to 10 [113]. Additionally, score 7 was further stratified into

3+4=7 and 4+3=7 due to better prognostic value and score 9 and 10 were laid together to 9-10, leading to a five tiered scoring system [111, 114]. A more modern adaption translates the Gleason scores into Gleason score groups 1 to 5. Group 1 represents the scores ≤ 6 and group 5 the scores 9-10 [109, 111]. This grouping system was accepted by the WHO in 2016 and a schematic of the Gleason grading system is shown in Figure 6 [115]. The benefit of grouping the scores into groups 1 to 5 reduces a patient's false perception of a grade 6 cancer to be advanced, while in fact it is the least severe form (*i.e.* the most differentiated) [109, 111].

Besides the Gleason grading system, the tumor-node-metastasis staging is used as well, to grade the cancer according to local tumor stage and size (T), affected locoregional lymph nodes (N), and distant metastases (M) [116].

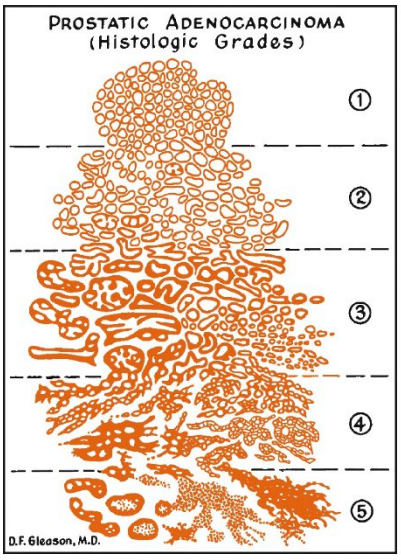

Original Gleason Grading		
Grades		Scores
1 – 5	Add together the two most prominent grades →	2 – 10

Conventional Grading			
Grades		Scores	Groups
3	Add together the two most prominent grades →	≤ 6	1
		3+4 = 7	2
4		4+3 = 7	3
		8	4
5		9-10	5

Figure 6. Gleason grading system. Left is the original drawing by Gleason D.F. [112]. In the middle and to the right the original and modified grading systems, respectively.

2.3.3.3 General Treatment Outline

Cancer staging is important for the risk stratification that allows more adequate therapy. In the case of localized disease, risk is typically divided into low risk, intermediate risk (with subdivisions low and high intermediate risk), and high risk. According to the risk classification and other factors, *e.g.* comorbidities and patient preferences, different treatment options are available. Choosing the appropriate treatment also depends on the absence or presence of metastases and whether the cancer is still sensitive to hormone treatment or not [75, 110, 117].

Localized Prostate Cancer

For patients with localized, low risk disease or favorable intermediate risk, active surveillance is a good option to avoid unnecessary side effects due to overtreatment with repeated follow-ups allowing the evaluation whether additional interventions are necessary [75, 110]. Otherwise, prostatectomy and radiotherapy are options for patients with localized PCa of any risk class and are applied with a curative attempt. However, patients of older age with comorbidities or otherwise lower life expectancy may benefit more from “watchful waiting” rather than active intervention due to the potential side effects and complications associated with intervention. Depending on the risk of disease spread, patients who do undergo prostatectomy should consider pelvic lymph node dissection and similarly, adjuvant androgen deprivation therapy along radiotherapy may be recommended [75, 110].

Progressive Prostate Cancer

For recurrent or metastatic PCa, it is important to differentiate between cancer cases that are still sensitive to androgen deprivation therapy (castration sensitive PCa) and those that have progressed beyond that stage (castration resistant PCa, CRPC) [75, 117].

In 1966, Charles Brenton Huggins received the Nobel Prize for Physiology or Medicine “for his discoveries concerning hormonal treatment of prostatic cancer” [118]. His work demonstrated that PCa reacts to androgen deprivation by means of surgical castration (bilateral orchiectomy), leading to clinical improvement [119]. Orchiectomy was shown to reduce total testosterone levels in serum to ~15 ng/dL (normal values: ~200-750 ng/dL) and patients with levels of less than 20 ng/dL had better survival prospective compared to individuals with levels higher than 20 ng/dL [120, 121].

This shows the strong dependency of PCa on androgens, whose primary organ of origin in males are the testes [11-13]. Although surgical castration is performed less often nowadays, the concept of depriving the tumor of androgens continues to find application in clinical practice by chemical castration using agonistic or antagonistic GnRH analogues. This therapy approach is referred to as androgen deprivation therapy and is the main pillar in PCa treatment [13, 75, 117, 122, 123]. An advantage of chemical castration over orchiectomy is the potential reversibility but a drawback of

agonistic GnRH analogues is their potential to cause a transient increase of testosterone that can lead to short term worsening of symptoms. This can be avoided by using GnRH receptor antagonists instead or by coadministration of anti-androgens [117, 123-125].

Anti-androgens are AR antagonists and can be classified as steroidal (*e.g.* cyproterone acetate) and non-steroidal (*e.g.* flutamide, bicalutamide, or enzalutamide) [13, 75]. Monotherapy with anti-androgens has been shown to be inferior to surgical or chemical castration alone [126, 127], but as an addition to GnRH analogues they can slightly improve survival rates [128, 129].

An alternative to anti-androgens for combinational therapy is abiraterone acetate (the prodrug of abiraterone) [130]. This compound targets extragonadal androgen synthesis by inhibition of CYP17A1, thus preventing the formation of the androgens DHEA and androstenedione [131]. A metabolite of abiraterone, Δ^4-abiraterone formed by the activity of HSD3B1/2, has anti-AR and other inhibitory properties that participate in abiraterone's overall pharmacology [131]. In order to limit the adverse mineralocorticoid excess prednisolone is coadministered with abiraterone acetate [132].

Addition of chemotherapy by the use of docetaxel to androgen deprivation therapy has shown to be beneficial and can be used for cotreatment as well [133]. Various combinations of drugs with androgen deprivation have been explored and are applied regularly in clinical practice [75, 134].

Even though androgen deprivation therapy or primary combinational therapy performs well initially, therapy fails eventually and PCa develops into a form that is termed CRPC and considered incurable [75]. Androgen deprivation therapy is continued nonetheless since remaining on GnRH analogue treatment in that stage has shown benefits [135, 136]. Overall, therapy for CRPC is not largely different from advanced hormone sensitive PCa. If not already in use, anti-androgens, abiraterone acetate, or docetaxel can be used as addition to the continued androgen deprivation therapy or alternatively challenge the cancer with another drug. Less conventional alternatives exist as well, for example bone targeting radionuclides [75, 117].

2.3.4 Late Stage Prostate Cancer

2.3.4.1 Disease Progression

Most cases of PCa rise from either luminal or basal epithelial cells in the peripheral zone of the prostate [12, 73-75, 137]. A rare but aggressive form of PCa, termed neuroendocrine PCa, may originate from neuroendocrine cells themselves, but it seems that a differentiation of "conventional" PCa (adenocarcinoma) towards a neuroendocrine phenotype, including a lack of AR, occurs more often [75, 77, 138]. This may happen through selection of cell populations that are resistant to androgen deprivation therapy [138-140]. Cellular markers can help differentiate between the cellular origins of PCa and current phenotype [75, 77, 138].

Part of disease progression is expanding through the basement membrane and extracellular matrix. This process involves loss of cellular polarity, loss of cell-cell and cell-stroma contact, leads to increased migratory capacity, and is commonly referred to as EMT [75, 141, 142]. An example of a protein involved in EMT is E-cadherin that participates in cell adhesion and is often lost. EMT allows PCa cells to detach from their primary site and disseminate to new sites *via* the lymphatic or vascular system. Typical sites for metastases to manifest are lymph nodes and bones [75, 141, 142].

PCa also progresses in terms of response to treatment [75, 143]. Prostatectomy and radiotherapy are curative attempts but are not always successful. In one study for example, chances for 5, 10, and 15 year survival without any form of recurrence after radical prostatectomy for localized disease were 84%, 74%, and 66%, respectively [144]. PCa relapse after local treatment can be due to previously undetected, occult metastases or some cancer cells surviving therapy [75]. And although androgen deprivation therapy performs well initially, therapy fails eventually, yet AR signaling continues [143, 145, 146]. It is at this stage that PCa is termed CRPC and considered incurable.

2.3.4.2 Transition to Castration Resistant Prostate Cancer

The continued AR-mediated signaling in PCa and its contribution to CRPC can be divided into different mechanisms, though they are not mutually exclusive (Figure 7). These include increased intratumoral androgen synthesis, increased sensitivity

towards androgens, increased ligand spectrum through mutations of the AR, and androgen independent signaling of the AR [9, 75, 143]. However, bypassing the AR through alternative signaling pathways is possible as well [147, 148].

Increased Androgen Production

Synthesis of androgens in tissues other than the testes is one mechanism how PCa progresses to a castration resistant form. The adrenals produce DHEA that can be used for the formation of 5α-DHT [149]. A stabilizing mutation in *HSD3B1*, leading to increased resistance to ubiquitination and proteasomal degradation without affecting the enzymatic activity, was reported. Compared to the wild-type enzyme, this led to increased 5α-DHT formation and faster tumor formation of xenografts with this mutation in castrated mice [150].

Abiraterone targets androgen synthesis by inhibition of CYP17A1 [131]. However, resistance to abiraterone can occur through increased expression of enzymes involved in androgen synthesis, including abiraterone's target CYP17A1 [151, 152], but also other enzymes in androgen synthesis, *e.g.* CYP11A1 and AKR1C3, have been reported to be upregulated under conditions reflecting CRPC [71, 153, 154].

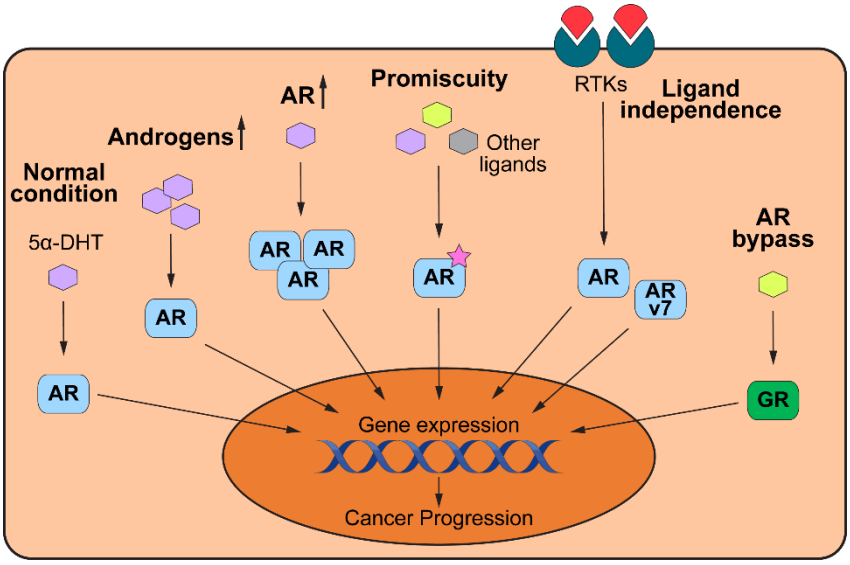

Figure 7. Mechanisms that can lead to CRPC. Under normal conditions, 5α-DHT binds to the AR and iniates transcriptional regulation that can be amplified by increased production of androgens or AR. Mutations of the AR can lead to promiscuity and increased ligand spectrum. Through other signaling pathways, *e.g.* through receptor tyrosine kinases (RTKs), or splice variants, AR signaling can be androgen independent. Bypass of the AR can occur through glucocorticoid receptor (GR) signaling.

Increased Sensitivity to Androgens

Increased sensitivity of the AR towards residual androgens after castration happens primarily through overexpression of AR which is more common in progressive disease compared to primary PCa [146, 155-158]. Cancer cells with higher levels of AR may have a growth advantage under active androgen deprivation therapy. Increased sensitivity to androgens can also occur through increased coactivators or by synergistic activation by other pathways (*e.g.* ERBB2) [158, 159].

Androgen Receptor Promiscuity

Mutations of the AR can lead to a broadened ligand spectrum. A great example is the mutation T877A present in the LNCaP cell line. This allows estradiol, progesterone, and even the anti-androgen flutamide to act as agonists [160, 161]. Another example is the F876L mutation that leads to agonistic behavior of enzalutamide [162]. AR promiscuity, turning bicalutamide agonistic, has also been observed in a model of AR overexpression, although it appeared that this was due to altered coactivator recruitment [146].

An interesting observation is that a stop of anti-androgen treatment can lead to a transient improvement in terms of PSA response in some patients – a phenomena referred to as anti-androgen withdrawal syndrome [163, 164]. It suggests that in these patients the AR has acquired mutations that render anti-androgens agonistic.

Ligand Independent Androgen Receptor

The AR can continue to mediate cellular effects by transcriptional activity independently of androgens by the occurrence of AR splice variants that lack the ligand binding domain [151, 165, 166]. The most commonly and best described one is the AR splice variant 7 (ARv7) that was reported to appear in about 50% of tumor samples (ca. 35% in adjacent non-tumor tissue) and a median ratio of ARv7 to full-length AR expression of ca. 20% [156, 167].

Another mechanism of the AR to become androgen independent is the increased signaling through other mediators. For example, ectopical expression of the AR in the AR-negative DU145 cells followed by treatment with insulin-like growth factor 1 or

interleukin-6 led to the transcriptional activation of the AR in the absence of androgens [168, 169]. Treatment of PCa cells with EGF induced AR phosphorylation and downstream signaling and levels of phosphorylated AR were observed to be higher in hormone refractory PCa [170, 171]. The EGFR was shown to be increased in advanced PCa and may contribute to disease progression [172, 173]. Also, treatment with forskolin led to AR transactivation, suggesting AR activation through protein kinase A [174, 175].

Androgen Receptor Bypass

Finally, PCa can be independent of the AR signaling. An LNCaP cell model with *AR* knock-out showed strong resistance against enzalutamide and loss of AR regulated gene expression could be replaced by the action of the glucocorticoid receptor (GR) [147]. In another example, an LNCaP model of AR independent growth was shown to be sustained by fibroblast growth factor receptor signaling [176].

Lastly, PCa may transition to a neuroendocrine phenotype [177] with a shift of transcriptional profile that can include a decrease of AR expression [178]. Loss of the retinoblastoma protein transcriptional corepressor 1 (RB1) and the tumor protein p53 may induce lineage plasticity, leading towards a neuroendocrine phenotype with resistance to the anti-androgen enzalutamide [139, 140].

3 AIMS OF THE THESIS

PCa is a common malignancy in males and signaling through the AR, mediated by androgens, is a principal aspect of the molecular biology of this disease. The importance of the androgens testosterone and 5α-DHT is exemplified by depriving the cancer cells of said androgens though surgical or chemical castration. This leads to cancer regression and is often supported by pharmacological inhibition of the AR and extragonadal androgen synthesis. Unfortunately though, cancer recurrence and progression to therapy resistance are common. Therefore, better understanding of the molecular biology of this disease and new therapeutic approaches are urgently needed.

Project 1 – HSD17B6:

Several enzymes, grouped as 3α-HSDs, were shown to convert 3α-Adiol to the main AR ligand 5α-DHT. This conversion is a key component of the backdoor pathway of androgen synthesis. We aimed to compare the ability of the 3α-HSDs to cause AR activation by overexpression of these enzymes in an intact cell system followed by treatment with 3α-Adiol. We also wanted to compare the performance of the 3α-HSDs to oxidize 3β-Adiol and the potential to prevent AR transactivation by reducing 5α-DHT. In order to find potential inhibitors, we collaborated with the Computational Pharmacy group to create a homology model of HSD17B6 for a virtual screening and intended to generate various expression constructs that can be used to establish an enzymatic activity assay for testing any potential hits.

Project 2 – DHRS7:

It was shown that the expression of DHRS7 is lower in higher grade PCa, that siRNA-mediated knock-down of *DHRS7* leads to an increased aggressive phenotype of LNCaP cells, and that DHRS7 is capable of inactivating the AR ligand 5α-DHT to 3α-Adiol. It was our goal to further understand the mechanism by which loss of DHRS7 can contribute to PCa progression. For that purpose, we used siRNA-mediated knock-down of *DHRS7* followed by treatment with 5α-DHT. To discover potentially involved pathways other than the AR, we performed proteomics after knock-down of *DHRS7* and wanted to support our findings by incorporating patient derived data.

4 PROJECT 1 – HSD17B6

4.1 Materials & Methods

Chemicals & Reagents:

CV-1 cells were a kind gift from Prof. Dr. Martin Spiess (Biozentrum, University of Basel, Switzerland). Minimum essential medium (51416C), trypsin (T4174), sodium pyruvate (S8636), the GenElute Plasmid Miniprep-Kit (PLN350-1KT), dNTPs (D7295-.2ML), Geneticin G-418 (A1720), radioimmunoprecipitation assay buffer (R0278), cOmplete Mini proteinase inhibitor cocktail (11 836 153 001), ampicillin (10 835 242 001), and the horse-radish peroxidase-conjugated anti-mouse antibody (A0168) were bought from Sigma-Aldrich (St. Louis, MO, USA). Fetal bovine serum (FBS) was obtained from Biowest (Nuaillé, France), Opti-MEM (51985-026) from Gibco, Life Technologies (Carlsbad, CA, USA), and polyethylenimine (PEI) (23966) from Polysciences, Inc. (Warrington, PA, USA). D-Luciferin sodium salt (BC218) was purchased from Synchem (Felsberg, Germany). The Galacto-Light Plus System (T1009) and Pierce bicinchoninic acid assay kit (23225) were bought from Thermo Fisher Scientific (Waltham, MA, USA). The SpectraMax L Microplate Reader was obtained from Molecular Devices (San Jose, CA, USA) and GraphPad Prism from GraphPad Software (San Diego, CA, USA). Penicillin-streptomycin (4-01F00-H) and L-Glutamine (5-10K00-H) were purchased from BioConcept (Allschwil, Switzerland) and the iProof HF DNA polymerase (1725301) from Bio-Rad Laboratories, Inc. (Hercules, CA, USA). The DpnI (R0176S) and BsmBI-v2 (R0739) restriction enzymes were purchased from New England Biolabs (Ipswitch, MA, USA). Primers for site directed mutagenesis and cloning were obtained from Microsynth (Balgach, Switzerland; Table S2). The PureYield Plasmid Maxiprep System (A2393), *Pfu* DNA Polymerase (M7741), Wizard SV Gel and PCR Clean-Up System, and T4 DNA ligase (M180A) were purchased from Promega (Madison, WI, USA) and the anti-HSD17B6 antibody (ab88892) from Abcam (Cambridge, UK). The anti-β-Actin antibody (sc-47778) was bought from Santa Cruz Technology (Dallas, TX, USA). The MEXi-293E cells (2-6001-001), pDSG-IBA103 vector (5-5220-001), MEXi-Cultivation (2-6010-010), and Transfection Medium (2-6011-010) were purchased from IBA Lifesciences (Goettingen, Germany) and the Fusion FX device from Vilber (Collégien, France). The

polyvinylidene fluoride membrane (IPVH00010) and Immobilon Western horse-radish peroxidase substrate kit (WBKLS0500) were obtained from Merck KGaA (Darmstadt, Germany). Plasmids expressing C-terminally FLAG-tagged RDH5 (NM_002905), RDH16 (NM_003708), and DHRS9 (NM_001142270) in pcDNA3.1 were purchased from GenScript (Piscataway Township, NJ, USA) and the other plasmids were available in house. 5α-DHT (A2570-011), 3α-Adiol (A1170-000), 3β-Adiol (1220-000), 5α-androstanedione (A1630-000), 3α-ADT (A2420-000), and 3β-ADT (A2490-000) were bought from Steraloids Inc. (Newport, RI, USA).

Cell Culture:

CV-1 cells were cultured in minimum essential medium with 10% FBS, 100 U/mL penicillin, 0.1 mg/mL streptomycin, 2 mM L-glutamine, and 1 mM sodium pyruvate (final concentrations) in a 5% CO_2 atmosphere at 37°C. Cells were passaged at roughly 70 - 80% confluence by rinsing them with PBS and trypsinization. Charcoal treated medium was prepared by incubation on a rotor for 1 h at room temperature with 4 mg/mL charcoal and centrifugation (2,500 g, room temperature, 5 min). This was done twice, followed by sterile filtration (0.2 µm). The MEXi-293E cells were cultured in MEXi-Cultivation medium with 50 mg/L G-418 and 8 mM glutamine (final concentrations) in a 5% CO_2 atmosphere at 37°C on a shaker and were passaged by diluting them 1:10 - 1:15 every 3 - 4 days.

Transactivation Assay:

CV-1 cells were seeded on 24-well plates (50’000/well), washed after 18 h with PBS and the medium was replaced by Opti-MEM. Cells were transfected with plasmids coding for a constitutively active luciferase (cLuc) (10 ng/well), an AR dependent β-galactosidase (MMTV-LacZ) (160 ng/well), AR (160 ng/well), and either HSD17B6, DHRS9, RDH5, RDH16, HSD17B10, or empty pcDNA3.1 vector (70 ng/well) with 1200 ng PEI in 50 µL Opti-MEM after the transfection mix was incubated at room temperature for 15 min. After 6 h, Opti-MEM was replaced by normal culture medium and after another 16 h, cells were washed with PBS and incubated for 2 h in charcoal treated medium. Then, medium was changed to a dilution series prepared in charcoal

treated medium containing the steroids as indicated. After 24 h, medium was removed and cells were lyzed in 60 µL Tropix lysis solution containing 0.5 mM dithiothreitol, incubated for 5 min at room temperature, and stored at -80°C for at least 30 min. Of the lysate, 20 µL were transferred to a 96-well plate to analyze luciferase activity by adding 100 µL D-luciferin solution (0.47 mM D-luciferin, 0.53 mM ATP, 0.27 mM CoA, 0.13 mM EDTA, 33.3 mM dithiothreitol, 8 mM $MgSO_4$, 20 mM tricine [pH 7.4]) and 20 µL to analyze β-galactosidase activity using the Galacto-Light Plus System (addition of 70 µL of Tropix GALACTON-Plus in Tropix Galacto Reaction Buffer Diluent, 1:100 [v/v], 30 min incubation in the dark at room temperature, followed by addition of 100 µL Tropix Accelerator II). A Spectramax L Microplate Reader (SoftMax Pro v5.4.6.005) was used to measure luminescence after plates were dark adapted for 1 min and the substrate was added. Activity of β-galactosidase was normalized to the luciferase activity and the DMSO control. The PureYield Plasmid Maxiprep System was used to generate plasmids on demand from glycerol-stocks of *Escherichia coli* expressing the desired construct.

Site Directed Mutagenesis:

Site directed mutagenesis was performed using the iProof HF DNA polymerase with 25 ng of plasmid template, 125 ng of forward and reverse primers, and 200 µM dNTPs. The PCR settings were as following: 30 s at 98°C, 12 cycles with melting for 30 s at 98°C, annealing for 1 min at 55 °C, and elongation for 3 min 15 s at 72°C, and finalized with 10 min at 72°C. Successful PCR was checked by loading 10 µL of the PCR product on a 0.8% agarose gel. The remaining PCR product was further processed for the transformation of competent cells.

Transformation of Competent Cells:

The parent template in the remaining PCR product was digested by incubation with 10 U of DpnI for 1 h at 37°C. Of the digest, 5 µL were used for transformation into competent cells by incubation on ice for 20 min, heat pulsed for 90 s at 42°C, incubation on ice for 5 min, addition of 1 mL of super optimal broth with glucose (SOC; 2% tryptone [w/v], 0.5% yeast extract [w/v], 8.56 mM NaCl, 2.5 mM KCl, 10 mM $MgCl_2$, 7.15 mM

glucose), and incubation for 1 h at 37°C. After spinning down, the supernatant was removed until about 50 µL was left which was transferred on agar plates prepared from lysogy broth (171 mM NaCl, 1% tryptone [w/v], 0.5% yeast extract [w/v], 100 µg/mL ampicillin with added 2% agar [w/v]) and incubated overnight at 37°C. Colonies were picked the next day and incubated overnight in 4 mL lysogy broth. DNA was isolated using the GenElute Plasmid Miniprep-Kit and sequenced at Microsynth using a standard CMV-forward primer.

Cloning into the pDSG-IBA103 Vector:

PCR was performed using the *Pfu* DNA Polymerase with 1000 ng of DNA template, 200 nM of forward and reverse primer, and 200 µM dNTPs. The PCR settings were as following: 3 min at 94°C, 35 cycles with melting for 30 s at 94°C, annealing for 30 s at 60°C, and elongation for 2 min at 72°C, and finalized with 5 min at 72°C. The PCR product was run on a 1% agarose gel, cut out and purified using the Wizard SV Gel and PCR Clean-Up System. The purified PCR product was then cloned into the pDSG-IBA103 vector according to the StarGate Direct transfer cloning protocol with the T4-DNA Ligase and the BsmBI-v2 restriction enzyme by incubation for 1 h at 37°C. Of the product, 10 µL were used to transform competent cells as described above, plated on agar plates prepared with 100 µL of 10 mM IPTG and 40 µL of 50 mg/mL X-Gal, and incubated overnight at 37°C. White colonies were selected and further processed as described above.

Transfection of MEXI-293E cells:

MEXi-293E cells (10.5×10^6 in 7 mL) were collected in a Falcon tube and centrifuged (200 g, 2 min, room temperature). They were then suspended in 7 mL of transfection medium and placed on a 10 cm dish in the cell incubator for 10 min. The pDGS-IBA103 vector coding for HSD17B6 was added dropwise (1500 ng/mL) and cells were placed into the incubator for 10 min. PEI was added dropwise (4.5 µg/mL) and the cells placed into the incubator for 3 h. Cells were then diluted 1:2 with culture medium and incubated for 48 h until lysis.

Western Blot:

Transfected and non-transfected MEXi-293E cells were counted, transferred to a Falcon tube, centrifuged (200 g, 2 min, room temperature), and washed with 5 mL of PBS. Cells were then lyzed with 100 µL radioimmunoprecipitation assay buffer containing proteinase inhibitor per 1 × 10^6 cells. Protein concentration was determined by Pierce bicinchoninic acid assay, samples were boiled for 5 min at 95°C in Laemmli buffer (5 mM Tris-HCl, pH 6.8, 10% glycerol [v/v], 0.2% sodium dodecyl sulfate [w/v], 1% bromophenol blue [w/v], 5% β-mercaptoethanol [v/v]), and stored at -20°C until Western blot. Twenty µg of protein were separated by SDS-PAGE (12.5% gel) and transferred to a polyvinylidene fluoride membrane. The membrane was blocked with 10% [w/v] defatted milk in TBS-T (1.11 g/L Tween 20, 20 mM Trizma Base, 137 mM NaCl, pH 7.6) at room temperature for 1 h. Incubation with the primary antibodies was done overnight at 4°C in 5% [w/v] milk in TBS-T (dilution 1:1000 for HSD17B6, 1:2000 for β-Actin). Membranes were washed four times for 15 min in TBS-T, incubated with secondary antibody (dilution 1:5000) for 1 h at room temperature, and washed again four times for 15 min in TBS-T before acquiring the image using the HRP substrate kit in a Fusion FX device.

Statistics:

Statistical significance was tested using GraphPad Prism (v5.04) by applying two-way ANOVA test followed by Bonferroni multiple comparison post-test. *P*-value < 0.05 was considered to indicate a statistically significant difference.

4.2 Results

To investigate the ability of HSD17B6, DHRS9, RDH5, and RDH16 to activate the AR by oxidizing 3α- or 3β-Adiol, as well as preventing AR activation by 3-oxoreduction of 5α-DHT, a transactivation assay using CV-1 cells was performed.

Initially, we wanted to include HSD17B10 in these experiments. However, earlier studies either indicated no activity [10] or only at high substrate concentrations, *i.e.* 5 µM and higher [49, 50]. Our preliminary experiment did not detect any relevant activity with any substrate even at the highest concentration of 100 nM, with the

exception of a trend to increased AR transactivation for 3α-Adiol (Figure 8). For this reason, we did not further study this enzyme

Treatment of cells expressing HSD17B6, DHRS9, RDH5, RDH16, or empty vector control with 5α-DHT led to a concentration dependent AR transactivation. No differences were observed when comparing cells transfected with empty control vector to those expressing DHRS9, RDH5, or RDH16. The only statistically significant differences were seen with cells expressing HSD17B6 at the two highest concentrations (33.3 and 100 nM, Figure 9).

3α-Adiol showed an AR transactivation at high concentrations (33.3 and 100 nM) with the empty vector control, but the expression of any of the 3α-HSDs (except HSD17B10) led to a significantly higher AR transactivation. Statistically significantly increased AR transactivation was achieved at concentrations as low as 0.10 nM in cells expressing RDH16 and 0.33 nM with HSD17B6 and RDH5. With DHRS9, statistically significantly higher AR transactivation was observed at concentrations of 10 nM and higher (Figure 9), indicating it possesses weaker 3α-HSD activity than HSD17B6, RDH5, and RDH16.

Similarly to 3α-Adiol, 3β-Adiol showed increased AR transactivation in cells with empty vector control, starting at concentrations of 3.33 nM. There was no difference in AR transactivation when cells expressed DHRS9, RDH5, or RDH16. However, when expressing HSD17B6, there was a clear trend of increased AR transactivation at

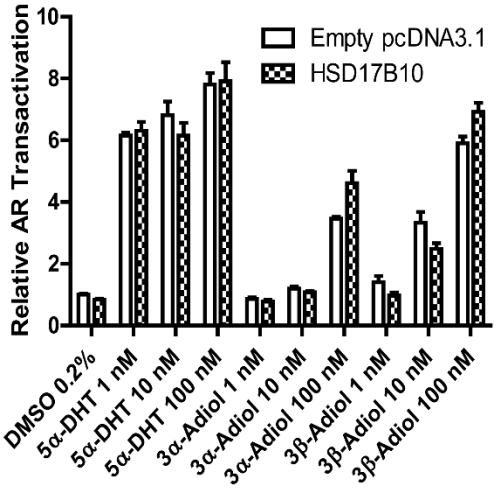

Figure 8. Relative AR transactivation by HSD17B10. CV-1 cells were transfected with HSD17B10 or empty pcDNA3.1 and treated with 5α-DHT, 3α-Adiol, or 3β-Adiol. AR transactivation was normalized to DMSO and empty vector control. A single experiment was performed in duplicates (n = 1).

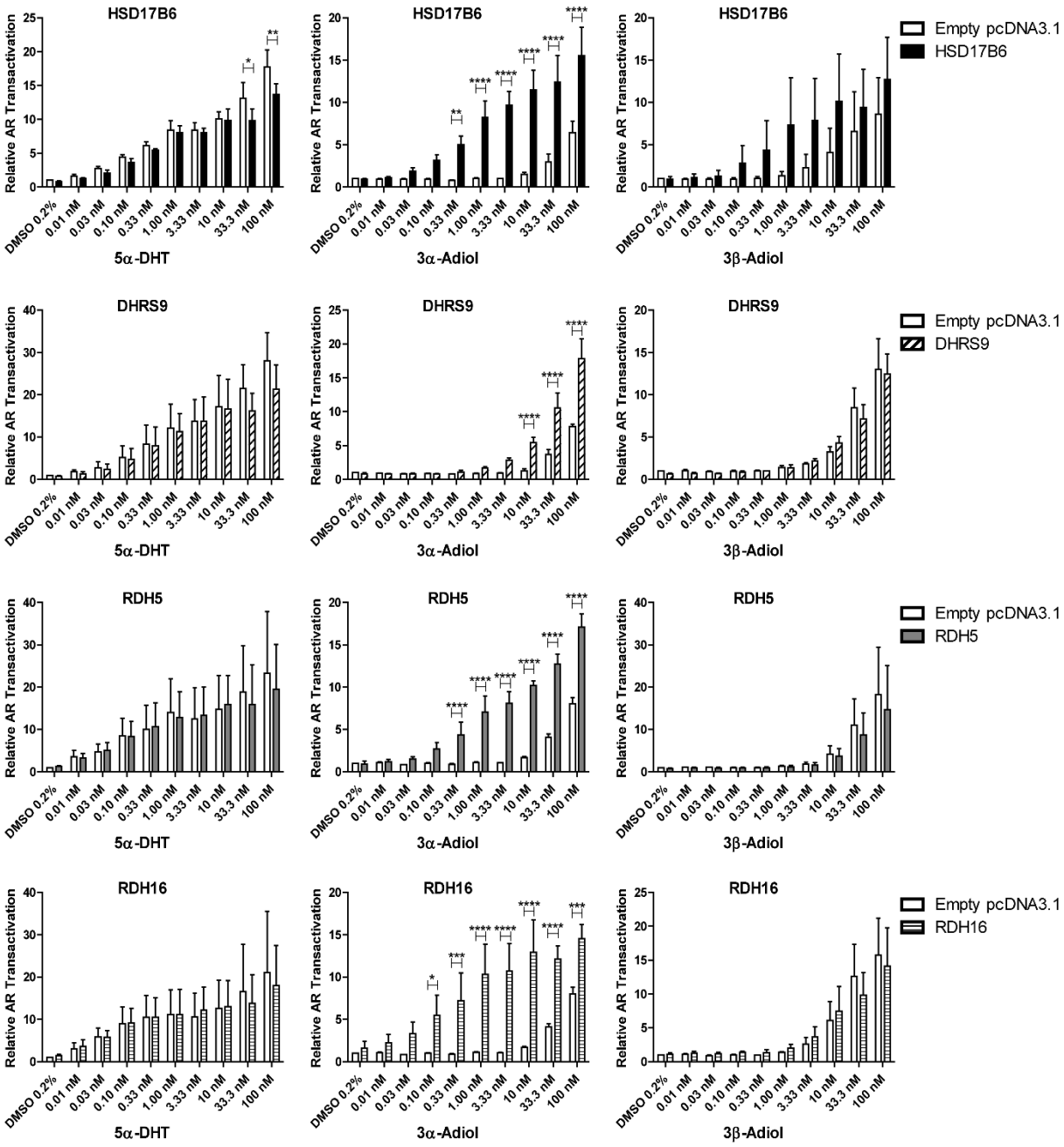

Figure 9. Relative AR transactivation by HSD17B6, DHRS9, RDH5, and RDH16. CV-1 cells were transfected with the corresponding enzyme or empty pcDNA3.1 and treated with 5α-DHT, 3α-Adiol, or 3β-Adiol. AR transactivation was normalized to DMSO and empty vector control. Three independent experiments were performed in triplicates (n = 3).

concentrations of 0.33 nM up to 10 nM, but the differences did not reach statistical significance (Figure 9).

3α-ADT is an essential intermediate product of the backdoor pathway [3, 5, 8, 14] and an oxidation of 3α-ADT has been reported for all 3α-HSDs [32, 38, 42, 50, 54, 56]. Because 3α/β-ADT and 5α-androstanedione are structurally similar to 3α/β-Adiol and 5α-DHT (a 17-carbonyl instead of a 17β-hydroxyl group, Figure 3), we tested whether we can see similar results when cells are treated with 3α-ADT, 3β-ADT, and 5α-androstanedione. We thus performed a preliminary experiment with all five 3α-HSDs

and the compounds 5α-androstanedione, 3α-ADT, and 3β-ADT at a concentration of 10 nM. The results showed no differences of AR transactivation among the different enzymes and empty control vector when cells were treated with 5α-androstanedione (Figure 10). Treatment with 3α-ADT led to an increased AR transactivation when cells expressed HSD17B6, RDH5, and RDH16. Lastly, when treating the cells with the isomer 3β-ADT, HSD17B6 was again the only enzyme whose expression led to increased AR transactivation. These results are overall comparable to those of 5α-DHT, 3α-Adiol, and 3β-Adiol (Figure 9).

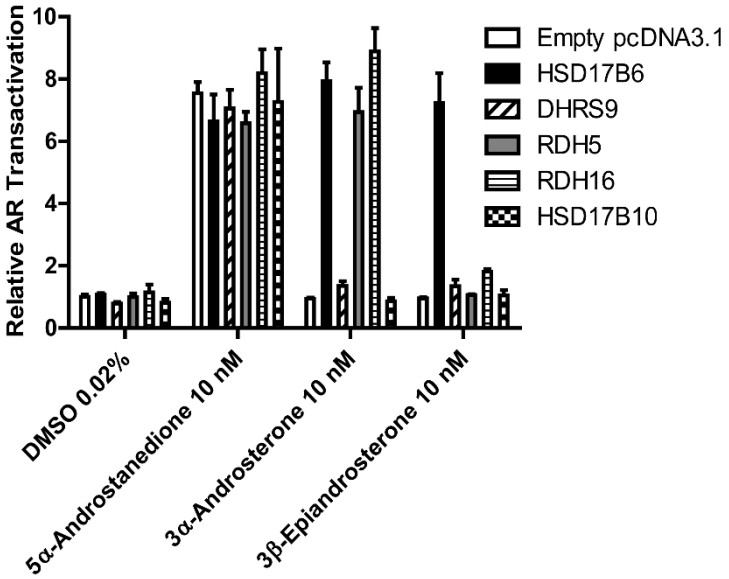

Figure 10. Relative AR transactivation by HSD17B6, DHRS9, RDH5, RDH16, and HSD17B10. CV-1 cells were transfected with the corresponding enzyme, or empty pcDNA3.1 and treated with 5α-androstanedione, 3α-ADT, or 3β-ADT. AR transactivation was normalized to DMSO and empty vector control. A single experiment was performed in duplicates (n = 1).

Based on the observation that HSD17B6 is the only enzyme capable of using both the 3α- and 3β-isomers of Adiol and ADT, we concluded that this enzyme may be most interesting to consider further as potential drug target. We aimed to apply an *in silico* screening to identify potential inhibitors and for that reason we collaborated with the Computational Pharmacy group of the University of Basel. Since no crystal structure or homology model of HSD17B6 exists, Dr. André Fischer and Dr. Martin Smieško generated a homology model based on the crystal structure of HSD17B1 (Protein Databank entry 1A27) (Figure 11). The developed homology model was then used to screen the ZINC database [179]. A first proposed hit list, kindly provided by Dr. André Fischer, can be found in the Supplementary Information (Table S3).

Selected hits of the *in silico* screening will have to be tested *in vitro* in the future. However, for that purpose, an enzymatic assay has to be developed first. Therefore,

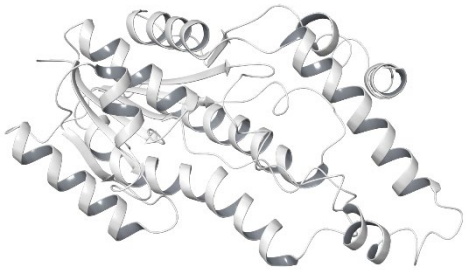

Figure 11. Homology model of HSD17B6. The model was generated based on the crystal structure of HSD17B1 with missing N- and C-terminus. The figure was kindly provided by Dr. André Fischer.

several expression constructs of HSD17B6 in the pDSG-IBA103 vector for the MEXi transfection system were generated. The MEXi mammalian expression system allows high protein expression and purification using a Twin-Strep-tag. Although the enzymatic activity of the protein has to be tested first and a purification might be challenging considering that HSD17B6 is bound to the ER membrane with the active site facing the ER lumen [180], this expression system might be useful. Before cloning HSD17B6 into the pDSG-IBA103 vector, we created a construct in pcDNA3.1 vector with an inactivating mutation by exchanging tyrosine 176 for a phenylalanine (Y176F) in the active site in order to have an enzymatic negative control available for future experiments. To be able to clone HSD17B6 into the pDSG-IBA103 vector, a silent mutation, exchanging guanine 234 for an adenine (g234a), was required to remove a restriction site. Because the Twin-Strep-tag might alter the enzyme's activity, constructs containing a stop codon in front of the Twin-Strep-tag were generated as well. Figure 12A shows the flow chart of the mutation and cloning process. One of the generated constructs was chosen to test the expression system. The successful expression of HSD17B6 in the pDSG-IBA103 vector in MEXi-293E cells is shown in Figure 12B.

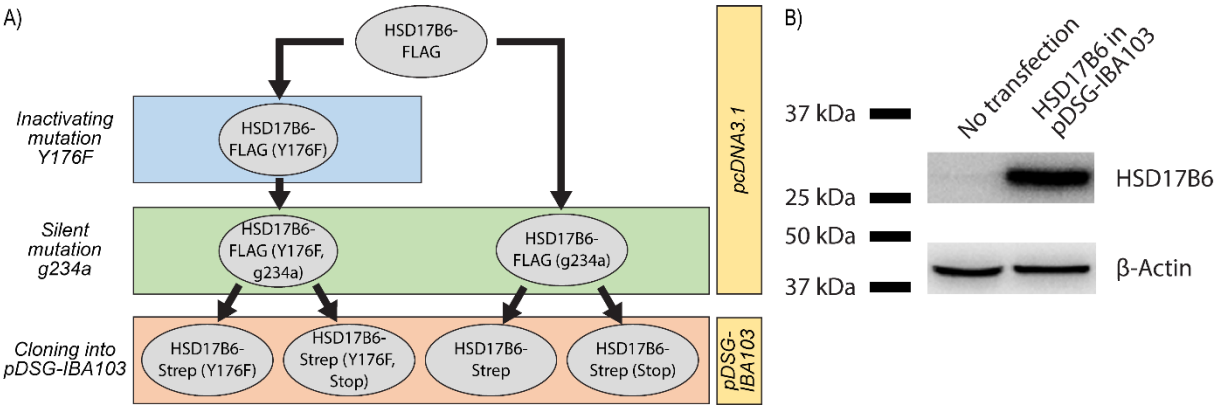

Figure 12. Generation and expression of HSD17B6-pDSG-IBA103 constructs. A) Template for the generation of new constructs was the FLAG-tagged HSD17B6 available in house. An inactivating mutation exchanging tyrosine 176 of the active site for a phenylalanine (Y176F) was introduced as an enzymatic negative control. Insertion into the pDSG-IBA103 vector required a silent mutation, exchanging guanine 234 for an adenine (g234a) to remove a restriction site. HSD17B6 with or without inactivating mutation Y176F was cloned into the pDSG-IBA103 vector with or without a stop codon in front of the Twin-Strep-tag (Strep). B) Western blot showing successful expression of one of the generated HSD17B6 constructs in MEXi-293E cells with β-Actin as loading control.

4.2 Discussion & Outlook

The backdoor pathway of androgen synthesis circumvents testosterone and instead uses 3α-ADT as a precursor for the generation of 5α-DHT *via* 3α-Adiol or 5α-androstanedione. This requires an oxidation of the 3α-hydroxyl group of either 3α-Adiol or 3α-ADT (Figure 3) [3, 5, 8]. A group of enzymes was reported to be capable of performing the oxidation of the 3α-hydroxyl group of various substrates and are termed 3α-HSDs based on this activity [10, 29, 30]. In some cases a reduction of 5α-DHT was reported and for HSD17B6 additionally an epimerase activity as well, converting 3α- to 3β-isomers [32, 42, 43, 50, 54, 56, 57]. Although the efficiency of 3α-Adiol to 5α-DHT conversion was compared among the 3α-HSDs previously [10], the oxidation of 3β-Adiol and reduction of 5α-DHT have not yet been addressed. The presented experiments addressed this lack of side-by-side comparison of the different activities towards these three substrates in an intact cell system.

HEK-293 cells are frequently used for *in vitro* experiments due to their easy transfection. The decision not to use them for the presented transactivation assay was based on the ability of HEK-293 cells to metabolize 3α-Adiol , which is likely to be mediated by CYP7B1 [181, 182], and an endogenous 3α-HSD leading to an activation of the AR after incubating HEK-293 cells with 3α-Adiol [183]. This would interfere with our transactivation assay and lead to an underestimation of the activity of the overexpressed 3α-HSDs. Instead, CV-1 cells were chosen because treatment with

10 nM of 3α-Adiol did not activate an ectopically overexpressed AR previously [30], although higher concentrations are able to do so as shown by our experiments (Figure 9). Additionally, treatment of CV-1 cells with high concentrations of 3α-Adiol (100 nM) led to the formation of 3α-ADT [30]. This suggests an oxidation of the 17β-hydroxyl group by an endogenously expressed enzyme. The enzyme responsible could be HSD17B6, since a weak 17β-oxidation by HSD17B6 was reported with testosterone and CV-1 cells were shown to express low levels of HSD17B6 [30, 53]. However, even though an endogenous oxidation of 3α-Adiol may be of concern, our transactivation assay was successfully showing increased AR activation at subnanomolar concentrations of 3α-Adiol when HSD17B6, RDH5, or RDH16 was overexpressed and similar trends were observed with 3β-Adiol and HSD17B6.

In general, no changes were observed regarding AR transactivation when cells were treated with 5α-DHT in the presence of above mentioned 3α-HSD enzymes. This is particularly relevant for HSD17B6 as it stands in contrast to a previous publication [57]. Muthusamy *et al.* showed that treating HSD17B6 overexpressing HEK-293 cells with 3α-Adiol or 5α-DHT led to slightly increased ERβ transactivation and lower EC_{50} values. They suggested that HSD17B6 is protective in PCa by metabolizing 5α-DHT and 3α-Adiol to the ERβ agonist 3β-Adiol and they showed decreased expression of HSD17B6 and ERβ in higher grade PCa [181]. This is in contrast though with their own observation that treatment with 3β-Adiol showed slightly reduced ERβ transactivation. Although HSD17B6 was able to convert radiolabeled 5α-DHT to 3β-Adiol, it was less than 15% [57]. Therefore, HSD17B6 is indeed able to reduce 5α-DHT to 3β-Adiol, but the equilibrium appears to be in favor of 5α-DHT. This is supported by the majority of the literature that refers to HSD17B6 as a 5α-DHT-generating enzyme [10, 29, 30, 59], but also by our experiments showing significantly decreased AR transactivation at high concentrations of 5α-DHT only, but increased AR transactivation already at subnanomolar concentrations of 3α- and 3β-Adiol. As such, HSD17B6 would not only increase the abundance of the AR ligand 5α-DHT, but also decrease the abundance of the antiproliferative ERβ ligand 3β-Adiol. It should be mentioned that even though the ERβ is generally regarded to be protective in PCa and ERα to be oncogenic, conflicting data exist and the role of the ERβ may depend on the particular isoform present [184].

Treatment with 3α-Adiol showed that expression of all 3α-HSDs, with the exception of HSD17B10, will lead to increased AR transactivation at concentrations of 10 nM or

even lower, suggesting an oxidation to 5α-DHT. This is not surprising, as it essentially confirms previous findings including the comparable potency of HSD17B6, RDH5, and RDH16 leading to higher AR transactivation, the lower potency of DHRS9, and virtually non-existent activity for HSD17B10 [10].

The more striking observation was that HSD17B6 was the only enzyme of the investigated 3α-HSDs to induce AR transactivation when treated with 3β-Adiol. This became even more interesting when a preliminary experiment showed essentially the same pattern when comparing the AR transactivation among the 3α-HSDs treated with 3α-ADT, 3β-ADT, and 5α-androstanedione. No difference was observed for any enzyme compared to empty vector control when treated with 5α-androstanedione, but several enzymes (HSD17B6, RDH5, and RDH16) led to AR transactivation with 3α-ADT, and only HSD17B6 when treated with 3β-ADT. The ability of 5α-androstanedione to transactivate the AR, either directly or after treatment with 3α/β-ADT, is most likely due to an endogenously expressed enzyme capable of 17β-reduction, converting 5α-androstanedione to 5α-DHT. HSD17B3 and AKR1C3 are two candidates to perform this reaction, or even HSD17B1 [3, 5]. The ability of HSD17B6 to lead to higher AR transactivation with 3β-Adiol and 3β-ADT might be related to the previously indicated epimerase activity [54]. Although 3α- to 3β-epimerization was preferred, a 3β- to 3α-epimerization was shown and the intermediate product 5α-DHT or 5α-androstanedione, respectively, could then lead to AR transactivation. The exact kinetics and equilibria of the oxidative, reductive, and epimerase activities remain elusive and while our applied transactivation assay was not suited to make such an in-depth analysis, overall it appears that HSD17B6 favors AR activation with a preferred formation of 5α-DHT.

Since HSD17B6 showed the widest substrate range regarding its potential to induce AR transactivation, it might be a more promising candidate as a drug target to prevent androgen synthesis *via* the backdoor pathway than the other 3α-HSDs. However, one factor that may compromise the utility of a HSD17B6 inhibitor is that this enzyme appears to be less expressed in advanced PCa and an inhibitor may therefore only find use in a subset of patients or in early disease [185]. *In silico* screening for inhibitors is a high throughput method to generate a list of potential candidates. Experiences with virtual screening for inhibitors of HSD17Bs have been made already [186]. For example, a ligand-based pharmacophore modeling followed by virtual screening led to the discovery of several inhibitors for HSD17B2, the most potent one showing an IC_{50}

value of 240 nM in following *in vitro* tests [187]. For HSD17B6, colleagues of the Computational Pharmacy group generated a homology model based on the crystal structure of HSD17B1. The low sequence identity among SDRs (10-30%; HSD17B6 and HSD17B1 26%) should be kept in mind when generating a novel homology model of an SDR based on the structure of another one [24]. However, one should also consider that the cofactor binding site Rossmann fold and the catalytic tetrad are well conserved in SDRs [24-26]. Also, even though sequence identities are low, several SDRs may act on the same substrates as it was shown by the presented experiment for 3α-Adiol. HSD17B1 is involved in estrogen metabolism but it can also use 5α-DHT as a substrate by reducing it to 3α- and 3β-Adiol [188, 189]. Hence, it performs the opposite reaction of HSD17B6. The opposite activities of HSD17B1 and HSD17B6 might be explained by their intracellular localization. While HSD17B6 is bound to the ER membrane, facing the oxidative environment of the lumen, and utilizing NAD+ as cofactor, HSD17B1 is located in the more reductive cytosolic milieu and utilizes NADPH as cofactor [47, 180]. It will be interesting to test the proposed inhibitors derived from the virtual screening in future studies and compare the *in vitro* with the *in silico* results.

Such an assay needs to be reliable with an acceptable throughput. Regarding HSD17B6, such a suitable assay remains to be developed. One option would be to use the generated pDSG-IBA103 constructs and the related MEXi-293E cell system to express large amounts of HSD17B6 protein. An initial experiment showed successful expression, but optimization might be required. Since the MEXi-293E cells grow in suspension they can be cultured in large bulks and preparation of microsomes is more convenient compared to microsomal preparation from adherent cells. The main advantage of using microsomes is the removal of cytosolic enzymes that could interfere with the substrate and/or product. A drawback is that the active site of HSD17B6 is facing the ER lumen and thus sonication is required to allow the substrate and potential inhibitor facilitated access to the catalytic site [47, 180]. Ideally, HSD17B6 would be extracted from the ER membrane and purified using the attached Twin-Strep-tag. However, isolation of the enzyme from the ER, the use of detergents, or the Twin-Strep-tag itself may have an impact on the enzyme's activity; issues that need to be carefully evaluated.

Analysis of substrate conversion could be done by analyzing cofactor usage, however, since AR transactivation with overexpressed HSD17B6 in CV-1 cells was

achieved with subnanomolar concentrations, the cofactor turn-over is equally small – in fact too small to detect a potent inhibitor according to previous experiments performed in our laboratory (unpublished results). A liquid chromatography-mass spectrometry (LC-MS) method may allow the discrimination of the analytes of interest, particularly the separation of 3α- and 3β-isomers, but LC-MS experiments may require derivatization of the substrate and product to achieve sufficient sensitivity and they are expensive and time-consuming.

A third possibility includes the use of radiolabeled compounds followed by separation using thin layer chromatography – a method regularly employed in our laboratory. But ^{3}H-3α-Adiol and ^{3}H-3β-Adiol are not commercially available. ^{3}H-3α-ADT is offered by one vendor only and may act as a surrogate, although its oxidation would not directly lead to the AR ligand 5α-DHT. Furthermore, visualization of these compounds requires treatment with sulfuric acid and heat exposure and initial experiences by colleagues revealed issues with the recovery of the radioactive signal, requiring extensive trouble shooting.

Another option would be applying the robust and reliable transactivation assay used in the presented experiments. However, there is a possibility that a potential inhibitor that may be confirmed in a cell-free assay will not be detected in intact cells due to the compound's inability to enter the cell or efficient efflux. It must also be confirmed that the tested compounds themselves do not inhibit the AR. However, the detection of an inhibitor by an intact, functional cell system may boost confidence in its utility, which may enhance the motivation to pursue a cell-free assay.

Because the generation of 5α-DHT from 3α- or 3β-ADT is a two-step conversion (Figure 3) in which HSD17B6 participates, inhibition of the 3α-oxidation would be of even greater interest in combination with inhibition of the 17β-reduction. A promising candidate is AKR1C3. Because of its activity it participates in both the conventional and backdoor pathway of androgen synthesis and has received attention as a potential drug target in PCa with several compounds being investigated for their potential to inhibit AKR1C3 [190]. This is supported by the increased expression of AKR1C3 in advanced PCa and in models reflecting CRPC, *e.g.* by resistance to enzalutamide or abiraterone acetate, and by knock-down of *AKR1C3* leading to decreased basal and androstenedione-induced expression of AR regulated genes [71, 152, 191-193].

One inhibitor (ASP9521) even reached a phase I/II clinical trial. It showed an acceptable safety profile but no response in the 13 patients that participated [194]. The

recruited patients already showed metastatic CRPC with disease progression after chemotherapy and inhibition of AKR1C3 (and for that matter HSD17B6 or other enzymes involved in the backdoor pathway) may exert their most potent activity in earlier disease stages while androgen deprivation therapy is still effective. Furthermore, unlike the SDRs, AKR subfamily members show a high sequence identity (AKR1C1-4 over 80%) [195]. Development of specific inhibitors is therefore challenging and this is of particular note since AKRs that are implicated in metabolizing 5α-DHT (AKR1C2 to 3α-Adiol and AKR1C1 to 3β-Adiol [20]), and thus effect a protective role, have been reported to be increased in progressive PCa as well [71]. Overlapping substrate specificity may also be of concern for an inhibitor of HSD17B6, since other enzymes, *e.g.* RDH5 or RDH16, could compensate for the loss of HSD17B6 activity and thus decrease the inhibitor's efficacy.

In order to proceed with this project, some preliminary experiments need to be repeated. Particularly the experiment that showed that HSD17B6 is the only enzyme capable of inducing AR transactivation with 3β-ADT is of importance. In case the pDSG-IBA103 vector constructs will be used, their activity (and inactivity of the ones containing the mutation Y176F) need to be tested and whether isolation using the Twin-Strep-tag is feasible. A final hit list of potential inhibitors needs to be curated and an enzymatic assay established. Discovery of an inhibitor of HSD17B6 can at the very least be a valuable tool to explore the function of HSD17B6 and the backdoor pathway of androgen synthesis. Ideally, inhibition of HSD17B6 or other 3α-HSDs may increase and prolong response to androgen deprivation therapy and delay the occurrence of CRPC.

5 PROJECT 2 – DHRS7

5.1 The Expression of DHRS7 Correlates Negatively with EGFR Expression and Positively with Survival Rate in Prostate Cancer

Manuscript submitted

Target journal: MDPI Cancers

Simon Stücheli[1], Selene Araya[1], Caner Ercan[2,3], John Gallon[3], Paul Jenö[4], Salvatore Piscuoglio[2,3], Luigi Terracciano[2], and Alex Odermatt[1]

[1] Division of Molecular and Systems Toxicology, Department of Pharmaceutical Sciences, University of Basel, Basel, Switzerland.

[2] Institute of Medical Genetics and Pathology, University Hospital Basel, Basel, Switzerland.

[3] Visceral Surgery and Precision Medicine Research Laboratory, Department of Biomedicine, University of Basel, Basel, Switzerland.

[4] Proteomics Core Facility, Biozentrum, University of Basel, Basel, Switzerland.

Contribution to the project:

Project planning

Experimental work

Analysis, interpretation, and visualization of data

Initial draft and revising the manuscript

cancers

MDPI

Article

The Expression of DHRS7 Correlates Negatively with EGFR Expression and Positively with Survival Rate in Prostate Cancer

Simon Stücheli [1], Selene Araya [1], Caner Ercan [2,3], John Gallon [3], Paul Jenö [4], Salvatore Piscuoglio [2,3], Luigi Terracciano [2], and Alex Odermatt [1,*]

[1] Division of Molecular and Systems Toxicology, Department of Pharmaceutical Sciences, University of Basel, Basel, Switzerland
[2] Institute of Medical Genetics and Pathology, University Hospital Basel, Basel, Switzerland
[3] Visceral Surgery and Precision Medicine Research Laboratory, Department of Biomedicine, University of Basel, Basel, Switzerland
[4] Proteomics Core Facility, Biozentrum, University of Basel, Basel, Switzerland
* Correspondence: alex.odermatt@unibas.ch; Tel.: +41 61 207 15 30

Citation: Stücheli, S.; Araya, S.; Ercan, C.; Gallon, J.; Moes, S.; Jenö, P.; Piscuoglio, S.; Terracciano, L.; Odermatt, A. Decreased Expression of DHRS7 Correlates with Increased Expression of EGFR and Lower Survival Rate in Prostate Cancer. *Cancers* **2021**, *13*, x. https://doi.org/10.3390/xxxxx

Academic Editor: Firstname Lastname

Received: date
Accepted: date
Published: date

Simple Summary: Prostate cancer is one of the most common malignancies in men. Current therapies are initially effective but often resistance develops, leading to tumor recurrence and death. Further research into molecular mechanisms involved in prostate cancer and therapy resistance is needed. We studied the role of DHRS7, a potential tumor suppressor with currently unknown physiological function, in prostate cancer cells using proteome and gene expression analyses. Despite the fact that DHRS7 can inactivate 5α-dihydrotestosterone, its effect on prostate cancer cells seems to be unrelated to androgen metabolism. When comparing three widely studied prostate cancer cell lines we observed a negative correlation between DHRS7 and EGFR expression. *DHRS7* knockdown enhanced EGFR expression and phosphorylation. Importantly, DHRS7 expression correlates negatively with EGFR expression and positively with survival rates in prostate cancer patients. This study suggests a tumor suppressor role for DHRS7 by modulating EGFR expression and activity in prostate cancer.

Abstract: Prostate cancer (PCa) is one of the most common malignancies in men, responsible for many cancer-related deaths. PCa typically responds to initial treatment, but resistance to therapy occurs, often leading to metastases and death. The dehydrogenase/reductase 7 (DHRS7, SDR34C1) is an "orphan" enzyme without known physiological function. DHRS7 was previously found to be decreased at higher stage PCa, and siRNA-mediated knockdown increased the aggressiveness of LNCaP cells. To further explore the role of DHRS7 in PCa, we analyzed the proteome of LNCaP cells following *DHRS7* knockdown to assess potentially altered pathways. Although DHRS7 can inactivate 5α-dihydrotestosterone, its effect on PCa cells seems to be androgen-independent. However, the proteome analyses indicated an increased expression of epidermal growth factor receptor (EGFR), which was confirmed by RT-qPCR and Western blotting. Comparison of androgen receptor (AR)-positive LNCaP and AR-negative PC-3 and DU145 PCa cell lines revealed a negative correlation between DHRS7 and EGFR expression. Furthermore, *DHRS7* knockdown enhanced EGF-induced EGFR phosphorylation. Importantly, analysis of patient samples revealed a negative correlation between DHRS7 and EGFR expression both at the mRNA and protein levels, and DHRS7 expression positively correlated with patient survival rates. These results suggest a protective role of DHRS7 in PCa, warranting further research.

Keywords: DHRS7; EGFR; STAT3; prostate cancer; survival; phosphorylation; androgen; metabolism.

1. Introduction

Prostate cancer (PCa) is the most common cancer and the third leading cause of cancer-related death of men in Europe [1]. PCa treatment needs to take into account several patient- and disease-related factors. For cases in which the disease is still confined to the prostate, prostatectomy and radiotherapy are frequently undertaken in a curative attempt. However, the tumor may no longer be confined to the primary site of disease and these treatments are often not successful, with nearly half of the patients showing a rise in the PCa biomarker prostate-specific antigen (PSA) and requiring further therapy [2].

Since PCa is generally dependent on androgens and androgen receptor (AR)-mediated signaling, PCa is tackled by hormonal therapy with the intent of disrupting androgen-mediated signaling by the use of antiandrogenic drugs and chemical castration [2,3]. In hormone-sensitive PCa, such androgen deprivation therapy initially leads to clinical improvement; however, therapy eventually fails in most patients. This can be explained by several mechanisms, including alternative routes of androgen production from adrenal precursors, diminished androgen inactivation, enhanced AR sensitivity due to post-translational modifications or abolished co-repressors, or by AR-independent signaling pathways [3]. Once hormonal therapy is no longer effective, the cancer is commonly referred to as castration resistant PCa (CRPC). CRPC is currently considered non-curable and available treatment options, *e.g.* chemotherapy, are limited [2]. Thus, research is needed to better understand the mechanisms and pathways involved in PCa progression and to identify new potential therapeutic targets.

The initial dependence of PCa on androgen signaling raised considerable attention to enzymes involved in androgen metabolism. The intratumoral formation of potent androgens may render advanced forms of PCa independent of the circulating levels of testosterone and 5α-dihydrotestosterone (5α-DHT). In this regard, several members of the short-chain dehydrogenase/reductase (SDR) superfamily were shown to metabolize androgens, including hydroxysteroid dehydrogenase (HSD) 17B3 (SDR12C2), converting androstenedione to testosterone [4-6], dehydrogenase/reductase (DHRS) 11 (SDR24C1), also exhibiting 17β-HSD activity [7], and the 3α-HSDs converting 3α-androstanediol (3α-Adiol) to 5α-DHT, *i.e.* HSD17B6 (SDR9C6), retinol dehydrogenase (RDH) 5 (SDR9C5,), RDH16 (SDR9C8) and DHRS9 (SDR9C4) [8-10]. Additionally, HSD3B1 (SDR11E1) that is required for the production of intratumoral androgens from adrenal precursors has been associated with the development of CRPC [11].

Another SDR enzyme with the capability to metabolize androgens but with still unknown physiological function is DHRS7 (SDR34C1). It was first isolated from retinal tissue but is expressed also in prostate, liver, adrenals, thyroid gland and other tissues [12-16]. *In vitro* experiments using purified protein showed a preference for cofactor NADPH over NADH to catalyze the reduction of a variety of substrates when used at high concentrations, including some carbonyl group containing xenobiotics, steroid hormones, including cortisone and androstenedione, as well as all-*trans*-retinal [13,17]. Later, experiments using HEK-293 cells expressing recombinant human DHRS7 confirmed cortisone as its substrate; however, it was converted to 20β-dehydrocortisone but not to cortisol [6]. Conversion of androstenedione to testosterone could not be confirmed by that study using intact cells and submicromolar concentrations. Instead, HEK-293 cells expressing DHRS7 were able to inactivate 5α-DHT to 3α-Adiol, and AR-dependent luciferase activity was lowered upon coexpression with DHRS7, although only at 5α-DHT concentrations of 1 nM and higher [6]. Later, this was supported by a study using *in silico* screening based on a homology model of DHRS7 and *in vitro* testing [18]. Together, these results suggested that DHRS7 might act as a tumor suppressor in early stage PCa by lowering intratumoral 5α-DHT concentrations, thereby decreasing AR activity. A tumor suppressor role of DHRS7 was further supported by observations that DHRS7 expression is abolished in metastatic PCa compared to primary PCa, and its expression declines with PCa progression as measured by the Gleason level [14,15]. The latter study also showed that siRNA-mediated *DHRS7* knockdown leads to increased migration and decreased adhesion of the

PCa cell lines LNCaP and PC-3 and the benign prostate hyperplasia cell line BPH1. Furthermore, in AR-positive LNCaP cells, *DHRS7* knockdown led to increased proliferation. Nevertheless, the fact that DHRS7 was not able to prevent AR transactivation at subnanomolar concentrations, reflecting physiological levels, and that *DHRS7* knockdown increased cell migration and decreased adhesion of AR-negative PC3 cells, indicated the existence of androgen-independent functions of DHRS7.

Therefore, to further explore the role of DHRS7 in PCa, we first investigated whether the effects of *DHRS7* knockdown on gene expression in LNCaP cells are androgen-dependent. The expression of three AR-target genes was measured after incubating LNCaP cells, following *DHRS7* knockdown, with 5α-DHT. Second, in an unbiased approach to identify genes and/or pathways affected by DHRS7, we performed a proteomics experiment in LNCaP cells after *DHRS7* knockdown. The expression of AR and three androgen-regulated target genes was further validated on the mRNA and protein level. Then, we performed a KEGG pathway annotation of the proteome data and searched for proteins annotated with PCa, which yielded 48 proteins, of which the transmembrane tyrosine kinase Epidermal Growth Factor (EGF) receptor (EGFR) and its downstream target Signal Transducer and Activator of Transcription (STAT) 3 [19-21] were further studied on the mRNA and protein level in LNCaP, PC3 and PC-3 cells. Finally, we tested a possible correlation between DHRS7 and EGFR expression in samples of PCa patients by analyzing The Cancer Genome Atlas (TCGA) database and by employing PCa tissue microarrays (TMA). The analysis of patient survival data revealed that lower DHRS7 expression and higher EGFR expression are both associated with decreased survival rates, whereas higher DHRS7 and lower EGFR expression seem to be beneficial. These results suggest a protective role of DHRS7 in PCa, which seems to be at least in part mediated through the EGFR pathway.

2. Materials and Methods

2.1. Chemicals and reagents

LNCaP (Cat# CRL-1740, RRID: CVCL_1379), PC-3 (Cat# CRL-1435, RRID: CVCL_0035), and DU145 (Cat# HTB-81, RRID: CVCL_0105) cells were purchased from American Type Culture Collection (Manassas, VA, USA). EGF (E9644), KAPA SYBR FAST qPCR Master Mix (KK4618), RPMI-1640 (R8758), cOmplete Mini (11 836 153 001) and cOmplete (04 693 116 001) Proteinase Inhibitor Cocktails, Minimum Essential Medium (51416C), mouse polyclonal anti-DHRS7 antibody for TMA (Cat# HPA031121, Lot# R30582, RRID: AB_10600803), and 5α-DHT (10300-1G-F) were obtained from Sigma-Aldrich (St. Louis, MO, USA). siRNAs were purchased from Horizon Discovery (Cambridge, UK; Table S1), and oligonucleotide primers for RT-qPCR from Microsynth (Balgach, Switzerland; Table S2). RapidOut DNA Removal Kit (K2981), Pierce bicinchoninic acid assay (23225), the EASY-nLC 1200 system, the Orbitrap Fusion Lumos instrument, and Proteome Discoverer 2.2 software were purchased from Thermo Fisher Scientific (Waltham, MA, USA). Lipofectamine RNAiMAX (13778-150) was bought from Invitrogen (Waltham, MA, USA), fetal bovine serum (FBS; S1810) from Biowest (Nuaillé, France), and QIAcube-equipment, RNeasy Mini Kit (74106), and the Rotor-Gene Q from Qiagen (Venlo, the Netherlands). The NanoDrop One^C was purchased from Witec AG (Sursee, Switzerland), Protein Assay Kit for Bradford Assay from Bio-Rad Laboratories (Hercules, CA, USA), PVDF membrane (IPVH00010) and Immobilon Western horse-radish peroxidase (HRP) substrate kit (WBKLS0500) were purchased from Merck KGaA (Darmstadt, Germany), and Ham's F-12K Medium (21127022) and Opti-MEM (51985-026) from Gibco (Life Technologies, Carlsbad, CA, USA). The Fusion FX instrument from Vilber (Collégien, France) and Lysyl endopeptidase (LysC) from Wako Chemicals (Neuss, Germany). Rabbit monoclonal anti-EGFR antibody (Cat# 790-4347, Clone 5B7, RRID: AB_2617183), rabbit anti-AR antibody (Cat#760-4605, clone SP107, RRID: not available) for TMA, and

the Ventana BenchMark immunostainer were purchased from Ventana (Roche, Basel, Switzerland). The BOND-III immunohistochemistry staining system and BOND Polymer Refine Detection kit (Cat# DS9800) were bought from Leica Biosystems (Wetzlar, Germany), the Takara PrimeScript RT reagent kit (Cat# RR037A) from Takara Bio Inc. (Kusatsu, Japan), and GraphPad Prism from GraphPad Software (RRID: SCR_002798, San Diego, CA, USA). Sep-Pak C18 cartridges, packed with 50 mg Sorbent (Cat# WAT054955) were obtained from Waters (Milford, MA, USA). The Vydac 218TPN C18 column (250 × 1 mm, 300 Å, 5 µm particle size) and ReproSil-Pur 120 C18-AQ reverse phase material (2.4 µm particle size) were purchased from Dr. Maisch GmbH (Ammerbuch-Entringen, Germany), and PD-10 desalting columns from GE Healthcare (Chicago, IL, USA). All other chemicals and reagents were obtained from either Sigma-Aldrich or AppliChem GmbH (Darmstadt, Germany). Antibodies used for Western blotting are listed in Table S3.

2.2. Cell culture

LNCaP cells were cultured in RPMI-1640, PC-3 in Ham's F-12K, and DU145 in Minimum Essential Medium. All cell culture media were supplemented with 10% FBS, 100 U/mL penicillin, 0.1 mg/mL streptomycin and Minimum Essential Medium additionally with 2 mM L-glutamine and 1 mM sodium pyruvate (final concentrations). All cell lines were cultured in a 5% CO_2 atmosphere at 37°C and passaged at roughly 70-80% confluence by rinsing with PBS, followed by trypsinization. For the experiments using 5α-DHT, 44 h after *DHRS7* knockdown, cells were incubated in serum-free medium for 4 h, followed by treatment with 5α-DHT in fresh serum-free medium for 24 h. Treatment with EGF (100 ng/mL for 1 or 5 min) was performed after cells were incubated for 4 h in serum-free medium, 48 h after *DHRS7* knockdown.

2.3. Knockdown using siRNA

Knockdown experiments were performed by transfection of cells (100,000 cells/mL) with 3.75 µL siRNA and 7.5 µL Lipofectamine RNAiMAX in 200 µL Opti-MEM for 6-well plates or 12.5 µL siRNA and 15 µL Lipofectamine RNAiMAX in 2 mL Opti-MEM for 10 cm dishes. Final siRNA concentration was 25 nM. The siRNA sequence targeting *DHRS7* was selected from three others in a previous study [14].

2.4. Gene expression analysis by RT-qPCR

Total RNA was isolated using QIAcube and RNeasy Mini Kit (Protocol for animal tissues and cells). RNA was quantified by NanoDrop One^C and genomic DNA removed using the RapidOut DNase Removal Kit. RNA (750 - 1000 ng) was reverse transcribed to cDNA using the Takara PrimeScript RT reagent kit according to the manufacturer's instructions. RT-qPCR was performed in a Rotor-Gene Q using KAPA SYBR FAST qPCR Master Mix with 4 ng of cDNA as template and 200 nM of oligonucleotide primers. Runs were started at 95°C for 5 min, followed by 40 cycles (10 s at 95°C, 15 s at 60°C, and 20 s at 72°C), and finalized with a melting ramp (72°C to 95°C, 1°C increment every 5 s). Ct-values were normalized to the housekeeping gene *PPIA* ($2^{-(\text{Ct gene of interest} - \text{Ct } PPIA)}$).

2.5. Protein expression analysis by Western blotting

Cells were homogenized in RIPA buffer containing cOmplete Mini proteinase inhibitor, centrifuged (16,100 g, 10 min, 4°C) and supernatant was collected. Protein concentration was assessed using the Pierce bicinchoninic acid assay according to the manufacturer's instruction. Samples were reduced by boiling (95°C, 5 min) in Laemmli buffer (5 mM Tris-HCl, pH 6.8, 10% glycerol [v/v], 0.2% sodium dodecyl sulfate [w/v], 1% bromophenol blue [w/v], 5% β-mercaptoethanol [v/v]) and stored at -20°C. Proteins (20 µg) were

separated by 7.5-12.5% SDS-PAGE and transferred to PVDF membranes. Membranes were blocked in 10% (w/v) commercially available, defatted milk in TBS-T (1.11 g/L Tween 20, 137 mM NaCl, 20 mM Trizma Base, pH 7.6) for 1 h at room temperature. Membranes were incubated with primary antibodies overnight at 4°C and with secondary antibodies for 1 h at room temperature in 5% defatted milk in TBS-T. Antibody-labelled proteins were visualized using the Immobilon Western Chemiluminescence HRP substrate kit in a Fusion FX instrument. Relative protein expression was assessed by densitometry using Fusion FX-associated EVOLUTION-CAPT software. The antibody dilutions applied in the experiments are listed in Table S3.

2.6. Proteome analyses in LNCaP cells

LNCaP cells subjected for 24 h, 36 h, or 48 h to *DHRS7* knockdown in 10 cm dishes were washed three times with ice-cold PBS and homogenized for 10 min in 1 mL ice-cold urea lysis buffer (8 M urea, 50 mM Tris-HCl pH 8.0, 75 mM NaCl, 1 mM PMSF) containing cOmplete protease inhibitors. Cells were then sonicated (3x 60 s, 4°C, 20% output, 2 min rest between cycles), centrifuged (12,000 g, 10 min, 4°C) and the supernatant was stored at -80°C. Protein concentration was measured by Bradford assay. The lysate was reduced (10 mM DTT, 55°C, 30 min) and alkylated (50 mM iodoacetamide, room temperature, 15 min, in the dark). The reaction was stopped by adding β-mercaptoethanol (0.33% [v/v]). Lysates were desalted on PD-10 columns, previously equilibrated with 20 mL of 4 M urea, 50 mM Tris-HCl pH 8.0, 150 mM NaCl, and proteins eluted with 4 M urea buffer with 50 mM Tris-HCl pH 8.0, and 75 mM NaCl in 10 fractions of 1 mL each. Protein containing fractions (as measured by 280 nm absorbance) were pooled and protein concentration determined with the Bradford assay. The samples were stored at -20°C. Samples were digested with endoproteinase LysC (2x 2 h, 37°C, enzyme to protein ratio 1:100 [w/w]), and the urea concentration was lowered to 2 M with 50 mM Tris-HCl pH 8.0, 75 mM NaCl, followed by trypsin digestion (the first trypsin digestion was for 2 h, 37°C, enzyme to protein ratio 1:100 [w/w], followed by a second trypsin aliquot and overnight incubation at 37°C). Trifluoroacetic acid (TFA, 1% [v/v]) was used to stop the digestion and to lower the pH < 2. Sep-Pak C18 cartridges, packed with 50 mg sorbent, were used to desalt the samples. The cartridges were primed with 250 µL methanol, then 250 µL 80% acetonitrile (ACN)/0.1% TFA and equilibrated (750 µL 0.1% TFA). Samples were applied to the cartridges, washed (1250 µL 0.1% TFA), and peptides eluted (350 µL 80% ACN/0.1% TFA). Absorbance at 280 nm was measured and the peptide concentration estimated according to Wisniewski *et al.* [22]. An aliquot containing 150 µg protein per sample was dried in a SpeedVac and stored at -20°C.

The dried peptides were dissolved in 55 µL solvent A (20 mM ammonium formate, pH 4.5) and injected onto a Vydac 218TPN C18 column (250 × 1 mm, 300 Å, 5 µm particle size) at 30 µL/min that had been equilibrated with solvent A. Bound peptides were eluted at 30 µL/min with a linear gradient from 2% to 50% solvent B (20 mM ammonium formate, pH 4.5, 80% ACN) in 100 min. 2 min fractions were collected and every sixth fraction of the peptide-containing part of the chromatogram was pooled to achieve an even distribution of peptides across all fractions. The peptide pools were dried in a SpeedVac and stored at -20°C for later analysis.

Individual peptide pools were dissolved in 30 µL of 0.1% formic acid in water and separated on a nano HPLC column (75 µm × 30 cm, packed in-house with ReproSil C18-AQ reverse-phase material, 2.4 µm particle size). All pools were injected three times as technical replicates (2 µL injection volume). The mobile phase was solvent A (0.1% formic acid in water) and B (80% ACN/0.1% formic acid). An EASY-nLC 1200 system, set to 0.25 µL/min, provided a linear gradient of solvent B: 0% for 5 min, from 0% to 35% over 155 min, to 100% over 5 min, followed by 15 min at 100%. The column was connected to an Orbitrap Fusion Lumos instrument. The eluting peptides were ionized at 1.9 kV and the instrument was operated in data dependent mode with a cycle time of 3 s. Precursor scans

in the Orbitrap had a scan range of 400 – 1600 m/z at a resolution of 120,000, with a maximum injection time of 100 ms. The data-dependent MS2 scans were done in the linear ion trap of the instrument and was set to allow for the maximal number of MS2 scans to be collected, with an injection time of 35 ms. The monoisotopic precursor selection (MIPS) mode was set to "Peptide", the intensity threshold to 5000, and the dynamic exclusion duration to 60 s. Only peptides with a charge state of 2 – 7 were included in the analysis.

Data obtained from the LC-MS/MS were searched against the SwissProt database using the Mascot and Sequest HT search engines of Proteome Discoverer 2.2. Precursor and fragment mass tolerance was set to 10 ppm and 0.6 Da, respectively. The peptide modifications methionine-oxidation and N-terminal acetylation were set to dynamic and cysteine-carbamidomethylation to static. Confidence of peptide matches was set to 1% false discovery rate. Relative protein quantification was done using the Minora Feature Detector. The detected proteins were filtered with the following criteria: Master proteins and master protein candidates, high protein false discovery rate confidence by either Mascot or Sequest HT, identification with at least 3 different peptides whereby at least 1 peptide was uniquely assigned to the given protein, and proteins being detected in all technical triplicates. The proteomics data sets of each time point were median normalized using an additional LNCaP sample that was not subjected to any treatment or reverse transfection (seeded on a 10 cm dish and lysed after 24 h). Perseus software version 1.6.14.0 was used to perform KEGG pathway annotation and heat map generation (Z-score normalization followed by hierarchical clustering with standard settings) [23,24].

2.7. TCGA data analysis

Expression data for 551 TCGA-PRAD samples were downloaded on 3rd March 2020 using the TCGAbiolinks R package) in the form of FPKM-UQ [25]. AR signaling scores were calculated as previously reported, using the log2 (FPKM) of 30 genes which define the AR signaling pathway [26].

2.8. Tissue Micro Array and Immunohistochemistry

One hundred twenty-four primary unselected prostate carcinomas treated at the University Hospital Basel between the years 1986 and 2015 were included in this study. Two TMAs of these 124 tumors were constructed as previously described [27]. Each punch was derived from the center of the tumor in an area with no necrosis so that each TMA spot consisted of more than 50% tumor cells. For 40 cases, adjacent non-malignant tissue was selected from the same donor block. Data were collected retrospectively in a non-stratified and non-matched manner including patient age, tumor diameter, tumor stage, Gleason grade, lymphovascular invasion, and clinical outcome. The clinical outcome measure of interest was overall survival time.

Immunohistochemical staining with anti-EGFR and anti-AR antibodies was performed on 4 μm thick sections using a Benchmark immunostainer according to the manufacturer's recommendations. For immunohistochemical staining with anti-DHRS7 antibody (dilution 1:600), antigen retrieval was performed with citrate buffer (pH 6.0) on a Leica Bond III IHC staining system using the BOND Polymer Refine Detection kit according to the manufacturer's instructions which provides rabbit anti-mouse IgG and anti-rabbit poly-HRP-IgG as secondary antibody and DAB chromogen. Images were acquired using an Olympus BX46 microscope. Protein expression in tissues was evaluated and scored by a board certified pathologist (C.E.) who was unaware of the clinical data. The expression was evaluated based on cytoplasmic and/or membrane staining for EGFR and DHRS7 and nuclear staining for AR. Each tumor was scored semi-quantitatively for each marker by multiplying the proportion (%) of positive cells with the staining intensity score (0, none; 1, weak; 2, moderate; 3, strong).

2.9. Statistical Analysis

To assess correlation of gene expression in the TCGA data, Spearman's correlation was calculated using all samples or samples split according to the indicated groups.

For the TMA, all analyses were performed in R (Version 3.6.3) [28]. The expression scores were visualized in ggplot, box plots, and ggscatter functions of the ggpubr package [29]. Statistical comparisons were performed using *t*-test or Wilcoxon's test where appropriate. Correlations were performed using the Spearman's correlation coefficient.

Patient survival analysis was performed using the survminer package. (version 0.4.8) [30]. Each feature was dichotomized for overall survival (OS) and progression-free survival (PFS) using optimal cut-off values calculated by the "surv_cutpoint" function. Survival times were evaluated using Kaplan-Meier survival curves and differences were analyzed using the log-rank test.

For all other experiments, GraphPad Prism software (version 5.04) was used for statistical evaluation by one- or two-way ANOVA with Bonferroni multiple comparison post-test or two-tailed *t*-test as indicated. P-value of < 0.05 was considered to indicate a statistically significant difference.

3. Results

3.1 Knockdown of DHRS7 does not alter AR-regulated gene expression

Based on the previous observation that DHRS7 is capable of metabolizing the potent AR agonist 5α-DHT to the inactive 3α-Adiol [6], we investigated whether 5α-DHT treatment following knockdown of *DHRS7* in AR-positive, androgen-dependent LNCaP cells would increase the expression of the AR target genes *KLK3*, *TMPRSS2* and *FKBP5* [31]. For this purpose, *DHRS7* was knocked-down using siRNA for 48 h prior to incubation for another 24 h in the presence of 5α-DHT at the concentration indicated and mRNA expression was checked by RT-qPCR. The results showed that *DHRS7* mRNA expression was abolished, and although a concentration-dependent increase of the analyzed AR-regulated genes could be observed, there was no difference between control and *DHRS7* knockdown, with the exception of *FKBP5* at 1 nM of 5α-DHT. Additionally, *AR* mRNA expression was unchanged or even tended to be decreased (Figure 1).

3.2 Knockdown of DHRS7 did not affect AR and AR target proteins but led to an increased EGFR and STAT3 expression in LNCaP cells

Because 5α-DHT treatment after *DHRS7* knockdown did not result in an upregulation of AR target genes, we performed a proteomics approach to search for other potentially altered pathways that could explain the more aggressive phenotype of LNCaP cells observed after *DHRS7* knockdown [14]. To assess protein changes over time, the proteome was analyzed after 24 h, 36 h, and 48 h of *DHRS7* knockdown (Figure S1 and Files S1-3).

We first wanted to confirm that AR target genes are not affected by *DHRS7* knockdown on the protein level (Figure 1). Therefore, we inspected the AR and its target proteins KLK3, TMPRSS2, and FKBP5. As shown in Figure 2a, the expression of DHRS7 gradually decreased with time following knockdown, whereas the expression of AR and FKBP5 changed only marginally. KLK3 and TMPRSS2 expression seemed to increase with elapsing time, irrespective of *DHRS7* knockdown. Upon knockdown, however, KLK3 and TMPRSS2 expression tended to be lower. Because the proteome analysis was performed only once at three different time points as a screening tool to generate hypotheses, we validated the obtained results on the mRNA and protein level by using RT-qPCR and Western blotting. Whereas the knockdown of *DHRS7* was clearly evident on the mRNA and protein level, no changes were observed for AR, KLK3, TMPRSS2 and FKBP5 (Figure 2b-d).

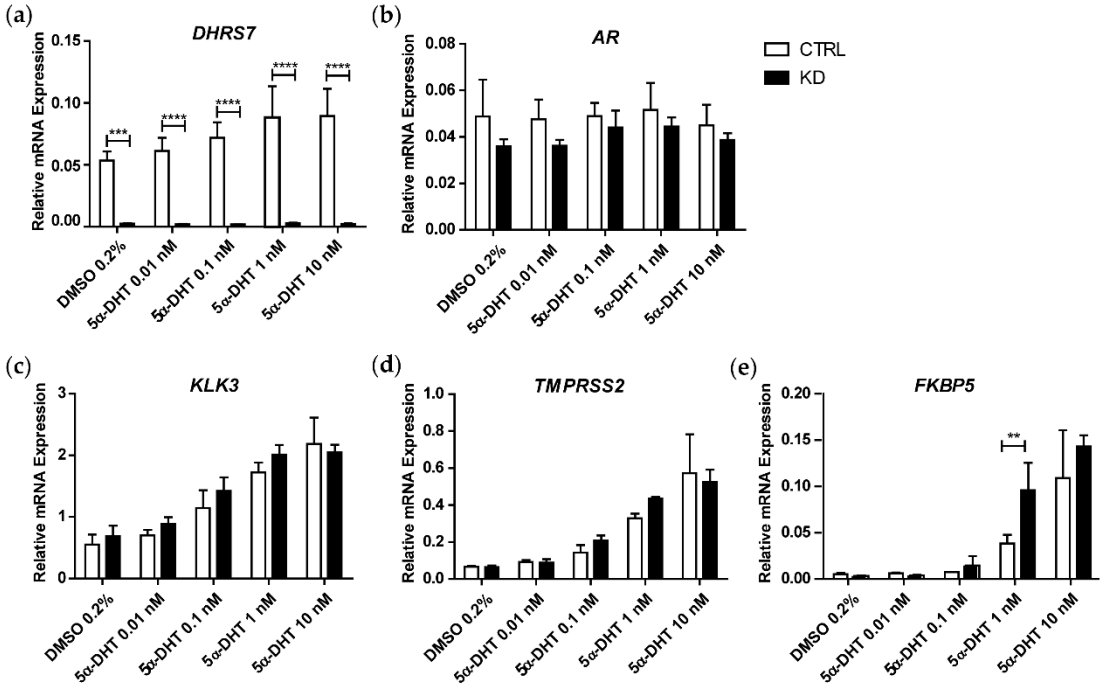

Figure 1. Effect of *DHRS7* knockdown on mRNA expression of *AR* and AR target genes. Comparison of mRNA expression (relative to *PPIA*) of (**a**) *DHRS7; (***b**) *AR;* (**c**) *KLK3;* (**d**) *TMPRSS2;* and (**e**) *FKBP5* in LNCaP cells after treatment with 5α-DHT for 24 h, following treatment of cells with mock siRNA or siRNA against *DHRS7* for 48 h. Error bars indicate mean ± SD of three independent experiments (n = 3). CTRL = control; KD = knockdown of *DHRS7*. Statistical significance was calculated using the two-way ANOVA test with Bonferroni multiple comparison post-test. ** $p < 0.01$; *** $p < 0.001$; **** $p < 0.0001$.

Next, because we were interested in pathway alterations related to PCa, we performed KEGG pathway annotation and searched for proteins annotated with "prostate cancer". Of the 6675 proteins that were detected at all time points 48 proteins were annotated with the term "prostate cancer". (Figure S2 and File S4). Most of these proteins showed rather minor changes (log_2-fold change < 0.5) following *DHRS7* knockdown, yet several proteins of known pathways seemed to be altered. Of the PI3K/Akt pathway, the PI3K catalytic subunit PIK3CB and the PI3K regulatory subunit PIK3R2 were elevated, but not AKT1 and AKT2. Among the Erk/MAPK pathway, MAP2K2 and MAPK1 were found to be lower after *DHRS7* knockdown. Additionally, the cycline-dependent kinase CDK2 and the cycline-dependent kinase inhibitor CDKN1A were both downregulated after 36 h and 48 h of *DHRS7* knockdown. Also, the protein levels of the transcriptional modulator CREB3L4, β-Catenin (CTNNB1), the transcriptional corepressor RB1 and the heat shock protein HSP90AA1 were decreased following *DHRS7* knockdown, whilst the transcription factor NKX3-1 and the NFκB-pathway member NFKB1 were found to be upregulated. Interestingly, an upregulation of the EGFR was clearly evident at all three time points analyzed (Figure 3a).

In the present study, we decided to further analyze the effect of *DHRS7* knockdown on EGFR as this receptor has been shown to play a key role in various cancers, including non-small-cell lung, breast and colorectal cancer. This led to the development and approval of both small molecule tyrosine kinase inhibitors (*e.g.* erlotinib) and antibodies (*e.g.* cetuximab) targeting the EGFR [32]. Furthermore, the transmembrane tyrosine kinase EGFR that is located at the plasma membrane is considered to be a master regulator of many signaling pathways that transduces externally received signals to modulate many biological processes important for cell growth and survival [33]. EGFR activation can affect the expression and activity of various proteins, including STAT3 [21,33,34]. Analysis of our proteomics data revealed a time-dependent increase of STAT3 after knockdown of

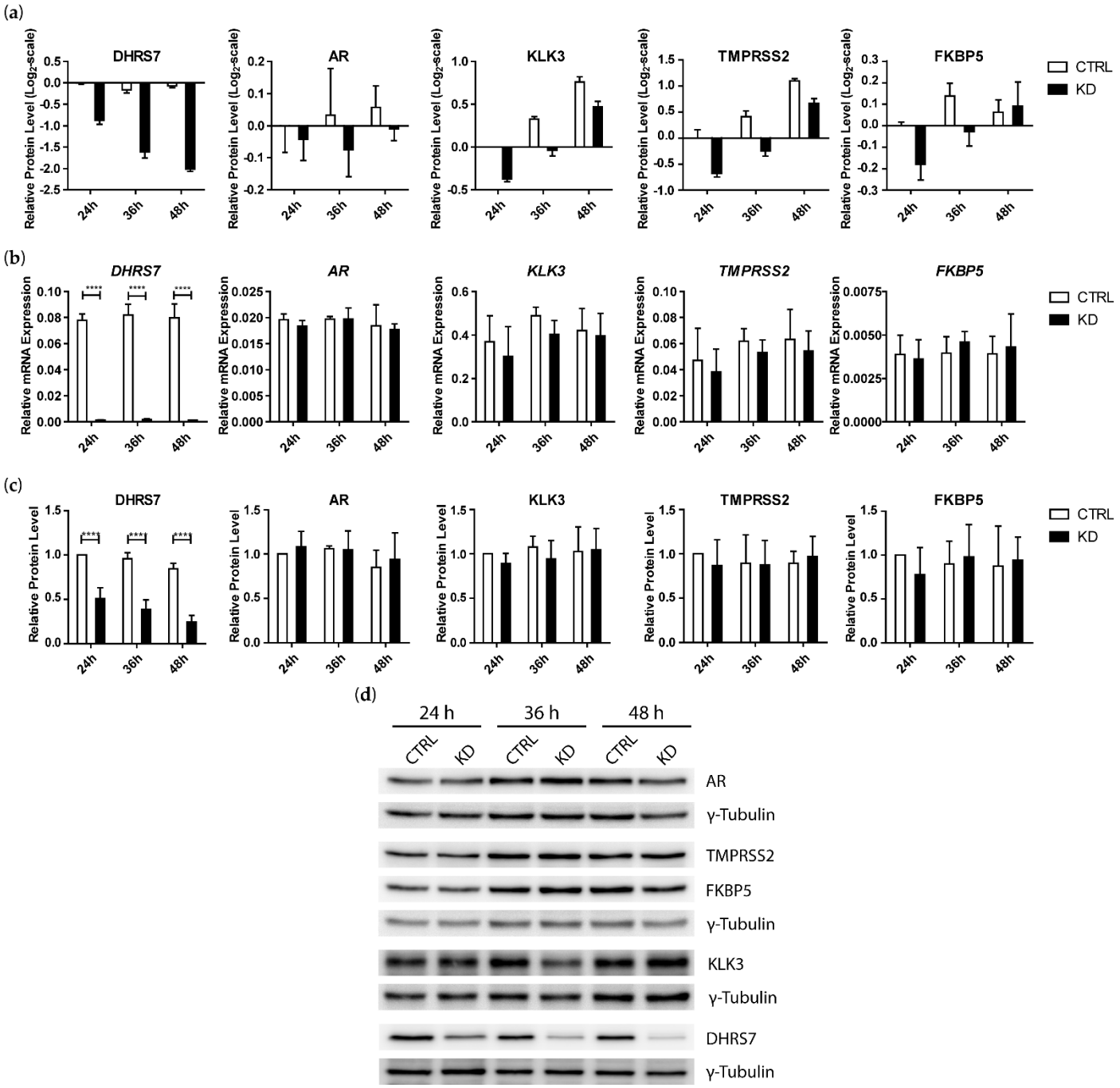

Figure 2. Expression of AR and its target genes KLK3, TMPRSS2 and FKBP5 in LNCaP after *DHRS7* knockdown. *DHRS7* was knocked-down in LNCaP cells for 24 h, 36 h and 48 h. (**a**) Relative protein expression from the proteomics experiments. Control at 24 h was set to zero and all other data sets were compared to the control at 24 h. (**b**) mRNA expression levels relative to that of *PPIA*. (**c**) Densitometry analysis of protein expression levels normalized to the control at 24 h and γ-Tubulin. (**d**) Representative Western Blot (one of three) with γ-Tubulin as loading control. Error bars indicate mean ± SD of the proteomics data (n = 1, technical triplicates, panel (**a**)) and mean ± SD of three independent experiments in the case of mRNA and densitometry (n = 3, panel (**b**) and (**c**)). CTRL = control; KD = knockdown of *DHRS7*. For mRNA and densitometry results statistical significance was calculated using the two-way ANOVA test with Bonferroni multiple comparison post -test. **** $p < 0.0001$

DHRS7 (Figure 3a). We performed RT-qPCR and Western blotting of LNCaP cells subjected to *DHRS7* knockdown and confirmed the time-dependent increase of EGFR and STAT3 expression seen in the proteomics data, which was statistically significant on the mRNA level at all time points and on the protein level after 48 h. (Figure 3b-d). Because Western blotting showed two bands for EGFR, we performed *EGFR* knockdown for 48 h

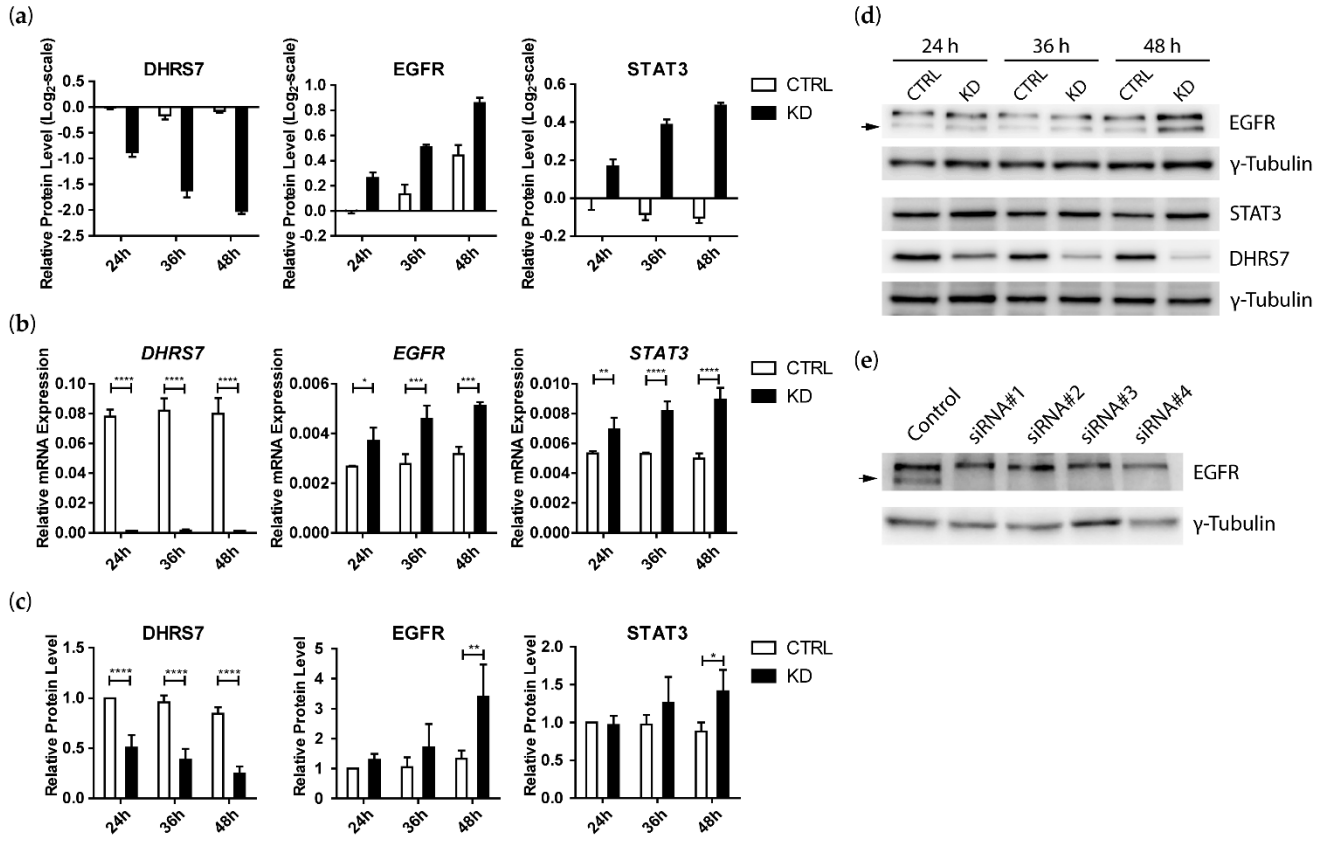

Figure 3. Effect of *DHRS7* knockdown on the expression of EGFR and STAT3 in LNCaP cells. Knockdown of *DHRS7* in LNCaP cells was performed for 24 h, 36 h, and 48 h. (**a**) Relative protein expression from the proteomics data sets. Control at 24 h was set to zero and all other data sets compared to the Control at 24 h. (**b**) mRNA expression levels relative to *PPIA*. (**c**) Densitometry analysis of protein expression levels normalized to Control at 24 h and γ-Tubulin. (**d**) Representative Western blot (one of three) with γ-Tubulin as loading control. (**e**) Knockdown of *EGFR* using four different siRNAs (n = 1). Error bars indicate mean ± SD of one experiment for the proteomics data (n = 1, technical replicates, panel (**a**)) and mean ± SD of three independent experiments for mRNA and densitometry (n = 3, panel (**b**) and (**c**)). CTRL = control; KD = knockdown of *DHRS7*. For mRNA and densitometry results, statistical significance was calculated using the two-way ANOVA test with Bonferroni multiple comparison post-test. * $p < 0.05$; ** $p < 0.01$; *** $p < 0.001$; **** $p < 0.0001$

using four different siRNAs, revealing that only the lower band corresponds to the EGFR (Figure 3e).

3.3 Inverse correlation of DHRS7 and EGFR expression in LNCaP, PC-3 and DU145 cells

Next, we tested whether knockdown of *DHRS7* leads to increased EGFR expression in other PCa cell lines. A comparison of DHRS7 expression in LNCaP, PC-3 and DU145 cells revealed that DHRS7 is expressed highest in LNCaP and less in PC-3 and DU145, with approximately 20% and 10% of the levels in LNCaP, respectively (Figure 4). An opposite expression pattern was observed for EGFR, with highest levels in DU145, about 60% less in PC-3 and ten-fold less in LNCaP. STAT3, which could not be detected in PC-3 cells, showed about 3-fold higher levels in DU145 compared to LNCaP cells, both at the mRNA and protein level (Figure 4). The AR could only be detected in LNCaP cells, both at the mRNA and protein level.

Next, we performed knockdown of *DHRS7* in PC-3 and DU145 cells. *DHRS7* mRNA and protein expression were efficiently diminished (Figure 5). In both PC-3 and DU145 cells, *DHRS7* knockdown led to a moderate trend increase in *EGFR* mRNA but a significant increase in EGFR protein levels. STAT3 showed elevated mRNA expression but only a trend increase at the protein level in DU145 cells.

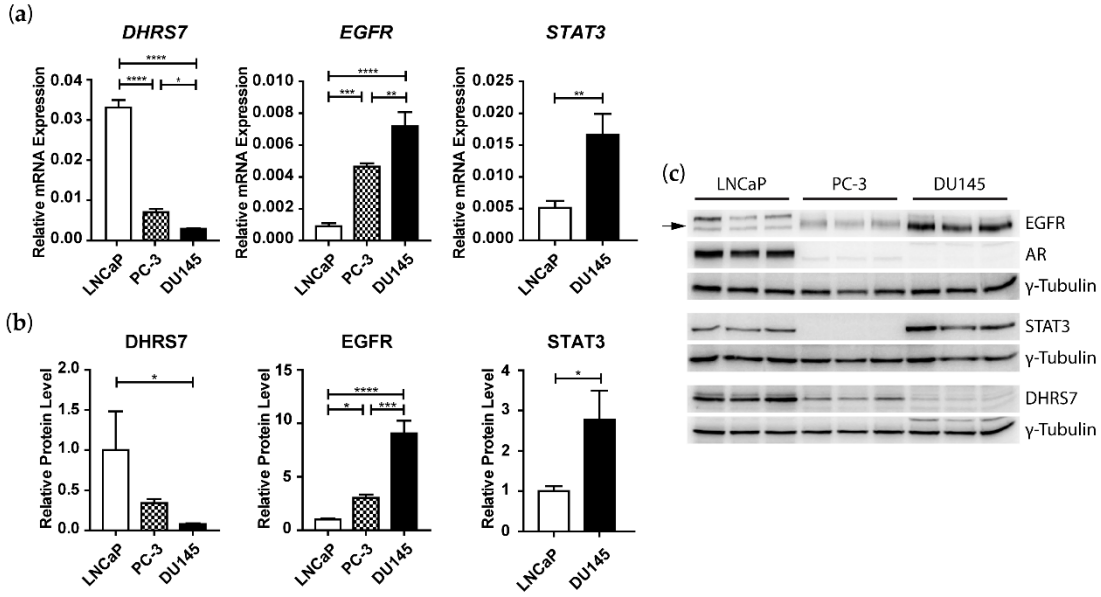

Figure 4. Comparison of DHRS7, EGFR, STAT3 and AR expression in LNCaP, PC-3 and DU145 cells. (**a**) mRNA expression levels relative to *PPIA*. (**b**) Densitometry analysis of protein expression levels normalized to LNCaP cells and γ-Tubulin loading control. (**c**) Western blot of three individual samples per cell line with γ-Tubulin as loading control. Error bars indicate mean ± SD of three independent samples (n = 3). Statistical significance was calculated using the one-way ANOVA test with Bonferroni multiple comparison post-test. * $p < 0.05$; ** $p < 0.01$; *** $p < 0.001$; **** $p < 0.0001$

3.4 Knockdown of DHRS7 leads to increased phosphorlyation of EGFR

Based on the observed increase of EGFR expression after knockdown of *DHRS7* in all three cell lines, we tested whether treatment of the cells with EGF would lead to enhanced EGFR phosphorylation in DHRS7 depleted cells. For that purpose, cells were subjected to *DHRS7* knockdown for 44 h prior to incubation in serum-free medium for 4 h and treatment with 100 ng/mL EGF for 1 min and 5 min, followed by Western blotting. Besides EGFR, we also assessed STAT3, Akt, and Erk1/2 phosphorylation and compared their expression levels between the three cell lines.

In LNCaP cells, knockdown of *DHRS7* led to increased EGFR expression compared to the control but treatment with EGF for 1 min and 5 min resulted in reduced EGFR expression (Figure 6), which might indicate decreased protein stability upon ligand-dependent activation of the receptor. Importantly, EGFR phosphorylation was elevated in knockdown compared to control cells. After 5 min of EGF treatment, the difference was statistically significant. STAT3 expression was higher in knockdown compared to control cells, and this effect was more pronounced following EGF treatment. This was accompanied by an increased STAT3 phosphorylation. Erk and Akt did not differ between knockdown and control cells. While there was no difference in the phosphorylation of Erk, Akt phosphorylation was significantly higher in *DHRS7* knockdown cells after 5 min of EGF treatment.

In PC-3 cells, the pattern of EGFR expression and phosphorylation resembled that observed in LNCaP cells, with elevated EGFR expression upon *DHRS7* knockdown and a trend increase in its phosphorylation (Figure 7). Also, Erk and Akt displayed no difference in their expression between knockdown and control cells; however, unlike in LNCaP cells treatment with EGF for 5 min showed a significant induction of Erk phosphorylation in control but not in *DHRS7* knockdown cells. Akt phosphorylation was enhanced by EGF after 1 min and 5 min, irrespective of *DHRS7* knockdown.

Also DU145 cells showed a similar pattern of EGFR expression and phosphorylation as seen in LNCaP and PC-3 cells with higher EGFR expression after *DHRS7* knockdown,

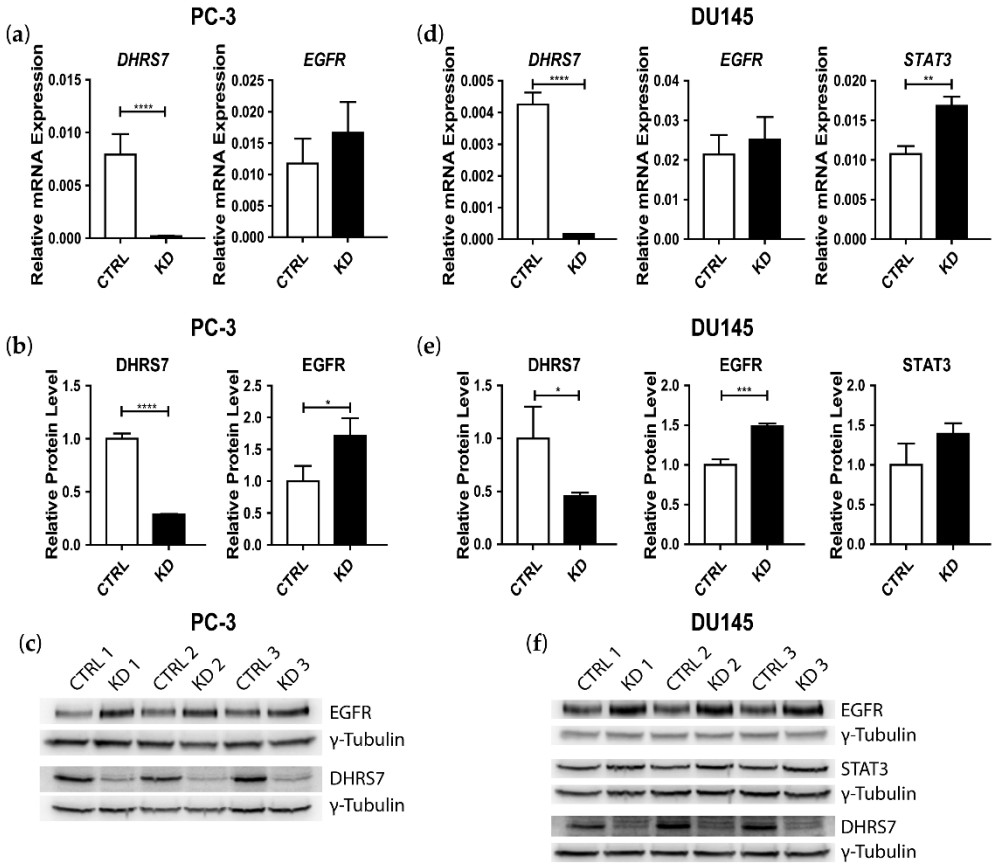

Figure 5. Effect of *DHRS7* knockdown on the expression of DHRS7, EGFR and STAT3 in PC-3 and DU145 cells. (**a**) and (**d**) mRNA expression levels relative to *PPIA* in PC-3 and DU145 cells, respectively. (**b**) and (**e**) Densitometry analysis of protein expression levels normalized to control and γ-Tubulin loading control in PC-3 and DU145 cells, respectively. (**c**) and (**f**) Western blot from samples of PC-3 and DU145 cells, respectively, with γ-Tubulin as loading control. Error bars indicate mean ± SD of at least three independent experiments (n = 3 - 5). CTRL = control; KD = knockdown of *DHRS7*. Statistical significance was calculated using two-tailed *t*-test. * $p < 0.05$; ** $p < 0.01$; *** $p < 0.001$; **** $p < 0.0001$

a less pronounced effect upon EGF treatment, and a slight increase in EGFR phosphorylation in DHRS7 depleted cells following EGF treatment (Figure 8). STAT3 expression increased after *DHRS7* knockdown and its phosphorylation showed a trend increase after 5 min of EGF treatment. While there was no difference in the expression of total Erk and Akt and Erk phosphorylation, Akt phosphorylation tended to be higher after EGF treatment and in DHRS7 depleted cells.

A comparison of Erk and Akt expression in LNCaP, PC-3 and DU145 cells showed no significant difference for Erk protein expression among the three cell lines, whereas Akt expression tended to be higher in PC-3 and was higher in DU145 compared to LNCaP cells (Figure S3).

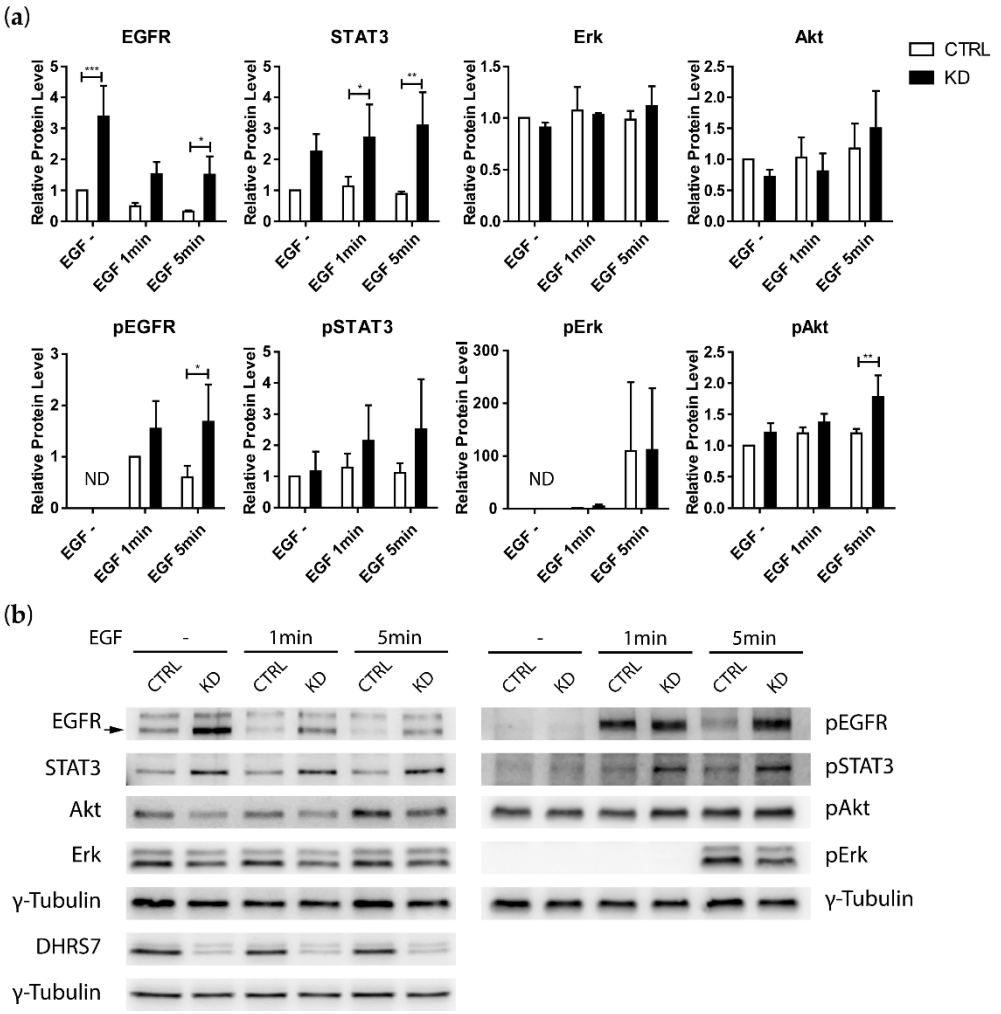

Figure 6. Effect of *DHRS7* knockdown in LNCaP cells treated with EGF. (**a**) Densitometry analysis of protein expression and phosphorylation levels normalized to control without treatment or after 1 min of treatment where appropriate, with γ-Tubulin as loading control. (**b**) Representative Western blot (one of three) with γ-Tubulin as loading control. Error bars indicate mean ± SD of three independent experiments (n = 3). CTRL = control; KD = knockdown of *DHRS7*. Statistical significance was calculated using the two-way ANOVA test with Bonferroni multiple comparison post-test. * $p < 0.05$; ** $p < 0.01$; *** $p < 0.001$

3.5 Analysis of the TCGA database revealed an inverse correlation between DHRS7 and EGFR expression

A previous study showed a negative correlation between DHRS7 expression and Gleason level in samples from PCa patients [14], and EGFR expression has repeatedly been reported to be increased at higher stages of PCa [35]. Based on our *in vitro* findings, we hypothesized an inverse correlation between DHRS7 and EGFR expression in PCa. Analysis of RNA expression using the TCGA database revealed a moderate but significant inverse correlation between *DHRS7* and *EGFR* expression (Spearman's correlation coefficient = -0.15; p-value ≤ 0.001) (Figure 9). Taking into account that PCa tends to become AR-independent and that EGFR is expressed at higher levels in advanced PCa [3,35], we stratified the TCGA data according to AR signaling by median. This slightly increased the inverse correlation in the data with lower AR signaling (Spearman's correlation coefficient = -0.19; p-value ≤ 0.01), whereas it reduced the inverse correlation in the data set of high AR signaling (Spearman's correlation coefficient = -0.1; p-value > 0.05). The mRNA expression of *DHRS7* and *STAT3* did not correlate but *EGFR* and *STAT3* mRNA expression

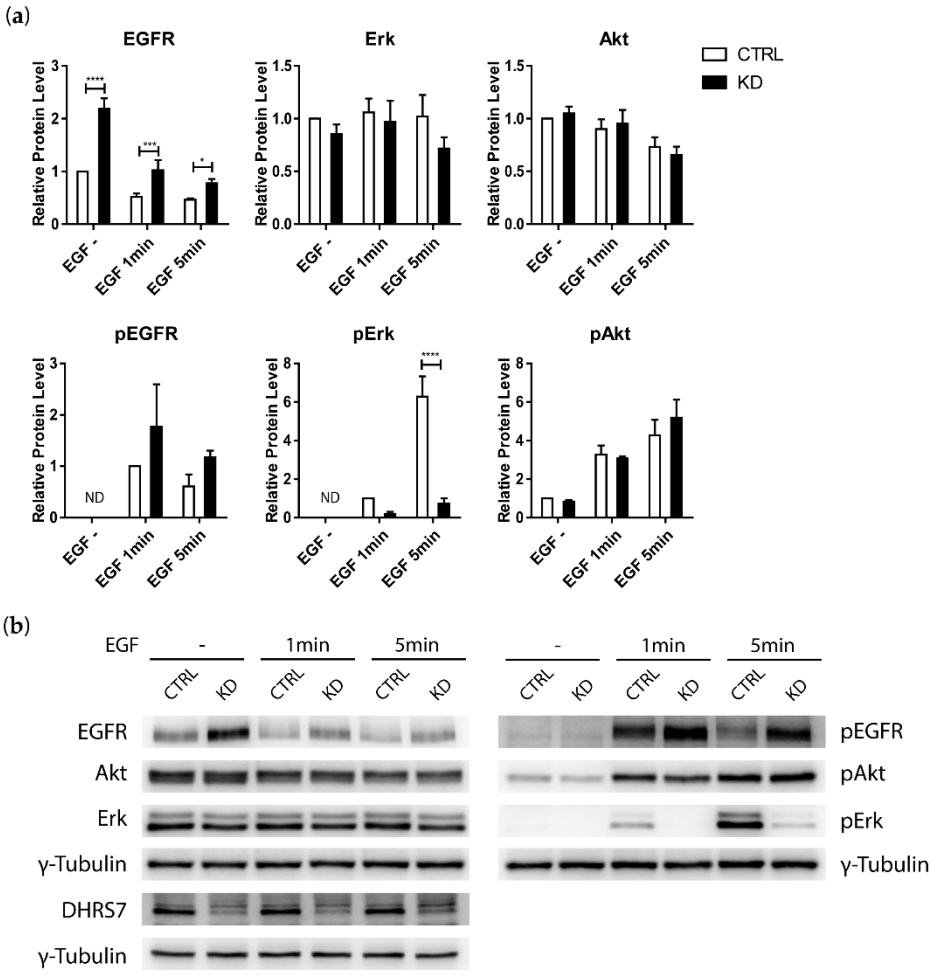

Figure 7. Effect of *DHRS7* knockdown on phosphorylation in PC-3 cells treated with EGF. (**a**) Densitometry analysis of protein expression and phosphorylation levels normalized to control, without or with EGF treatment as indicated. γ-Tubulin served as loading control. (**b**) Representative Western blot (one of three) with γ-Tubulin as loading control. Error bars indicate mean ± SD of three independent experiments (n = 3). CTRL = control; KD = knockdown of *DHRS7*. Statistical significance was calculated using the two-way ANOVA test with Bonferroni multiple comparison post-test. * $p < 0.05$; *** $p < 0.001$; **** $p < 0.0001$

showed a strong correlation (Spearman's correlation coefficient = 0.62; p-value ≤ 0.0001) (Figure S4).

3.6 Correlation of lower DHRS7 and higher EGFR expression with Gleason grade and reduced survival probability

To assess whether the correlation on the mRNA level can also be seen on the protein level, we stained TMA slides for DHRS7, EGFR and AR and observed an inverse correlation between DHRS7 and EGFR expression (Spearman's correlation coefficient = -0.25; p-value ≤ 0.05) (Figure 10a, b). A stratification on AR expression by median or mean did not improve the correlation (data not shown). Representative tumor slides are shown in Figure 10b. Overall, DHRS7 expression was higher in non-tumor samples compared to tumor samples (Figure 10c) and, accordingly, EGFR expression was higher in tumor samples compared to non-tumor prostate samples (Figure 10d). Stratification by Gleason grade revealed a gradual decline of DHRS7 expression, whereas the difference between non-tumor samples and Gleason grade 9 and 10 were statistically significant. In contrast, EGFR

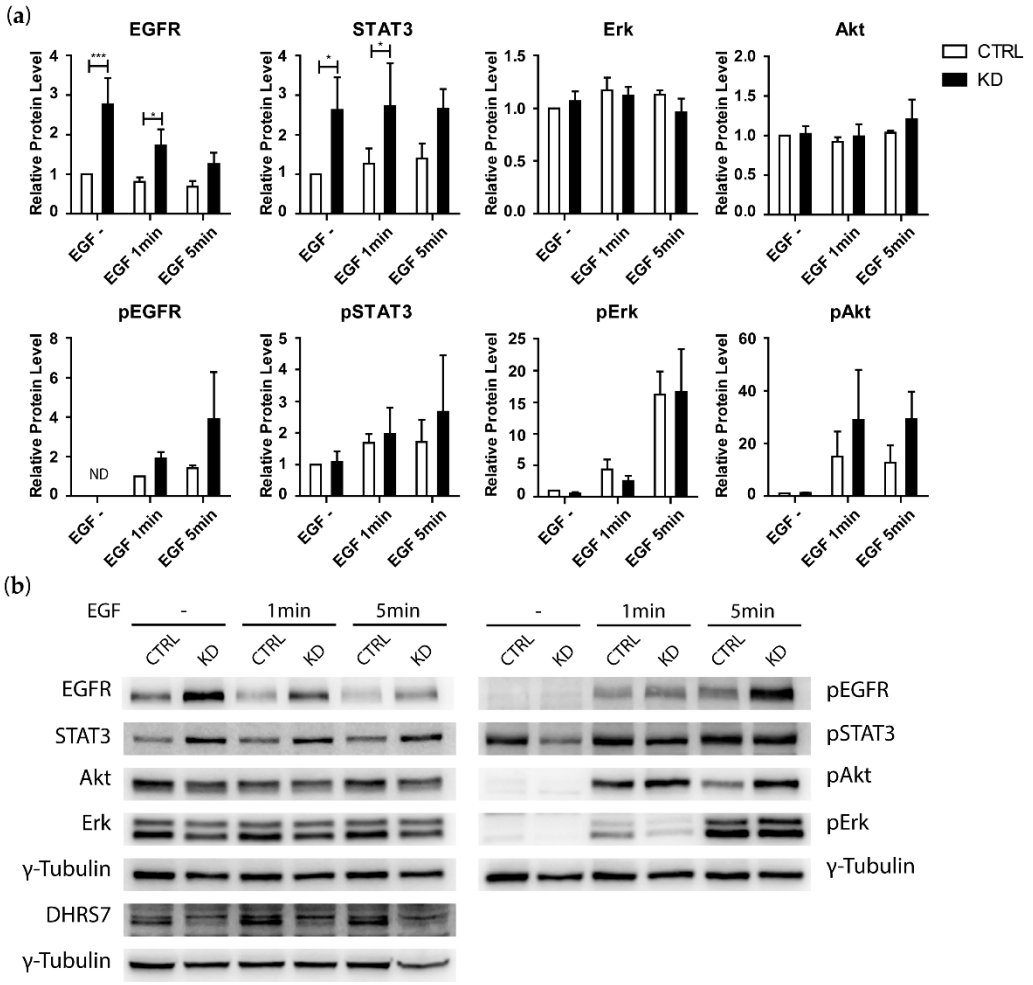

Figure 8. Effect of *DHRS7* knockdown on phosphorylation in DU145 cells treated with EGF. (**a**) Densitometry analysis of protein expression and phosphorylation levels normalized to control without or with EGF treatment as indicated. γ-Tubulin served as loading control. (**b**) Representative Western blot (one of three) with γ-Tubulin as loading control. Error bars indicate mean ± SD of three independent experiments (n = 3). CTRL = control; KD = knockdown of *DHRS7*. Statistical significance was calculated using the two-way ANOVA test with Bonferroni multiple comparison post-test. * $p < 0.05$; *** $p < 0.001$

expression showed a gradual increase with Gleason grade and the expression in non-tumor samples compared to tumor samples of any Gleason grade was statistically significantly different (Figure 10d).

In addition, we analyzed overall and disease-free survival rates of the patients in relation to the expression of DHRS7 and EGFR. High expression of DHRS7 was associated with higher overall survival probability (p-value ≤ 0.01) and showed a trend to be associated with disease free survival probability (p-value = 0.053); in contrast, high expression of EGFR was associated with worse survival probabilities; both overall (p-value ≤ 0.05) and disease free survival (p-value ≤ 0.01) (Figure 11).

4. Discussion

DHRS7 is a member of the SDR superfamily (SDR34C1) and its role in physiology remains unclear. The previous observation of an association of decreased DHRS7 expression with higher Gleason grade PCa emphasized the need to further investigate the role of this enzyme in PCa and to uncover its substrates [14]. Earlier studies provided evidence that DHRS7 is a multifunctional enzyme and may accept a variety of substrates, including xenobiotics, retinoids, and steroid hormones such as 5α-DHT [6,13,17]. The latter is of

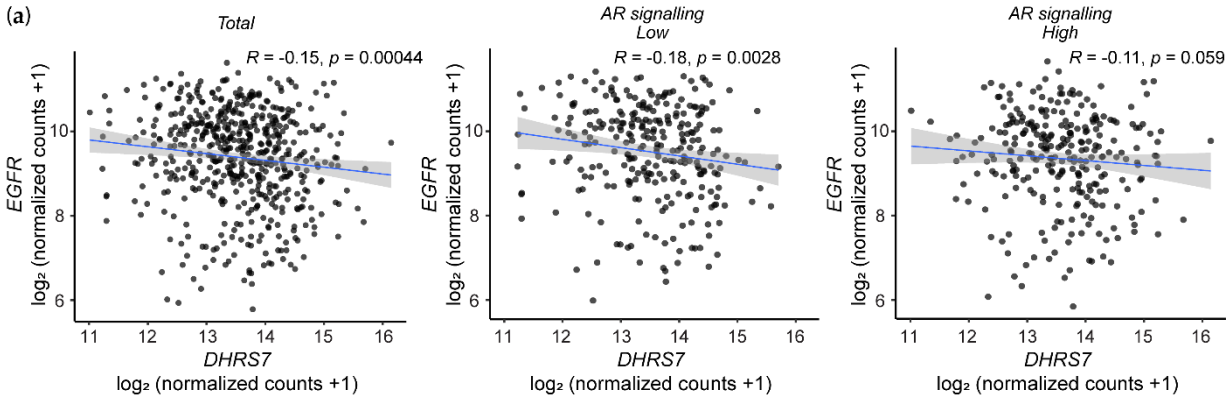

Figure 9. Results of TCGA data analysis. Correlation of *DHRS7* and *EGFR* mRNA expression in PCa samples of the total dataset (n = 551) or according to AR signaling (median separated, n = 275 each) of the TCGA database analysis.

particular interest since other SDR members have been shown to play a role in androgen metabolism, with relevance for the regulation of intratumoral androgen concentrations [4,6,8,9,36]. Especially the finding that DHRS7 is capable of inactivating 5α-DHT, the most potent AR ligand in men [3,9], to 3α-Adiol led to the hypothesis that DHRS7 acts as a tumor-suppressor in PCa by lowering intratumoral 5α-DHT levels [6].

However, the results of this study do not support an androgen-dependent effect of DHRS7 in PCa. First, a siRNA-mediated knockdown of *DHRS7* in the androgen-dependent LNCaP cells followed by treatment with 5α-DHT did not lead to differences in AR-regulated gene expression, even though a concentration-dependent increase of the AR target genes could be observed. This may be explained by an insufficient affinity of DHRS7 for 5α-DHT to allow efficient protection of AR. In line with the assumption that the conversion of 5α-DHT to 3α-Adiol by DHRS7 occurs only at supraphysiological concentrations of 5α-DHT is supported by the observation from cell-based experiments where DHRS7 was able to partially suppress AR transactivation but only at concentrations of 1 nM and higher [6]. The only exception was an increase of *FKBP5* after *DHRS7* knockdown when treated with 1 nM of 5α-DHT. FKBP5 functions as a co-chaperone in protein folding through its peptidyl-prolyl *cis-trans* isomerase activity and has been linked to stress response [37]. The expression of FKBP5 is not exclusively regulated by the AR, but also by the progesterone and glucocorticoid receptor. The latter might be involved in the expression changes of FKBP5 as DHRS7 was shown to be able to convert glucocorticoids to their 20β-hydroxylated metabolites [6]. Second, knockdown of *DHRS7* in LNCaP cells followed by proteome analysis did not detect any differences in the expression of AR and proteins that are typically increased by higher AR-activity (*e.g.* KLK3, TMPRSS2, FKBP5). Third, *DHRS7* knockdown showed similar effects on EGFR expression and phosphorylation in AR positive LNCaP and in AR negative PC-3 and DU145 cells. Thus, these findings

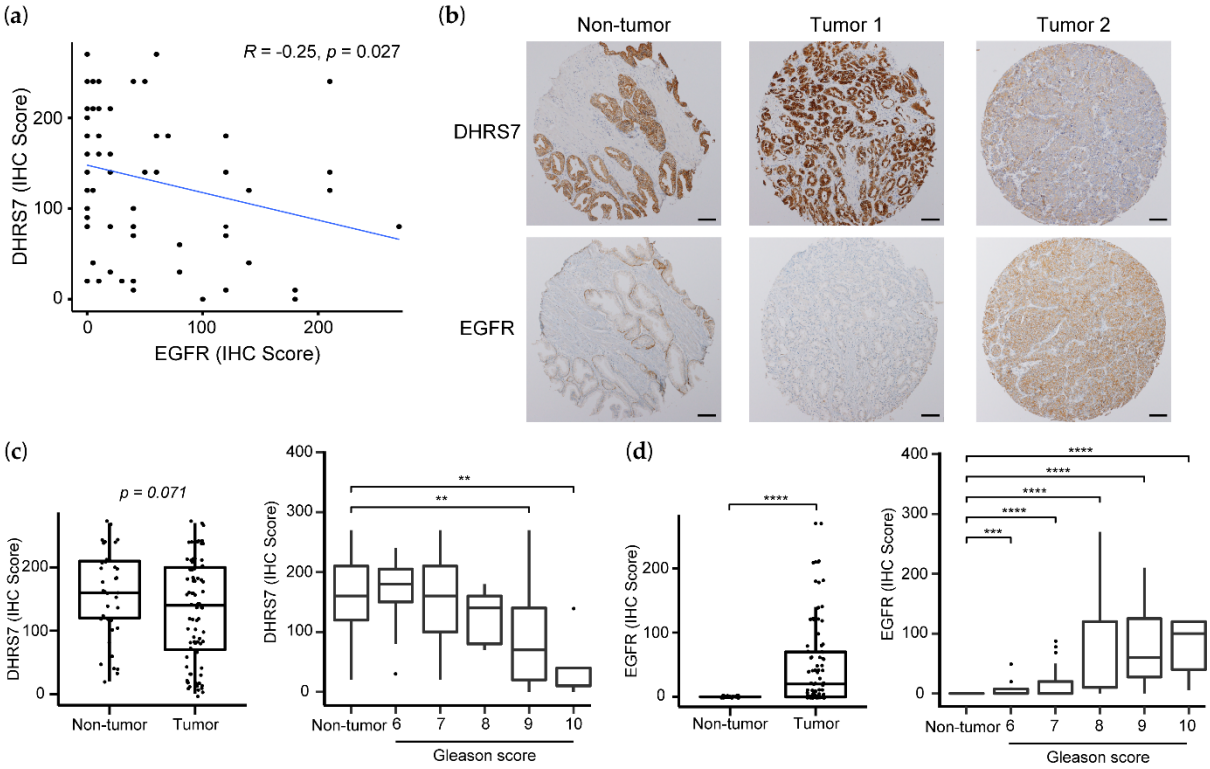

Figure 10. Correlation of DHRS7 and EGFR expression in PCa based on the analyses of TMA. (**a**) Correlation of DHRS7 and EGFR protein expression in PCa samples of the TMA analysis. (**b**) Representative staining results of the TMA in non-tumor and tumor tissue (scale bar 100 µm). Expression of DHRS7 (**c**) and EGFR (**d**) in non-tumor and tumor samples, total and grouped for Gleason score. Correlation was assessed using Spearman's correlation. Statistical significance was calculated by two-tailed *t*- test for comparing total numbers of non-tumor and tumor samples and by two-sided Wilcoxon's test. ** $p < 0.01$; *** $p < 0.001$; **** $p < 0.0001$

indicate that even though DHRS7 is capable of metabolizing 5α-DHT to the weak androgen 3α-Adiol [6], this seems not to be involved in the more rapid proliferation of LNCaP cells after *DHRS7* knockdown [14].

The results of the present study revealed a negative correlation between the expression of DHRS7 and the transmembrane tyrosine kinase EGFR, a receptor involved in various cancers with increased expression in PCa disease progression [32,33,38,39]. This negative correlation was evident in PCa patients' tumor samples, both at the mRNA and protein level (Figure 9, 10), as well as in AR-positive and -negative PCa cell lines (Figure 5). Nevertheless, there is evidence for an inverse correlation between AR and EGFR expression in PCa disease progression [40], and a shift from AR towards EGFR expression could contribute to the resistance towards AR targeting therapy in advanced PCa. A functional interaction between DHRS7 and EGFR is further evidenced by the fact that knockdown of *DHRS7* in PCa cells enhanced EGFR expression and phosphorylation. The loss of DHRS7 parallels a loss of prostate epithelial structure and may be related to the epithelial to mesenchymal transition. During this transition, dependence on AR is often lost and enhanced EGFR-mediated signaling may promote tumor progression. The role of DHRS7 in this process needs further investigation.

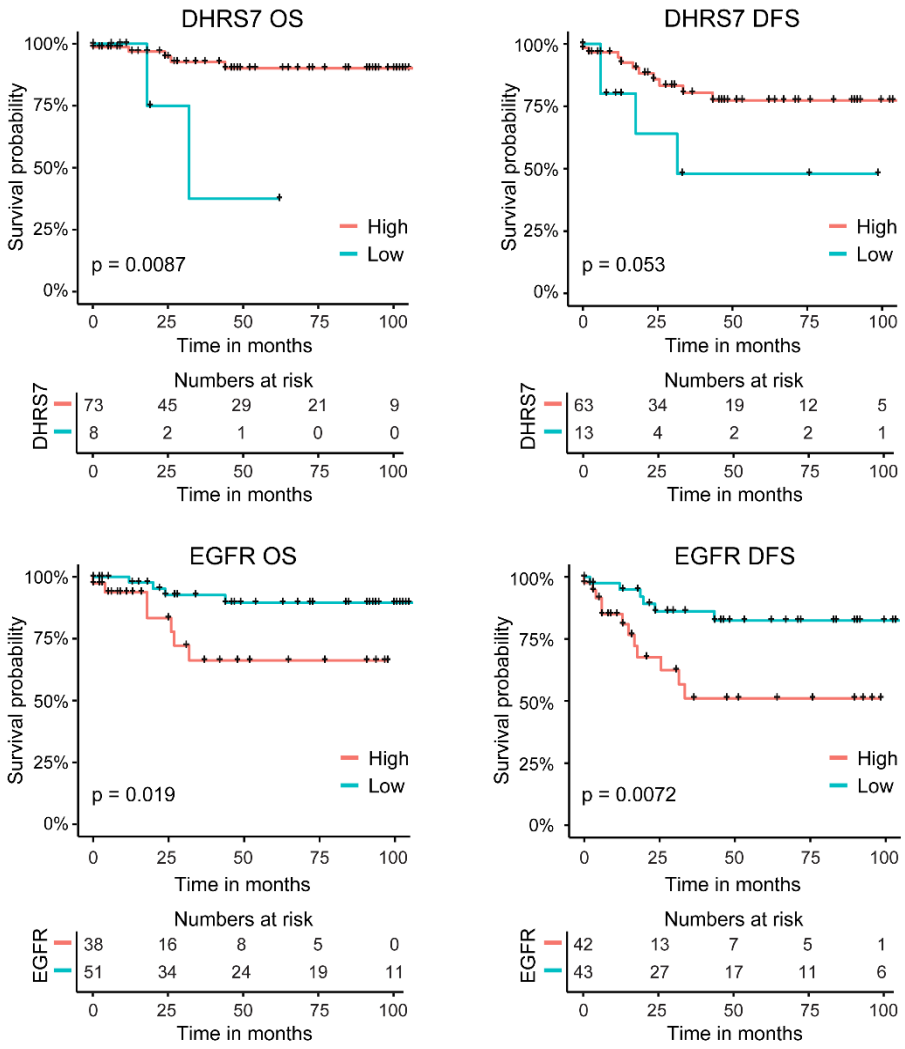

Figure 11. Correlation of DHRS7 and EGFR protein expression with survival probability. Kaplan-Meier curves showing the overall and disease-free survival probabilities of PCa patients in respect to DHRS7 and EGFR expression derived from TMA staining. OS = overall survival; DFS = disease-free survival. Statistical significance was calculated using the log-rank test.

Our approach based on the KEGG pathway annotation "Prostate cancer" to select a protein for further analyses can be considered a first step to link DHRS7 with PCa. Follow-up experiments are needed to unravel proteins whose expression can be linked clearly to a knockdown of *DHRS7*.

Both antibodies against signaling receptors on the plasma membrane of cancer cells and small molecule kinase inhibitors are used in oncology to treat various cancers, such as lung and colorectal cancer [32]. The EGFR could be an attractive target in advanced PCa. Phase II clinical trials investigated the use of the EGFR kinase inhibitors (gefitinib, lapatinib, erlotinib) in PCa, with moderate response but a number of patients showing stable disease [41-44]. Unfortunately, EGFR expression was not always assessed in these studies and a successful response to these therapies may require stratification of patients. In this regard, a major pathway through which EGFR is mediating its effects includes PI3K/Akt [45]. The primary negative regulator of PI3K is PTEN, a gene that is frequently altered or completely lost in PCa [46,47]. In colorectal cancer, the response of EGFR to treatment with cetuximab was dependent on PTEN status and in PC-3 cells, restoration of PTEN expression improved response to cetuximab-induced apoptosis and inhibition of cell proliferation [48,49]. Thus, besides EGFR, patients may need to be stratified for their PTEN status in order to achieve a satisfactory response. In this regard, a small trial using

EGFR-targeting cetuximab in combination with docetaxel indicated a better response depending on EGFR and PTEN expression [50].

In cell-based experiments, we assessed the effect of *DHRS7* knockdown on the three key downstream mediators STAT3, Akt and Erk and observed differences among the cell lines applied. In LNCaP and DU145 cells, it seems that the signal is propagated via increased STAT3 and increased Akt phosphorylation. In contrast, in PC-3 cells, STAT3 could not be detected and Akt phosphorylation was not affected after *DHRS7* knockdown but, surprisingly, the phosphorylation of Erk was abolished. STAT3 is considered to be oncogenic, including in the prostate [51]. For example, higher presence of phosphorylated STAT3 was detected in samples from PCa patients and *STAT3* knockdown led to increased apoptosis in DU145 cells [52,53]. Whether *DHRS7* knockdown mediated these effects via EGFR or whether STAT3, Akt and Erk may be affected by other pathways influenced by DHRS7 remains to be studied. Thus, besides a negative correlation between DHRS7 and EGFR expression and the effects of *DHRS7* knockdown on EGFR expression and phosphorylation, the mechanism by which DHRS7 exerts these effects remains unknown.

Interestingly, retrospective cohort studies found that men exposed to the mineralocorticoid receptor (MR) antagonist spironolactone had a lower PCa risk [54,55], suggesting a tumor promoting role of the MR. This receptor is stimulated by the steroids aldosterone and cortisol [56]. The stimulation of ectopically expressed MR by aldosterone in Chinese hamster ovary cells led to an induction of EGFR expression, which could be inhibited by spironolactone [57]. Similarly, HEK cells transfected with MR showed increased activity of an ectopically expressed EGFR promoter construct when treated with aldosterone [58]. Stimulation by EGF also lead to activation of the downstream mediator Erk [57]. Adrenalectomized rats under aldosterone treatment showed enhanced EGFR expression in kidney cortex homogenate compared to animals without aldosterone treatment [57]. A previous *in vitro* study showed the potential of DHRS7 to catalyze the 20-oxoreduction of corticosteroids [6], thereby leading to inactive or less active metabolites. Whether expression of EGFR *via* MR stimulation is of relevance in disease and whether DHRS7 is able to prevent MR-mediated EGFR expression under physiological circumstances remains to be addressed.

The ligand-binding pocket of DHRS7 is highly lipophilic. This can be inferred from the finding that DHRS7 accepts steroids and all-*trans* retinal as substrates [13,17]. However, substrates other than the so far identified ones are likely to be involved in the observed effects in PCa cells. An interesting group of potential lipophilic substrates are prostaglandins. An increase of cell proliferation, adhesion and migration was observed in PGE_2 treated PC-3 cells [59]. Furthermore, PGE_2 treatment of normal gastric epithelial and colon cancer cells led to an activation of EGFR and Erk [60]. Another group of substrates of potential interest includes arachidonic acid derived metabolites. Interactome profiling of the cannabinoid receptor 2 (CB2) expressed in HEK-293 identified DRHS7 as an interactor that was detected only in CB2 expressing cells [61]. Ligands of the CB2 are lipophilic compounds, *e.g.* 2-arachidonoyl glycerol [62], and increased DHRS7 expression in CB2 expressing cells might indicate a role in the synthesis or metabolism of lipid derivatives related to the CB2 signaling. The use of lipidomics, with a focus on certain subgroups of compounds (*e.g.* retinoids, fatty acids or prostaglandins) could be a valuable tool for the discovery of further substrates of DHRS7.

5. Conclusions

Despite the previous observation that DHRS7 is able to metabolize DHT, the results of the present study emphasize relevant androgen-independent effects of this enzyme in PCa cells. Using proteomics as a screening tool, we identified a time-dependent increase of EGFR expression in LNCaP cells following siRNA-mediated knockdown of *DHRS7* ex-

pression. This observation was successfully confirmed using RT-qPCR and Western blotting in LNCaP cells and in two additional PCa derived cell lines – PC-3 and DU145. The three PCa cell lines applied showed an inverse correlation between DHRS7 and EGFR expression. Knockdown of *DHRS7* followed by treatment with EGF led to increased receptor phosphorylation. Importantly, we found an inverse correlation, both on the mRNA and protein level, between the expression of DHRS7 and EGFR in samples from PCa patients. The expression of DHRS7 and EGFR correlated with the Gleason grade and additionally with the overall and disease-free survival rates of PCa patients. This study will help to further elucidate the potentially protective role of DHRS7 in PCa. Further research is needed to elucidate the exact molecular mechanism underlying the link between DHRS7 and EGFR, to assess whether the inverse correlation of DHRS7 and EGFR expression can be replicated in metastatic PCa samples, as well as to identify the physiological substrate(s) of DHRS7.

Supplementary Materials: The following are available online at www.mdpi.com/xxx/s1, Figure S1: Heat maps of the proteomics data after knockdown of *DHRS7* in LNCaP cells. Figure S2: Proteins with the KEGG annotation "Prostate cancer". Figure S3: Expression of Erk and Akt in LNCaP, PC-3 and DU145 cells. Figure S4: Correlation of the TCGA data of *STAT3* with *DHRS7* and *EGFR*. Table S1: siRNA sequences used for knockdown experiments. Table S2: Primers used for RT-qPCR. Table S3: Antibodies used for Western blotting. File S1: Proteomics data after 24 h. File S2: Proteomics data after 36 h. File S3: Proteomics data after 48 h. File S4: Annotation of proteomics data.

Author Contributions: Conceptualization, S.S., A.S., and O.A.; methodology, S.S., A.S., E.C., G.J., and J.P.; validation, S.S., E.C., and G.J.; formal analysis, S.S., E.C., and G.J.; investigation, S.S., A.S., E.C., and G.J.; resources, O.A., P.S., and T.L.; data curation, S.S., E.C., and G.J.; writing—original draft preparation, S.S.; writing—review and editing, S.S., A.S., E.C., G.J., J.P., P.S., T.L., and O.A.; visualization, S.S., E.C., and G.J.; supervision, O.A.; project administration, O.A.; funding acquisition, O.A. All authors have read and agreed to the published version of the manuscript.

Funding: This research was funded by the Swiss National Science Foundation, grant 31003A-179400 to O.A.

Institutional Review Board Statement: The study was conducted according to the guidelines of the Declaration of Helsinki, and approved by the local ethics committee (Ethics Committee of Basel, EKBB 361/12).

Informed Consent Statement: Written informed consent was obtained from all patients in accordance with the requirements of the local Ethical Committee (EKBB, Ref.Nr.EK: 176/07).

Data Availability Statement: All relevant data are within the manuscript and in its supporting information files. All related study data will be provided after the publication according to the related data management plan as open access at https://zenodo.org/. The generated proteomics data will be available on the public PRIDE database repository (project accession number: XXXX, [LINK]).

Acknowledgments: We would like to thank Dr. Danilo Ritz, Proteomics Core Facility, University of Basel, for his help with the analysis of the proteomics data.

Conflicts of Interest: The authors declare no conflict of interest.

Appendix A

Table S1. siRNA sequences used for knockdown experiments

Target Gene	Sequence (5′ – 3′)	Cat#
DHRS7	GAA AGA AGU UUG GAU CUC A	D-009573-02
EGFR #1	CCG CAA AUU CCG AGA CGA A	D-003114-32
EGFR #2	CAA AGU GUG UAA CGG AAU A	D-003114-33
EGFR #3	GUA ACA AGC UCA CGC AGU U	D-003114-34
EGFR #4	GAG GAA AUA UGU ACU ACG A	D-003114-35
Non-targeting control	UGG UUU ACA UGU UUU CUG A	D-001810-03-05

Table S2. Primers used for RT-qPCR

Target Gene	Forward (5′ – 3′)	Reverse (5′ – 3′)
AR	GAC ATG CGT TTG GAG ACT GC	TTC CCT TCA GCG GCT CTT TT
DHRS7	GAG TTT GGT AGA ATC GAC ATT GTG	GAA AGA GGT ACA GAT ATG ATA CCC
EGFR	GGC AGG AGT CAT GGG AGA A	GCG ATG GAC GGG ATC TTA G
FKBP5	GAA TAC ACC AAA GCT GT	CTC TTC CTT GGC ATC CT
KLK3	AGG CCT TCC CTG TAC AC	GTC TTG GCC TGG TCA TTT CC
PPIA	CAT CTG CAC TGC CAA GAC TGA	TGC AAT CCA GCT AGG CAT G
STAT3	CAG CAG CTT GAC ACA CGG TA	AAA CAC CAA AGT GGC ATG TGA
TMPRSS2	CTG CCA AGG TGC TTC TC	TTA GCC GTC TGC CCT C

Table S3. Antibodies used for Western blotting.

						Dilutions	
Target Protein	**Cat#**	**Manufacturer**	**Clonality**	**RRID**	**Host species**	**Primary Antibody**	**Secondary Antibody**
Akt	9272, Lot# 15	Cell Signaling Technology (Danvers, MA, USA)	Polyclonal	AB_329827	Rabbit	1:2000	1:5000
Phospho-Akt	4060, Lot# 19	Cell Signaling Technology	Monoclonal (D9E)	AB_2315049	Rabbit	1:2000	1:5000
AR	sc-7305, Lot# H3116	Santa Cruz Technology (Dallas, TX, USA)	Monoclonal (441)	AB_626671	Mouse	1:2000	1:5000
DHRS7	SAB1400567, Lot# J5091	Sigma-Aldrich	Polyclonal	AB_1847656	Mouse	1:2000	1:5000
EGFR	sc-373746, Lot# C2919	Santa Cruz Technology	Monoclonal (A-10)	AB_10920395	Mouse	1:1000	1:5000
Phospho-EGFR	sc-81488, Lot# C2019	Santa Cruz Technology	Monoclonal (15A2)	AB_1125777	Mouse	1:1000	1:5000
Erk	4695, Lot# 28	Cell Signaling Technology	Monoclonal (137F5)	AB_390779	Rabbit	1:2000	1:5000
Phospho-Erk	4370S, Lot# 28	Cell Signaling Technology	Monoclonal (D13.14.4E)	AB_2315112	Rabbit	1:1000	1:5000
FKBP5	sc-271547, Lot# C1918	Santa Cruz Technology	Monoclonal (D-4)	AB_10649040	Mouse	1:2000	1:2000
KLK3	sc-65602. Lot# A0913	Santa Cruz Technology	Monoclonal (SPM352)	AB_2134512	Mouse	1:75	1:5000
STAT3	sc-8019, Lot# A1719	Santa Cruz Technology	Monoclonal (F-2)	AB_628293	Mouse	1:2000	1:5000
Phospho-STAT3	sc-8059, Lot# L1619	Santa Cruz Technology	Monoclonal (B-7)	AB_628292	Mouse	1:2000	1:5000
TMPRSS2	sc-515727, Lot# H0916	Santa Cruz Technology	Monoclonal (H-4)	AB_2892118	Mouse	1:1000	1:5000
γ-Tubulin	T5192, Lot# 059M4807V	Sigma-Aldrich	Polyclonal	261690	Rabbit	1:2000	1:5000
Mouse IgG	A0168, Lot# 079M4881V	Sigma-Aldrich	Polyclonal	AB_257867	Goat	-	-
Rabbit IgG	7074S, Lot# 22	Cell Signaling Technology	Polyclonal	AB_2099233	Goat	-	-

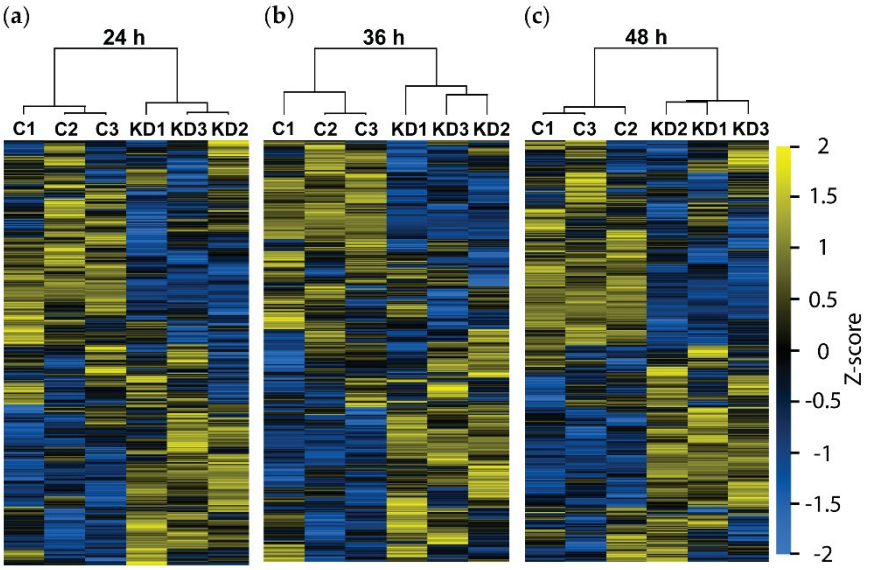

Figure S1. Heat maps of the proteomics data after knockdown of *DHRS7* in LNCaP cells. Representation of protein changes following *DHRS7* knockdown for (**a**) 24 h; (**b**) 36 h; and (**c**) 48 h. Expression levels were normalized using Z-score followed by hierarchical clustering with the Perseus software. Each time point was measured in three technical replicates. C = control; KD = knockdown of *DHRS7*. Yellow: proteins that were upregulated; blue: proteins that were downregulated.

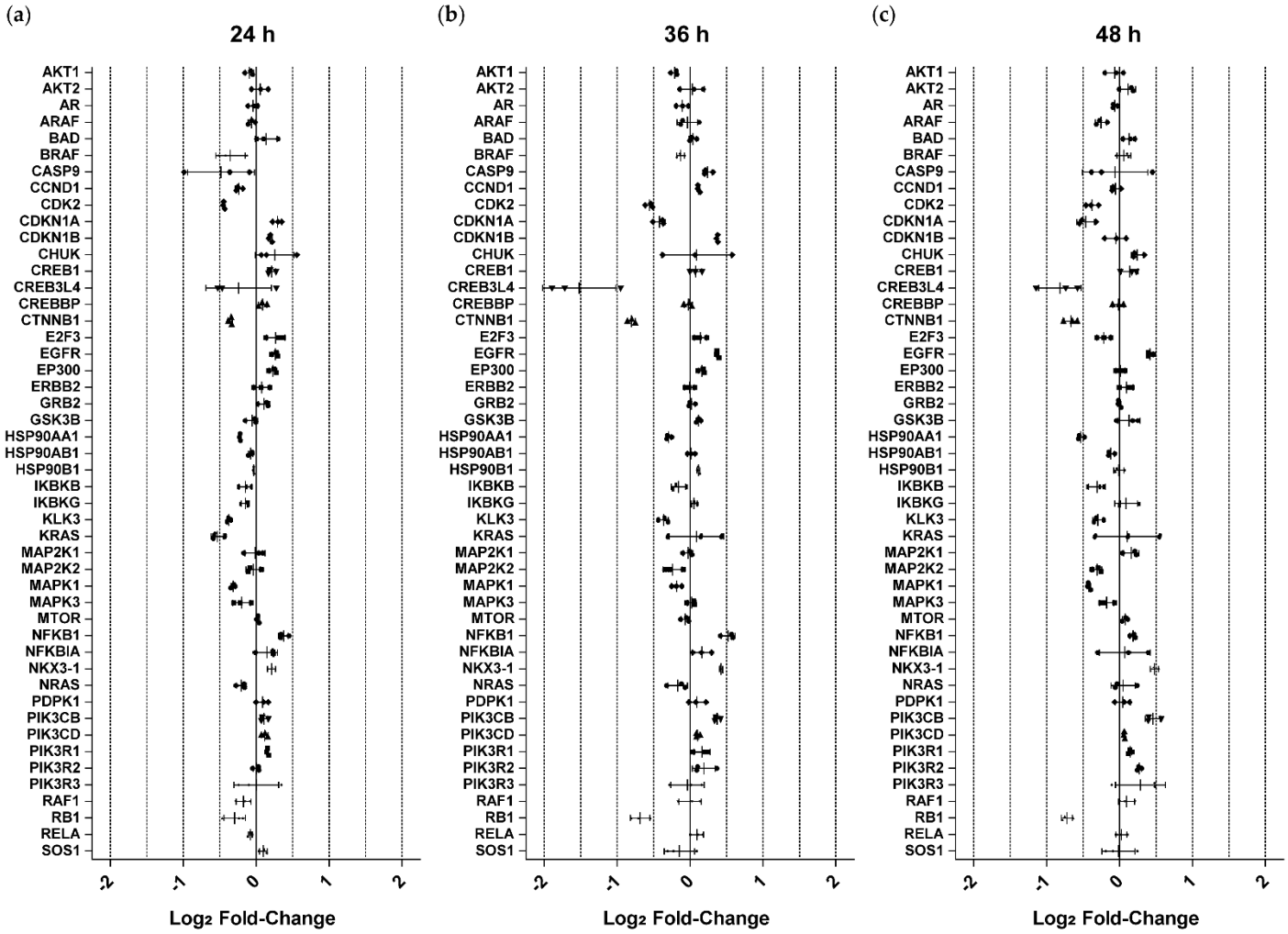

Figure S2. Proteins with the KEGG annotation "Prostate cancer". Knockdown of *DHRS7* in LNCaP cells was performed for (**a**) 24 h; (**b**) 36 h; and (**c**) 48 h. Expression levels are displayed as $\log_2$ fold-change (Knockdown compared to control). Data points indicate technical triplicates wih their mean ± SD (n = 1).

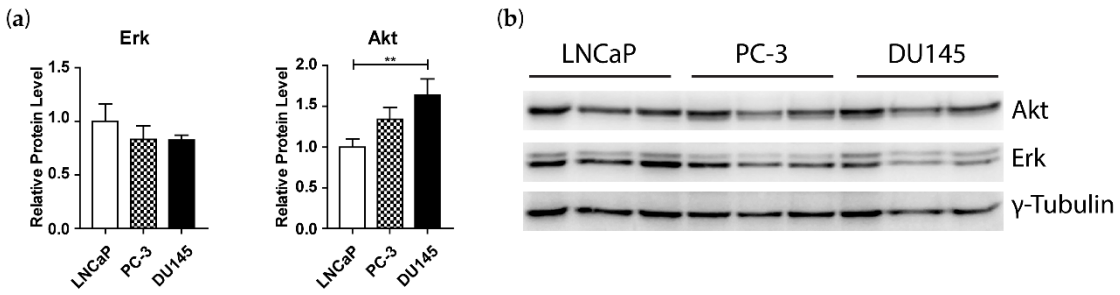

Figure S3. Expression of Erk and Akt in LNCaP, PC-3 and DU145 cells. (**a**) Densitometry analysis of protein expression levels normalized to the levels in LNCaP cells and to the γ-Tubulin loading contol. (**b**) Western blot of three individual samples per cell line with γ-Tubulin as loading control. Error bars indicate mean ± SD of three independent samples (n = 3). Statistical significance was calculated using one-way ANOVA test with Bonferroni multiple comparison post-test. ** $p < 0.01$

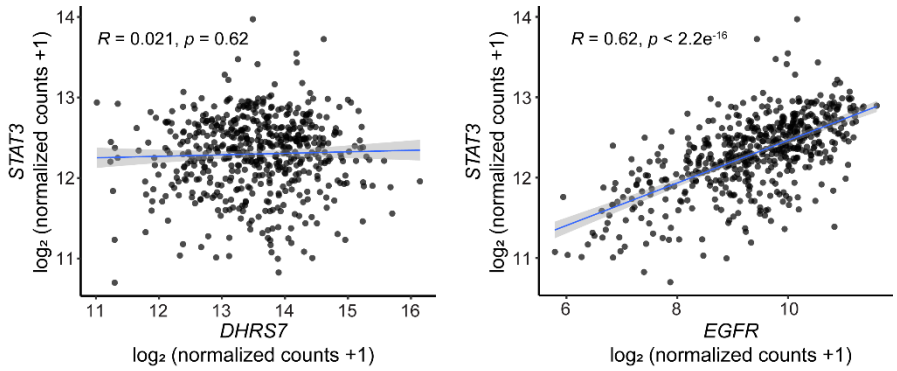

Figure S4. Correlation of the TCGA data of *STAT3* with *DHRS7* and *EGFR* in PCa. Correlation was assessed using Spearman's correlation.

References

1. Ferlay, J.; Colombet, M.; Soerjomataram, I.; Dyba, T.; Randi, G.; Bettio, M.; Gavin, A.; Visser, O.; Bray, F. Cancer incidence and mortality patterns in Europe: Estimates for 40 countries and 25 major cancers in 2018. *Eur J Cancer* **2018**, *103*, 356-387, doi:10.1016/j.ejca.2018.07.005.
2. Rebello, R.J.; Oing, C.; Knudsen, K.E.; Loeb, S.; Johnson, D.C.; Reiter, R.E.; Gillessen, S.; Van der Kwast, T.; Bristow, R.G. Prostate cancer. *Nat Rev Dis Primers* **2021**, *7*, 9, doi:10.1038/s41572-020-00243-0.
3. Feldman, B.J.; Feldman, D. The development of androgen-independent prostate cancer. *Nat Rev Cancer* **2001**, *1*, 34-45, doi:10.1038/35094009.
4. Andersson, S.; Geissler, W.M.; Wu, L.; Davis, D.L.; Grumbach, M.M.; New, M.I.; Schwarz, H.P.; Blethen, S.L.; Mendonca, B.B.; Bloise, W.; et al. Molecular genetics and pathophysiology of 17 beta-hydroxysteroid dehydrogenase 3 deficiency. *J Clin Endocrinol Metab* **1996**, *81*, 130-136, doi:10.1210/jcem.81.1.8550739.
5. Geissler, W.M.; Davis, D.L.; Wu, L.; Bradshaw, K.D.; Patel, S.; Mendonca, B.B.; Elliston, K.O.; Wilson, J.D.; Russell, D.W.; Andersson, S. Male pseudohermaphroditism caused by mutations of testicular 17 beta-hydroxysteroid dehydrogenase 3. *Nat Genet* **1994**, *7*, 34-39, doi:10.1038/ng0594-34.
6. Araya, S.; Kratschmar, D.V.; Tsachaki, M.; Stucheli, S.; Beck, K.R.; Odermatt, A. DHRS7 (SDR34C1) - A new player in the regulation of androgen receptor function by inactivation of 5alpha-dihydrotestosterone? *J Steroid Biochem Mol Biol* **2017**, *171*, 288-295, doi:10.1016/j.jsbmb.2017.04.013.
7. Endo, S.; Morikawa, Y.; Kudo, Y.; Suenami, K.; Matsunaga, T.; Ikari, A.; Hara, A. Human dehydrogenase/reductase SDR family member 11 (DHRS11) and aldo-keto reductase 1C isoforms in comparison: Substrate and reaction specificity in the reduction of 11-keto-C19-steroids. *J Steroid Biochem Mol Biol* **2020**, *199*, 105586, doi:10.1016/j.jsbmb.2020.105586.
8. Biswas, M.G.; Russell, D.W. Expression cloning and characterization of oxidative 17beta- and 3alpha-hydroxysteroid dehydrogenases from rat and human prostate. *J Biol Chem* **1997**, *272*, 15959-15966, doi:10.1074/jbc.272.25.15959.
9. Penning, T.M.; Bauman, D.R.; Jin, Y.; Rizner, T.L. Identification of the molecular switch that regulates access of 5alpha-DHT to the androgen receptor. *Mol Cell Endocrinol* **2007**, *265-266*, 77-82, doi:10.1016/j.mce.2006.12.007.
10. Bauman, D.R.; Steckelbroeck, S.; Williams, M.V.; Peehl, D.M.; Penning, T.M. Identification of the major oxidative 3alpha-hydroxysteroid dehydrogenase in human prostate that converts 5alpha-androstane-3alpha,17beta-diol to 5alpha-dihydrotestosterone: a potential therapeutic target for androgen-dependent disease. *Mol Endocrinol* **2006**, *20*, 444-458, doi:10.1210/me.2005-0287.

11. Hettel, D.; Sharifi, N. HSD3B1 status as a biomarker of androgen deprivation resistance and implications for prostate cancer. *Nat Rev Urol* **2018**, *15*, 191-196, doi:10.1038/nrurol.2017.201.
12. Haeseleer, F.; Palczewski, K. Short-chain dehydrogenases/reductases in retina. *Methods Enzymol* **2000**, *316*, 372-383, doi:10.1016/s0076-6879(00)16736-9.
13. Stambergova, H.; Zemanova, L.; Lundova, T.; Malcekova, B.; Skarka, A.; Safr, M.; Wsol, V. Human DHRS7, promising enzyme in metabolism of steroids and retinoids? *J Steroid Biochem Mol Biol* **2016**, *155*, 112-119, doi:10.1016/j.jsbmb.2015.09.041.
14. Seibert, J.K.; Quagliata, L.; Quintavalle, C.; Hammond, T.G.; Terracciano, L.; Odermatt, A. A role for the dehydrogenase DHRS7 (SDR34C1) in prostate cancer. *Cancer Med* **2015**, *4*, 1717-1729, doi:10.1002/cam4.517.
15. Stanbrough, M.; Bubley, G.J.; Ross, K.; Golub, T.R.; Rubin, M.A.; Penning, T.M.; Febbo, P.G.; Balk, S.P. Increased expression of genes converting adrenal androgens to testosterone in androgen-independent prostate cancer. *Cancer Res* **2006**, *66*, 2815-2825, doi:10.1158/0008-5472.CAN-05-4000.
16. Henry, G.H.; Malewska, A.; Joseph, D.B.; Malladi, V.S.; Lee, J.; Torrealba, J.; Mauck, R.J.; Gahan, J.C.; Raj, G.V.; Roehrborn, C.G.; et al. A Cellular Anatomy of the Normal Adult Human Prostate and Prostatic Urethra. *Cell Rep* **2018**, *25*, 3530-3542 e3535, doi:10.1016/j.celrep.2018.11.086.
17. Stambergova, H.; Skarydova, L.; Dunford, J.E.; Wsol, V. Biochemical properties of human dehydrogenase/reductase (SDR family) member 7. *Chem Biol Interact* **2014**, *207*, 52-57, doi:10.1016/j.cbi.2013.11.003.
18. Zemanova, L.; Kirubakaran, P.; Pato, I.H.; Stambergova, H.; Vondrasek, J. The identification of new substrates of human DHRS7 by molecular modeling and in vitro testing. *Int J Biol Macromol* **2017**, *105*, 171-182, doi:10.1016/j.ijbiomac.2017.07.012.
19. Song, L.; Turkson, J.; Karras, J.G.; Jove, R.; Haura, E.B. Activation of Stat3 by receptor tyrosine kinases and cytokines regulates survival in human non-small cell carcinoma cells. *Oncogene* **2003**, *22*, 4150-4165, doi:10.1038/sj.onc.1206479.
20. Garcia, R.; Bowman, T.L.; Niu, G.; Yu, H.; Minton, S.; Muro-Cacho, C.A.; Cox, C.E.; Falcone, R.; Fairclough, R.; Parsons, S.; et al. Constitutive activation of Stat3 by the Src and JAK tyrosine kinases participates in growth regulation of human breast carcinoma cells. *Oncogene* **2001**, *20*, 2499-2513, doi:10.1038/sj.onc.1204349.
21. Zhong, Z.; Wen, Z.; Darnell, J.E., Jr. Stat3: a STAT family member activated by tyrosine phosphorylation in response to epidermal growth factor and interleukin-6. *Science* **1994**, *264*, 95-98, doi:10.1126/science.8140422.
22. Wisniewski, J.R.; Zougman, A.; Nagaraj, N.; Mann, M. Universal sample preparation method for proteome analysis. *Nat Methods* **2009**, *6*, 359-362, doi:10.1038/nmeth.1322.
23. Tyanova, S.; Temu, T.; Sinitcyn, P.; Carlson, A.; Hein, M.Y.; Geiger, T.; Mann, M.; Cox, J. The Perseus computational platform for comprehensive analysis of (prote)omics data. *Nat Methods* **2016**, *13*, 731-740, doi:10.1038/nmeth.3901.
24. Kanehisa, M.; Goto, S. KEGG: kyoto encyclopedia of genes and genomes. *Nucleic Acids Res* **2000**, *28*, 27-30, doi:10.1093/nar/28.1.27.
25. Colaprico, A.; Silva, T.C.; Olsen, C.; Garofano, L.; Cava, C.; Garolini, D.; Sabedot, T.S.; Malta, T.M.; Pagnotta, S.M.; Castiglioni, I.; et al. TCGAbiolinks: an R/Bioconductor package for integrative analysis of TCGA data. *Nucleic Acids Res* **2016**, *44*, e71, doi:10.1093/nar/gkv1507.
26. Beltran, H.; Prandi, D.; Mosquera, J.M.; Benelli, M.; Puca, L.; Cyrta, J.; Marotz, C.; Giannopoulou, E.; Chakravarthi, B.V.; Varambally, S.; et al. Divergent clonal evolution of castration-resistant neuroendocrine prostate cancer. *Nat Med* **2016**, *22*, 298-305, doi:10.1038/nm.4045.
27. Taha-Mehlitz, S.; Bianco, G.; Coto-Llerena, M.; Kancherla, V.; Bantug, G.R.; Gallon, J.; Ercan, C.; Panebianco, F.; Eppenberger-Castori, S.; von Strauss, M.; et al. Adenylosuccinate lyase is oncogenic in colorectal cancer by causing mitochondrial dysfunction and independent activation of NRF2 and mTOR-MYC-axis. *Theranostics* **2021**, *11*, 4011-4029, doi:10.7150/thno.50051.

28. R Development Core Team *R: A language and environment for statistical computing*, R Foundation for Statistical Computing: Vienna, Austria, 2010.
29. Kassambara, A. *ggpubr: 'ggplot2' Based Publication Ready Plots*, 2020.
30. Kassambara, A., Kosinski, M., Biecek, P. *survminer: Drawing Survival Curves using'ggplot2'*.
31. Makkonen, H.; Kauhanen, M.; Paakinaho, V.; Jaaskelainen, T.; Palvimo, J.J. Long-range activation of FKBP51 transcription by the androgen receptor via distal intronic enhancers. *Nucleic Acids Res* **2009**, *37*, 4135-4148, doi:10.1093/nar/gkp352.
32. Ciardiello, F.; Tortora, G. EGFR antagonists in cancer treatment. *N Engl J Med* **2008**, *358*, 1160-1174, doi:10.1056/NEJMra0707704.
33. Yarden, Y.; Sliwkowski, M.X. Untangling the ErbB signalling network. *Nat Rev Mol Cell Biol* **2001**, *2*, 127-137, doi:10.1038/35052073.
34. Yarden, Y.; Pines, G. The ERBB network: at last, cancer therapy meets systems biology. *Nat Rev Cancer* **2012**, *12*, 553-563, doi:10.1038/nrc3309.
35. Lorenzo, G.D.; Bianco, R.; Tortora, G.; Ciardiello, F. Involvement of growth factor receptors of the epidermal growth factor receptor family in prostate cancer development and progression to androgen independence. *Clin Prostate Cancer* **2003**, *2*, 50-57, doi:10.3816/cgc.2003.n.013.
36. Labrie, F. Combined blockade of testicular and locally made androgens in prostate cancer: a highly significant medical progress based upon intracrinology. *J Steroid Biochem Mol Biol* **2015**, *145*, 144-156, doi:10.1016/j.jsbmb.2014.05.012.
37. Zannas, A.S.; Wiechmann, T.; Gassen, N.C.; Binder, E.B. Gene-Stress-Epigenetic Regulation of FKBP5: Clinical and Translational Implications. *Neuropsychopharmacology* **2016**, *41*, 261-274, doi:10.1038/npp.2015.235.
38. Hernes, E.; Fossa, S.D.; Berner, A.; Otnes, B.; Nesland, J.M. Expression of the epidermal growth factor receptor family in prostate carcinoma before and during androgen-independence. *Br J Cancer* **2004**, *90*, 449-454, doi:10.1038/sj.bjc.6601536.
39. Schlomm, T.; Kirstein, P.; Iwers, L.; Daniel, B.; Steuber, T.; Walz, J.; Chun, F.H.; Haese, A.; Kollermann, J.; Graefen, M.; et al. Clinical significance of epidermal growth factor receptor protein overexpression and gene copy number gains in prostate cancer. *Clin Cancer Res* **2007**, *13*, 6579-6584, doi:10.1158/1078-0432.CCR-07-1257.
40. Baek, K.H.; Hong, M.E.; Jung, Y.Y.; Lee, C.H.; Lee, T.J.; Park, E.S.; Kim, M.K.; Yoo, J.H.; Lee, S.W. Correlation of AR, EGFR, and HER2 Expression Levels in Prostate Cancer: Immunohistochemical Analysis and Chromogenic In Situ Hybridization. *Cancer Res Treat* **2012**, *44*, 50-56, doi:10.4143/crt.2012.44.1.50.
41. Whang, Y.E.; Armstrong, A.J.; Rathmell, W.K.; Godley, P.A.; Kim, W.Y.; Pruthi, R.S.; Wallen, E.M.; Crane, J.M.; Moore, D.T.; Grigson, G.; et al. A phase II study of lapatinib, a dual EGFR and HER-2 tyrosine kinase inhibitor, in patients with castration-resistant prostate cancer. *Urol Oncol* **2013**, *31*, 82-86, doi:10.1016/j.urolonc.2010.09.018.
42. Small, E.J.; Fontana, J.; Tannir, N.; DiPaola, R.S.; Wilding, G.; Rubin, M.; Iacona, R.B.; Kabbinavar, F.F. A phase II trial of gefitinib in patients with non-metastatic hormone-refractory prostate cancer. *BJU Int* **2007**, *100*, 765-769, doi:10.1111/j.1464-410X.2007.07121.x.
43. Nabhan, C.; Lestingi, T.M.; Galvez, A.; Tolzien, K.; Kelby, S.K.; Tsarwhas, D.; Newman, S.; Bitran, J.D. Erlotinib has moderate single-agent activity in chemotherapy-naive castration-resistant prostate cancer: final results of a phase II trial. *Urology* **2009**, *74*, 665-671, doi:10.1016/j.urology.2009.05.016.
44. Gravis, G.; Bladou, F.; Salem, N.; Goncalves, A.; Esterni, B.; Walz, J.; Bagattini, S.; Marcy, M.; Brunelle, S.; Viens, P. Results from a monocentric phase II trial of erlotinib in patients with metastatic prostate cancer. *Ann Oncol* **2008**, *19*, 1624-1628, doi:10.1093/annonc/mdn174.
45. Oda, K.; Matsuoka, Y.; Funahashi, A.; Kitano, H. A comprehensive pathway map of epidermal growth factor receptor signaling. *Mol Syst Biol* **2005**, *1*, 2005 0010, doi:10.1038/msb4100014.

46. Jamaspishvili, T.; Berman, D.M.; Ross, A.E.; Scher, H.I.; De Marzo, A.M.; Squire, J.A.; Lotan, T.L. Clinical implications of PTEN loss in prostate cancer. *Nat Rev Urol* **2018**, *15*, 222-234, doi:10.1038/nrurol.2018.9.
47. Viswanathan, S.R.; Ha, G.; Hoff, A.M.; Wala, J.A.; Carrot-Zhang, J.; Whelan, C.W.; Haradhvala, N.J.; Freeman, S.S.; Reed, S.C.; Rhoades, J.; et al. Structural Alterations Driving Castration-Resistant Prostate Cancer Revealed by Linked-Read Genome Sequencing. *Cell* **2018**, *174*, 433-447 e419, doi:10.1016/j.cell.2018.05.036.
48. Frattini, M.; Saletti, P.; Romagnani, E.; Martin, V.; Molinari, F.; Ghisletta, M.; Camponovo, A.; Etienne, L.L.; Cavalli, F.; Mazzucchelli, L. PTEN loss of expression predicts cetuximab efficacy in metastatic colorectal cancer patients. *Br J Cancer* **2007**, *97*, 1139-1145, doi:10.1038/sj.bjc.6604009.
49. Bouali, S.; Chretien, A.S.; Ramacci, C.; Rouyer, M.; Becuwe, P.; Merlin, J.L. PTEN expression controls cellular response to cetuximab by mediating PI3K/AKT and RAS/RAF/MAPK downstream signaling in KRAS wild-type, hormone refractory prostate cancer cells. *Oncol Rep* **2009**, *21*, 731-735.
50. Cathomas, R.; Rothermundt, C.; Klingbiel, D.; Bubendorf, L.; Jaggi, R.; Betticher, D.C.; Brauchli, P.; Cotting, D.; Droege, C.; Winterhalder, R.; et al. Efficacy of cetuximab in metastatic castration-resistant prostate cancer might depend on EGFR and PTEN expression: results from a phase II trial (SAKK 08/07). *Clin Cancer Res* **2012**, *18*, 6049-6057, doi:10.1158/1078-0432.CCR-12-2219.
51. Yu, H.; Jove, R. The STATs of cancer--new molecular targets come of age. *Nat Rev Cancer* **2004**, *4*, 97-105, doi:10.1038/nrc1275.
52. Campbell, C.L.; Jiang, Z.; Savarese, D.M.; Savarese, T.M. Increased expression of the interleukin-11 receptor and evidence of STAT3 activation in prostate carcinoma. *Am J Pathol* **2001**, *158*, 25-32, doi:10.1016/S0002-9440(10)63940-5.
53. Mora, L.B.; Buettner, R.; Seigne, J.; Diaz, J.; Ahmad, N.; Garcia, R.; Bowman, T.; Falcone, R.; Fairclough, R.; Cantor, A.; et al. Constitutive activation of Stat3 in human prostate tumors and cell lines: direct inhibition of Stat3 signaling induces apoptosis of prostate cancer cells. *Cancer Res* **2002**, *62*, 6659-6666.
54. Hiebert, B.M.; Janzen, B.W.; Sanjanwala, R.M.; Ong, A.D.; Feldman, R.D.; Kim, J.O. Impact of spironolactone exposure on prostate cancer incidence amongst men with heart failure: A Pharmacoepidemiological study. *Br J Clin Pharmacol* **2021**, *87*, 1801-1813, doi:10.1111/bcp.14568.
55. Mackenzie, I.S.; Morant, S.V.; Wei, L.; Thompson, A.M.; MacDonald, T.M. Spironolactone use and risk of incident cancers: a retrospective, matched cohort study. *Br J Clin Pharmacol* **2017**, *83*, 653-663, doi:10.1111/bcp.13152.
56. Arriza, J.L.; Weinberger, C.; Cerelli, G.; Glaser, T.M.; Handelin, B.L.; Housman, D.E.; Evans, R.M. Cloning of human mineralocorticoid receptor complementary DNA: structural and functional kinship with the glucocorticoid receptor. *Science* **1987**, *237*, 268-275, doi:10.1126/science.3037703.
57. Krug, A.W.; Grossmann, C.; Schuster, C.; Freudinger, R.; Mildenberger, S.; Govindan, M.V.; Gekle, M. Aldosterone stimulates epidermal growth factor receptor expression. *J Biol Chem* **2003**, *278*, 43060-43066, doi:10.1074/jbc.M308134200.
58. Grossmann, C.; Krug, A.W.; Freudinger, R.; Mildenberger, S.; Voelker, K.; Gekle, M. Aldosterone-induced EGFR expression: interaction between the human mineralocorticoid receptor and the human EGFR promoter. *Am J Physiol Endocrinol Metab* **2007**, *292*, E1790-1800, doi:10.1152/ajpendo.00708.2006.
59. Madrigal-Martinez, A.; Constancio, V.; Lucio-Cazana, F.J.; Fernandez-Martinez, A.B. PROSTAGLANDIN E2 stimulates cancer-related phenotypes in prostate cancer PC3 cells through cyclooxygenase-2. *J Cell Physiol* **2019**, *234*, 7548-7559, doi:10.1002/jcp.27515.
60. Pai, R.; Soreghan, B.; Szabo, I.L.; Pavelka, M.; Baatar, D.; Tarnawski, A.S. Prostaglandin E2 transactivates EGF receptor: a novel mechanism for promoting colon cancer growth and gastrointestinal hypertrophy. *Nat Med* **2002**, *8*, 289-293, doi:10.1038/nm0302-289.

61. Sharaf, A.; Mensching, L.; Keller, C.; Rading, S.; Scheffold, M.; Palkowitsch, L.; Djogo, N.; Rezgaoui, M.; Kestler, H.A.; Moepps, B.; et al. Systematic Affinity Purification Coupled to Mass Spectrometry Identified p62 as Part of the Cannabinoid Receptor CB2 Interactome. *Front Mol Neurosci* **2019**, *12*, 224, doi:10.3389/fnmol.2019.00224.

62. Howlett, A.C.; Barth, F.; Bonner, T.I.; Cabral, G.; Casellas, P.; Devane, W.A.; Felder, C.C.; Herkenham, M.; Mackie, K.; Martin, B.R.; et al. International Union of Pharmacology. XXVII. Classification of cannabinoid receptors. *Pharmacol Rev* **2002**, *54*, 161-202, doi:10.1124/pr.54.2.161.

5.2 Discussion & Outlook

Similarly to orphan receptors without known ligand, DHRS7 can be considered an orphan enzyme without assigned physiological substrate. The lower expression of DHRS7 in higher grade PCa biopsies as shown bei Seibert *et al.* however proclaimed a potentially protective role in PCa [63]. In addition, siRNA-mediated knock-down of *DHRS7* led to an increased proliferation and migration and decreased adhesion of the androgen dependent LNCaP cells. This further hinted towards a functional role in PCa and that the lost expression in PCa is not merely a secondary effect. Considering the dependency of PCa on androgens and the continuous role of the AR even in CRPC [143, 145, 146], the observations of Seibert *et al.* suggested the role of DHRS7 is to metabolize 5α-DHT. In theory, the loss of DHRS7 would lead to higher intratumoral concentrations of 5α-DHT and thus higher AR activation. The potential for DHRS7 to accept 5α-DHT as substrate was supported by the fact that it is part of the SDR superfamily of which several members are known to metabolize steroid hormones and that DHRS7 was shown to use steroid hormones as substrates previously [23, 28, 64, 67]. The work of Araya *et al.* followed up on this hypothesis and showed that DHRS7 is indeed capable of metabolizing 5α-DHT to 3α-Adiol and by doing so, decreasing AR activation in HEK-293 cells transfected with DHRS7 [27]. These studies appear to complement each other and suggest that the role of DHRS7 in the prostate is to prevent excessive AR activation.

It was the next logical step to test this hypothesis in an endogenous system. For this purpose, an siRNA-mediated knock-down of *DHRS7* was performed and followed by a treatment with 5α-DHT. Theoretically, this should lead to higher concentrations of 5α-DHT and higher AR dependent gene expression. However, this was not the case even though a concentration dependent increase of AR regulated gene expression was overall detected. The only exception was an increased expression of FK506 binding protein 5 (*FKBP5*) in cells after *DHRS7* knock-down treated with 1 nM of 5α-DHT. This isolated case could indicate a serendipitous finding. A link between FKBP5 and stress as well as an interaction of FKBP5 with other pathways, including that of the GR, have been described [196]. Overall, FKBP5 is not particularly specific to AR signaling and neither is its expression exclusively regulated by the AR [196]. It might be possible that the increased *FKBP5* expression in our singular case is because of

the combined effects of knock-down of *DHRS7* (and its secondary effects), treatment with 5α-DHT, and treatment-induced cellular stress.

It so appears that although DHRS7 is able to metabolize 5α-DHT, it is not the physiological function. To identify what processes contribute to the aggressive phenotype of LNCaP cells after knock-down of *DHRS7*, the proteome was analyzed following 24 h, 36 h, and 48 h after knock-down. Unchanged expression of the AR and a lack of increase proteins that are upregulated by the AR – kallikrein related peptidase 3 (KLK3; PSA), transmembrane serine protease 2 (TMPRSS2), and FKBP5 – further support the note that DHRS7 is not involved in AR signaling. KLK3 and TMPRSS2 even showed a trend to be less expressed after knock-down.

At this point the proteomics experiment must be discussed critically. First and foremost, it was performed once only, preventing the application of valuable statistical analyses. Consequently, a volcano plot allowing easy visualization of the expression changes and to lay unbiased focus on proteins with the largest and statistically significant fold-changes was not feasible [197]. For large data analysis it is common to perform pathway enrichment analysis, *e.g.* according to KEGG pathways or gene ontology terms [198, 199]. This approach was tested but it was decided that it is not appropriate in our case. Many tools exist with their own strengths and limitations but my own experiences are mostly limited to DAVID bioinformatics because it is freely available online and was recommended to me by a former colleague [200]. Consequently, the discussed considerations below primarily relate to my experiences with this tool and do not necessarily reflect pathway enrichment analysis in general.

One reason why we decided conventional pathway enrichment was not appropriate in our case is that the changes in our proteomics dataset are mostly small. Only 1.2% of the proteins (79 of 6’675) showed a $\log_2$-fold change greater than +1 or -1. For comparison, a study comparing glioma with control samples identified 12’687 proteins of which 45% showed a two-fold different expression level [201]. Reasons for the overall small changes in our case could be that all samples originated from the same cell line. In other words, the analyzed cell populations were still rather homogenous compared to a case of healthy versus disease tissue. Another potential explanation is that an siRNA-mediated knock-down is hardly ever 100% effective. In our experiments, knock-down was performed for up to 48 h. Previous experiments showed mRNA levels of DHRS7 are increasing again after 72 h [63]. Apparently the knock-down reaches its peak at 48 h with about 25% of DHRS7 protein still remaining. To include more proteins

for a pathway enrichment analysis, one could simply lower the threshold of fold-change, but this could incorporate too many proteins whose change may be neglectable biologically. Furthermore, the direction of change (up- or downregulation) will not be considered. Two proteins with similar functions will likely contribute to the enrichment of the same pathway (*e.g.* apoptosis), but through a change in opposite direction, the effect may be cancelled out biologically. The same applies for proteins that are changed in the same direction but with opposite functions (*e.g.* pro- and antiapoptotic). The setup of our proteomics experiment itself complicated analysis as well by the three different time points. This can provide additional interesting insight, but raises the question which changes at what time point are of greater importance – the early changes, potentially sensitive to the knock-down, or the late changes, when the knock-down is most effective? It also raises the question how to deal with findings that show irregular changes (*e.g.* a downregulation at early time points, but an upregulation at late time points). Pathway enrichment analysis does not take into account phosphorylation or similar regulatory mechanisms. This is a limitation of our proteomics in general because our results are based on expression changes yet many processes are controlled primarily by phosphorylation status [202]. Our experiment was not set up to detect such posttranslational modifications. Therefore it is possible to miss out on potentially interesting proteins simply because they were not changed on an expressional level. In light of these considerations, we opted to perform a simple KEGG pathway annotation and to filter for proteins annotated with the term “Prostate cancer” and those that could be detected in all three time points and to select an interesting candidate [198]. This is somewhat biased towards proteins that are already known to be involved in PCa and prevents more novel findings. One may argue though that PCa is the setting we are interested in and that incorporating one protein without known physiological role (DHRS7) is already challenging enough.

Although the changes of protein expression were moderate, some particular ones stood out. The cell cycle associated cyclin dependent kinase 2 (CDK2) was decreased, but so was its inhibitor cyclin dependent kinase inhibitor 1A [203]. The cAMP-responsive element binding protein 3 like 4 showed some of the strongest downregulation (log_2-fold change of -1.5 after 36 h), which was associated with a decrease of androgen stimulated proliferation and decreased AR activity [204]. β-Catenin (CTNNB1) is known for its role in the Wnt signaling pathway whose excessive activation is related to diseases including cancer. However, under unstimulated

conditions, CTNNB1 is continuously targeted for degradation [205]. A decrease of CTNNB1 in our experiment suggests a downregulation of this pathway. Heat shock protein 90 (HSP90) is required for full AR activation by androgens and exposure of prostate stromal cells to extracellular HSP90α induces migration, phosphorylation of the extracellular signal-regulated kinase (Erk), and secretion of cytokines [206, 207], yet the inducible HSP90AA1, which is often deleted in PCa [208], was decreased in our dataset. Mitogen-activated protein kinase (MAPK)/Erk signaling is involved in many cellular processes including proliferation, survival, and motility [209], but again Erk2 encoded by MAPK1 is decreased in our proteomics data set, although our Western blot did not confirm this. The phosphatidylinositol-4,5-bisphosphate 3-kinase catalytic subunit β (PIK3CB), increased in our dataset, is one of the class I catalytic subunits of the phosphatidylinositol 3-kinase (PI3K) protein complex that is often altered in different cancers [210]. In PC-3 cells, knock-down of *PIK3CB* reduced colony formation and downstream signaling as measured by AKT serine/threonine kinase (Akt) phosphorylation and decreased tumor volume *in vivo* [211]. RB1 is one the more strongly downregulated proteins in our proteomics and a mouse model of RB1 and tumor protein p53 loss induced neuroendocrine differentiation and resistance to anti-androgen therapy [139, 140]. Even though some proteins presented themselves as candidates for us to follow on based on their comparatively larger expression changes and nature, the direction of their differential expression limited our excitement. For example CDK2, CTNNB1 and MAPK1 are associated with proliferation and cancer, yet they were decreased in our data. More in line would have been PIK3CB and RB1 that are also known for their contribution to malignancy and their differential expression suited an increased aggression of LNCaP cells. But ultimately we decided to focus our efforts on the EGFR for several reasons: It was upregulated at all time points with an increasing difference compared to the control cells and an increase of one of its downstream targets, signal transducer and activator of transcription (STAT) 3, was identified as well after *DHRS7* knock-down [212-214]. The EGFR receives extracellular signals and propagates them through various downstream pathways that culminate in different effects, such as proliferation [215-217].

For these reasons and because overexpression and mutations of EGFR have been desrcibed in different cancers, including lung [218, 219], brain [220], and colorectal cancer [221], antibodies and small molecule kinase inhibitors targeting the EGFR have been developed and are routinely used in cancer therapy [222]. The EGFR was shown

to be increased in PCa in several studies and in one it was also significantly associated with younger patient age [172, 173, 223-225]. Therefore, increased expression of EGFR in PCa could be an interesting drug target as well.

Several phase II clinical trials have addressed this but results were moderate. Studies with lapatinib, gefitinib, and erlotinib had comparable results in that some patients responded by a decrease of PSA, but stable disease was more common or even no response at all [226-231]. EGFR expression was not assessed in all studies and when it was, correlation with response was not investigated due to lack of response and low numbers of patients. A combinational treatment of docetaxel with cetuximab in metastatic CRPC with 35 patients showed a confirmed response of ≥ 50% PSA decline in 7 patients and ≥ 30% in 11 patients [232]. Importantly, expression of EGFR and phosphatase and tensin homolog (PTEN) correlated with progression free survival, suggesting that targeting EGFR in PCa may be beneficial for certain patient populations.

Increased expression of EGFR and STAT3 in our proteomics was confirmed independently by Western blot and RT-qPCR. An increase of EGFR after *DHRS7* knock-down in the AR negative PC-3 and DU145 cells is another indicator that loss of DHRS7 and the resulting cell phenotype described by Seibert *et al.* is not linked to the AR [63]. In the same study, knock-down of *DHRS7* in PC-3 cells led to increased migration and decreased adhesion, but no increase of proliferation.

Our *in vitro* findings regarding DHRS7 and EGFR expression were translated into a clinical aspect by analyzing The Cancer Genome Atlas (TCGA) data and by tissue microarray (TMA) staining. Both showed an inverse correlation between DHRS7 and EGFR. For the TCGA data, the correlation improved after stratifying according to AR signaling. This may imply that loss of AR signaling can be compensated by the EGFR. Similar to this, a previous study showed an inverse correlation between AR and EGFR expression [225]. In the TMA however, stratification did not improve the correlation, potentially because of limited sample numbers. In the case of both DHRS7 and EGFR, the decrease and increase, respectively, correlated with Gleason score. The loss of DHRS7 according to Gleason score thus confirms the previous finding of Seibert *et al.* and the increase of EGFR in PCa other studies [63, 172, 173, 223, 224]. Additional impact of DHRS7 and EGFR in clinical cases of PCa is provided by the observed survival rates. Higher DHRS7 expression was associated with better survival rates, whereas higher EGFR expression was associated with worse survival rates.

The mechanism by which loss of DHRS7 induces EGFR expression is unknown. The increased *EGFR* mRNA indicates an increased expression on a transcriptional level rather than decreased degradation. The mineralocorticoid receptor (MR) can be activated by cortisol and aldosterone [233]. Treatment with the latter induced EGFR expression in kidney cortex homogenates of adrenalectomized rats and primary human renal cortical cells and transfection of CHO cells with MR induced EGFR expression, which could be prevented by the MR inhibitor spironolactone [234]. In a similar fashion, transfection of the MR into HEK-293 cells led to increased activation of an ectopically expressed EGFR promoter construct [235]. Interestingly, retrospective cohort studies showed a reduced PCa risk in males exposed to spironolactone treatment [236, 237]. DHRS7 was shown to metabolize cortisone to 20β-dihydrocortisone and as such it might be interesting to see whether DHRS7 is able to limit ligand exposure of the MR [27]. Whether this is the case and whether this may play a role in disease remains to be investigated. Identification of other transcription factors that regulate EGFR expression could further help to link the loss of DHRS7 with increased EGFR expression.

In addition to gene expression changes, treatment with EGF after knock-down of *DHRS7* also led to higher detectable levels of phosphorylated EGFR, possibly a direct consequence of the increased levels of total EGFR. One may argue that increased numbers of EGFR proteins expressed on the cell surface sensitize a cell to EGF molecules in the surrounding. One of the early studies on the EGFR suggested that EGFR phosphorylation is dependent on the receptor concentration [238]. This can be compared to PCa cells with AR overexpression that is considered to mediate increased sensitivity to low androgen concentrations after castration [157]. This is supported by a study in which cells expressing higher amounts of EGFR required higher concentrations of EGFR-targeting antibody to inhibit EGFR phosphorylation. But interestingly, cells with higher EGFR expression were more susceptible to antibody induced cytolysis by monocytes or other immunologic effectors [239].

Downstream of EGFR, we investigated the phosphorylation status of STAT3, Erk and Akt. In summary it appeared that the signal was propagated in a cell line specific manner. Although not statistically significant, LNCaP seemed to favor STAT3. This is not surprising since STAT3 showed higher expression levels after *DHRS7* knock-down. The STAT family has been implicated in different malignancies [240]. In PCa, STAT3 is mostly considered oncogenic, *e.g.* by increased expression or

phosphorylation in PCa samples or increased apoptosis of PCa cells after knock-down of *STAT3* [241, 242], but conflicting results exist. A mouse model of *PTEN* loss increased STAT3 expression and phosphorylation (according to an oncogenic nature) but loss of *STAT3* in the same *PTEN*-loss mice led to even greater tumor growth than *PTEN* loss alone [243]. The precise effects of increased STAT3 in the setting of decreased DHRS7 expression thus need to be elucidated.

Although we detected a strong increase of Erk phosphorylation upon EGF treatment in control cells it did not appear to be increasingly phosphorylated after *DHRS7* knock-down. Interestingly, in the PC-3 cells phosphorylation of Erk barely increased after *DHRS7* knock-down while in control cells it increased substantially. One may speculate about the reasons but only studies directed towards this surprising observation will be able to elucidate it. In order to strengthen the link between loss of DHRS7 and increased EGFR and downstream signaling, one may also test EGFR inhibitors to see whether their efficacy decreases after knock-down of *DHRS7*. Assays that measure proliferation or similar parameters can further supplement this.

PTEN is one of the most commonly lost or altered genes in PCa [244]. Its activity of converting phosphatidylinositol 3,4,5-triphosphate (PIP_3) to phosphatidylinositol 4,5-biphosphate stands in direct opposition of the activity of class I PI3K [245]. PIP_3 allows the 3-phosphoinositide dependent protein kinase 1 (commonly known as PDK1) to phosphorylate Akt, leading to downstream effects. Our experiments led to statistically significant increase of Akt phosphorylation in LNCaP cells and a strong trend in DU145 cells. This suggests that the increase of EGFR along with a higher activation induced by EGF can lead to increased signaling *via* the PI3K/Akt pathway. All three cell lines showed baseline phosphorylation of Akt even when untreated with EGF but the increase of phosphorylation in DU145 was the strongest which is in line with its highest EGFR expression. Increased PI3K/Akt signaling (including loss of PTEN) has been associated with resistance to ERBB2 targeting trastuzumab in breast cancer and response to EGFR targeting cetuximab in colorectal cancer and PC-3 cells [246-248]. The PI3K/Akt pathway was discussed as a potential drug target in PCa but success would depend on PTEN status and as such, PTEN was proposed as a potential prognostic marker in PCa [245].

Careful patient stratification according to the expression and/or mutation status of EGFR, PTEN, AR, and more could be essential to successful therapy. DHRS7 could be part of such a potential protein signature. A study investigating differential gene

expression of the various cell types in healthy prostate found high expression of DHRS7 and to be specific to luminal epithelial cells [81]. For diagnostic and cancer staging purposes, prostate biopsy is performed regularly [110]. Standard biopsies could be coupled to routine staining procedures for key proteins to stratify patients according to risk, set them up for adequate treatment, and thus move PCa care towards precision medicine.

More convenient than biopsies are blood tests. In case DHRS7 truly plays a role in PCa progression, once its substrate has been defined, surveillance of the substrate, the product, or the product to substrate ratio might be used as a biomarker (assuming it can be detected and quantified robustly in blood samples).

So the question rises – what is the substrate of DHRS7? And further: how can we identify it? One approach would be to use an *in silico* screening. A homology model based on HSD11B1 was generated before and virtual screening predicted 5α-DHT as a substrate, supporting the finding of Araya *et al.* [27, 69]. Our group has taken early steps towards an *in silico* approach as well (unpublished data), but at that point it was not convincing enough to follow up on it and so the focus was laid somewhere else. The study by Zemanová *et al.* was published in 2017 and advancements in computer technologies are frequent. Revisiting an *in silico* approach while incorporating the knowledge up to date may lead to new interesting hypotheses.

Another method would be the use of metabolomics. Both the experiments carried out by Seibert *et al.* that led to the observation of more aggressive growth of LNCaP cells and our proteomics experiment after knock-down of *DHRS7* were performed in normal cell culture conditions that included FBS [63]. One can assume that the substrate of DHRS7 can be found in said culture medium. Thus, changes induced by knock-down of *DHRS7* should in theory be detectable within the medium with a sufficiently sensitive analytical method. Metabolomics has been applied to various cancer cell lines already, including PCa cell lines, and changes to choline and amino acid metabolism and others have been observed [249-251]. One group suggested to identify the role of a protein with unknown function as following: inducing the loss of the protein's activity (*e.g.* by gene deletion), doing this likewise for a protein whose activity is known, and compare the altered metabolome of the two cell populations. They claim that the loss of proteins with similar functions will lead to similar metabolic signatures, which can give a hint towards the unknown metabolic function of the protein of interest [252]. Although interesting, applicability in the case of DHRS7 is

questionable. Proteins to compare it to would be other members of the SDR superfamily, however, they only show 10-30% sequence identity and a large variety of different substrates [23, 24, 28]. Untargeted metabolomics might be too challenging and focusing on one particular group of metabolites could be a viable option, for example by performing lipidomics with a focus on prostaglandins, retinoids, or steroids.

Prostaglandins and other eicosanoids are lipophilic compounds involved in inflammation and cancer [253]. PGE_2 treatment was able to induce phosphorylation of EGFR and Erk in normal gastric epithelial and colon cancer cells that could be prevented by the use of EGFR kinase inhibitors [254]. Prostaglandins are generated from arachidonic acid and one of its derivates, 2-arachidonoylglycerol, is an agonist of the cannabinoid receptor type 2 (CB2) [253, 255]. Affinity purification coupled to MS in HEK-293 cells stably expressing CB2 detected DHRS7 as an interacting partner with CB2. Additionally, DHRS7 was only detected in these CB2-expressing cells [256]. This may indicate a role of DHRS7 in lipid metabolism instead of steroid metabolism. It would be interesting to investigate whether expression of CB2 and/or treatment with its agonists in PCa or other cell lines could induce an increased expression of DHRS7. It may also be worth to investigate whether DHRS7 is capable of metabolizing CB2 related compounds. This becomes further interesting considering that in spermatozoa 2-arachidonoylglycerol is hydrolyzed in a progesterone dependent fashion by abhydrolase domain containing 2 (ABHD2) [257] – a protein with a $\log_2$-fold change of > +1 at all time points in our proteomics data, leading us further towards lipid metabolism. In fact, earlier experiments attempted to investigate ABHD2, unfortunately though, we were unable to confirm an increase of ABHD2 by RT-qPCR or Western blot. It might be worth though to readdress this protein in light of reported ABHD2 inhibitors [258].

Speaking of inhibitors, looking from a toxicological point of view, if DHRS7 is truly protective in PCa, its inhibition should be avoided. Exposure to xenobiotics that can inhibit DHRS7 over prolonged time could lead to increased PCa risk. It has already been shown that xenobiotics can be accepted by DHRS7 as substrates, including NNK [64, 67, 68], one of the strongest carcinogens derived from tobacco smoke [259]. Although no publication could be found that discusses NNK in the context of PCa, tobacco smoking is considered a risk factor for PCa and interestingly, DHRS7 was found to be less expressed in lung cancer tissue of current and former smokers compared to lung cancer tissue of patients who never smoked [260, 261]. Therapeutic

drugs should not inhibit DHRS7 either, particularly those intended for PCa treatment as this may reduce their therapeutic effect. However, highest expression of DHRS7 can be found in healthy prostate and low grade PCa for which primary care are prostatectomy and radiotherapy [75]. Drugs for PCa treatment are generally used for progressed disease, when DHRS7 expression tends to be decreased already.

In conclusion, our study on DHRS7 further strengthens the hypothesis that it plays a protective role in PCa but it is apparently not linked to AR signaling. Instead, it seems that there is a relationship between loss of DHRS7 and an increase of EGFR. This is not only based on *in vitro* findings alone but is supported by patient derived samples. This study provides an interesting starting point from where to continue investigating the relationship between these two proteins and motivates to identify the substrate of the orphan enzyme DHRS7.

6 OTHER CONTRIBUTIONS

6.1 Summary

Other contributions have been achieved by participating in several side projects. First, a new potential biomarker for the activity of HSD11B1 in mice was identified by measuring the ratio of certain bile acids [262]. Second, the LC-MS method employed for the identification of said bile acids was further improved and validated [263]. Third, this optimized LC-MS method was used to measure the bile acid profile in a mouse model of alveolar echinococcosis (AE) [264]. Lastly, the same mouse model was used to assess expression changes of proteins related to endoplasmic reticulum stress (ERS) [265].

The main role of HSD11B1 is the conversion of inactive cortisone to cortisol. Together with its counterpart HSD11B2 that performs the opposite reaction they participate in the regulation of the activity of the GR and MR [266]. Because imbalances of glucocorticoids have been linked to various adverse health effects, the use of inhibitors targeting HSD11B1 has received attention [267]. Besides cortisone, other substrates for HSD11B1 exist, including the bile acid 7-oxolithocholic acid [268]. In our study, using four different mouse models for decreased HSD11B1 activity, we showed that the ratio of ursodeoxycholyltaurine to 7-oxolithocholyltaurine performs better as a biomarker for HSD11B1 activity in murine plasma samples than individual compounds [262]. Importantly, humans are able to convert 7-oxolithocholic acid to ursodeoxycholic acid as well, but glycine conjugates dominate over taurine conjugates [269, 270]. In theory, this biomarker can be applied not only to mice, but to humans as well – a hypothesis that is currently under investigation.

The above study by Weingartner *et al.* used an LC-MS method based on a previously published one but with slight modifications [271]. However, there was room for further optimization. This led to a publication with a focus on the development and validation of a LC-MS method to detect bile acids and bile acid conjugates in both human and murine serum, plasma, and liver tissue [263]. Of particular note are the additional analytes allo bile acids, which are 5α- instead of 5β-reduced [272].

The developed method was used to assess the bile acid composition in serum and liver samples of a mouse model of AE [264]. This disease is caused by ingesting the

eggs of *Echinococcus multilocularis*, commonly known as the fox tape worm. The primary organ affected is the liver, in which tumor-like growths occur with a risk of spreading to other organs, including the brain [273-275]. The only curative treatment is surgical removal of the infected tissue and while adjuvant pharmacological therapy, *e.g.* albendazole (ABZ), is available, it is parasitostatic only [273, 274]. Mice infected with *E. multilocularis* showed a different bile acid profile in both serum and liver. Particularly in serum, there was an increase in the ratio of total taurine-conjugated to total unconjugated bile acids. Treatment with ABZ returned the bile acid profiles back to normal, without affecting bile acid composition in mock infected mice [264]. Enzymes involved in bile acid synthesis, Cyp7a1 and Akr1d1, as well as bile acid transporters ATP-binding cassette sub-family B member 11 and solute carrier family 10 member 1 (also known as BSEP and NTCP, respectively), tended to be decreased in mice infected with *E. multilocularis*. An effect that was also reversed by ABZ treatment [264].

In the same mouse model we investigated alterations of ERS related proteins [265]. Other pathogens, mainly viruses, bacteria, and protozoan parasites, have shown to affect ERS and unfolded protein response (UPR) [276-278]. Both ABZ and a programmed death-ligand 1 (PD-L1) targeting antibody (αPD-L1) were shown previously to reduce parasite weight in *E. multilocularis* infected mice and αPD-L1 treatment also to reduce inflammatory cytokines in the liver [279]. We thus investigated whether ABZ can decrease inflammatory markers as well and whether ABZ and αPD-L1 treatment has an effect on ERS and UPR associated proteins in AE. Our results showed an increase of the UPR master regulator glucose-binding protein 78 and an increase of the activating transcription factor 6 branch of UPR, whereas the protein kinase R like ER kinase and inositol-requiring enzyme 1 (IRE1) branches were decreased [265]. These changes were reversed by the treatment with ABZ and αPD-L1 but did not affect expression levels of UPR associated proteins in mock infected mice. Furthermore, ABZ was able to decrease inflammatory cytokines in the liver. We also identified an increase of two microRNAs in infected mice that were decreased again upon treatment with ABZ. One of them, microRNA-1839-5p, has a target site in the mRNA of IRE1α and could therefore explain the decreased expression level of IRE1α.

6.2 The ratio of ursodeoxycholyltaurine to 7-oxolithocholyltaurine serves as a biomarker of decreased 11β-hydroxysteroid dehydrogenase 1 activity in mouse

Published Article

Michael Weingartner[1#], Simon Stücheli[1#], Denise V. Kratschmar[1], Julia Birk[1], Petra Klusonova[1], Karen E. Chapman[2], Gareth G. Lavery[3], and Alex Odermatt[1]

[1] Division of Molecular and Systems Toxicology, Department of Pharmaceutical Sciences, University of Basel, Basel, Switzerland.

[2] University/BHF Centre for Cardiovascular Science, University of Edinburgh, Queen's Medical Research institute, Edinburgh, UK.

[3] Institute of Metabolism and Systems Research, University of Birmingham, Birmingham, UK.

[#] These authors contributed equally to the present study.

Contribution to the project:

Experimental work

Analysis and interpretation of data

Revising the manuscript

Received: 29 April 2020 | Revised: 6 December 2020 | Accepted: 27 December 2020

DOI: 10.1111/bph.15367

Themed Issue: Oxysterols, Lifelong Health and Therapeutics

RESEARCH PAPER

The ratio of ursodeoxycholyltaurine to 7-oxolithocholyltaurine serves as a biomarker of decreased 11β-hydroxysteroid dehydrogenase 1 activity in mouse

Michael Weingartner[1] | Simon Stücheli[1] | Denise V. Kratschmar[1] | Julia Birk[1] | Petra Klusonova[1] | Karen E. Chapman[2] | Gareth G. Lavery[3] | Alex Odermatt[1]

[1]Division of Molecular and Systems Toxicology, Department of Pharmaceutical Sciences, University of Basel, Basel, Switzerland

[2]Queen's Medical Research Institute, University/BHF Centre for Cardiovascular Science, University of Edinburgh, Edinburgh, UK

[3]Institute of Metabolism and Systems Research, University of Birmingham, Birmingham, UK

Correspondence
Alex Odermatt, Division of Molecular and Systems Toxicology, Department of Pharmaceutical Sciences, University of Basel, Klingelbergstrasse 50, 4056 Basel, Switzerland.
Email: alex.odermatt@unibas.ch

Funding information
Biological Sciences Research Council David Phillips Fellowship, Grant/Award Number: BB/G023468/1 (to G.G.L); Schweizerischer Nationalfonds zur Förderung der Wissenschaftlichen Forschung, Grant/Award Number: 31003A-179400 (to A.O.)

Background and Purpose: 11β-Hydroxysteroid dehydrogenase 1 (11β-HSD1) regulates tissue-specific glucocorticoid metabolism and its impaired expression and activity are associated with major diseases. Pharmacological inhibition of 11β-HSD1 is considered a promising therapeutic strategy. This study investigated whether alternative 7-oxo bile acid substrates of 11β-HSD1 or the ratios to their 7-hydroxy products can serve as biomarkers for decreased enzymatic activity.

Experimental Approach: Bile acid profiles were measured by ultra-HPLC tandem-MS in plasma and liver tissue samples of four different mouse models with decreased 11β-HSD1 activity: global (11KO) and liver-specific 11β-HSD1 knockout mice (11LKO), mice lacking hexose-6-phosphate dehydrogenase (*H6pd*KO) that provides cofactor NADPH for 11β-HSD1 and mice treated with the pharmacological inhibitor carbenoxolone. Additionally, 11β-HSD1 expression and activity were assessed in *H6pd*KO- and carbenoxolone-treated mice.

Key Results: The enzyme product to substrate ratios were more reliable markers of 11β-HSD1 activity than absolute levels due to large inter-individual variations in bile acid concentrations. The ratio of the 7β-hydroxylated ursodeoxycholyltaurine (UDC-Tau) to 7-oxolithocholyltaurine (7oxoLC-Tau) was diminished in plasma and liver tissue of all four mouse models and decreased in *H6pd*KO- and carbenoxolone-treated mice with moderately reduced 11β-HSD1 activity. The persistence of 11β-HSD1 oxoreduction activity in the face of H6PD loss indicates the existence of an alternative NADPH source in the endoplasmic reticulum.

Abbreviations: 11β-HSD, 11β-hydroxysteroid dehydrogenase; 11KO, global 11β-HSD1 knockout; 11LKO, liver-specific 11β-HSD1 knockout; 7oxoDCA, 7-oxodeoxycholic acid; 7oxoLCA, 7-oxolithocholic acid; 7oxoLC-Tau, 7-oxolithocholyltaurine; CA, cholic acid; CDCA, chenodeoxycholic acid; CDC-Gly, chenodeoxycholylglycine; CDC-Tau, chenodeoxycholyltaurine; CHAPS, 3-[(3-cholamidopropyl)dimethylammonio]-1-propanesulfonate; C-Gly, cholylglycine; C-Tau, cholyltaurine; CTRL, control; DCA, deoxycholic acid; DC-Tau, deoxycholyltaurine; ER, endoplasmic reticulum; H6PD, hexose-6-phosphate dehydrogenase; *H6pd*KO, global *H6pd* knockout; HDCA, hyodeoxycholic acid; LCA, lithocholic acid; LC-Tau, lithocholyltaurine; LLOD, lower limit of detection; MCA, muricholic acid; MOPS, 3-(*N*-morpholino)propanesulfonic acid; MC-Tau, muricholyltaurine; UDCA, ursodeoxycholic acid; UDC-Gly, ursodeoxycholylglycine; UDC-Tau, ursodeoxycholyltaurine; UHPLC–MS/MS, ultra-HPLC tandem-MS.

Michael Weingartner and Simon Stücheli contributed equally to the present study.

Conclusions and Implications: The plasma UDC-Tau/7oxo-LC-Tau ratio detects decreased 11β-HSD1 oxoreduction activity in different mouse models. This ratio may be a useful biomarker of decreased 11β-HSD1 activity in pathophysiological situations or upon pharmacological inhibition.

LINKED ARTICLES: This article is part of a themed issue on Oxysterols, Lifelong Health and Therapeutics. To view the other articles in this section visit http://onlinelibrary.wiley.com/doi/10.1111/bph.v178.16/issuetoc

KEYWORDS
11β-hydroxysteroid dehydrogenase, bile acid, biomarker, disease, glucocorticoid, inhibitor

1 | INTRODUCTION

A dysregulation of glucocorticoid production or a hyposensitivity or hypersensitivity to these hormones has been associated with major diseases such as osteoporosis, cognitive and mood disturbances, cardio-metabolic disorders, cancer and immune diseases (Quax et al., 2013). Besides a tightly regulated synthesis, the tissue-specific metabolism has a key role in mediating glucocorticoid-regulated functions. **11β-Hydroxysteroid dehydrogenase type 1 (11β-HSD1)** and **type 2 (11β-HSD2)** catalyse the conversion of inactive 11-oxoglucocorticoids (cortisone, 11-dehydrocorticosterone) to potent 11β-hydroxyglucocorticoids (cortisol, corticosterone) and the reverse reaction, respectively, and both enzymes are cell specifically expressed (Odermatt & Kratschmar, 2012). 11β-HSD1, although catalysing both oxidation and oxoreduction *in vitro*, predominantly acts as an oxoreductase *in vivo* due to co-expression with hexose-6-phosphate dehydrogenase (H6PD) that provides NADPH co-substrate in the endoplasmic reticulum (ER) (Atanasov et al., 2004; Banhegyi et al., 2004; Lavery et al., 2006) (Figure 1). 11β-HSD1 is essential for the therapeutic effects of pharmacologically administered cortisone and **prednisone** (Hult et al., 1998).

Rodent studies and clinical investigations demonstrated an association between excessive 11β-HSD1 activity and adverse health effects including insulin resistance and type II diabetes mellitus, osteoporosis, impaired wound healing, skin aging, cognitive impairment and glaucoma (Gathercole et al., 2013; Terao & Katayama, 2016; Wyrwoll et al., 2011). Therefore, 11β-HSD1 attracted high attention for potential therapeutic applications and a variety of small molecule inhibitors have been developed in order to assess their effects in preclinical and clinical studies (Feig et al., 2011; Freude et al., 2016; Hardy et al., 2020; Markey et al., 2017; Rosenstock et al., 2010; Schwab et al., 2017; Scott et al., 2014; Tiganescu et al., 2018; Webster et al., 2017; Ye et al., 2017).

Biomarkers of *in vivo* 11β-HSD1 activity can facilitate preclinical and clinical investigations into states of 11β-HSD1 deficiency and the efficacy of pharmacological inhibitors. Currently, decreased ratios of urinary (tetrahydrocorticosterone + allo-tetrahydrocorticosterone)/tetrahydro-11-dehydrocorticosterone and (tetrahydrocortisol + allo-tetrahydrocortisol)/tetrahydrocortisone are used as biomarkers for decreased 11β-HSD1 activity in rodents and human, respectively (Abrahams et al., 2012; Courtney et al., 2008; Freude et al., 2016; Jamieson et al., 1999; Lavery et al., 2013; Webster et al., 2017). However, these ratios require analysis of urine samples (usually 24-h sampling) and small sample volumes remain a challenge when analysing mouse urine. Moreover, the tetrahydro-glucocorticoid ratios are strongly influenced by 11β-HSD2 activity, as are plasma or serum cortisol/cortisone and corticosterone/11-dehydrocorticosterone ratios (Quinkler & Stewart, 2003; Ulick et al., 1979, 1990). These glucocorticoid metabolite ratios are therefore not useful to monitor disease states with altered 11β-HSD1 activity or to assess 11β-HSD1 inhibitors in preclinical and clinical studies.

Besides cortisone and 11-dehydrocorticosterone, 11β-HSD1 can catalyse the carbonyl reduction of a broad range of substrates,

What is already known

- 11β-HSD1 catalyses the oxoreduction of 11-oxo-glucocorticoids and 7-oxo bile acids.
- Pharmacological inhibition of 11β-HSD1 is considered a promising strategy to treat glucocorticoid-dependent diseases.

What this study adds

- Ratio UDC-Tau/7oxoLC-Tau detects decreased 11β-HSD1 activity in genetically modified mouse models and upon pharmacological inhibition.
- These ratios are better markers of decreased 11β-HSD1 activity than concentrations of individual bile acids.

What is the clinical significance

- UDC-Tau/7oxoLC-Tau ratio provides a biomarker of the efficacy of pharmacological 11β-HSD1 inhibition in preclinical models.

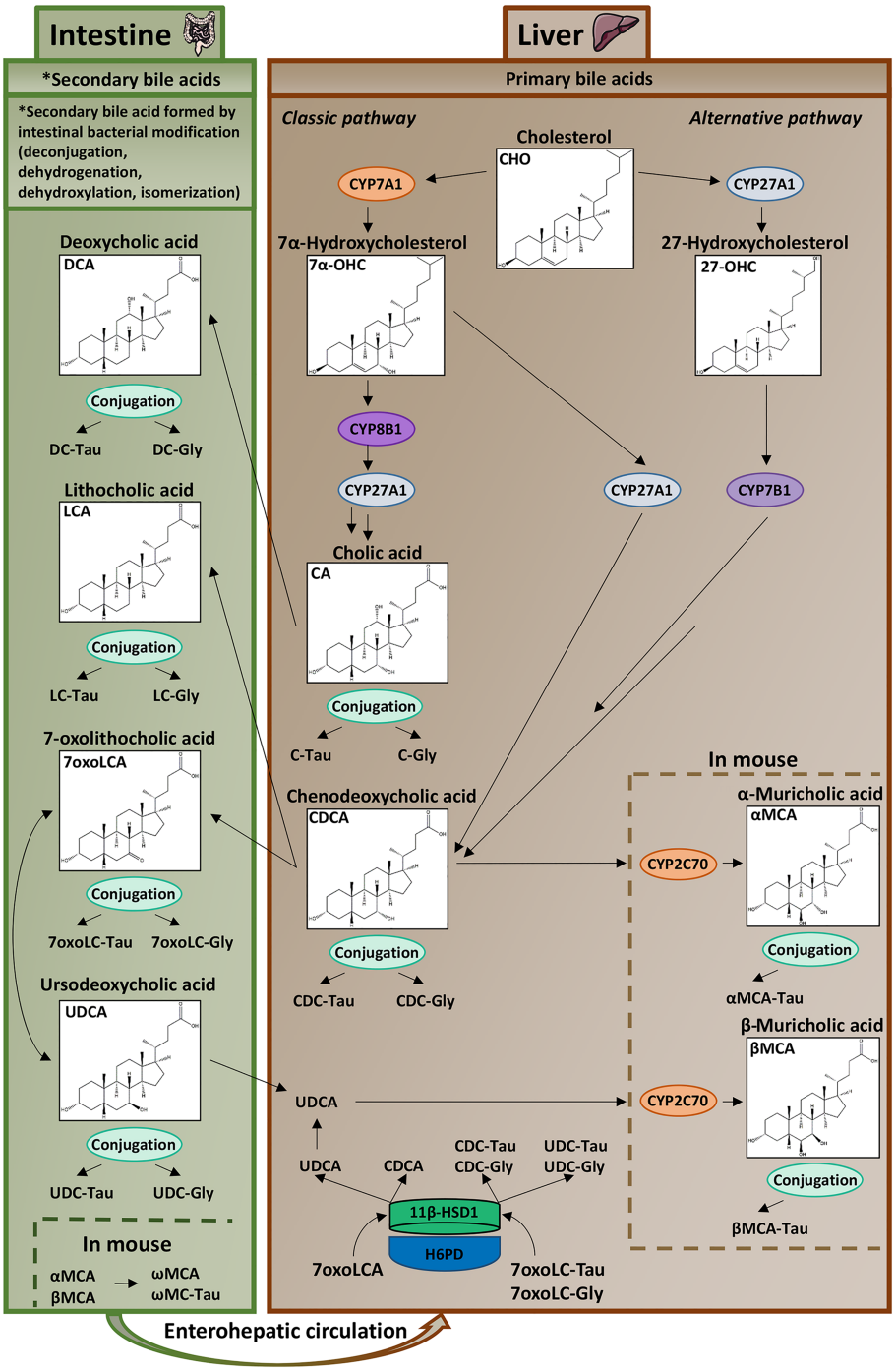

FIGURE 1 Schematic overview of bile acid homeostasis and a role for 11β-HSD1. 11β-HSD1 catalyses the carbonyl reduction of the substrates cortisone and 7oxoLCA to the corresponding products cortisol, and UDCA and CDCA, respectively. 11β-HSD1 activity requires regeneration of cofactor NADPH from $NADP^+$ by H6PD-dependent conversion of glucose-6-phosphate (G6P) to 6-phosphogluconate (6PG). The formation of muricholic acid metabolites by murine Cyp2c70 is indicated

including 11-oxygenated glucocorticoids, progestins and androgens, 7-oxygenated androgens, oxysterols and bile acids and several xenobiotics (Odermatt & Klusonova, 2015).

Experiments using human liver microsomes and HEK-293 cells expressing human 11β-HSD1 and H6PD revealed that human 11β-HSD1 can convert the gut microbiota-derived 7-oxolithocholic acid (7oxoLCA) and its taurine- and glycine-conjugated forms to chenodeoxycholic acid (CDCA) and to a lesser extent to the 7β-stereoisomer ursodeoxycholic acid (UDCA) and their taurine- and glycine-conjugated forms (Odermatt et al., 2011). Unlike human 11β-HSD1, the mouse and rat enzymes are not stereo specific and were found to equally produce CDCA and UDCA (Arampatzis et al., 2005). A comparison of liver-specific 11β-HSD1 knockout (11LKO) and control (CTRL) mice showed completely abolished 7oxoLCA oxoreduction in liver microsomes from 11LKO, indicating that 11β-HSD1 is the major if not only enzyme catalysing this reaction in the liver. Plasma and intrahepatic levels of 7oxoLCA and its taurine-conjugated form 7-oxolithocholyltaurine (7oxoLC-Tau) were found to be increased in 11LKO and in global 11β-HSD1 knockout (11KO) mice (Penno et al., 2013). Furthermore, 11KO mice exhibited increased plasma and intrahepatic levels of most bile acids, resembling a mild cholestasis phenotype.

Because we previously observed marked inter-animal variation in circulating bile acid levels, we hypothesized that the ratios of 7β-hydroxy- to 7-oxo-bile acids might serve as biomarkers for decreased 11β-HSD1 activity and that such ratios may be superior markers than individual metabolite levels. We analysed plasma and liver tissue bile acids in 11KO and 11LKO mice in order to calculate the ratios of UDCA/7oxoLCA, CDCA/7oxoLCA, ursodeoxycholyltaurine (UDC-Tau)/7oxoLC-Tau and chenodeoxycholyltaurine (CDC-Tau)/7oxoLC-Tau (Penno et al., 2014; Penno, Morgan, et al., 2013). Furthermore, we analysed bile acid composition in plasma and liver tissue samples from global *H6pd* knockout (*H6pd*KO) mice as a model of decreased 11β-HSD1 oxoreduction activity and from C57BL/6JRj mice treated with the pharmacological inhibitor carbenoxolone.

2 | METHODS

2.1 | Materials

Cholic acid (CA), CDCA, deoxycholic acid (DCA), lithocholic acid (LCA), UDCA, deoxycholylglycine, chenodeoxycholylglycine (CDC-Gly), CDC-Tau, cortisone, cortisol, corticosterone, 11-dehydrocorticosterone, carbenoxolone, [2,2,4,4-$^{2}H_4$]-CA (>98% isotopic purity), [2,2,4,4-$^{2}H_4$]-CDCA (>98% isotopic purity) and [2,2,4,4-$^{2}H_4$]-LCA (>98% isotopic purity) were obtained from Sigma-Aldrich (St. Louis, MO, USA). 7-Oxodeoxycholic acid (7oxoDCA), 7oxoLCA, hyodeoxycholic acid (HDCA), α-muricholic acid (αMCA), βMCA, ωMCA, ursodeoxycholylglycine (UDC-Gly), lithocholyltaurine (LC-Tau), α-muricholyltaurine (αMC-Tau), βMC-Tau, ωMC-Tau and [2,2,4,4-$^{2}H_4$]-DCA (>98% isotopic purity) were purchased from Steraloids (Newport, RI, USA). Cholylglycine (C-Gly), cholyltaurine (C-Tau), deoxycholyltaurine (DC-Tau) and UDC-Tau were obtained from Calbiochem (Läufelfingen, Switzerland). [2,2,4,4-$^{2}H_4$]-UDCA (>98% isotopic purity), [2,2,4,4-$^{2}H_4$]-C-Gly (>98% isotopic purity), [2,2,4,4-$^{2}H_4$]-CDC-Gly (>98% isotopic purity), [2,2,4,4-$^{2}H_4$]-UDC-Gly (>98% isotopic purity) and [2,2,4,6,6,17α,21,21-$^{2}H_8$]-corticosterone were purchased from CDN isotopes (Pointe-Claire, Quebec, Canada). 7oxoLC-Tau and 7-oxolithocholylglycine were a kind gift from Dr. Alan F. Hofmann (University of California, San Diego, CA, USA). [1,2,6,7-^{3}H]-Cortisol was purchased from PerkinElmer (Schwerzenbach, Switzerland), [1,2-^{3}H]-cortisone from Anawa (Kloten, Switzerland) and scintillation cocktail (IrgaSafe Plus) from Zinsser Analytic GmbH (Frankfurt am Main, Germany). Ultra-HPLC tandem-MS (UHPLC–MS/MS)-grade purity methanol, acetonitrile and formic acid were obtained from Biosolve (Dieuze, France). RIPA buffer, β-mercaptoethanol, HRP-conjugated goat anti-mouse secondary antibody (Cat#A0168, LOT#079M4881V, RRID:AB_257867), rabbit polyclonal anti-H6PD antibody (Cat#HPA004824, LOT#A06407 RRID:AB_1079037), dNTPs, KAPA SYBR® FAST qPCR Kit, polyvinylidene difluoride membranes (Cat# IPVH00010, pore size: 0.45 μm), Immobilon Western Chemiluminescence HRP substrate kit and protease inhibitor cocktail were purchased from Merck (Darmstadt, Germany). Rabbit polyclonal anti-11β-HSD1 antibody (Cat#10004303, LOT#126826-12, RRID:AB_10077698) was purchased from Cayman chemicals (Ann Arbor, MI, USA), HRP-conjugated goat anti-rabbit secondary antibody (Cat# 7074, LOT#22, RRID:AB_2099233) from Cell Signaling (Cambridge, UK) and mouse monoclonal anti-β-actin (ACTB) antibody (Cat#sc-47778, LOT#D0618, Clone#C4, RRID:AB_2714189) from Santa Cruz Biotechnology (Dallas, TX, USA). Pierce® bicinchoninic acid protein assay kit and RapidOut DNA Removal kit were purchased from Thermo Fisher Scientific (Waltham, MA, USA), RNeasy Mini Kit from Qiagen (Venlo, Netherlands), GoScript Reverse Transcriptase, Oligo-dT primers and RNasin® Ribonuclease Inhibitor from Promega (Madison, WI, USA) and primers for RT-qPCR from Microsynth AG (Balgach, Switzerland). HEK-293 cells (RRID:CVCL_0045) were purchased from the American Type Culture Collection (Manassas, VA, USA). FBS was obtained from Connectorate (Dietikon, Switzerland). Penicillin/streptomycin and non-essential amino acids were purchased from BioConcept (Allschwil, Switzerland). All other reagents were purchased from Sigma-Aldrich.

2.2 | Animal experimentation

Animal studies are reported in compliance with the ARRIVE guidelines (Percie du Sert et al., 2020) and with the recommendations made by the *British Journal of Pharmacology* (Lilley et al., 2020). 11KO mice were described earlier (Semjonous et al., 2011); a targeted deletion of exon 5 in *Hsd11b1* was obtained using the Cre-loxP system. E14TG2a embryonic stem cells bearing a triloxed allele were injected into C57BL/6J (RRID:IMSR_JAX:000664) blastocysts and chimeric mice were mated with C57BL/6J females. Mice heterozygous for a triloxed allele were crossed with ZP3-Cre to create the null allele and bread to homozygosity to generate 11KO. 11KO were intercrossed to maintain the C57BL/6J/129SvJ background. To obtain 11LKO, the floxed homozygous 11KO mice on the mixed C57BL/6J/129SvJ background were crossed with Albumin-Cre transgenic mice on a C57BL/6J background to target Cre expression to hepatocytes (Lavery et al., 2012). Mice were group housed at the University of Birmingham (Birmingham, UK), in a climate-controlled facility under standard conditions on a 12-h light/dark cycle and fed ad libitum with standard chow (Cat#D12328, Research Diets, Inc., New Brunswick, USA) and free access to drinking water. 11KO, 11LKO and their respective control littermates, 15-week-old male mice, were fasted overnight and anaesthetized with isoflurane prior to collection of blood samples by intra-cardiac puncture and isolation of livers. Samples were collected between 7:00 and 10:00. Studies with 11KO and 11LKO were conducted under Home Office license PPL 70/8516, following approval by the Joint Ethics and Research Governance Committee of the University of Birmingham in accordance with the United Kingdom Animals (Scientific Procedures) Act, 1986 and the EU Directive 2010/63/EU for animal experiments.

For *H6pd*KO mice, a deletion of exons 2 and 3 in *H6pd* was generated by homologous recombination in 129SvJ embryonic stem cells, followed by injection into C57BL/6J blastocysts and resulting

chimeric mice were mated with C57BL/6J female mice. Mice were intercrossed to maintain the C57BL/6J/129SvJ background. From these, heterozygous mice were intercrossed to obtain *H6pd*KO mice and control littermates (*H6pd*^{tm1Pmst}, RRID:MGI:3624665, Lavery et al., 2006). *H6pd*KO mice were transferred from the University of Birmingham to the PharmaCenter animal facility (University of Basel, Switzerland), where they were bred and housed. The C57BL/6JRj (RRID:MGI:2670020) mice used for carbenoxolone treatment were purchased from Janvier Laboratories (Saint Berthevin, France). These animals were acclimatized to the new environment (Basel, Switzerland) for 1 week prior to the experiment. Experiments with *H6pd*KO and C57BL/6JRj mice were performed on 10- to 12-week-old males. The Cantonal Veterinary Office in Basel, Switzerland, approved all procedures (cantonal licenses 2758_26280 and 2758_29462). Mice were group housed in acclimate-controlled facility under standard conditions and a 12-h light/12-h dark cycle with free access to standard chow (Cat#3432, KLIBA NAFAG, Kaiseraugst, Switzerland) and drinking water in ventilated cages. All experiments were performed between 7:00 and 10:00. Mice (not fasted) were killed by exposure to CO_2 until respiratory arrest was observed, absence of pain reaction was verified and cardiac puncture was performed immediately to collect blood. Plasma samples were prepared by centrifugation at 2,000× *g*, 10 min, 4°C and stored at −80°C. Liver tissue samples were either immediately used for 11β-HSD1 activity assay or snap frozen in liquid nitrogen and stored at −80°C until further analysis. In experiments including carbenoxolone treatment, C57BL/6JRj mice received carbenoxolone (100 mg·kg^{-1}·day^{-1}) for 4 days via i.p. injection (50 mg·kg^{-1} in PBS at 7:00 and 17:00). The dose was established in preliminary experiments. Animals for the carbenoxolone treatment were distributed, treated and killed in randomized block design (study performed at the beginning of 2017). Only the person handling the animals was aware of the group allocation. Animals which displayed obvious signs of health issues like excessive loss of weight (more than 20%) were excluded from the study. These criteria were defined prior to the study. *H6pd*KO and corresponding control littermates were randomly assigned to groups. Resulting sample material from plasma and liver tissue (experimental unit) was extracted, measured and analysed in a blinded and simple randomized design. Final sample batches from UHPLC–MS/MS analysis were transferred to Excel and unblinded for statistical evaluations.

2.3 | Quantification of bile acids and steroids

Stock solutions of analytes, internal standards (10 mmol·L^{-1}) and mixtures of analytes (Penno et al., 2013) were prepared in methanol. Calibrators for plasma analysis of bile acids (25 µl) or steroids (50 µl) were prepared by serial dilution of charcoal-treated mouse plasma spiked with analytes. Calibration curves for liver samples were prepared by serial dilution of analytes in PBS (200 µl, pH 7.2). Calibration curves for cell culture supernatant were prepared by serial dilution in serum-free culture medium. All calibrators were subsequently treated as samples. An internal standard mixture was prepared of $^{2}H_4$-CA, $^{2}H_4$-CDCA, $^{2}H_4$-DCA, $^{2}H_4$-UDCA, $^{2}H_4$-C-Gly, $^{2}H_4$-CDC-Gly, $^{2}H_4$-UDC-Gly and $^{2}H_4$-LCA for quantification of bile acids in plasma and liver, of $^{2}H_4$-CDCA, $^{2}H_4$-UDCA and $^{2}H_4$-LCA for bile acid quantification in cell culture supernatant, and of $^{2}H_8$-corticosterone and $^{2}H_4$-cortisone for steroid quantification.

Plasma samples (25 µl) for bile acids were diluted with water (75 µl), spiked with internal standard (100 nmol·L^{-1}) and subjected to protein precipitation by isopropanol (900 µl). Samples were incubated (30 min, 4°C, 1,400 rpm) and centrifuged (10 min, 4°C, 16,000× *g*), and supernatants were transferred into a fresh tube. Liver samples (approximately 30 mg) were homogenized using a Precellys 24 tissue homogenizer (Bertin Instruments, Montigny-le-Bretonneux, France) (4°C, 3×, 30 s at 6,500 rpm, cycle break 30 s) in water–chloroform–methanol (1 ml, 20/20/60; v/v/v) containing internal standard (100 nmol·L^{-1}). Samples were incubated (15 min, 850 rpm, 37°C) and centrifuged (10 min, 25°C, 16,000× *g*), and supernatants (800 µl) were transferred to a fresh tube. All plasma and liver samples were re-extracted and supernatants combined. Cell culture supernatant (450 µl) was spiked with internal standard (100 nmol·L^{-1}), subjected to protein precipitation by isopropanol (1 ml), incubated (30 min, 4°C, 1,300 rpm) and centrifuged (10 min, 4°C, 16,000× *g*), and the resulting supernatant was transferred to a fresh tube. Supernatants of plasma (2 ml), liver (1.6 ml), and cell culture (1.45 ml) were evaporated to dryness using a Genevac EZ-2 evaporator (35°C). Plasma samples (50 µl) for steroids were spiked with internal standard (3.3 nmol·L^{-1}) and extracted by solid phase extraction (3 cc, Oasis HLB cartridges) as described (Strajhar et al., 2016). Extracts (1 ml) were evaporated to dryness (35°C). Sample residues for bile acid detection were reconstituted (10 min, 25°C, 1,300 rpm) in methanol–water (50/50 v/v; 50 µl for plasma, 200 µl for liver, 50 µl for cell culture supernatant). Sample residues for steroid measurement were reconstituted (10 min, 4°C, 1,300 rpm) in methanol (25 µl). All reconstituted samples were sonicated (10 min, 25°C) and centrifuged (10 min, 25°C, 16,000× *g*), and supernatants were transferred to glass vials.

The injection volume for bile acid detection was 2 µl (plasma and cell culture supernatant) or 3 µl (liver) and for plasma steroids 5 µl. Samples were stored at −20°C until analysis by UHPLC–MS/MS as described earlier (Penno, Arsenijevic, et al., 2013) with minor modifications. Briefly, analytes were detected by multiple reaction monitoring using an Agilent Triple Quadrupole 6490 instrument with electrospray ionization and polarity switching. Analytes were separated with a reverse-phase column (Acquity UPLC BEH C18, 1.7 µm, 2.1 × 150 mm, Waters, Milford, MA, USA) at 65°C within 17.5 min for bile acids or 10 min for steroids. The mobile phase consisted of water–acetonitrile–formic acid (A) (95/5/0.1, v/v/v) and (B) (5/95/0.1, v/v/v). Gradient elution (% mobile phase B) was performed at constant flow (0.63 ml·min^{-1}): bile acids, 0–8 min (25%); 8–17.5 min (35–68.25%); 17.5–18 min (68.25–25%); followed by a washout 18–20 min (25–100%) and 20–22 min (100%); and steroids, 0–10 min (25–70%); followed by a washout 10–12 min (100%). The column was post run reconstituted to initial

%B within 2 min prior to further injections. Data acquisition and quantification were performed using MassHunter (Acquisition software version B.09.00, build 9.0.9037.0 and quantitative software version B.07.01, build 7.1.524.0).

2.4 | Expression of mouse 11β-HSD1 in HEK-293 cells and oxoreduction of 7oxoLCA

HEK-293 cells, cultured in DMEM supplemented with 10% FBS, 10 mmol·L^{-1} HEPES, 100 units·ml^{-1} penicillin, 0.1 mg·ml^{-1} streptomycin and non-essential amino acids in a 5% CO_2 atmosphere at 37°C, were transfected with plasmid expressing mouse 11β-HSD1 bearing a C-terminal FLAG epitope (Arampatzis et al., 2005) using the calcium phosphate transfection method. The medium was changed 8 h after transfection and after 48 h, cells were cultured in medium containing G-418 as selection antibiotic (800 μg·ml^{-1}). HEK-293 cells stably expressing mouse 11β-HSD1 are referred to as MO1F cells. Cells (100,000 per well) were seeded on poly-L-lysine coated 24-well plates. After 24 h, cells were washed twice with serum-free culture medium and incubated with 400 nmol·L^{-1} 7oxoLCA, either with or without 5 μmol·L^{-1} carbenoxolone, for 0, 4 and 24 h. Of the supernatant, 450 μl was then transferred to a 2-ml tube and stored at −20°C until bile acid quantification.

2.5 | *In vivo* 11β-HSD1 activity assessment

Mice were injected i.p. with 5 mg·kg^{-1} of cortisone (in DMSO). After 10 min, mice were killed by CO_2 asphyxiation and cardiac puncture was performed immediately to collect blood. Plasma was prepared and stored as described above. Plasma was extracted, and cortisone and cortisol levels were measured by UHPLC–MS/MS as described above.

2.6 | *Ex vivo* activity assay

Freshly isolated liver tissue samples (50–100 mg) were placed in tubes, followed by injection of radiolabelled substrate mixture (10 μl containing either 950 nmol·L^{-1} cortisone + 50 nmol·L^{-1} ^{3}H-cortisone [60 Ci·mmol^{-1}] or 950 nmol·L^{-1} cortisol + 50 nmol·L^{-1} of ^{3}H-cortisol [70 Ci·mmol^{-1}]). Samples were incubated at 16°C for 10 min. Freshly isolated epididymal white adipose tissue samples (50–100 mg) were similarly treated but incubated for 10 min at 37°C. Reactions were terminated by snap freezing and stored at −80°C. For the extraction of cortisone and cortisol, samples were sonicated for 30 s in 200-μl water; 750-μl ethyl acetate was added, followed by incubation (15 min, 4°C, 1,300 rpm) then centrifugation (10 min, 4°C, 16,100× *g*). The supernatant (600 μl) was transferred to a fresh tube and the extraction repeated. Combined supernatants (1.2 ml) were evaporated to dryness in a Genevac EZ-2 (35°C). Residues were reconstituted in 1.2-ml methanol by sonication (10 min, 25°C), followed by evaporation to dryness and storage at −80°C. To the white adipose tissue samples, 1-ml methanol was added, samples were vortexed for 10 s and centrifuged (10 min, 25°C, 21,000× *g*), and supernatant (950 μl) was transferred to a new tube. Samples were evaporated to dryness and stored at −80°C. Residues of the liver and white adipose tissue samples were then reconstituted in 40-μl methanol containing 0.5 mmol·L^{-1} of cortisone and cortisol, by sonication (10 min, 25°C). Samples (10 μl) were then separated on SIL G-25 UV TLC plates (Macherey-Nagel, Düren, Germany) in chloroform/methanol (90/10, v/v) and analysed by scintillation counting.

2.7 | Quantification of mRNA expression by RT-qPCR

Liver samples (approximately 14 mg) were homogenized (6,500 rpm, 4°C, 30 s; Precellys 24 tissue homogenizer in 400-μl RLT buffer [RNeasy Mini, Qiagen]) and centrifuged (3 min, 25°C, 16,000× *g*). Total RNA was isolated from the supernatant (QIAcube, standard protocol for animal tissues and cells, Qiagen) and genomic DNA was removed by DNAse digestion. RNA was quantified and transcribed (500 ng) into cDNA and then qPCR was performed (4-ng cDNA per reaction in triplicate, 40 cycles) using KAPA SYBR® FAST. Oligonucleotide primers: *Hsd11b1* forward 5′-TGG TGC TCT TCC TGG CCT-3′, reverse 5′- CCC AGT GAC AAT CAC TTT CTT T-3′; *H6pd* forward 5′- CTT GAA GGA GAC CAT AGA TGC G-3′, reverse 5′- TGA TGT TGA GAG GCA GTT CC-3′; peptidylpropyl isomerase A (Ppia) forward 5′- CAA ATG CTG GAC CAA ACA CAA ACG-3′, reverse 5′- GTT CAT GCC TTC TTT CAC CTT CCC-3′. Comparison of gene expression was performed using the 2-ΔCT method with *Ppia* as the internal control (Schmittgen & Livak, 2008).

2.8 | Protein expression analysis by Western blot

Liver samples (approximately 6 mg) were homogenized (6,500 rpm, 30 s, 4°C, Precellys 24 tissue homogenizer) in RIPA buffer (450 μl) containing protease inhibitor cocktail and centrifuged (4 min, 4°C, 16,000× *g*). Protein concentration was quantified by using a bicinchoninic acid protein assay and samples were prepared (5 min at 95°C) in Laemmli solubilization buffer (60 mmol·L^{-1} Tris–HCl, 10% glycerol, 0.01% bromophenol blue, 2% sodium dodecyl sulfate, pH 6.8, 5% β-mercaptoethanol). The protein extract (20 μg) was separated by 14% SDS-PAGE and transferred to polyvinylidene difluoride membranes. The membranes were blocked (1 h, 25°C) in TBS-T (5% defatted milk, 20 mmol·L^{-1} Tris buffered saline with 0.1% Tween-20). All antibody dilutions and incubations were performed in TBS-T. 11β-HSD1 protein expression was measured with rabbit polyclonal anti-11β-HSD1 antibody (1:1,000, 4°C, overnight). The membrane was washed and incubated with HRP-conjugated goat anti-rabbit secondary antibody (1:2,000, 25°C, 1 h). H6PD

protein expression was determined using rabbit polyclonal anti-H6PD antibody (1:1,000, 4°C, overnight) and HRP-conjugated goat anti-rabbit secondary antibody (1:2,000, 25°C, 1 h). ACTB was detected using mouse monoclonal anti-ACTB antibody (1:1,000, 4°C, overnight) followed by HRP-conjugated goat anti-mouse secondary antibody (1:4,000, 25°C, 1 h). Protein content was visualized by Immobilon Western Chemiluminescence HRP substrate kit. 11β-HSD1 and H6PD were quantified by densitometry normalized to ACTB protein levels using ImageJ software (version 1.53n, RRID:SCR_003070). The Immuno-related procedures used comply with the recommendations made by the *British Journal of Pharmacology* (Alexander et al., 2018).

2.9 | Estimation of NADPH levels in the ER

A method by Rogoff et al. (2010) to estimate NADPH content in liver microsomes was modified. Approximately 100 mg of frozen mouse liver tissue was thawed and homogenized in nine volumes of buffer containing 50 mmol·L^{-1} KCl, 2 mmol·L^{-1} $MgCl_2$, 0.25 mol·L^{-1} sucrose, 20 mmol·L^{-1} Tris, pH 7.5 and protease inhibitor cocktail. The homogenate was centrifuged at 12,000× *g* at 4°C for 20 min and the supernatant was centrifuged again at 105,000× *g* at 4°C for 60 min. The resulting pellet was resuspended in 600 μl homogenization buffer and centrifuged again at 105,000× *g* at 4°C for 60 min. The pellet was then resuspended in 50-μl buffer containing 100 mmol·L^{-1} KCl, 20 mmol·L^{-1} NaCl, 1 mmol·L^{-1} $MgCl_2$, 20 mmol·L^{-1} 3-(*N*-morpholino) propanesulfonic acid (MOPS), pH 7.2 and protease inhibitor cocktail. Protein concentration was determined by using a bicinchoninic acid assay. Resuspended microsomes (protein concentration: 0.5 mg·ml^{-1}) were permeabilized with alamethicin (0.1 mg·mg^{-1} protein) and 3-[(3-cholamidopropyl)dimethylammonio]-1-propanesulfonate (CHAPS) 0.25% (w/v) and EDTA (final concentration of 160 nmol·L^{-1}) were added. Permeabilized microsomes were incubated for 30 min at 4°C with mixing every 5 min. Next, 100 μl of microsomal preparation per well were incubated in a 96-well plate at 25°C for 5 min. The absorbance of total reduced pyridine nucleotides ([NADPH] + [NADH]) was measured at wavelength 335–345 nm. NADPH levels were then determined by incubating 100 μl of permeabilized microsomes with 1.4 IU GSH reductase and 0.75 mmol·L^{-1} of oxidized GSH for 20 min at 25°C whilst shaking at 350 rpm. The resulting decrease in absorbance is a measure of the NADPH content. Absorbance of total reduced pyridine nucleotides was measured against buffer in the absence of microsomes. To determine NADPH content, the absorbance of buffer containing 1.4 IU and 0.75 mmol·L^{-1} GSSG was subtracted from the absorbance obtained from the microsomal preparation. All samples were tested at least in duplicate.

2.10 | Statistical analysis

Sample size ranged from seven to 20 animals. The different sample sizes for the different parameters measured were chosen according to experiments from previous studies where statistically significant effects have been observed. Data were tested for normal distribution by a D'Agostino and Pearson omnibus normality test followed by a non-parametric (two-tailed) Mann–Whitney *U* test for analysis of significance. Data represent mean ± SEM. All statistical analyses were performed using GraphPad Prism 5.0 software (RRID:SCR_002798), and $P < 0.05$ was considered significant. Effect sizes were determined for bile acid concentrations measured by UHPLC–MS/MS in plasma and liver samples from transgene or treated mice versus their respective controls (Table S1). Data represent the effect size calculated based on Cohen's *d* effect size (ES *d*) with correction of unequal sample sizes for the analysis of data from non-parametric analysis (Mann–Whitney *U* test) calculated as Hedges' *g* with corresponding confidence intervals of the effect size. The data and statistical analysis comply with the recommendations of the *British Journal of Pharmacology* on experimental design and analysis in pharmacology (Curtis et al., 2018).

2.11 | Nomenclature of targets and ligands

Key protein targets and ligands in this article are hyperlinked to corresponding entries in the IUPHAR/BPS Guide to PHARMACOLOGY http://www.guidetopharmacology.org and are permanently archived in the Concise Guide to PHARMACOLOGY 2019/20 (Alexander et al., 2019).

3 | RESULTS

3.1 | Increased circulating bile acids in 11KO mice

A previous study indicated that 11β-HSD1 is the only enzyme catalysing the conversion of 7oxoLCA to CDCA and UDCA, reporting an accumulation of 7oxoLCA and 7oxoLC-Tau in plasma and liver tissue from 11KO mice, although with large inter-individual variations (Penno, Morgan, et al., 2013). Here, we have performed a reanalysis of the bile acid profiles from the previous study which shows increased levels of almost all bile acids (primary and secondary, free and conjugated) in plasma samples from 11KO mice, compared to control littermates, resembling a mild cholestasis phenotype (Table 1). However, due to the high inter-individual variations, only some values reached significance. The levels of taurine-conjugated bile acids were almost an order of magnitude higher than those of their free forms. Because glycine-conjugated bile acids are considered to be of minor importance or absent in mice, consistent with previous findings (Alnouti et al., 2008; Garcia-Canaveras et al., 2012; Penno et al., 2014), they were not included in the analysis here. In liver tissue of 11KO, free bile acids were elevated or tended to be elevated, with the exception of the 7β-hydroxylated bile acid βMCA that was fourfold lower. The taurine-conjugated bile acids showed a weak trend to be increased in livers of 11KO. However, 7oxoLC-Tau was more than 10-fold higher in livers of 11KO mice compared to control littermates (CTRL) and UDC-Tau was about 30-fold lower.

TABLE 1 Bile acid profiles in plasma and liver of 11KO mice

	Plasma (nmol·L^{-1})		Liver (fmol·mg^{-1})	
	CTRL	11KO	CTRL	11KO
Analyte	(*n* = 18)	(*n* = 17)	(*n* = 9)	(*n* = 9)
CA	703 ± 323	18,836 ± 10,398	1,673 ± 558	6,911 ± 4,710
CDCA	13.9 ± 3.8	192 ± 108	38 ± 10	49 ± 16
DCA	289 ± 71	1,603 ± 687	239 ± 53	318 ± 88
7oxoDCA	908 ± 439	29,886 ± 14,966*	1,396 ± 455	13,196 ± 9,162
HDCA	17.7 ± 4.0	236 ± 70*	74 ± 15	343 ± 124*
αMCA	101 ± 48	4,578 ± 2,091*	340 ± 90	4,018 ± 2,136*
βMCA	572 ± 165	826 ± 355	3,457 ± 968	897 ± 387*
ωMCA	604 ± 190	2,351 ± 1,182	1,461 ± 450	1,506 ± 644
UDCA	69 ± 18	486 ± 223	168 ± 38	291 ± 184
7oxoLCA	10.2 ± 3.1	201 ± 100*	18.2 ± 4.4	67 ± 24
αMCA/βMCA	0.22 ± 0.05	9.1 ± 5.0*	0.12 ± 0.21	3.65 ± 0.60*
UDCA/7oxoLCA	41 ± 18	16.9 ± 13.8*	13.7 ± 4.2	4.5 ± 1.2
CDCA/7oxoLCA	4.6 ± 2.4	1.93 ± 0.98	2.3 ± 0.5	1.03 ± 0.14*
C-Tau	3,578 ± 2,331	110,304 ± 94,731	32,352 ± 7,659	51,276 ± 15,249
CDC-Tau	266 ± 175	3,961 ± 3,339	991 ± 185	1,980 ± 765
DC-Tau	1,412 ± 863	12,212 ± 9,988	5,760 ± 1,324	7,711 ± 2,315
LC-Tau	6.3 ± 4.5	89 ± 69	59 ± 11	85 ± 21
αMCA-Tau + βMCA-Tau	4,203 ± 2,384	29,184 ± 23,757	19,635 ± 4,314	20,556 ± 7,700
ωMCA-Tau	5,132 ± 2,836	17,184 ± 13,056	24,404 ± 4,625	14,609 ± 4,313
UDC-Tau	331 ± 185	2,947 ± 2,920	1,673 ± 350	53 ± 27*
7oxoLC-Tau	143 ± 77	5,931 ± 3,962	174 ± 34	2,718 ± 1,135*
UDC-Tau/7oxoLC-Tau	2.2 ± 0.3	0.30 ± 0.11*	9.5 ± 1.6	0.020 ± 0.004*
CDC-Tau/7oxoLC-Tau	1.05 ± 0.23	0.63 ± 0.09	6.9 ± 1.1	0.83 ± 0.06*
Sum primary BA	1,458 ± 493.0	23,782 ± 12,339	5,675 ± 1,570	12,167 ± 7,413
Sum primary BA-Tau	8,379 ± 4,391	137,957 ± 117,634	54,651 ± 12,386	73,866 ± 23,548

Note: The results represent mean ± SEM (nmol·L^{-1} and fmol·mg^{-1} for plasma and liver, respectively). Analyte concentrations with a S/N ≤ 3 represent the LLOD of the UHPLC–MS/MS method. Samples yielding a concentration below LLOD were included as LLOD/2 (nmol·L^{-1} and fmol·mg^{-1}, respectively) in the calculations of a specific analyte. Blue- and yellow-coloured boxes indicate statistically significant increases and decreases, respectively. Unequal group sizes reflect exclusion of one plasma sample due to insufficient collection of blood sample volume and the availability of only nine livers due to the use of nine randomly assigned livers for gene expression analyses in a previous study.

Abbreviations: 11KO, global *Hsd11b1* knockout; CTRL, control littermates.

*$P < 0.05$ significantly different as indicated; non-parametric, Mann–Whitney *U* test (two-tailed).

3.2 | The UDC-Tau/7oxoLC-Tau ratio in plasma and liver tissue detects the lack of 11β-HSD1 activity in 11KO mice

The concentrations of the 11β-HSD1 substrates 7oxoLCA and 7oxoLC-Tau increased about 20-fold and 40-fold, respectively, in plasma of 11KO compared to CTRL (Table 1, Figure S1), with large inter-individual variations, as reported earlier (Penno, Morgan, et al., 2013). It needs to be noted that no outliers were excluded from the analysis. The respective products of 11β-HSD1, that is, CDCA, UDCA and their taurine-conjugated forms, also were higher in 11KO plasma compared to CTRL, although clearly less pronounced than the 7-oxo metabolites. In liver tissue, 7oxoLCA was 3.7-fold and 7oxoLC-Tau 15-fold higher in 11KO compared to CTRL (Table 1, Figure S2). The respective products CDCA, UDCA and CDC-Tau tended to increase, whereas UDC-Tau decreased 30-fold. Importantly, the 11β-HSD1 product to substrate ratios (the ratio of CDCA and UDCA and their taurine-conjugated forms to the respective 7oxo metabolites) showed less variation than the individual metabolite concentrations (Figures S1 and S2). UDC-Tau/7oxoLC-Tau was the most distinguishing marker for the lack of 11β-HSD1 activity when considering both plasma and liver tissue samples (Table 1, Figure 2).

Interestingly, in plasma and liver tissue of 11KO mice, the levels of the 7α-hydroxylated bile acid αMCA were 45-fold and 12-fold

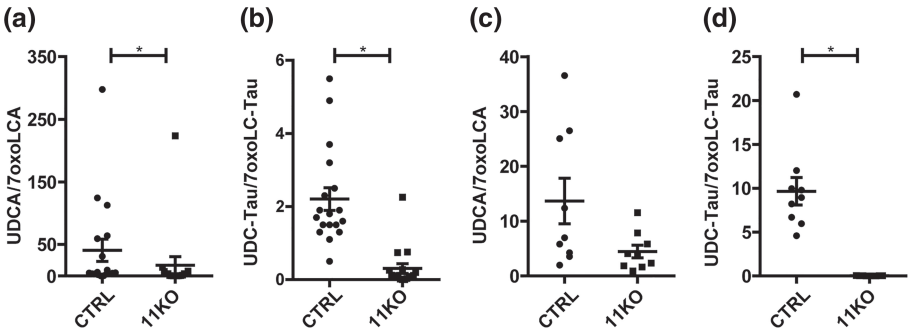

FIGURE 2 Plasma and liver tissue UDCA/7oxoLCA and UDC-Tau/7oxoLC-Tau ratios in 11KO mice. (a) UDCA/7oxoLCA ratios and (b) UDC-Tau/7oxoLC-Tau ratios in plasma of 11KO mice (CTRL n = 18; 11KO n = 17); (c) UDCA/7oxoLCA ratios and d) UDC-Tau/7oxoLC-Tau ratios in liver tissue of 11KO mice (CTRL n = 9; 11KO n = 9). Analyte concentrations defined by a S/N ≤ 3 represent the LLOD of the UHPLC–MS/MS method. Samples yielding a concentration below LLOD were included as LLOD/2 (nmol·L^{-1} and fmol·mg^{-1} for plasma and liver, respectively) in the calculations of a specific analyte. The results represent mean ± SEM. *P < 0.05 significantly different as indicated; non-parametric, Mann–Whitney U test (two-tailed). Unequal group sizes reflect exclusion of one plasma sample due to insufficient collection of blood sample volume and the availability of only nine livers due to the use of nine randomly assigned livers for gene expression analysis in a previous study

higher than in CTRL, whereas its 7β-hydroxylated form βMCA was not different in CTRL plasma but 3.8-fold lower in liver tissue (Table 1). The respective αMCA/βMCA ratios were 40-fold and 30-fold higher in 11KO compared to CTRL, suggesting a possible effect of 11β-HSD1 on isomerization. Due to a limitation of the applied analytical method, αMC-Tau and βMC-Tau could not be separated and therefore, the corresponding ratio not determined.

3.3 | 11LKO mice exhibit decreased plasma and liver tissue UDC-Tau/7oxoLC-Tau ratios

The liver shows the highest 11β-HSD1 expression; nevertheless, an earlier study reported 25–30% residual *in vivo* (whole body) 11β-HSD1 oxoreduction activity in 11LKO mice lacking 11β-HSD1 specifically in hepatocytes (Lavery et al., 2006). Thus, 11LKO mice represent a model of reduced 11β-HSD1 activity but with complete loss of activity in hepatocytes.

The free bile acids in plasma and liver tissue of 11LKO tended to be higher compared to CTRL (Table 2), an effect considerably more pronounced in 11KO (Table 1). 7oxoLCA was 11-fold higher in plasma and twofold in liver tissue (Table 2). The plasma UDCA/7oxoLCA and CDCA/7oxoLCA ratios were sevenfold and twofold lower in 11LKO compared to CTRL, whilst remaining unchanged in liver tissue. Plasma 7oxoLC-Tau was slightly more abundant than its free form and it was 20-fold higher in 11LKO than in CTRL, whilst CDC-Tau was not different, and UDC-Tau was sixfold lower in 11LKO, resulting in significantly decreased product to substrate ratios (Table 2, Figure 3; see also Figure S3 for individual data points). In liver tissue, 7oxoLC-Tau was 5.5-fold increased, CDC-Tau not different and UDC-Tau threefold lower in 11LKO compared to CTRL (Table 2; see also Figure S4). In agreement with 11KO, the CDC-Tau/7oxoLC-Tau and UDC-Tau/7oxoLC-Tau ratios were lower in 11LKO liver tissue compared to CTRL (fivefold and 16-fold, respectively). The αMCA/βMCA ratio was 3.3-fold higher in plasma and 7.3-fold in liver tissue of 11LKO (Table 2).

3.4 | *H6pd*KO mice exhibit moderately decreased 11β-HSD1 oxoreduction activity

Previous characterization of *H6pd*KO mice suggested, based on experiments using microsomal preparations, a complete loss of 11β-HSD1 oxoreduction activity (Lavery et al., 2006). To assess the conversion of 11-oxo- to 11β-hydroxyglucocorticoids *in vivo*, *H6pd*KO mice and control littermates received cortisone i.p. and were killed 10 min later, followed by measuring formed cortisol. 11β-HSD1 oxoreduction activity was reduced to approximately 60% of the level in control mice (Figure 4a), despite comparable hepatic 11β-HSD1 mRNA and protein expression (Figure 4b,c). As expected, H6PD mRNA and protein expression were abolished in *H6pd*KO. Similarly, *ex vivo* oxoreduction was reduced in liver of *H6pd*KO mice to half the activity of controls (Figure 4d). There was a corresponding increase in dehydrogenase activity to approximately fivefold the level in control liver (Figure 4e). The ratio of oxoreduction to dehydrogenase activity was estimated to be about five in CTRL and 0.5 in *H6pd*KO liver tissue. Similar experiments in white adipose tissue showed approximately 40% residual oxoreduction activity in *H6pd*KO compared to CTRL, whilst dehydrogenase activity increased 30-fold to 40-fold (Figure S5). Thus, in contrast to the expectation of a complete loss of 11β-HSD1 oxoreduction activity, these results revealed a moderately decreased oxoreduction in *H6pd*KO mice despite an increase in dehydrogenase activity.

An estimation of the impact of the lack of H6PD on NADPH levels in the ER using liver microsomes indicated that the content of total reduced pyridine nucleotides (NADPH + NADH) did not differ between control and *H6pd*KO (Figure 4f), but NADPH content of *H6pd*KO mouse liver microsomes was moderately lower by approximately 30% compared to control (Figure 4g).

TABLE 2 Bile acid profiles in plasma and liver of 11LKO mice

	Plasma (nmol·L^{-1})		Liver (fmol·mg^{-1})	
	CTRL	11LKO	CTRL	11LKO
Analyte	(*n* = 17)	(*n* = 16)	(*n* = 17)	(*n* = 16)
CA	528 ± 87	3,141 ± 1,837	2,004 ± 606	5,589 ± 1,271*
CDCA	15.2 ± 3.3	42 ± 14	17.4 ± 3.1	26 ± 6
DCA	148 ± 33	184 ± 87	66 ± 22	94 ± 32
7oxoDCA	188 ± 55	2,306 ± 1,488	985 ± 455	6,477 ± 1,679*
HDCA	25 ± 5	33 ± 12	33 ± 8	82 ± 23
αMCA	67 ± 17	425 ± 285	356 ± 91	2,685 ± 749*
βMCA	904 ± 145	276 ± 104*	2,693 ± 619	2,423 ± 511
ωMCA	888 ± 149	937 ± 479	1,268 ± 356	3,178 ± 763
UDCA	75 ± 10	77 ± 37	103 ± 26	249 ± 52*
7oxoLCA	6.8 ± 1.3	76 ± 38	28 ± 5	63 ± 17
αMCA/βMCA	0.18 ± 0.10	0.60 ± 0.09*	0.13 ± 0.02	0.96 ± 0.13*
UDCA/7oxoLCA	32 ± 12	4.5 ± 2.4*	5.0 ± 1.1	6.0 ± 1.0
CDCA/7oxoLCA	3.9 ± 1.6	1.86 ± 0.97*	0.91 ± 0.12	0.74 ± 0.12
C-Tau	2,993 ± 1,687	2,091 ± 1,778	59,664 ± 15,995	66,470 ± 11,753
CDC-Tau	76 ± 48	78 ± 53	2,355 ± 515	2,667 ± 536
DC-Tau	200 ± 106	289 ± 149	3,843 ± 1,822	2,367 ± 735
LC-Tau	16.0 ± 0.7	1.81 ± 0.70	50 ± 13	40 ± 9
αMCA-Tau + βMCA-Tau	1,854 ± 851	2,878 ± 1,923	30,702 ± 6,384	29,952 ± 6,056
ωMCA-Tau	2,133 ± 1,324	1,286 ± 1,088	32,951 ± 6,074	28,000 ± 4,968
UDC-Tau	103 ± 60	16.1 ± 9.8*	2,754 ± 531	886 ± 489*
7oxoLC-Tau	9.1 ± 3.3	187 ± 110	560 ± 123	3,101 ± 935*
UDC-Tau/7oxoLC-Tau	158 ± 149	0.72 ± 0.22*	6.5 ± 1.1	0.40 ± 0.22*
CDC-Tau/7oxoLC-Tau	122 ± 120	0.78 ± 0.12*	5.6 ± 1.3	1.09 ± 0.11*
Sum primary BA	1,588 ± 179	3,962 ± 2,156	5,174 ± 1,266	10,971 ± 2,449
Sum primary BA-Tau	5,026 ± 2,272	5,063 ± 3,625	95,475 ± 19,081	99,975 ± 17,536

Note: The results represent mean ± SEM (nmol·L^{-1} and fmol·mg^{-1} for plasma and liver, respectively). Analyte concentrations defined by a S/N ≤ 3 represent the LLOD of the UHPLC–MS/MS method. Samples yielding a concentration below LLOD were included as LLOD/2 (nmol·L^{-1} and fmol·mg^{-1}, respectively) in the calculations of a specific analyte. Blue- and yellow-coloured boxes indicate statistically significant increases and decreases, respectively. Unequal group sizes reflect exclusion of one 11LKO animal due to unexpected health issues prior to reaching the age for the experiment.
Abbreviations: 11LKO, liver-specific *Hsd11b1* knockout; CTRL, control littermates.
*P < 0.05, significantly different as indicated; non-parametric, Mann–Whitney U test (two-tailed).

3.5 | The UDC-Tau/7oxoLC-Tau ratio detects decreased 11β-HSD1 oxoreductase activity in *H6pd*KO mice

Next, plasma and liver tissue bile acid profiles between *H6pd*KO and control mice were compared. Unlike in 11KO, primary and taurine-conjugated bile acids were not generally elevated in plasma of *H6pd*KO mice (Table 3). 7oxoLCA was 1.8-fold higher in *H6pd*KO plasma, whilst UDCA was threefold lower and CDCA not different between the two genotypes. The ratio of CDCA/7oxoLCA only tended lower, whereas UDCA/7oxoLCA was 3.7-fold lower in *H6pd*KO plasma (Figure 4h). 7oxoLC-Tau was about ninefold higher in *H6pd*KO plasma than in CTRL, whereas UDC-Tau was not different and CDC-Tau tended to increase. Both ratios CDC-Tau/7oxoLC-Tau and UDC-Tau/7oxoLC-Tau (Figure 4h; see also Figure S6) were significantly lower in *H6pd*KO plasma. In agreement with 11KO and 11LKO, these observations were supported by a similar bile acid profile in liver tissue with almost threefold increased 7oxoLCA and twofold decreased UDCA in *H6pd*KO but no difference in CDCA (Table 3, Figure S7). The CDCA/7oxoLCA and UDCA/7oxoLCA ratios were twofold and fivefold lower, respectively, in *H6pd*KO liver tissue (Table 3, Figure 4i). The levels of the taurine-conjugated bile acids were about an order of magnitude higher than those of their free forms. 7oxoLC-Tau was fourfold higher in *H6pd*KO compared to control, but due to inter-individual variation, the value did not reach significance. CDC-Tau was not different between the two

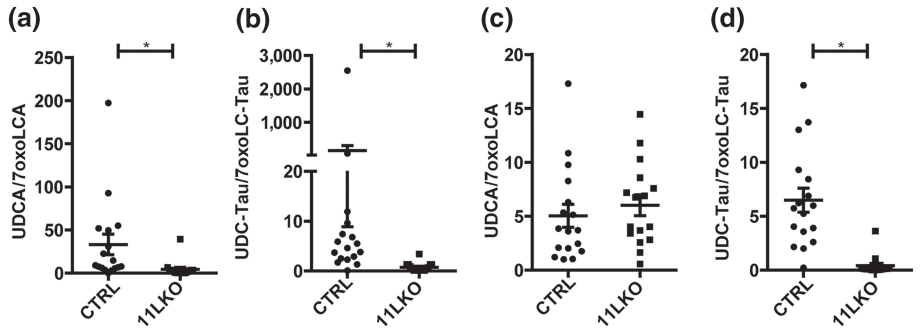

FIGURE 3 Plasma and liver tissue UDCA/7oxoLCA and UDC-Tau/7oxoLC-Tau ratios in 11LKO mice. (a) UDCA/7oxoLCA ratios and (b) UDC-Tau/7oxoLC-Tau ratios in plasma of 11LKO mice (CTRL n = 17; 11LKO n = 16); (c) UDCA/7oxoLCA ratios and (d) UDC-Tau/7oxoLC-Tau ratios in liver tissue of 11LKO mice (CTRL n = 17; 11LKO n = 16). Analyte concentrations defined by a S/N ≤ 3 represent the LLOD of the UHPLC–MS/MS method. Samples yielding a concentration below LLOD were included as LLOD/2 (nmol·L^{-1} and fmol·mg^{-1} for plasma and liver, respectively) in the calculations of a specific analyte. The results represent mean ± SEM. *P < 0.05 significantly different as indicated; non-parametric, Mann–Whitney U test (two-tailed). Unequal group sizes reflect exclusion of one 11LKO animal due to unexpected health issues prior to reaching the age for the experiment

genotypes, whilst UDC-Tau decreased twofold. The ratios CDC-Tau/7oxoLC-Tau and UDC-Tau/7oxoLC-Tau (Figure 4i; see also Figure S7) were threefold and fivefold lower, respectively, in *H6pd*KO liver tissue.

As seen in 11KO and 11LKO, the ratio of αMCA/βMCA was significantly higher in *H6pd*KO plasma (fourfold) and liver tissue (fivefold). In *H6pd*KO mice, this was due to significantly lower βMCA. αMCA was not different between the genotypes (Table 3).

3.6 | The UDC-Tau/7oxoLC-Tau ratio detects pharmacologically diminished 11β-HSD1 activity

The UDC-Tau/7oxoLC-Tau ratio detected the reduced 11β-HSD1 activity due to genetic alteration of its expression (11KO, 11LKO) or reaction direction (*H6pd*KO). To see if enzyme inhibition without genetic manipulation also can be detected, the known 11β-HSD1 inhibitor carbenoxolone was used. Inhibition by carbenoxolone of 11β-HSD1-dependent metabolism of 7oxoLCA was first assessed *in vitro*. HEK-293 cells stably expressing murine 11β-HSD1 (MO1F cells) showed a time-dependent conversion of 7oxoLCA to comparable amounts of UDCA and CDCA, with almost complete metabolism of 7oxoLCA after 24 h (Figure S8). Incubation with carbenoxolone almost fully blocked the formation of UDCA and CDCA, supporting the use of product/substrate ratios as markers of 11β-HSD1 activity.

Next, mice were treated i.p. with 100 mg·kg^{-1}·day^{-1} of carbenoxolone for 4 days. carbenoxolone treatment decreased cortisone to cortisol conversion by approximately 30%, revealing moderate 11β-HSD1 inhibition (Figure 5a). Interestingly, analysis of mRNA showed a reduction in *Hsd11b1* mRNA expression and a trend for increased *H6pd* mRNA (Figure 5b). This was corroborated by similar effects on H6PD (30% increase) and 11β-HSD1 (50–60% decrease) protein expression (Figure 5c), suggesting that besides pharmacological inhibition, a reduced expression contributed to the lower 11β-HSD1 activity in this model.

Analysis of bile acid profiles revealed that the sum of free primary bile acids tended to be lower (2.5-fold) in plasma upon carbenoxolone treatment, whereas taurine-conjugated primary bile acids seemed to be not affected (Table 4). 7oxoLCA concentrations were below the lower limit of detection (LLOD) in plasma and liver tissue samples in this mouse cohort, so the respective product/substrate ratios with UDCA and CDCA could not be calculated. In plasma of carbenoxolone-treated mice, 7oxoLC-Tau tended to increase, whilst UDC-Tau and CDC-Tau were not affected by carbenoxolone (Figure S9). Nevertheless, CDC-Tau/7oxoLC-Tau and UDC-Tau/7oxoLC-Tau (Figure 5d; see also Figure S9) were 1.6-fold and twofold lower in plasma of carbenoxolone-treated mice. In liver tissue, only UDC-Tau/7oxoLC-Tau was predictive for decreased 11β-HSD1 activity (2.6-fold decreased; Table 4, Figures 5e and S10).

In contrast to the other three mouse models, the αMCA/βMCA ratio was unchanged in plasma and even threefold lower in liver tissue; thus, this ratio is not indicative of altered 11β-HSD1 activity.

4 | DISCUSSION

This proof-of-concept study proposes that the UDC-Tau/7oxoLC-Tau ratio can serve as a biomarker for decreased 11β-HSD1 activity *in vivo*. The UDC-Tau/7oxoLC-Tau ratio in plasma and liver tissue successfully detected complete loss of 11β-HSD1 activity in 11KO mice, loss of hepatic 11β-HSD1 activity in 11LKO mice and moderately decreased oxoreduction activity in *H6pd*KO- and carbenoxolone-treated mice. Of note, the four models differed with respect to their genetic background (11KO, 11LKO and *H6pd*KO on a mixed C57BL/6J/129SvJ background, carbenoxolone group were C57BL/6JRj) that can affect lipid and bile acid homeostasis (Jolley et al., 1999), feeding regimen (11KO and 11LKO fasted overnight, the other two models *ad libitum* feeding; some differences in the composition of the chow) and environment (different animal facilities) that can

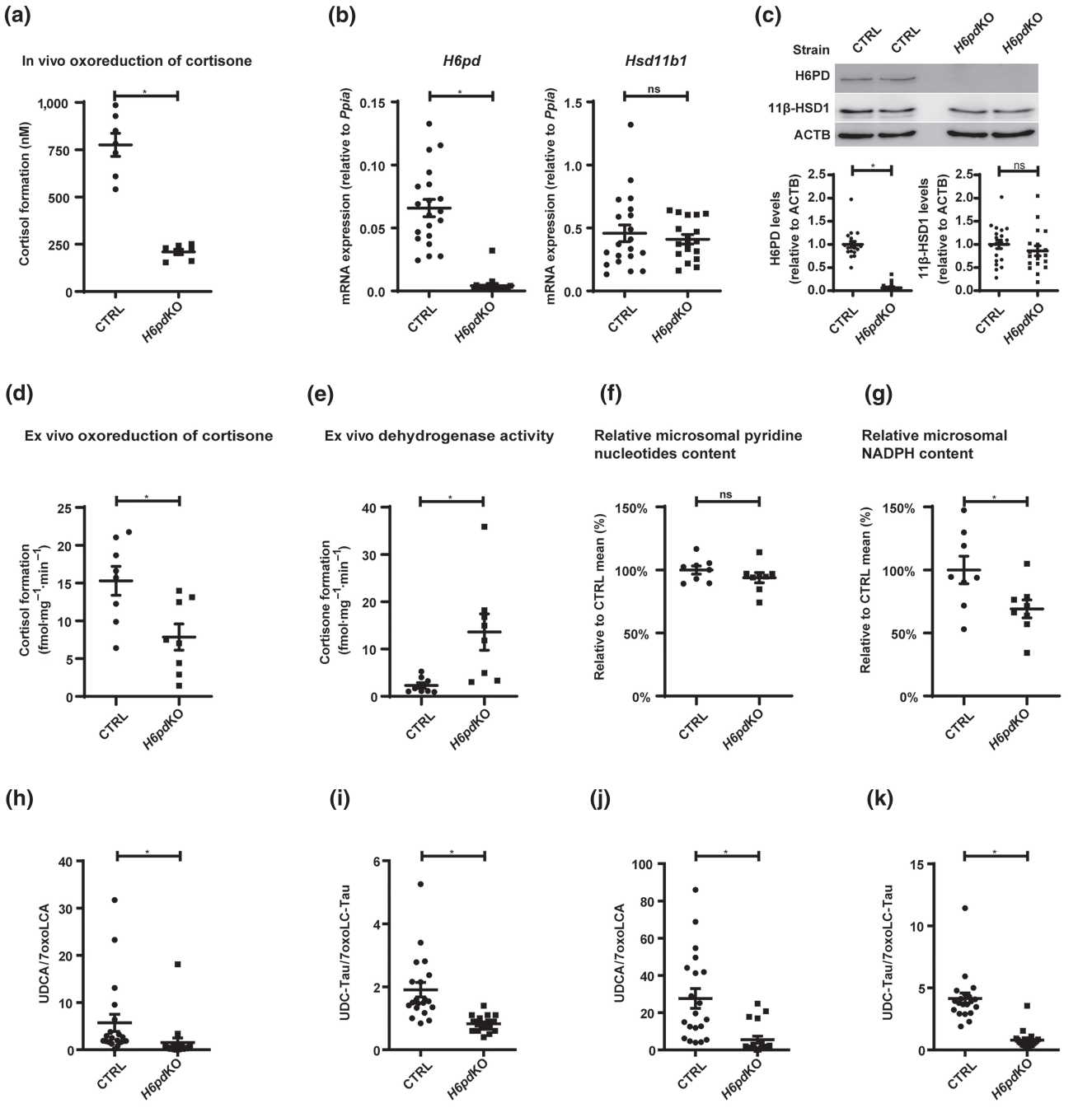

FIGURE 4 Characterization of 11β-HSD1 expression and activity and plasma and liver tissue UDCA/7oxoLCA and UDC-Tau/7oxoLC-Tau ratios in *H6pd*KO mice. (a) Estimation of the cortisone to cortisol conversion *in vivo*, determined as plasma concentration (nmol·L^{-1}) of cortisol 10 min after i.p. administration of 5 mg·kg^{-1} of cortisone (in DMSO) (CTRL n = 7; *H6pd*KO n = 7). (b) mRNA and (c) Western blot and semi-quantitative analysis of protein levels of H6PD and 11β-HSD1 in CTRL and *H6pd*KO animals (CTRL n = 20; *H6pd*KO n = 18). (d) Conversion of cortisone to cortisol and (e) of cortisol to cortisone determined ex vivo in mouse liver tissue (CTRL n = 8; *H6pd*KO n = 8). (f) Reduced pyridine nucleotides content and (g) NADPH content in mouse liver microsomes (relative to the mean of the CTRL; CTRL n = 8; *H6pd*KO n = 8). (h) UDCA/7oxoLCA ratios and (i) UDC-Tau/7oxoLC-Tau ratios in plasma of *H6pd*KO mice (CTRL n = 20; *H6pd*KO n = 18); (j) UDCA/7oxoLCA ratios and (k) UDC-Tau/7oxoLC-Tau ratios in liver tissue of *H6pd*KO mice (CTRL n = 20; *H6pd*KO n = 18). Analyte concentrations defined by a S/N ≤ 3 represent the LLOD of the UHPLC–MS/MS method. Samples yielding a concentration below LLOD were included as LLOD/2 (nmol·L^{-1} and fmol·mg^{-1} for plasma and liver, respectively) in the calculations of a specific analyte. Results represent mean ± SEM. *P < 0.05 significantly different as indicated; non-parametric, Mann–Whitney U test (two-tailed). Unequal group sizes reflect exclusion of two *H6pd*KO animals from further analysis due to the occurrence of liver cysts

TABLE 3 Bile acid profiles in plasma and liver of *H6pd*KO mice

	Plasma (nmol·L^{-1})		Liver (fmol·mg^{-1})	
	CTRL *H6pd*KO	*H6pd*KO	CTRL	*H6pd*KO
Analyte	(*n* = 20)	(*n* = 18)	(*n* = 20)	(*n* = 18)
CA	385 ± 245	214 ± 100	6,174 ± 1,321	4,324 ± 1,460
CDCA	8.8 ± 4.0	8.6 ± 1.5	304 ± 54	280 ± 55
DCA	187 ± 39	113 ± 13*	244 ± 31	166 ± 23
7oxoDCA	142 ± 97	167 ± 88	4,332 ± 1,175	4,555 ± 1,647
HDCA	18.4 ± 5.7	17.5 ± 2.5	350 ± 67	277 ± 39
αMCA	32 ± 16	37 ± 18	2,921 ± 688	2,544 ± 596
βMCA	259 ± 138	54 ± 19*	9,297 ± 1,932	2,652 ± 512*
ωMCA	71 ± 26	43 ± 9	2,154 ± 367	1,087 ± 183
UDCA	45 ± 24	15.4 ± 5.7*	365 ± 57	174 ± 48*
7oxoLCA	12.0 ± 2.4	20 ± 2*	37 ± 13	103 ± 28
αMCA/βMCA	0.12 ± 0.01	0.51 ± 0.06*	0.23 ± 0.02	0.98 ± 0.15*
UDCA/7oxoLCA	5.7 ± 1.8	1.53 ± 0.99*	28 ± 5	5.5 ± 1.9*
CDCA/7oxoLCA	1.38 ± 0.53	0.77 ± 0.39	20 ± 3	10.5 ± 3.5*
C-Tau	5,602 ± 3,712	9,620 ± 8,041	565,130 ± 129,003	394,188 ± 108,185
CDC-Tau	234 ± 133	429 ± 317	28,597 ± 7,271	30,359 ± 7,770
DC-Tau	381 ± 238	565 ± 404	25,629 ± 5,137	19,979 ± 5,696
LC-Tau	4.7 ± 3.9	12.2 ± 10.7	947 ± 67	997 ± 114
αMCA-Tau + βMCA-Tau	1,247 ± 877	854 ± 733	354,892 ± 80,362	193,231 ± 45,864
ωMCA-Tau	2,436 ± 1,627	2,974 ± 2,355	151,216 ± 38,734	80,001 ± 14,690
UDC-Tau	228 ± 161	293 ± 244	22,609 ± 5,964	9,885 ± 2,777*
7oxoLC-Tau	72 ± 46	651 ± 569	5,541 ± 1,045	22,711 ± 6,325
UDC-Tau/7oxoLC-Tau	1.91 ± 0.23	0.83 ± 0.06*	4.1 ± 0.4	0.80 ± 0.18*
CDC-Tau/7oxoLC-Tau	3.03 ± 0.32	1.70 ± 0.10*	5.0 ± 0.5	1.75 ± 0.24*
Sum primary BA	730 ± 426	333 ± 142	19,060 ± 3,852	9,975 ± 2,444
Sum primary BA-Tau	14,127 ± 9,474	22,922 ± 19,167	971,227 ± 220,934	627,664 ± 162,026

Note: The results represent mean ± SEM (nmol·L^{-1} and fmol·mg^{-1} for plasma and liver, respectively). Analyte concentrations defined by a S/N ≤ 3 represent the LLOD of the UHPLC–MS/MS method. Samples yielding a concentration below LLOD were included as LLOD/2 (nmol·L^{-1} and fmol·mg^{-1}, respectively) in the calculations of a specific analyte. Blue- and yellow-coloured boxes indicate statistically significant increases and decreases, respectively. Unequal group sizes reflect exclusion of two *H6pd*KO animals from further analysis due to the occurrence of liver cysts.

Abbreviations: CTRL, control littermates; *H6pd*KO, global *H6pd* knockout.

*$P < 0.05$, significantly different as indicated; non-parametric, Mann–Whitney *U* test (two-tailed).

impact the microbiome and thereby influence bile acid homeostasis (Rausch et al., 2016). A biomarker reporting decreased 11β-HSD1 oxoreduction activity in plasma opens the possibility for non-invasive applications in preclinical studies of pharmacological inhibitors for potential therapeutic applications; whether it can also be used to explore the pathophysiological role of 11β-HSD1 in situations of elevated activity remains to be investigated (Gathercole et al., 2013). Determination of this ratio in liver tissue at the end of the study can provide additional information.

The plasma UDCA/7oxoLCA ratio was also a marker for decreased 11β-HSD1 activity. However, because the levels of free bile acids are lower than those of their taurine-conjugated forms and were below the LLOD in some mice, this is likely to be less useful practically than the ratio of the taurine-conjugated metabolites. Whilst in mice and rats taurine-conjugated bile acids are predominant and the UDC-Tau/7oxoLC-Tau ratio is easier to assess, the ratio of the free UDCA/7oxoLCA has the advantage to be species independent, as glycine-conjugated bile acids are predominant in human and other higher mammals (Alnouti et al., 2008; Garcia-Canaveras et al., 2012; Penno et al., 2014). Improvements of the analytical sensitivity may be achieved by measuring just UDCA and 7oxoLCA, using larger sample volumes, and optimizing extraction specifically for these two bile acids, which should permit this ratio to be a good and reliable species-independent marker.

Although murine 11β-HSD1 converts 7oxoLC-Tau to UDC-Tau and CDC-Tau (Odermatt et al., 2011), the UDC-Tau/7oxoLC-Tau ratio was superior to the CDC-Tau/7oxoLC-Tau for detecting decreased 11β-HSD1 activity. A possible explanation may be the significant

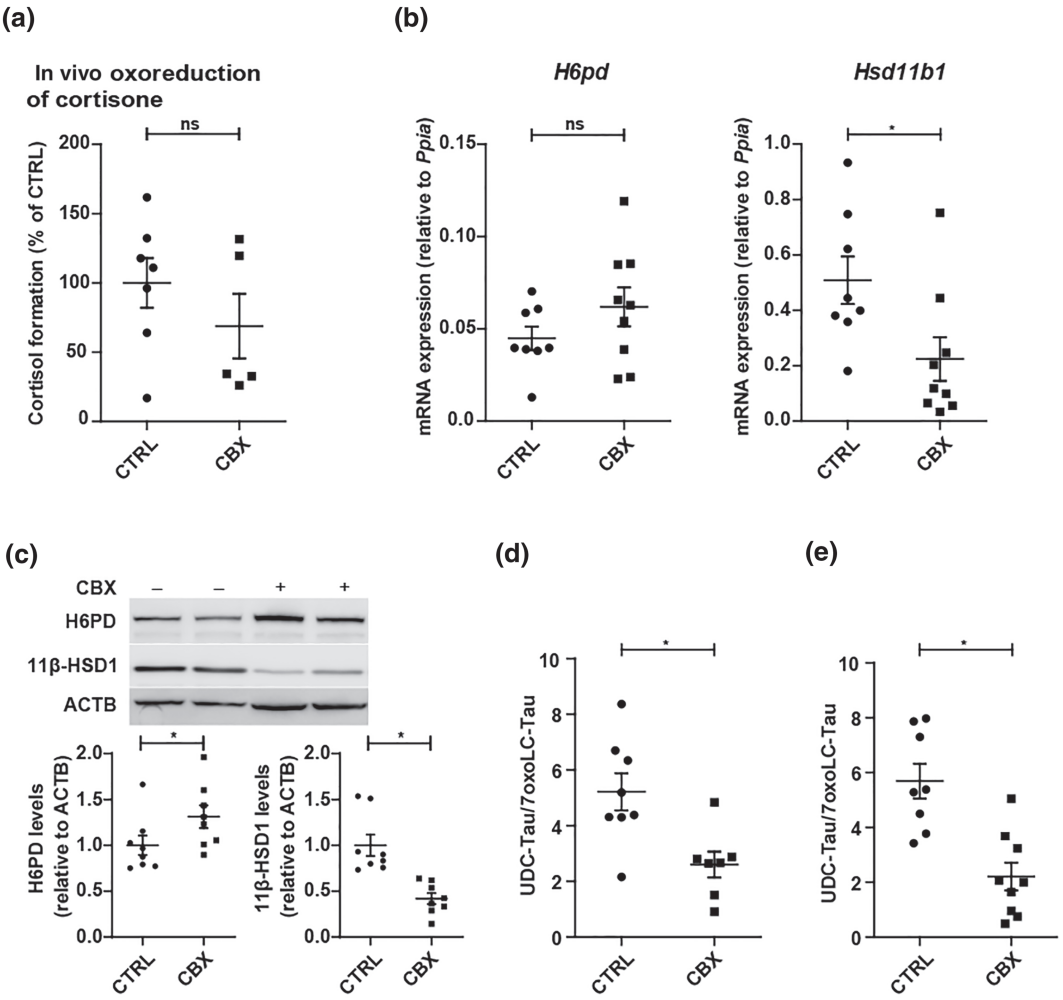

FIGURE 5 Characterization of 11β-HSD1 expression and activity and plasma and liver tissue UDC-Tau/7oxoLC-Tau ratios in carbenoxolone-treated mice. Control mice were treated with the pharmacologic 11β-HSD1 inhibitor carbenoxolone (CBX, 100 mg·kg^{-1}·day^{-1}, i.p.) or PBS (CTRL). (a) Conversion of cortisone to cortisol *in vivo*, measured after i.p. administration of 5 mg·kg^{-1} of cortisone (in DMSO) (CTRL n = 7; CBX n = 5). (b) mRNA expression of *H6pd* and *Hsd11b1* in CTRL- and CBX-treated animals (CTRL n = 8; CBX n = 9). (c) Western blot and semi-quantitative analysis of protein levels of H6PD and 11β-HSD1 in CTRL- and CBX-treated mice (CTRL n = 8; CBX n = 8). (d) UDC-Tau/7oxoLC-Tau ratios in CTRL mice treated with PBS (CTRL) or the pharmacologic 11β-HSD1 inhibitor carbenoxolone (CBX 100 mg·kg^{-1}·day^{-1}, i.p.) (CTRL n = 8; CBX n = 9) in plasma and (e) in liver tissue. Analyte concentrations defined by a S/N ≤ 3 represent the LLOD of the UHPLC–MS/MS method. Samples yielding a concentration below LLOD were included as LLOD/2 (nmol·L^{-1} and fmol·mg^{-1} for plasma and liver, respectively) in the calculations of a specific analyte. Results represent mean ± SEM. No outliers were excluded. *P < 0.05 significantly different as indicated; non-parametric, Mann–Whitney U test (two-tailed). Unequal group sizes reflect exclusion of one animal of the CTRL group due to unexpected health issues prior to the experiment and exclusion of two plasma samples of the CBX group due to insufficient collection of blood sample volume

contribution of de novo CDCA synthesis to the circulating and liver tissue levels of CDC-Tau, whereas UDC-Tau and 7oxoLC-Tau are primarily formed from gut microbiota-derived UDCA and 7oxoLCA.

Interestingly, an increase in the ratio of αMCA/βMCA, formed by cytochrome P450 2C70 from CDCA and UDCA, respectively (Takahashi et al., 2016), nicely detected the decreased 11β-HSD1 activity in the three genetically modified mouse models. However, in carbenoxolone-treated mice, this ratio was not changed in plasma and showed an opposite change in liver. Plausibly, carbenoxolone inhibits cytochrome P450 2C70 or decreases its expression. Carbenoxolone might also affect gut microbiota as it was earlier shown to alter colonic mucus (Finnie et al., 1996). This merits future investigation.

Pharmacological treatment using carbenoxolone led to approximately 30% decreased 11β-HSD1 activity. It needs to be noted that the level of 11β-HSD1 inhibition is an estimation and it was determined at one given time point (i.e., at about 8 am) and the formation of cortisol upon injection of cortisone was determined after 10 min. Nevertheless, inhibition of 11β-HSD1 could be demonstrated and the bile acid biomarker detected the decreased activity. The results suggested that besides direct inhibition, a reduced enzyme expression contributed to the decreased activity. carbenoxolone also inhibits 11β-HSD2 (Stewart et al., 1990). However, our preliminary observations suggest that this enzyme does not accept CDCA and UDCA as substrates, therefore unlikely affecting the bile acid ratios of interest.

TABLE 4 Bile acid profiles in plasma and liver in mice with decreased 11β-HSD1 oxoreduction activity by pharmacologic inhibition using carbenoxolone

	Plasma (nmol·L^{-1})		Liver (fmol·mg^{-1})	
	CTRL	CBX	CTRL	CBX
Analyte	(*n* = 8)	(*n* = 7)	(*n* = 8)	(*n* = 9)
CA	1,000 ± 795	408 ± 275	513 ± 84	329 ± 71
CDCA	145 ± 120	11.0 ± 2.3	242 ± 17	114 ± 45
DCA	592 ± 245	169 ± 62*	186 ± 15	61 ± 21*
7oxoDCA	237 ± 178	281 ± 212	46 ± 17	88 ± 50
HDCA	146 ± 90	26 ± 12	224 ± 17	113 ± 34*
αMCA	162 ± 110	42 ± 17	288 ± 33	129 ± 42*
βMCA	659 ± 481	318 ± 179	1,608 ± 136	4,409 ± 1,557
ωMCA	238 ± 134	47 ± 25	306 ± 25	580 ± 183
UDCA	226 ± 126	39 ± 18*	99 ± 14	17.8 ± 6.2*
7oxoLCA	NA	NA	NA	NA
αMCA/βMCA	0.24 ± 0.05	0.28 ± 0.15	0.18 ± 0.02	0.06 ± 0.02*
UDCA/7oxoLCA	NA	NA	NA	NA
CDCA/7oxoLCA	NA	NA	NA	NA
C-Tau	7,002 ± 4,900	9,530 ± 6,466	63,049 ± 11,354	48,334 ± 9,673
CDC-Tau	339 ± 223	265 ± 175	5,274 ± 533	3,975 ± 857
DC-Tau	348 ± 275	222 ± 124	6,723 ± 719	2,114 ± 766*
LC-Tau	8.8 ± 5.6	2.01 ± 1.22	1,271 ± 127	541 ± 81*
αMCA-Tau + βMCA-Tau	1,876 ± 1,853	1,383 ± 943	55,442 ± 6,370	63,438 ± 12,465
ωMCA-Tau	3,124 ± 1,998	12,920 ± 11,548	25,304 ± 3,379	32,334 ± 8,484
UDC-Tau	296 ± 221	332 ± 251	4,071 ± 501	1,125 ± 174*
7oxoLC-Tau	84 ± 56	125 ± 94	836 ± 178	760 ± 209
UDC-Tau/7oxoLC-Tau	5.2 ± 0.7	2.6 ± 0.5*	5.7 ± 0.6	2.2 ± 0.5*
CDC-Tau/7oxoLC-Tau	2.6 ± 0.4	1.60 ± 0.38*	7.7 ± 1.0	6.2 ± 1.0
Sum primary BA	2,192 ± 1,630	818 ± 483	2,463 ± 192	4,869 ± 1,611
Sum primary BA-Tau	9,513 ± 7,033	11,511 ± 7,034	127,836 ± 17,002	116,873 ± 15,450

Note: The results represent mean ± SEM (nmol·L^{-1} and fmol·mg^{-1} for plasma and liver, respectively). Analyte concentrations defined by a S/N ≤ 3 represent the LLOD of the UHPLC–MS/MS method. Samples yielding a concentration below LLOD were included as LLOD/2 (nmol·L^{-1} and fmol·mg^{-1}, respectively) in the calculations of a specific analyte. Yellow-coloured boxes indicate statistically significant decreases. Unequal group sizes reflect exclusion of one animal of the CTRL group due to unexpected health issues prior to the experiment and exclusion of two plasma samples of the carbenoxolone (CBX group due to insufficient collection of blood sample volume.

Abbreviations: CBX, mice treated with the pharmacologic 11β-HSD1 inhibitor carbenoxolone (100 mg·kg^{-1}·day^{-1}, i.p.); CTRL, control mice treated with PBS; NA, not analysed, if most values were below LLOD.

*$P < 0.05$, significantly different as indicated; non-parametric, Mann–Whitney *U* test (two-tailed).

*H6pd*KO mice retained approximately 50% of 11β-HSD1 oxoreduction activity measured in control animals. This is consistent with observations made in isolated macrophage from *H6pd*KO mice, which also retained about 50–60% 11β-HSD1 oxoreduction activity (Marbet et al., 2018). Based on earlier experiments using liver microsomes (Lavery et al., 2006), it was anticipated that in the absence of H6PD, 11β-HSD1 would function exclusively as dehydrogenase and the effect on the respective bile acid ratios would be comparable with that in 11KO mice, yet the accumulation of 7oxo metabolites and the ratios derived from them clearly were less pronounced. These findings indicate the existence of a yet unknown mechanism generating NADPH in the ER capable of driving 11β-HSD1 reaction direction towards oxoreduction activity. This is supported by the continued presence of NADPH in the *H6pd*KO liver, albeit at reduced levels, seen previously (Rogoff et al., 2010) and also found here. A possible candidate for generating NADPH within the ER includes luminal 6-phosphogluconate dehydrogenase (Bublitz et al., 1987). However, the gene encoding this enzyme still remains to be identified.

The mild cholestasis phenotype of 11KO mice with 10-fold to 20-fold increased plasma bile acids (Table 1, Penno et al., 2014) raises some concerns that pharmacological 11β-HSD1 inhibition might induce cholestasis. In paediatric patients with adrenal insufficiency

and cholestasis, glucocorticoid treatment reversed the hepatic phenotype (Al-Hussaini et al., 2012; Cheung et al., 2003), indicating a direct role of glucocorticoids in maintaining bile acid homeostasis. However, no evidence for cholestasis was seen in the present study when 11β-HSD1 was inhibited by carbenoxolone and there was only a trend increase of total free but not conjugated bile acids in 11LKO mice and no change of total bile acids in *H6pd*KO mice. These observations do not support concerns of a general risk of cholestasis upon inhibition of 11β-HSD1. The more pronounced effect on plasma and liver tissue bile acid profiles in 11KO mice may be explained by the fact that they lack 11β-HSD1 during all stages of life and throughout the enterohepatic circuit and also by altered hypothalamus–pituitary–adrenal axis, whereas 11LKO only lack hepatic 11β-HSD1, and *H6pd*KO- and carbenoxolone-treated mice retain partial 11β-HSD1 activity.

A suitable biomarker reporting the *in vivo* 11β-HSD1 activity in health and disease situations or upon pharmacological interventions could greatly facilitate such studies. The currently used urinary (tetrahydrocorticosterone + allo-tetrahydrocorticosterone)/tetrahydro-11-dehydrocorticosterone ratio has limited value as it can lead to erroneous conclusions because of interference through altered 11β-HSD2 and 5α-reductase activities and feedback modulation. Furthermore, it needs 24-h urine sampling that due to small collection volume and contamination by food and faeces and the stress of metabolic cage housing may lead to erroneous results.

Although our data support the UDC-Tau/7oxoLC-Tau ratio as a useful *in vivo* marker of 11β-HSD1 activity, our study has several limitations:- (1) the present study included only male mice at 10–15 weeks of age and it will be important to study also mice at both young and very old age that may exhibit metabolic differences as well as female mice, being mindful of the effect of the oestrous cycle on bile acid homeostasis (Papacleovoulou et al., 2011); (2) the impact of feeding and diet should be studied; (3) samples were taken in the morning between 7 and 10 am and the influence of circadian rhythm and/or stress should be assessed; (4) in case of pharmacological inhibition, a possible interference of the compound with hepatic enzymes and transporters that also are involved in bile acid homeostasis needs to be kept in mind; (5) the impact of the microbiome on the production of UDCA and 7oxoLCA needs to be investigated; it has been shown that 11β-HSD1 deficiency alters the microbiome in a diet-specific manner (Johnson et al., 2017); (6) disease models with altered 11β-HSD1 activity should be studied and (7) the sensitivity of the LC–MS/MS-based quantification method can be increased by measuring specifically the bile acid metabolites needed for the ratio and by increasing sample volume and optimizing extraction. In follow-on research, the predictivity of the UDC-Tau/7oxoLC-Tau ratio for detecting altered 11β-HSD1 activity should be investigated in mouse models addressing the abovementioned factors. Finally, experiments in humans are required to establish whether such a bile acid ratio is a useful biomarker to detect altered 11β-HSD1 activity upon pharmacological treatment or in disease situations.

ACKNOWLEDGEMENTS

We thank Dr. Antonio Checa, Karolinska Institutet, Sweden, for his statistical support and advice.

AUTHOR CONTRIBUTIONS

M.W., S.S., D.V.K., J.B. and P.K. designed and conducted the experiments, analysed data, and reviewed the paper; K.E.C. consulted for the study and reviewed the paper; G.G.L. consulted for the study and reviewed the paper; and A.O. designed the experiments, supervised the study and wrote the paper.

CONFLICT OF INTEREST

The authors have nothing to disclose.

DECLARATION OF TRANSPARENCY AND SCIENTIFIC RIGOUR

This Declaration acknowledges that this paper adheres to the principles for transparent reporting and scientific rigour of preclinical research as stated in the *BJP* guidelines for Design & Analysis, Immunoblotting and Immunochemistry and Animal Experimentation, and as recommended by funding agencies, publishers, and other organizations engaged with supporting research.

DATA AVAILABILITY STATEMENT

The data that support the findings of this study are available from the corresponding author upon reasonable request. All related study data will be provided according to the related data management plan as open access at https://zenodo.org/.

REFERENCES

Abrahams, L., Semjonous, N. M., Guest, P., Zielinska, A., Hughes, B., Lavery, G. G., & Stewart, P. M. (2012). Biomarkers of hypothalamic-pituitary-adrenal axis activity in mice lacking 11β-Hsd1 and H6pdh. *Journal of Endocrinology*, *214*, 367–372. https://doi.org/10.1530/JOE-12-0178

Alexander, S. P. H., Roberts, R. E., Broughton, B. R. S., Sobey, C. G., George, C. H., Stanford, S. C., … Ahluwalia, A. (2018). Goals and practicalities of immunoblotting and immunohistochemistry: A guide for submission to the *British Journal of Pharmacology*. *British Journal of Pharmacology*, *175*, 407–411. https://doi.org/10.1111/bph.14112

Alexander, S. P. H., Fabbro, D., Kelly, E., Mathie, A., Peters, J. A., Veale, E. L., … …GTP collaborators. (2019). The Concise Guide to PHARMACOLOGY 2019/20: Enzymes. *British Journal of Pharmacology*, *176*, S297–S396. https://doi.org/10.1111/bph.14752

Al-Hussaini, A., Almutairi, A., Mursi, A., Alghofely, M., & Asery, A. (2012). Isolated cortisol deficiency: A rare cause of neonatal cholestasis. *Saudi Journal of Gastroenterology*, *18*, 339–341. https://doi.org/10.4103/1319-3767.101137

Alnouti, Y., Csanaky, I. L., & Klaassen, C. D. (2008). Quantitative-profiling of bile acids and their conjugates in mouse liver, bile, plasma, and urine using LC–MS/MS. *Journal of Chromatography. B, Analytical Technologies in the Biomedical and Life Sciences*, *873*, 209–217. https://doi.org/10.1016/j.jchromb.2008.08.018

Arampatzis, S., Kadereit, B., Schuster, D., Balazs, Z., Schweizer, R. A., Frey, F. J., … Odermatt, A. (2005). Comparative enzymology of 11β-hydroxysteroid dehydrogenase type 1 from six species. *Journal of Molecular Endocrinology*, *35*, 89–101. https://doi.org/10.1677/jme.1.01736

Atanasov, A. G., Nashev, L. G., Schweizer, R. A., Frick, C., & Odermatt, A. (2004). Hexose-6-phosphate dehydrogenase determines the reaction direction of 11β-hydroxysteroid dehydrogenase type 1 as an oxoreductase. *FEBS Letters*, *571*, 129–133. https://doi.org/10.1016/j.febslet.2004.06.065

Banhegyi, G., Benedetti, A., Fulceri, R., & Senesi, S. (2004). Cooperativity between 11β-hydroxysteroid dehydrogenase type 1 and hexose-

6-phosphate dehydrogenase in the lumen of the endoplasmic reticulum. *Journal of Biological Chemistry*, *279*, 27017–27021. https://doi.org/10.1074/jbc.M404159200

Bublitz, C., Lawler, C. A., & Steavenson, S. (1987). The topology of phosphogluconate dehydrogenases in rat liver microsomes. *Archives of Biochemistry and Biophysics*, *259*, 22–28. https://doi.org/10.1016/0003-9861(87)90465-6

Cheung, M., Bansal, S., Aw, M. M., Buchanan, C. R., Mieli-Vergani, G., & Dhawan, A. (2003). Liver failure in a neonate with congenital adrenal hyporesponsiveness. *European Journal of Pediatrics*, *162*, 558. https://doi.org/10.1007/s00431-003-1249-0

Courtney, R., Stewart, P. M., Toh, M., Ndongo, M. N., Calle, R. A., & Hirshberg, B. (2008). Modulation of 11β-hydroxysteroid dehydrogenase (11βHSD) activity biomarkers and pharmacokinetics of Pf-00915275, a selective 11βHSD1 inhibitor. *The Journal of Clinical Endocrinology and Metabolism*, *93*, 550–556. http://www.ncbi.nlm.nih.gov/entrez/query.fcgi?cmd=Retrieve&db=PubMed&dopt=Citation&list_uids=17986636, https://doi.org/10.1210/jc.2007-1912

Curtis, M. J., Alexander, S., Cirino, G., Docherty, J. R., George, G. H., Giembycz, M. A., … Ahluwali, A. (2018). Experimental design and analysis and their reporting II: updated and simplified guidance for authors and peer reviewers. *British Journal of Pharmacology*, *175*, 987–993. https://doi.org/10.1111/bph.14153

Feig, P. U., Shah, S., Hermanowski-Vosatka, A., Plotkin, D., Springer, M. S., Donahue, S., … Kaufman, K. D. (2011). Effects of an 11β-hydroxysteroid dehydrogenase type 1 inhibitor, MK-0916, in patients with type 2 diabetes mellitus and metabolic syndrome. *Diabetes, Obesity & Metabolism*, *13*, 498–504. https://doi.org/10.1111/j.1463-1326.2011.01375.x

Finnie, I. A., Campbell, B. J., Taylor, B. A., Milton, J. D., Sadek, S. K., Yu, L. G., & Rhodes, J. M. (1996). Stimulation of colonic mucin synthesis by corticosteroids and nicotine. *Clinical Science (London, England: 1979)*, *91*, 359–364. https://doi.org/10.1042/cs0910359

Freude, S., Heise, T., Woerle, H. J., Jungnik, A., Rauch, T., Hamilton, B., … Graefe-Mody, U. (2016). Safety, pharmacokinetics and pharmacodynamics of BI 135585, a selective 11β-hydroxysteroid dehydrogenase-1 (HSD1) inhibitor in humans: Liver and adipose tissue 11β-HSD1 inhibition after acute and multiple administrations over 2 weeks. *Diabetes, Obesity & Metabolism*, *18*, 483–490. https://doi.org/10.1111/dom.12635

Garcia-Canaveras, J. C., Donato, M. T., Castell, J. V., & Lahoz, A. (2012). Targeted profiling of circulating and hepatic bile acids in human, mouse, and rat using a UPLC-MRM-MS-validated method. *Journal of Lipid Research*, *53*, 2231–2241. https://doi.org/10.1194/jlr.D028803

Gathercole, L. L., Lavery, G. G., Morgan, S. A., Cooper, M. S., Sinclair, A. J., Tomlinson, J. W., & Stewart, P. M. (2013). 11β-Hydroxysteroid dehydrogenase 1: Translational and therapeutic aspects. *Endocrine Reviews*, *34*, 525–555. https://doi.org/10.1210/er.2012-1050

Hardy, R. S., Botfield, H., Markey, K., Mitchell, J. L., Alimajstorovic, Z., Westgate, C. S. J., … Sinclair, A. J. (2020). 11βHSD1 inhibition with AZD4017 improves lipid profiles and lean muscle mass in idiopathic intracranial hypertension. *Journal of Clinical Endocrinology and Metabolism*, *106*, 174–187. https://doi.org/10.1210/clinem/dgaa766

Hult, M., Jornvall, H., & Oppermann, U. C. (1998). Selective inhibition of human type 1 11β-Hydroxysteroid dehydrogenase by synthetic steroids and Xenobiotics. *FEBS Letters*, *441*, 25–28. https://doi.org/10.1016/s0014-5793(98)01515-4

Jamieson, A., Wallace, A. M., Andrew, R., Nunez, B. S., Walker, B. R., Fraser, R., … Connell, J. M. (1999). Apparent cortisone reductase deficiency: A functional defect in 11β-hydroxysteroid dehydrogenase type 1. *Journal of Clinical Endocrinology and Metabolism*, *84*, 3570–3574. https://doi.org/10.1210/jcem.84.10.6031

Johnson, J. S., Opiyo, M. N., Thomson, M., Gharbi, K., Seckl, J. R., Heger, A., & Chapman, K. E. (2017). 11β-Hydroxysteroid dehydrogenase-1 deficiency alters the gut microbiome response to Western diet. *Journal of Endocrinology*, *232*, 273–283. https://doi.org/10.1530/JOE-16-0578

Jolley, C. D., Dietschy, J. M., & Turley, S. D. (1999). Genetic differences in cholesterol absorption in 129/Sv and C57BL/6 mice: Effect on cholesterol responsiveness. *American Journal of Physiology*, *276*, G1117–G1124. https://doi.org/10.1152/ajpgi.1999.276.5.G1117

Lavery, G. G., Idkowiak, J., Sherlock, M., Bujalska, I., Ride, J. P., Saqib, K., … Stewart, P. M. (2013). Novel H6PDH mutations in two girls with premature adrenarche: 'Apparent' and 'true' CRD can be differentiated by urinary steroid profiling. *European Journal of Endocrinology of the European Federation of Endocrine Societies*, *168*, K19–K26. https://doi.org/10.1530/EJE-12-0628

Lavery, G. G., Walker, E. A., Draper, N., Jeyasuria, P., Marcos, J., Shackleton, C. H., … Stewart, P. M. (2006). Hexose-6-phosphate dehydrogenase knock-out mice lack 11 β-hydroxysteroid dehydrogenase type 1-mediated glucocorticoid generation. *Journal of Biological Chemistry*, *281*, 6546–6551. https://doi.org/10.1074/jbc.M512635200

Lavery, G. G., Zielinska, A. E., Gathercole, L. L., Hughes, B., Semjonous, N., Guest, P., … Stewart, P. M. (2012). Lack of significant metabolic abnormalities in mice with liver-specific disruption of 11β-hydroxysteroid dehydrogenase type 1. *Endocrinology*, *153*, 3236–3248. https://doi.org/10.1210/en.2012-1019

Lilley, E., Stanford, S. C., Kendall, D. E., Alexander, S. P., Cirino, G., Docherty, J. R., … Ahluwalia, A. (2020). ARRIVE 2.0 and the *British Journal of Pharmacology*: Updated guidance for 2020. *British Journal of Pharmacology*, *177*(16), 3611–3616. https://bpspubs.onlinelibrary.wiley.com/doi/full/10.1111/bph.15178

Marbet, P., Klusonova, P., Birk, J., Kratschmar, D. V., & Odermatt, A. (2018). Absence of hexose-6-phosphate dehydrogenase results in reduced overall glucose consumption but does not prevent 11β-hydroxysteroid dehydrogenase-1-dependent glucocorticoid activation. *The FEBS Journal*, *285*, 3993–4004. https://doi.org/10.1111/febs.14642

Markey, K. A., Ottridge, R., Mitchell, J. L., Rick, C., Woolley, R., Ives, N., … Sinclair, A. J. (2017). Assessing the efficacy and safety of an 11β-hydroxysteroid dehydrogenase type 1 inhibitor (AZD4017) in the idiopathic intracranial hypertension drug trial, IIH: DT: Clinical methods and design for a phase II randomized controlled trial. *JMIR Research Protocol*, *6*, e181. https://doi.org/10.2196/resprot.7806

Odermatt, A., Da Cunha, T., Penno, C. A., Chandsawangbhuwana, C., Reichert, C., Wolf, A., … Baker, M. E. (2011). Hepatic reduction of the secondary bile acid 7-oxolithocholic acid is mediated by 11β-hydroxysteroid dehydrogenase 1. *The Biochemical Journal*, *436*, 621–629. https://doi.org/10.1042/BJ20110022

Odermatt, A., & Klusonova, P. (2015). 11β-Hydroxysteroid dehydrogenase 1: Regeneration of active glucocorticoids is only part of the story. *Journal of Steroid Biochemistry and Molecular Biology*, *151*, 85–92. https://doi.org/10.1016/j.jsbmb.2014.08.011

Odermatt, A., & Kratschmar, D. V. (2012). Tissue-specific modulation of mineralocorticoid receptor function by 11β-hydroxysteroid dehydrogenases: An overview. *Molecular and Cellular Endocrinology*, *350*, 168–186. https://doi.org/10.1016/j.mce.2011.07.020

Papacleovoulou, G., Abu-Hayyeh, S., & Williamson, C. (2011). Nuclear receptor-driven alterations in bile acid and lipid metabolic pathways during gestation. *Biochimica et Biophysica Acta*, *1812*, 879–887. https://doi.org/10.1016/j.bbadis.2010.11.001

Penno, C. A., Arsenijevic, D., Da Cunha, T., Kullak-Ublick, G. A., Montani, J.-P., & Odermatt, A. (2013). Quantification of multiple bile acids in uninephrectomized rats using ultra-performance liquid chromatography-tandem mass spectrometry. *Analytical Methods*, *5*, 1155–1164. https://doi.org/10.1039/c3ay26520j

Penno, C. A., Morgan, S. A., Rose, A. J., Herzig, S., Lavery, G. G., & Odermatt, A. (2014). 11β-Hydroxysteroid dehydrogenase-1 is involved

in bile acid homeostasis by modulating fatty acid transport protein-5 in the liver of mice. *Molecular Metabolism*, *3*, 554–564. https://doi.org/10.1016/j.molmet.2014.04.008

Penno, C. A., Morgan, S. A., Vuorinen, A., Schuster, D., Lavery, G. G., & Odermatt, A. (2013). Impaired oxidoreduction by 11β-hydroxysteroid dehydrogenase 1 results in the accumulation of 7-oxolithocholic acid. *Journal of Lipid Research*, *54*, 2874–2883. https://doi.org/10.1194/jlr.M042499

Percie du Sert, N., Hurst, V., Ahluwalia, A., Alam, S., Avey, M. T., Baker, M., … Würbel, H. (2020). The ARRIVE guidelines 2.0: Updated guidelines for reporting animal research. *PLoS Biology*, *18*(7), e3000410. https://doi.org/10.1371/journal.pbio.3000410

Quax, R. A., Manenschijn, L., Koper, J. W., Hazes, J. M., Lamberts, S. W., van Rossum, E. F., & Feelders, R. A. (2013). Glucocorticoid sensitivity in health and disease. *Nature Reviews. Endocrinology*, *9*, 670–686. https://doi.org/10.1038/nrendo.2013.183

Quinkler, M., & Stewart, P. M. (2003). Hypertension and the cortisol-cortisone shuttle. *Journal of Clinical Endocrinology and Metabolism*, *88*, 2384–2392. https://doi.org/10.1210/jc.2003-030138

Rausch, P., Basic, M., Batra, A., Bischoff, S. C., Blaut, M., Clavel, T., … Baines, J. F. (2016). Analysis of factors contributing to variation in the C57BL/6J fecal microbiota across German animal facilities. *International Journal of Medical Microbiology*, *306*, 343–355. https://doi.org/10.1016/j.ijmm.2016.03.004

Rogoff, D., Black, K., McMillan, D. R., & White, P. C. (2010). Contribution of hexose-6-phosphate dehydrogenase to NADPH content and redox environment in the endoplasmic reticulum. *Redox Report*, *15*, 64–70. https://doi.org/10.1179/174329210X12650506623249

Rosenstock, J., Banarer, S., Fonseca, V. A., Inzucchi, S. E., Sun, W., Yao, W., … Huber, R. (2010). The 11-β-hydroxysteroid dehydrogenase type 1 inhibitor INCB13739 improves hyperglycemia in patients with type 2 diabetes inadequately controlled by metformin monotherapy. *Diabetes Care*, *33*, 1516–1522. https://doi.org/10.2337/dc09-2315

Schmittgen, T. D., & Livak, K. J. (2008). Analyzing real-time PCR data by the comparative C_T method. *Nature Protocols*, *3*, 1101–1108. https://www.ncbi.nlm.nih.gov/pubmed/18546601, https://doi.org/10.1038/nprot.2008.73

Schwab, D., Sturm, C., Portron, A., Fuerst-Recktenwald, S., Hainzl, D., Jordan, P., … DuBiner, H. (2017). Oral administration of the 11β-hydroxysteroid-dehydrogenase type 1 inhibitor RO5093151 to patients with glaucoma: An adaptive, randomised, placebo-controlled clinical study. *BMJ Open Ophthalmol*, *1*, e000063. https://doi.org/10.1136/bmjophth-2016-000063

Scott, J. S., Goldberg, F. W., & Turnbull, A. V. (2014). Medicinal chemistry of inhibitors of 11β-hydroxysteroid dehydrogenase type 1 (11β-HSD1). *Journal of Medicinal Chemistry*, *57*, 4466–4486. https://doi.org/10.1021/jm4014746

Semjonous, N. M., Sherlock, M., Jeyasuria, P., Parker, K. L., Walker, E. A., Stewart, P. M., & Lavery, G. G. (2011). Hexose-6-phosphate dehydrogenase contributes to skeletal muscle homeostasis independent of 11β-hydroxysteroid dehydrogenase type 1. *Endocrinology*, *152*, 93–102. https://doi.org/10.1210/en.2010-0957

Stewart, P. M., Wallace, A. M., Atherden, S. M., Shearing, C. H., & Edwards, C. R. (1990). Mineralocorticoid activity of carbenoxolone: Contrasting effects of carbenoxolone and liquorice on 11β-hydroxysteroid dehydrogenase activity in man. *Clinical Science (London, England : 1979)*, *78*, 49–54. https://doi.org/10.1042/cs0780049

Strajhar, P., Schmid, Y., Liakoni, E., Dolder, P. C., Rentsch, K. M., Kratschmar, D. V., … Liechti, M. E. (2016). Acute effects of lysergic acid diethylamide on circulating steroid levels in healthy subjects. *Journal of Neuroendocrinology*, *28*(3), 12374–12386. https://doi.org/10.1111/jne.12374

Takahashi, S., Fukami, T., Masuo, Y., Brocker, C. N., Xie, C., Krausz, K. W., … Gonzalez, F. J. (2016). Cyp2c70 is responsible for the species difference in bile acid metabolism between mice and humans. *Journal of Lipid Research*, *57*, 2130–2137. https://doi.org/10.1194/jlr.M071183

Terao, M., & Katayama, I. (2016). Local cortisol/corticosterone activation in skin physiology and pathology. *Journal of Dermatological Science*, *84*, 11–16. https://doi.org/10.1016/j.jdermsci.2016.06.014

Tiganescu, A., Hupe, M., Uchida, Y., Mauro, T., Elias, P. M., & Holleran, W. M. (2018). Topical 11β-hydroxysteroid dehydrogenase type 1 inhibition corrects cutaneous features of systemic glucocorticoid excess in female mice. *Endocrinology*, *159*, 547–556. https://doi.org/10.1210/en.2017-00607

Ulick, S., Levine, L. S., Gunczler, P., Zanconato, G., Ramirez, L. C., Rauh, W., … New, M. I. (1979). A syndrome of apparent mineralocorticoid excess associated with defects in the peripheral metabolism of cortisol. *Journal of Clinical Endocrinology and Metabolism*, *49*, 757–764. https://doi.org/10.1210/jcem-49-5-757

Ulick, S., Tedde, R., & Mantero, F. (1990). Pathogenesis of the type 2 variant of the syndrome of apparent mineralocorticoid excess. *Journal of Clinical Endocrinology and Metabolism*, *70*, 200–206. https://doi.org/10.1210/jcem-70-1-200

Webster, S. P., McBride, A., Binnie, M., Sooy, K., Seckl, J. R., Andrew, R., … Walker, B. R. (2017). Selection and early clinical evaluation of the brain-penetrant 11β-hydroxysteroid dehydrogenase type 1 (11β-HSD1) inhibitor UE2343 (Xanamem). *British Journal of Pharmacology*, *174*, 396–408. https://doi.org/10.1111/bph.13699

Wyrwoll, C. S., Holmes, M. C., & Seckl, J. R. (2011). 11β-Hydroxysteroid dehydrogenases and the brain: From zero to hero, a decade of progress. *Frontiers in Neuroendocrinology*, *32*, 265–286. https://doi.org/10.1016/j.yfrne.2010.12.001

Ye, X. Y., Chen, S. Y., Wu, S., Yoon, D. S., Wang, H., Hong, Z., … Robl, J. A. (2017). Discovery of clinical candidate 2-((2*S*,6*S*)-2-phenyl-6-hydroxyadamantan-2-yl)-1-(3′-hydroxyazetidin-1-yl)ethanone [BMS-816336], an orally active novel selective 11β-hydroxysteroid dehydrogenase type 1 inhibitor. *Journal of Medicinal Chemistry*, *60*, 4932–4948. https://doi.org/10.1021/acs.jmedchem.7b00211

SUPPORTING INFORMATION

Additional supporting information may be found online in the Supporting Information section at the end of this article.

How to cite this article: Weingartner M, Stücheli S, Kratschmar DV, et al. The ratio of ursodeoxycholyltaurine to 7-oxolithocholyltaurine serves as a biomarker of decreased 11β-hydroxysteroid dehydrogenase 1 activity in mouse. *Br J Pharmacol*. 2021;178:3309–3326. https://doi.org/10.1111/bph.15367

6.3 Development and Validation of a Highly Sensitive LC-MS/MS Method for the Analysis of Bile Acids in Serum, Plasma, and Liver Tissue Samples

Published Article

Cristina Gómez, Simon Stücheli, Denise V. Kratschmar, Jamal Bouitbir, and Alex Odermatt

Division of Molecular and Systems Toxicology, Department of Pharmaceutical Sciences, University of Basel, Basel, Switzerland.

Contribution to the project:

Experimental work

Figure generation

Revising the manuscript

metabolites

MDPI

Article

Development and Validation of a Highly Sensitive LC-MS/MS Method for the Analysis of Bile Acids in Serum, Plasma, and Liver Tissue Samples

Cristina Gómez, Simon Stücheli, Denise V. Kratschmar, Jamal Bouitbir and Alex Odermatt *

Division of Molecular and Systems Toxicology, Department of Pharmaceutical Sciences, University of Basel, Klingelbergstrasse 50, 4056 Basel, Switzerland; cristina.gomezcastella@unibas.ch (C.G.); simon.stuecheli@unibas.ch (S.S.); denise.kratschmar@unibas.ch (D.V.K.); jamal.bouitbir@unibas.ch (J.B.)
* Correspondence: alex.odermatt@unibas.ch

Received: 22 June 2020; Accepted: 7 July 2020; Published: 9 July 2020

Abstract: Bile acids control lipid homeostasis by regulating uptake from food and excretion. Additionally, bile acids are bioactive molecules acting through receptors and modulating various physiological processes. Impaired bile acid homeostasis is associated with several diseases and drug-induced liver injury. Individual bile acids may serve as disease and drug toxicity biomarkers, with a great demand for improved bile acid quantification methods. We developed, optimized, and validated an LC-MS/MS method for quantification of 36 bile acids in serum, plasma, and liver tissue samples. The simultaneous quantification of important free and taurine- and glycine-conjugated bile acids of human and rodent species has been achieved using a simple workflow. The method was applied to a mouse model of statin-induced myotoxicity to assess a possible role of bile acids. Treatment of mice for three weeks with 5, 10, and 25 mg/kg/d simvastatin, causing adverse skeletal muscle effects, did not alter plasma and liver tissue bile acid profiles, indicating that bile acids are not involved in statin-induced myotoxicity. In conclusion, the established LC-MS/MS method enables uncomplicated sample preparation and quantification of key bile acids in serum, plasma, and liver tissue of human and rodent species to facilitate future studies of disease mechanisms and drug-induced liver injury.

Keywords: bile acid; LC-MS; statin myotoxicity; biomarker; adverse drug effect; disease

1. Introduction

Bile acids are important for the digestion and absorption of lipids and fat-soluble vitamins in the intestine but also for the regulation of cholesterol homeostasis in the liver. Besides, they are bioactive molecules signaling through receptors such as farnesoid X receptor, pregnane X receptor, vitamin D receptor, sphingosine-1-phosphate receptor 2, and G protein-coupled bile acid receptor 1 in order to modulate lipid and glucose homeostasis, with relevance to cardio-metabolic disease and cancer [1,2]. Several individual bile acids are considered biomarkers of disease or drug-induced liver injury (DILI) [3–5] and improved quantification methods are therefore needed.

Bile acids are steroidal C24 carboxylic acids, synthesized in the liver from cholesterol. In humans, the two primary bile acids cholic acid (CA) and chenodeoxycholic acid (CDCA) are synthesized in hepatocytes by the classical and alternative pathway, respectively [6,7] (Figure 1). In rats and mice, the primary bile acids consist mainly of CA and the muricholic acid (MCA) metabolites αMCA and βMCA that are derived by cytochrome P450 (CYP) 2C70 from CDCA and ursodeoxycholic acid (UDCA), respectively [8]. In guinea pigs, 7-oxolithocholic acid (7oxoLCA) is a major primary bile acid, in contrast to human, rat, and mouse where it is a secondary bile acid and only found at low levels under

healthy conditions [9]. The newly synthesized bile acids are conjugated on the side chain to mainly glycine in humans and taurine in rodents, and to a lesser extent on the steroid nucleus to sulfate and glucuronide, followed by excretion mainly through the bile [6,7]. In the intestine, the primary bile acids undergo modifications by intestinal bacteria through deconjugation, dihydroxylation, epimerization, and oxidation, resulting in secondary bile acids including lithocholic acid (LCA), deoxycholic acid (DCA), and their 7-oxo forms, as well as UDCA [10,11]. Secondary bile acids also undergo conjugation to taurine and glycine in the liver and intestine. Due to the function of the steroid 5β-reductase (aldo–keto reductase (AKR)1D1) all major bile acids are 5β-reduced. However, some bile acids escape AKR1D1 metabolism, leading to allo-bile acids with a α- rather than β-oriented hydrogen at C5 [10,12].

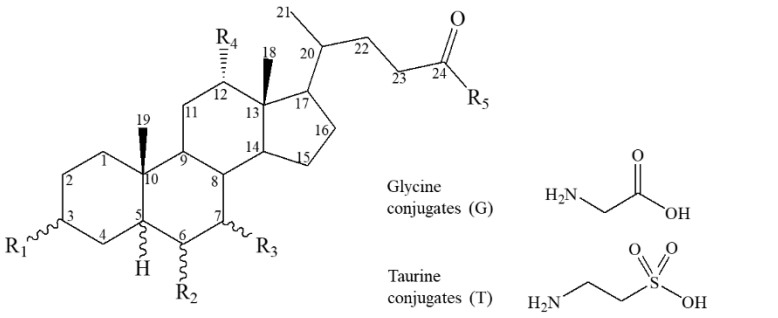

Compound	Abbreviation	R_1	R_2	R_3	R_4	R_5	C5	Conjugates (R_5)	
Cholic acid	CA	α-OH	H	α-OH	OH	OH	β-H	TCA	GCA
α-muricholic acid	αMCA	α-OH	β-OH	α-OH	H	OH	β-H	TαMCA	-
β-muricholic acid	βMCA	α-OH	β-OH	β-OH	H	OH	β-H	TβMCA	-
ω-muricholic acid	ωMCA	α-OH	α-OH	β-OH	H	OH	β-H	TωMCA	-
γ-muricholic acid	γMCA	α-OH	α-OH	α-OH	H	OH	β-H	-	-
Ursodeoxycholic acid	UDCA	α-OH	H	β-OH	H	OH	β-H	TUDCA	GUDCA
Hyodeoxycholic acid	HDCA	α-OH	α-OH	H	H	OH	β-H	-	-
Chenodeoxycholic acid	CDCA	α-OH	H	α-OH	H	OH	β-H	TCDCA	GCDCA
Deoxycholic acid	DCA	α-OH	H	H	OH	OH	β-H	TDCA	GDCA
Lithocholic acid	LCA	α-OH	H	H	H	OH	β-H	TLCA	GLCA
3-oxo-lithocholic acid	3oxoLCA	O	H	H	H	OH	β-H	-	-
6,7-dioxo-lithocholic acid	6,7dioxoLCA	α-OH	O	O	H	OH	β-H	-	-
7-oxo-deoxycholic acid	7oxoDCA	α-OH	H	O	OH	OH	β-H	-	-
7-oxo-lithocholic acid	7oxoLCA	α-OH	H	O	H	OH	β-H	T7oxoLCA	G7oxoLCA
12-oxo-lithocholic acid	12oxoLCA	α-OH	H	H	O	OH	β-H	-	-
Allo-cholic acid	Allo-CA	α-OH	H	α-OH	OH	OH	α-H	-	-
Allo-deoxycholic acid	Allo-DCA	α-OH	H	H	OH	OH	α-H	-	-
Allo-lithocholic acid	Allo-LCA	α-OH	H	H	H	OH	α-H	-	-
Allo-3β-deoxycholic acid	Allo-3βDCA	β-OH	H	H	OH	OH	α-H	-	-
Allo-3β-lithocholic acid	Allo-3βLCA	β-OH	H	H	H	OH	α-H	-	-
Allo-12β-deoxycholic acid	Allo-12βDCA	α-OH	H	H	β-OH	OH	α-H	-	-

Figure 1. Chemical structures of bile acids included in the LC-MS/MS method.

An efficient bile acid transport by hepatocytes and terminal ileal enterocytes mediates recycling of bile acids by the enterohepatic circulation [13,14]. This is a highly efficient process and only about 5% of total bile acids are lost via excretion through the feces. The excreted amount is replenished by de novo synthesis to preserve a constant bile acid pool [15]. Disruption of bile acid transport, for example by inhibition of hepatic mitochondrial function of bile acid export proteins such as a bile salt export pump (BSEP), can cause cholestasis with accumulation of bile acids in hepatocytes and then provoke liver injury due to their detergent-like effects [16,17]. Cholestasis also results in increased circulating bile acid levels with distinct alterations in individual bile acid metabolites [2,5,18,19].

An increase in circulating total bile acids is an accepted biomarker of hepatobiliary impairment and disease [17,20]. However, the hydrophobic LCA and DCA are considered the most cytotoxic bile acids [17], and their accumulation causes impairments in hepatocytes such as mitochondrial dysfunction, oxidative stress, endoplasmic reticulum stress, and damage and disruption of cell membranes leading to apoptosis and necrosis [20,21]. A recent study observed that the ratio of taurine- and glycine-conjugated CA and CDCA over their free forms were better predictors of DILI due to inhibited mitochondrial function and BSEP transport than total bile acids [22]. Thus, the measurement of individual bile acids can provide important mechanistic understanding. Bile acids can also serve as functional biomarkers providing information on deficiencies of specific enzymes involved in the metabolism of bile acids [23–26]. The development and validation of methods for targeted quantification of bile acids are essential to understand their mechanisms of action in vivo. Moreover, the diagnosis of rare diseases related to cholesterol biosynthesis and metabolism as well as for the detection of DILI can be accomplished by the determination of bile acid profiles in body fluids.

Over the last decade, several methods using different platforms, including liquid chromatography-tandem mass spectrometry (LC-MS/MS) based methods, have been reported for bile acid separation, detection, and quantification [27–36]. The simultaneous analysis of bile acids in biological samples such as serum, plasma, and liver biopsies is challenging because of their structural similarities and limits of detection. Most of the developed methods exert some disadvantages, mainly caused by a series of laborious sample preparation steps, limited sensitivity of detection, or a lack of specificity due to insufficient chromatographic baseline separation of isobaric bile acids. Accordingly, highly sensitive and specific methods to quantify bile acids in biological samples are needed.

The present study aimed to develop and validate a highly sensitive and specific method for the rapid and simultaneous quantification of a number of bile acids by LC-MS/MS. Compared to previously reported methods, the first goal was to achieve an improvement of the method in terms of simplicity, metabolic coverage by including free and conjugated metabolites, and applicability for different matrices and species. A second goal included the validation of the method using real samples. For this purpose, the developed method was applied to quantify bile acid profiles in plasma and liver tissue samples from mice treated for three weeks with increasing doses of the 3-hydroxy-3-methylglutaryl coenzyme A (HMG-CoA) reductase inhibitor simvastatin. Although statins are in general well tolerated in patients, they can lead mainly to skeletal muscle side effects. The clinical manifestations start from myalgia, myopathy to potentially fatal rhabdomyolysis in rare cases [37,38]. These adverse skeletal muscle effects were observed at the doses used in this study [39–41]. Therefore, we assessed whether inhibition of *de novo* cholesterol formation [38,42] and the production of intermediates of cholesterol synthesis such as ubiquinone (CoQ10) and dolichols [38] by simvastatin might disrupt bile acid homeostasis and contribute to myotoxicity.

2. Results and Discussion

2.1. Establishment of the LC-MS/MS Method for Quantification of Bile Acids

The present study employed LC-MS/MS for the direct detection and quantification of 36 different free, taurine- and glycine-conjugated bile acids in serum, plasma, and liver tissue. These analytes include important bile acids of human (free and mainly glycine-conjugated) and rodents (free and mainly taurine-conjugated) but also some additional bile acids found in guinea-pig (7oxoLCA and its conjugated forms) and such being relevant with regard to activities of specific enzymes (7oxoLCA, allo-bile acids, and their conjugated forms) [9–12]. In order to select the best transitions for the identification and confirmation of each bile acid included in the method, individual working standard solutions were applied to the optimizer compound software. The best collision energy was obtained for each multiple reaction monitoring (MRM) transition. Both positive and negative ionization modes were carried out. For each bile acid, the transition with the highest sensitivity was chosen as a quantifier (Table 1) and at least one other transition was selected as a qualifier for each compound. LC gradient elution pattern was optimized in order to achieve baseline separation for all compounds. Different column temperatures and flow rates were tested and the parameters resulting in better separation were selected (see section LC-MS/MS instrumental conditions). Retention times are listed in Table 1. MS parameters such as desolvation gas flow, sheath gas flow, nebulizer pressure, capillary voltage, and nozzle voltage were chosen using the optimizer software of the instrument. Optimal parameters are described in the materials and methods section.

The current method contains multiple improvements compared to previously published methods [27–35]. One of the main advantages is the incremented metabolic coverage including free and conjugated bile acids, as well as allo-bile acids and 7-oxo metabolites [27–29,31,32,34,35]. A better baseline chromatographic separation of the isobaric metabolites was achieved [23,29–31,33,35]. Furthermore, lower values for limit of detection (LOD) and limit of quantification (LOQ) were observed for most of the metabolites analyzed in the present study (Tables 1 and 2) [28,31,34,35], despite using a lower injection volume into the LC-MS/MS system [27,28,30,31,33–35]. The amount of sample material required was lower compared to similar reported methods [27,28,30–35], which represents a great advantage for studies using rodent models where usually limited sample volume is available.

Table 1. Method characteristics and validation parameters for the quantification of bile acids in serum and plasma by LC-MS/MS. Abbreviations: CE: collision energy; RT: retention time; R2: linearity; LOD: limit of detection; LOQ: limit of quantitation; LC: low concentration; MC: medium concentration; HC: high concentration, ND: not detected.

Compound	Abbreviation	Transition	ESI	CE (V)	RT (min)	r2	LOD (ng/mL)	LOQ (ng/mL)	Plasma Extraction Recovery			Stability at 4 °C *	
									LC (*n* = 6)	MC (*n* = 6)	HC (*n* = 6)	Plasma Calibration Curve (%)	Plasma Sample (%)
Cholic Acid	CA	373.3 > 355.2	+	8	9.81	0.999	0.45	1.36	111 ± 4	78 ± 6	83 ± 6	2.3	2.7
Chenodeoxycholic acid	CDCA	357.2 > 104.9	+	50	13.76	0.997	0.03	0.09	104 ± 7	81 ± 5	80 ± 6	0.3	0.5
ω-muricholic acid	ωMCA	373.3 > 159.1	+	20	6.29	0.999	0.01	0.02	113 ± 12	77 ± 6	85 ± 7	0.7	0.1
α-muricholic acid	αMCA	373.3 > 355.2	+	15	6.50	0.992	0.17	0.52	98 ± 11	76 ± 5	86 ± 10	1.1	2
β-muricholic acid	βMCA	391.3 > 355.2	+	16	6.85	0.997	0.10	0.30	94 ± 15	75 ± 4	83 ± 6	0.4	1.9
γ-muricholic acid	γMCA	373.3 > 355	+	10	8.14	0.991	0.29	0.86	87 ± 3	79 ± 6	85 ± 6	0.3	ND
Ursodeoxycholic acid	UDCA	357.2 > 95	+	35	9.92	0.997	0.04	0.12	94 ± 11	86 ± 4	86 ± 5	0.5	ND
Hyodeoxycholic acid	HDCA	357.2 > 95.1	+	40	10.34	0.994	0.41	1.23	85 ± 22	84 ± 4	88 ± 5	0.1	3.5
Deoxycholic acid	DCA	391.3 > 345	-	36	14.14	0.991	0.11	0.33	135 ± 9	80 ± 5	84 ± 5	1.2	3.9
Lithocholic acid	LCA	359.3 > 135.1	+	24	17.19	0.997	0.48	1.46	<LOD	66 ± 6	82 ± 5	1.2	ND
3-oxo-lithocholic acid	3oxoLCA	357.3 > 80.9	+	48	17.43	0.992	0.67	2.02	<LOD	82 ± 5	85 ± 7	3	ND
7-oxolithocholic acid	7oxoLCA	373.3 > 355.1	+	35	11.80	0.995	0.82	2.49	75 ± 15	72 ± 4	83 ± 6	1.4	ND
6,7-dioxo-lithocholic acid	6,7dioxoLCA	405.3 > 351.1	+	32	11.71	0.998	0.08	0.24	<LOD	1 ± 0.3	1 ± 0.2	0.7	ND
12-oxo-lithocholic acid	12oxoLCA	391.3 > 145.1	+	12	12.25	0.998	0.68	2.07	112 ± 13	68 ± 4	81 ± 5	2.5	0.4
7-oxo-deoxycholic acid	7oxoDCA	371.3 > 353.2	+	8	6.81	0.990	0.44	1.34	111 ± 15	83 ± 7	85 ± 8	2.3	2.6
Allo-cholic acid	Allo-CA	373.3 > 355.2	+	12	9.44	0.998	0.06	0.19	90 ± 9	77 ± 5	83 ± 6	0.3	1.7
Allo-deoxycholic acid	Allo-DCA	391.3 > 345	-	36	13.91	0.990	0.14	0.41	100 ± 12	64 ± 6	87 ± 6	0.7	5.9
Allo-3β-deoxycholic acid	Allo-3βDCA	391.3 > 345.1	-	40	10.10	0.992	0.51	1.53	86 ± 7	81 ± 5	83 ± 6	0.7	2.9
Allo-12β-deoxycholic acid	Allo-12βDCA	391.3 > 345.1	-	36	11.94	0.994	0.09	0.28	<LOD	80 ± 7	90 ± 6	0.2	ND
Allo-3β-lithocholic acid	Allo-3βLCA	359.3 > 135.1	+	25	15.56	0.987	0.75	2.26	<LOD	54 ± 5	82 ± 4	1.6	ND
Allo-lithocholic acid	Allo-LCA	359.3 > 135.1	+	25	17.08	0.995	0.45	1.37	<LOD	87 ± 4	91 ± 7	3.5	ND
Tauro-cholic acid	TCA	480.3 > 461.9	+	8	5.45	0.999	0.12	0.38	136 ± 15	82 ± 5	83 ± 5	0.3	2.4
Tauro-chenodeoxycholic acid	TCDCA	464.2 > 126	+	28	7.91	0.998	0.05	0.14	109 ± 8	80 ± 5	80 ± 6	0.1	2.4
Tauro-ω-muricholic acid	TωMCA	480.3 > 126	+	24	2.82	0.996	0.06	0.17	128 ± 21	77 ± 5	82 ± 5	0.1	2.7

Table 1. *Cont.*

Compound	Abbreviation	Transition	ESI	CE (V)	RT (min)	r2	LOD (ng/mL)	LOQ (ng/mL)	Plasma Extraction Recovery			Stability at 4 °C *	
									LC (n = 6)	MC (n = 6)	HC (n = 6)	Plasma Calibration Curve (%)	Plasma Sample (%)
Tauro-α-muricholic acid	TαMCA	480.3 > 126	+	24	3.07	0.996	0.06	0.17	129 ± 15	79 ± 6	81 ± 5	0.5	2.6
Tauro-β-muricholic acid	TβMCA	480.3> 126	+	24	3.30	0.998	0.04	0.11	131 ± 16	77 ± 4	78 ± 6	0.4	0.8
Tauro-ursodeoxycholic acid	TUDCA	464.2 > 126	+	28	5.20	0.995	0.03	0.10	105 ± 15	80 ± 5	83 ± 6	0.1	0.1
Tauro-deoxycholic acid	TDCA	498.2 > 124.2	-	45	8.79	0.995	0.05	0.14	117 ± 3	80 ± 8	85 ± 3	0.4	0.8
Tauro-7-oxolithocholic acid	T7oxoLCA	480.3 > 126	+	24	5.84	0.996	0.05	0.15	89 ± 5	78 ± 4	83 ± 6	0.5	ND
Tauro-lithocholic acid	TLCA	482.2 > 80	-	56	13.11	0.995	0.08	0.25	107 ± 5	70 ± 5	82 ± 5	0.9	ND
Glyco-cholic acid	GCA	464.4 >74	-	37	6.63	0.998	0.02	0.05	85 ± 5	81 ± 5	84 ± 6	0.4	2.8
Glyco-chenodeoxycholic acid	GCDCA	448.2 > 74	-	30	10.58	0.994	0.02	0.08	98 ± 5	82 ± 5	86 ± 6	0.8	0.5
Glyco-ursodeoxycholic acid	GUDCA	448.2 > 74	-	37	6.43	0.998	0.02	0.06	99 ± 12	80 ± 4	85 ± 6	0.3	3.4
Glyco-deoxycholic acid	GDCA	448.2 > 74	-	30	11.43	0.998	0.011	0.033	97 ± 9	81 ± 4	87 ± 6	0.4	ND
Glyco-lithocholic acid	GLCA	432.2 > 74	-	41	14.59	0.995	1.18	3.58	103 ± 13	70 ± 4	78 ± 5	0.1	ND
Glyco-7-oxo-lithocholic acid	G7oxoLCA	446.2 > 74	-	37	7.63	0.998	0.05	0.16	84 ± 12	79 ± 5	83 ± 6	1.7	ND

* Percentage of variation from the first to the second injection after one week at 4 °C.

Table 2. Method characteristics and validation parameters for the quantification bile acids in liver tissue by LC-MS/MS. Abbreviations: CE: collision energy; RT: retention time; R2: linearity; LOD: limit of detection; LOQ: limit of quantitation; LC: low concentration; MC: medium concentration; HC: high concentration, ND: not detected.

Compound	Abbreviation	Transition	ESI	CE (V)	RT (min)	r2	LOD (ng/mL)	LOQ (ng/mL)	Liver Extraction Recovery			Stability at 4 °C *	
									LC (n = 6)	MC (n = 6)	HC (n = 6)	Liver Calibration Curve (%)	Liver Sample (%)
Cholic Acid	CA	373.3 > 355.2	+	8	9.81	0.999	0.60	1.81	103 ± 3	93 ± 4	104 ± 9	0.3	3.6
Chenodeoxycholic acid	CDCA	357.2 > 104.9	+	50	13.76	0.991	1.46	4.41	<LOD	84 ± 8	97 ± 5	0.5	0.4
ω-muricholic acid	ωMCA	373.3 > 159.1	+	20	6.29	0.998	0.06	0.18	105 ± 6	83 ± 5	101 ± 5	0.8	3.3
α-muricholic acid	αMCA	373.3 > 355.2	+	15	6.50	0.999	0.04	0.13	95 ± 10	87 ± 4	98 ± 3	0.5	2.3
β-muricholic acid	βMCA	391.3 > 355.2	+	16	6.85	0.994	0.32	0.97	101 ± 9	85 ± 5	103 ± 7	0	3.6
γ-muricholic acid	γMCA	373.3 > 355	+	10	8.14	0.997	0.58	1.76	87 ± 6	93 ± 4	96 ± 4	0.2	ND
Ursodeoxycholic acid	UDCA	357.2 > 95	+	35	9.92	0.995	0.10	0.30	<LOD	94 ± 10	105 ± 9	3.1	6.2
Hyodeoxycholic acid	HDCA	357.2 > 95.1	+	40	10.34	0.998	0.58	1.74	<LOD	92 ± 6	95 ± 6	0.5	2.6
Deoxycholic acid	DCA	391.3 > 345	-	36	14.14	0.996	0.64	1.94	88 ± 14	80 ± 6	96 ± 9	0.1	1.5
Lithocholic acid	LCA	359.3 > 135.1	+	24	17.19	0.979	1.20	3.64	<LOD	83 ± 5	105 ± 5	0.4	ND
3-oxo-lithocholic acid	3oxoLCA	357.3 > 80.9	+	48	17.43	0.994	0.70	2.13	<LOD	89 ± 26	104 ± 10	0.5	ND
7-oxolithocholic acid	7oxoLCA	373.3 > 355.1	+	35	11.80	0.998	1.07	3.26	<LOD	96 ± 4	106 ± 11	0.7	ND
12-oxo-lithocholic acid	12oxoLCA	391.3 > 145.1	+	32	12.25	0.999	2.55	7.72	99 ± 10	89 ± 4	99 ± 9	0.9	0.1
6,7-dioxo-lithocholic acid	6,7dioxoLCA	405.3 > 351.1	+	12	11.71	0.999	6.19	18.76	100 ± 10	86 ± 4	103 ± 9	3.1	ND
7-oxo-deoxycholic acid	7oxoDCA	371.3 > 353.2	+	8	6.81	0.995	0.038	0.115	92 ± 6	95 ± 10	116 ± 9	1	1.8
Allo-cholic acid	Allo-CA	373.3 > 355.2	+	12	9.44	0.998	0.14	0.41	88 ± 4	95 ± 4	105 ± 7	1.8	0.7
Allo-deoxycholic acid	Allo-DCA	391.3 > 345	-	36	13.91	0.995	0.41	1.23	93 ± 7	93 ± 5	90 ± 6	0.9	ND
Allo-3β-deoxycholic acid	Allo-3βDCA	391.3 > 345.1	-	40	10.10	0.999	0.36	1.08	92 ± 6	89 ± 4	97 ± 7	0.1	ND
Allo-12β-deoxycholic acid	Allo-12βDCA	391.3 > 345.1	-	36	11.94	0.991	0.03	0.10	<LOD	99 ± 15	97 ± 9	0.6	ND
Allo-3β-lithocholic acid	Allo-3βLCA	359.3 > 135.1	+	25	15.56	0.995	0.45	1.36	<LOD	104 ± 3	98 ± 4	1.3	2.4
Allo-lithocholic acid	Allo-LCA	359.3 > 135.1	+	25	17.08	0.997	0.17	0.52	<LOD	91 ± 10	84 ± 8	2.4	ND
Tauro-cholic acid	TCA	480.3 > 461.9	+	8	5.45	0.998	0.30	0.89	137 ± 10	88 ± 5	96 ± 5	0.5	3.9
Tauro-chenodeoxycholic acid	TCDCA	464.2 > 126	+	28	7.91	0.992	0.52	1.56	103 ± 15	84 ± 5	108 ± 7	0.6	0.3
Tauro-ω-muricholic acid	TωMCA	480.3 > 126	+	24	2.82	0.998	0.149	0.452	143 ± 17	95 ± 6	108 ± 5	0.6	0.9

Table 2. *Cont.*

Compound	Abbreviation	Transition	ESI	CE (V)	RT (min)	r2	LOD (ng/mL)	LOQ (ng/mL)	Liver Extraction Recovery			Stability at 4 °C *	
									LC (*n* = 6)	MC (*n* = 6)	HC (*n* = 6)	Liver Calibration Curve (%)	Liver Sample (%)
Tauro-α-muricholic acid	TαMCA	480.3 > 126	+	24	3.07	0.999	0.10	0.30	127 ± 8	94 ± 6	106 ± 4	1	1.9
Tauro-β-muricholic acid	TβMCA	480.3> 126	+	24	3.30	0.999	0.09	0.27	189 ± 29	91 ± 7	108 ± 7	0	0.6
Tauro-ursodeoxycholic acid	TUDCA	464.2 > 126	+	28	5.20	0.993	0.45	1.35	104 ± 10	92 ± 6	101 ± 10	0.2	1.5
Tauro-deoxycholic acid	TDCA	498.2 > 124.2	-	45	8.79	0.991	0.82	2.48	78 ± 10	95 ± 8	107 ± 8	0.8	3.5
Tauro-7-oxolithocholic acid	T7oxoLCA	480.3 > 126	+	24	5.84	0.998	0.18	0.55	98 ± 6	87 ± 6	105 ± 5	0.2	4.5
Tauro-lithocholic acid	TLCA	482.2 > 80	-	56	13.11	0.986	7.21	21.86	99 ± 9	93 ± 6	91 ± 5	0.2	1.2
Glyco-cholic acid	GCA	464.4 >74	-	37	6.63	0.997	0.11	0.34	103 ± 3	90 ± 4	103 ± 3	0.5	1.4
Glyco-chenodeoxycholic acid	GCDCA	448.2 > 74	-	30	10.58	0.996	0.05	0.16	100 ± 2	93 ± 3	99 ± 6	2.4	1
Glyco-ursodeoxycholic acid	GUDCA	448.2 > 74	-	37	6.43	0.999	0.03	0.09	102 ± 6	91 ± 7	103 ± 6	2.7	1.2
Glyco-deoxycholic acid	GDCA	448.2 > 74	-	30	11.43	0.993	0.057	0.172	95 ± 3	89 ± 6	101 ± 4	0.5	ND
Glyco-lithocholic acid	GLCA	432.2 > 74	-	41	14.59	0.992	0.13	0.40	87 ± 5	94 ± 5	93 ± 5	3	ND
Glyco-7-oxo-lithocholic acid	G7oxoLCA	446.2 > 74	-	37	7.63	0.999	0.06	0.19	88 ± 4	91 ± 4	96 ± 3	0.4	ND

* Percentage of variation from the first to the second injection after one week at 4 °C.

2.2. Method Validation

The method was then validated following the recommendations for bioanalytical method validation [43] (Tables 1 and 2) and confirmed to be selective and specific. Specifically, the absence of interfering substances at the retention times of the compounds of interest and internal standards were verified in charcoal-stripped plasma and charcoal-stripped serum.

LOD and LOQ were determined for all compounds for both extraction protocols. Using the extraction protocol for plasma and serum samples, the LOD ranged from 0.01 to 1 ng/mL and the LOQ ranged from 0.02 to 3.5 ng/mL (Table 1). The LOD for the liver extraction protocol ranged from 0.03 to 7 ng/mL and the LOQ from 0.09 to 21 ng/mL (Table 2). Carryover was assessed by injecting five consecutive blank samples after a calibration standard at the upper limit of quantification, for both extraction protocols. No carryover could be detected for the analytes and the internal standards, as there were no chromatographic peaks present at the transitions at the corresponding retention times. Linearity of the calibration curves was assessed by using linear regression analysis of a triplicate of the 10-level calibration curve prepared independently for both extraction protocols. All calibration curves were linear, with squared correlation coefficients (r2) ranging from 0.990 – 0.999 for the majority of the compounds in both extraction protocols, except for allo-3β-lithocholic acid (allo-3βLCA) using the serum/plasma extraction protocol and LCA and tauro-lithocholic acid (TLCA) with the liver extraction protocol (Tables 1 and 2). Extraction recovery was evaluated by comparing the responses of a spiked matrix with and without extraction, and calculated for each analyte at low, medium, and high concentrations (2.5, 50, and 250 ng/mL) (Tables 1 and 2). Stability was determined by analyzing extracted samples and calibrators immediately as well as after storage at 4 °C for one week. Concentrations obtained were compared and variations lower than 10% were obtained throughout, regardless of the storage period. All bile acids were found to be stable at 4 °C for at least one week.

The method was then tested using different matrices from human and mouse (Figure 2). The list of bile acids included in the LC-MS/MS method for quantification is represented by three different colors, indicating the robust detection and quantification of the compound (green), presence at a low concentration around LOQ, or absence in few tested samples (yellow), and absence in most samples (red) (concentrations at Table S1). In contrast to humans, where glycine-conjugated bile acids are the major components of the bile acid pool with a ratio of glycine to taurine-conjugated bile acids of about 3:1 in adult males, taurine conjugates represent the most abundant bile acids in the mouse and rat [7]. All primary and secondary bile acids could be robustly quantified, with the exception of LCA and its conjugates. Some of the allo-bile acids and 7oxo bile acids were either present at low concentrations around LOQ or not detected. This is not unexpected, as these bile acids represent minor metabolites that are thought to be increased in certain enzyme deficiencies or diseases [23,44].

Name	Mouse serum	Mouse plasma	Mouse Liver	Human plasma
CA				
CDCA				
ωMCA				
αMCA				
βMCA				
γMCA				
UDCA				
HDCA				
DCA				
LCA				
3oxoLCA				
7oxoLCA				
12oxoLCA				
6,7dioxoLCA				
7oxoDCA				
Allo-CA				
Allo-DCA				
Allo-3βDCA				
Allo-12βDCA				
Allo-3βLCA				
Allo-LCA				
TCA				
TCDCA				
TωMCA				
TαMCA				
TβMCA				
TUDCA				
TDCA				
T7oxoLCA				
TLCA				
GCA				
GCDCA				
GUDCA				
GDCA				
GLCA				
G7oxoLCA				

Figure 2. List of bile acids included in the LC-MS/MS method for quantification. The newly established method was applied to different matrices including plasma of human and mouse, as well as mouse serum and liver tissue. Colors indicate compound detection and quantification: Green: Compound detected in samples used for this test. Yellow: Compound detected at a very low concentration, close to LOQ or not detected in all samples tested. Red: Compound not detected in most samples.

2.3. *Application of the Method*

The method was applied to plasma and liver tissue samples from mice treated for three weeks with simvastatin at three different doses (5, 10, and 25 mg/kg/d). Simvastatin, similar to other statins, inhibits HMG-CoA reductase that catalyzes the rate-limiting step of cholesterol biosynthesis and is widely used to treat hypercholesterolemia [45]. The main adverse effects of statins are skeletal muscle-associated symptoms, seen in up to 30% of treated patients, with rhabdomyolysis as a rare but potentially fatal form [38]. Since bile acids are produced from cholesterol, we tested the hypothesis that inhibition of hepatic cholesterol synthesis by simvastatin might alter bile acid homeostasis and that this potentially contributes to statin-induced myotoxicity. In mice treated daily for three weeks at 5 mg/kg, grip strength and muscle endurance capacity were decreased while plasma lactate levels were elevated after exercise compared to control mice. Additionally, disturbances of mitochondrial function could be detected with impaired oxidative metabolism [39,40].

More than 20 different bile acids were detected and quantified in plasma and liver tissue of simvastatin treated mice, including free (Figure 3A,C) and taurine-conjugated (Figure 3B,D) metabolites (concentrations at Table S2). As expected, taurine-conjugated bile acids were predominant in mouse, whereas glycine-conjugated metabolites were either undetectable or present at low levels [6,7] and therefore not further considered. The results showed no significant changes between simvastatin treated and control mice in the concentrations of any bile acid, including major and minor metabolites. To better understand our observation, we measured plasma lipid profile including total cholesterol, high-density lipoprotein cholesterol (HDLc), and low- and very low-density lipoprotein cholesterol (LDLc/VLDLc) (Figure S1). We did not detect any significant difference between simvastatin-treated and control mice in the aforementioned lipid markers. These results are in accordance with a previous study in which the treatment with simvastatin at 30 mg/kg for two weeks did not change the lipid profile in mice [46]. Since bile acids are amphipathic molecules derived from cholesterol, the unchanged lipid profile could be the obvious reason why the treatment with simvastatin at the tested doses did not change the bile acid profile in mice. Moreover, these results are in line with an earlier study of Fu et al., in which they treated mice with atorvastatin at 100 mg/kg/d for one week [47]. Although they observed an induction of Cyp7a1, the rate-limiting enzyme in bile acid synthesis, total bile acids in serum and liver tissue did not change. However, their data did not exclude the possibility that individual bioactive bile acids might be altered. In the present study, application of the newly established bile acid quantification method, covering a large number of metabolites, did not show any significant differences in the free and taurine-conjugated bile acids measured in both plasma and liver tissue (Figure 3). This data is in line with observations in other studies using different species such as rabbit and human patients, where simvastatin did not alter the bile acid profiles [48,49]. Together, the data indicate that the cholesterol-lowering effect of simvastatin does not result in disruption of bile acid homeostasis and therefore is not involved in the observed simvastatin-induced myotoxicity.

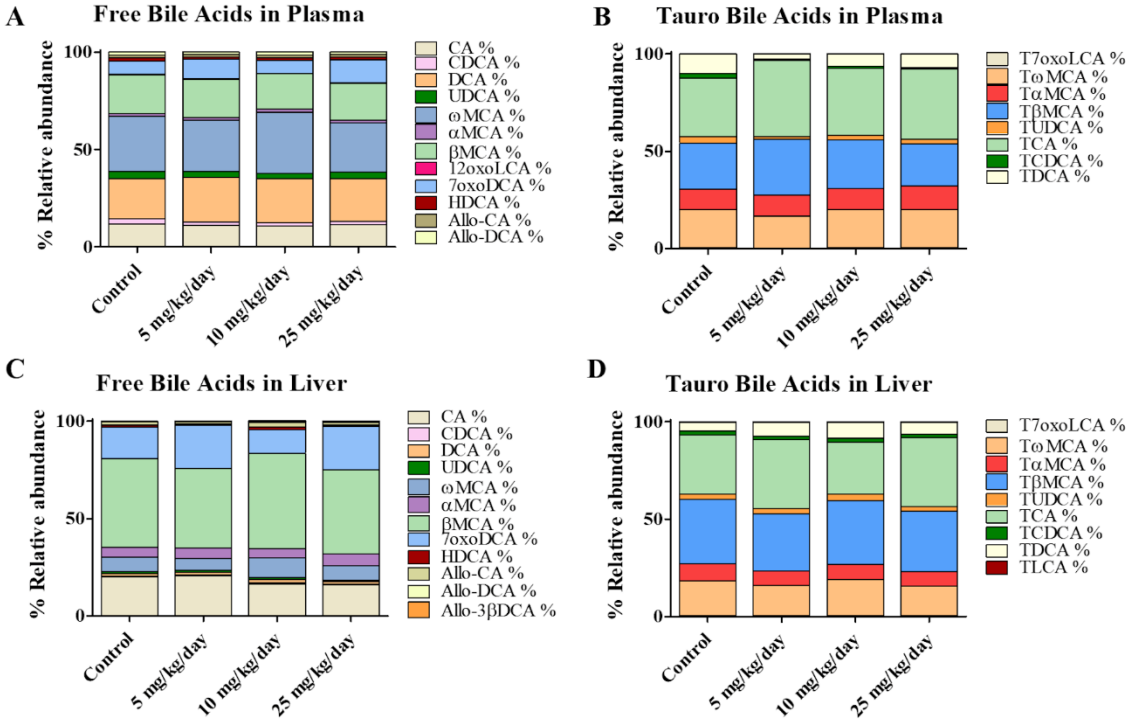

Figure 3. Bile acid composition analyzed in mouse plasma and liver tissue samples. Data represent relative abundances (%). The four groups correspond to control, and simvastatin exposure in mice at three different doses: 5, 10, and 25 mg/kg/day. (**A**,**C**) Profiles of free bile acids in plasma and liver tissue, respectively; (**B**,**D**) Taurine-conjugated bile acids in plasma and liver, respectively. $n = 6$ per group.

3. Materials and Methods

3.1. Chemicals and Reagents

Ultrapure water was obtained using a Milli-Q® Integral 3 purification system equipped with an EDS-Pak® Endfilter for the removal of endocrine active substances (Merck Millipore, Burlington, MA, USA). Acetonitrile (HPLC-S Grade) was purchased from Biosolve (Dieuze, France), chloroform stabilized with ethanol (HPLC Grade) from Scharlab (Sentmenat, Spain), methanol (CHROMASOLV™ LC-MS grade) from Honeywell (Charlotte, NC, USA), isopropanol (EMSURE® for analysis) from Merck Millipore and formic acid (Puriss. p.a. ≥ 98%) from Sigma-Aldrich (St. Louis, MO, USA).

7oxoLCA was purchased from BioTrend (Köln, Deutschland), tauro-cholic acid, tauro-ursodeoxycholic acid, and glyco-cholic acid were obtained from Calbiochem (San Diego, CA, USA), and tauro-chenodeoxycholic acid, CA, UDCA, glyco-chenodeoxycholic acid, glyco-deoxycholic acid, DCA, CDCA, and LCA from Sigma-Aldrich. Tauro-α-muricholic acid, tauro-β-muricholic acid, tauro-ω-muricholic acid, αMCA, βMCA, ωMCA, 7-oxodeoxycholic acid, glyco-ursodeoxycholic acid, tauro-deoxycholic acid, hyodeoxycholic acid, TLCA, glyco-lithocholic acid, dehydrolithocholic acid, 12-oxolithocholic acid, 6,7-dioxolithocholic acid, and γMCA were obtained from Steraloids (Newport, RI, USA). Tauro-7-oxolithocholic acid and glyco-7-oxolithocholic acid. Allo-cholic acid, allo-deoxycholic acid, allo-lithocholic acid, allo-3β-deoxycholic acid, allo-3β-LCA, and allo-12β-deoxycholic acid were kindly provided by Prof. Alan F. Hofmann (San Diego). Deuterated standards used as internal standards, i.e., (2,2,4,4-2H4)-glyco-chenodeoxycholic acid, (2,2,4,4-2H4)-glyco-cholic acid, (2,2,4,4-2H4)-glyco-ursodeoxycholic acid, and (2,2,4,4-2H4)-UDCA were obtained from CDN Isotopes (Pointe-Claire, Quebec, Canada). (2,2,4,4-2H4)-CA, (2,2,4,4-2H4)-CDCA, and (2,2,4,4-2H4)-LCA were purchased from Sigma-Aldrich. (2,2,4,4-2H4)-DCA was purchased from Steraloids.

3.2. Serum, Plasma, and Liver Tissue Samples from Mice and Plasma from Humans Used for Method Development

Blood and liver tissue samples of 10–12 weeks old male C57BL/6J mice were collected in agreement with the guidelines for care and use of laboratory animals, accepted by the cantonal veterinary authority of Basel in Switzerland (License 2758).

Human plasma from 16 healthy subjects (8 men and 8 women; mean ± SD age 24.8 ± 2.6 years) was obtained from a previously reported study [50] conducted in accordance with the Declaration of Helsinki and International Conference on Harmonization Guidelines in Good Clinical Practice and approved by the local Ethics Committee and Swiss Agency for Therapeutic Products (Swissmedic). The study was registered at ClinicalTrials.gov: http://clinicaltrials.gov/ct2/show/NCT01465685.

3.3. Mice Treated with Simvastatin

Male C57BL/6J mice (n = 24, 14 weeks old, approximately 29–32 g of bodyweight) were acclimatized one week prior to the start of the study and housed in a standard facility with 12 h light-dark cycles and controlled temperature (22 ± 2 °C). The mice were fed a standard pellet chow and water ad libitum. All experiments were performed in agreement with the guidelines from Directive 2012/63/EU of the European Parliament on the protection of animals used for scientific purposes. The experiments performed in this animal study were reviewed and accepted by the cantonal veterinary authority of Basel in Switzerland and were performed in agreement with the guidelines for care and use of laboratory animals (License 3035).

After acclimatization, mice were randomly divided into four groups: (1) mice treated with vehicle (control, n = 6); (2) mice treated with simvastatin at 5 mg/kg/d (n = 6); (3) mice treated with simvastatin at 10 mg/kg/d (n = 6); and (4) mice treated with simvastatin at 25 mg/kg/d (n = 6). The mice were treated by oral gavage for three weeks. Following treatment for 21 days, mice were anesthetized with an intraperitoneal injection of ketamine (100 mg/kg) and xylazine (10 mg/kg) (Graeub AG, Switzerland). Then, blood was collected into heparin-coated tubes by intracardiac puncture. Plasma was separated

by centrifugation at 3000× *g* for 15 min. Plasma samples were kept at −80 °C for later analysis. The liver was immediately collected, frozen in liquid nitrogen, and stored at −80 °C for later analysis.

3.4. Bile Acids Extraction from Plasma and Serum

For the analysis of bile acids, 25 µL of plasma and serum samples diluted at a ratio of 1:4 (*v*/*v*) with MilliQ water were used. Samples were subjected to protein precipitation by adding 1 mL of 2-propanol containing a mixture of deuterated internal standards. Extraction was performed with continuous shaking at 4 °C for 30 min at 1400 rpm on a Thermomixer C (Eppendorf AG, Hamburg, Germany) and then centrifuged at 16000× *g* for 10 min. Supernatants were transferred to new tubes and evaporated to dryness by using a Genevac EZ-2 system (SP Scientific, Warminster, PA, USA) at 35 °C. Extracts were resuspended in 100 µL methanol:water (1:1, *v*/*v*), incubated at 4 °C for 10 min at 1400 rpm, sonicated in a water bath for 10 min at room temperature, and finally transferred to LC-MS vial for analysis.

3.5. Bile Acids Extraction from Mouse Liver Tissue

Liver samples (30 ± 5 mg) were homogenized using oxide beads (1.4 mm Zirconium) on the Precellys 24 Tissue Homogenizer (Bertin Instruments, Montigny-le-Bretonneux, France) with three cycles (30 s at 6500 rpm, 30 s break between each cycle) in 1 mL of extraction mixture (water-chloroform-methanol; 1:1:3; *v*/*v*/*v*) including deuterated internal standards. Samples were incubated for 15 min at 37 °C with continuous shaking at 850 rpm on a Thermomixer C and centrifuged at 16,000× *g* for 10 min at 20 °C. 800 µL of supernatant were transferred to a 2 mL tube and kept on ice. Another 800 µL of extraction mixture were added to the samples and the extraction process was repeated once more as described. The final 1.6 mL were evaporated to dryness in a Genevac EZ-2 at 35 °C. The residue was reconstituted in 200 µL methanol-water 1:1 (*v*/*v*), incubated for 10 min at 1300 rpm and at 20 °C, and then sonicated in a water bath for 10 min at room temperature. Next, the samples were centrifuged at 16,000× *g* for 10 min at 20 °C and 100 µL of the supernatant were transferred to LC-MS vials and stored at −20 °C for later analysis.

3.6. Calibration and Quality Control Standard Preparation

Bile acid standard or internal standard stock solutions at concentrations of 1 mg/mL were prepared by dissolving each standard in methanol and stored at −80 °C. Individual working solutions were prepared by diluting them with the appropriate amount of methanol. A mixture of all internal standards was prepared for sample preparation. A mixture of all the compounds was prepared to spike the highest level of the calibration curve. A ten-point calibration curve was prepared by serial dilution of the working standard mix solution into charcoal-stripped serum, plasma, or phosphate-buffered saline (PBS). Quality controls were prepared by spiking the working standard solution mix (at 2.5, 50, and 100 ng/mL) in charcoal stripped serum, plasma or PBS. Calibrators and quality controls then went through the sample preparation process described above.

3.7. LC-MS/MS Instrumental Conditions

The analysis was carried out using an Agilent 1290 UPLC coupled to an Agilent 6490 triple quadrupole mass spectrometer equipped with an electrospray ionization (ESI) source (Agilent Technologies, Basel, Switzerland). Drying gas as well as nebulizing gas was nitrogen. The desolvation gas flow was set at 15 L/min, the sheath gas flow at 11 L/min, and the nebulizer pressure at 20 psi. The nitrogen desolvation temperature was set at 290 °C, sheath gas temperature at 250 °C. Capillary voltage was optimized for each segment from 2000 to 5000 V. Nozzle voltage was set at 2000 V and cell accelerator voltage at 5 V. Chromatographic separation of bile acids was achieved using reversed-phase column (ACQUITY UPLC BEH C18, 130 Å, 1.7 µm, 2.1 mm × 15 mm, Waters, Milford, MA, USA), at a flow of 0.5 mL/min and a column temperature of 55 °C. The mobile phase consisted of ultrapure water and acetonitrile (95:5, *v*/*v*) with 0.1% formic acid (solvent A) and acetonitrile and ultrapure water (95:5, *v*/*v*) with 0.1% formic acid (solvent B). The following gradient pattern was used for the separation

of bile acids: 0 min, 25% B, 3.1 min, 35% B, 9 min, 38% B, 15 min, 65% B, 18 min, 65% B, 20 min, 100% B, 22 min, 25% B, and additional 2 min post-run at initial conditions. The injection volume was set at 3 µL.

Data acquisition was performed using MRM mode. At least two transitions (quantifier and qualifier transitions) were selected for each compound in positive or negative ESI mode depending on the compound. Collision energy was optimized for each transition (Tables 1 and 2).

3.8. Method Validation

The following parameters were evaluated: LOD, LOQ, linearity, stability at 4 °C, carryover, and extraction recovery. The absence of any interfering substance at the retention time of the compounds of interest was verified [43].

The LOQ was defined as the lowest concentration at which the peak response was ten times that of the noise (10 S/N), and the LOD was the extrapolated concentration with a signal-to-noise ratio of three (3 S/N). Calibration curves were prepared daily and spiked with internal standards. In order to evaluate the linearity, 10 calibration curve points were analyzed by the optimized method. The linearity of the calibration curves was then determined using linear regression analysis of a triplicate of the 10-level calibration curve prepared independently for both extraction protocols described above. Carryover was assessed by injecting five consecutive blank samples after injection of the highest calibration standard for both extraction protocols. The stability of the bile acids at 4 °C was evaluated in plasma and liver tissue samples to investigate whether the concentrations of the compounds were stable over time. Extracts were analyzed, kept at 4 °C for one week, and reanalyzed.

The extraction recovery was assessed at three concentration levels (2.5, 50, and 250 ng/mL). The analysis of six replicates of a charcoal-treated plasma sample spiked with the compounds before extraction, and six replicates of the same charcoal treated plasma sample to which the analytes were added after extraction. The ratio of the peak areas between the analytes and the internal standard obtained from the extracted spiked samples was compared with ratios obtained for samples in which the analytes were added after extraction of the matrix (representing 100% extraction recovery). In order to evaluate the extraction recovery for the liver sample extraction protocol bovine serum albumin (1 mg/mL) was used as a matrix. Precision was measured as the relative standard deviation of the ratios of the peak areas of the compound to the internal standard. The concentration range for the quantification was optimized for each matrix.

The extraction protocols were applied to different matrices in order to evaluate its performance before being applied to a real cohort of samples. The method was tested in human and mouse serum and plasma as well as mouse liver tissue samples.

3.9. Data Analysis and Statistics

For LC-MS/MS data, MassHunter Acquisition and Quantitative Analysis vB.07.01 (Agilent Technologies, Inc.) were used for quantification. Statistical analysis was performed using nonparametric multiple *t*-tests, groups were compared by using the Wilcoxon signed rank test. Statistical analysis and graphs were performed in GraphPad Prism v5.02 (GraphPad Software).

4. Conclusions

We developed and validated an LC-MS/MS method for the simultaneous quantification of 36 different bile acids in serum, plasma, and liver tissue samples. This simple method solved issues of separation of isobaric bile acids seen in previous methods and its applicability was demonstrated using human and mouse samples. The method covers the most important free and taurine- and glycine-conjugated bile acids as well as some minor metabolites of interest in certain enzyme deficiencies. This broad coverage and the small sample amount needed allows future application of the method for clinical studies as well as preclinical studies including species such as mouse, rat, and guinea-pig. Finally, application of the method in a study of simvastatin treated mice showed that the

cholesterol-lowering drug, at doses causing myotoxicity, did not affect bile acid profiles in plasma and liver tissue, indicating that bile acids are not involved in the mechanism of statin-induced myotoxicity.

Supplementary Materials: The following are available online at http://www.mdpi.com/2218-1989/10/7/282/s1, Figure S1: Lipid profile measured in simvastatin-treated and control mice, Table S1: Concentrations of individual bile acids quantified in serum, plasma and liver tissue from mice and in human plasma, Table S2: Concentrations of individual bile acids quantified in plasma and liver tissue in simvastatin-treated and control mice.

Author Contributions: Conceptualization and Methodology, S.S., D.V.K., J.B., and C.G.; Data Acquisition and Analysis, C.G.; Validation, C.G.; Writing—Original Draft Preparation, C.G.; Writing—Review and Editing, C.G., S.S., D.V.K., J.B., A.O.; Supervision, A.O.; Project Administration, A.O.; Funding Acquisition, A.O. All authors have read and agreed to the published version of the manuscript.

Funding: The financial support received from the Swiss National Science Foundation Grant 31003A-179400 (A.O.) is acknowledged.

Conflicts of Interest: The authors declare no conflict of interest.

References

1. Ahmad, T.R.; Haeusler, R.A. Bile acids in glucose metabolism and insulin signalling—Mechanisms and research needs. *Nat. Rev. Endocrinol.* **2019**, *15*, 701–712. [CrossRef] [PubMed]
2. Jia, W.; Xie, G.; Jia, W. Bile acid–microbiota crosstalk in gastrointestinal inflammation and carcinogenesis. *Nat. Rev. Gastroenterol. Hepatol.* **2018**, *15*, 111–128. [CrossRef] [PubMed]
3. Cepa, S.; Potter, D.; Wong, L.; Schutt, L.; Tarrant, J.; Pang, J.; Zhang, X.; Andaya, R.; Salphati, L.; Ran, Y.; et al. Individual serum bile acid profiling in rats aids in human risk assessment of drug-induced liver injury due to BSEP inhibition. *Toxicol. Appl. Pharm.* **2018**, *338*, 204–213. [CrossRef]
4. Slopianka, M.; Herrmann, A.; Pavkovic, M.; Ellinger-Ziegelbauer, H.; Ernst, R.; Mally, A.; Keck, M.; Riefke, B. Quantitative targeted bile acid profiling as new markers for DILI in a model of methapyrilene-induced liver injury in rats. *Toxicology* **2017**, *386*, 1–10. [CrossRef]
5. Schadt, H.S.; Wolf, A.; Pognan, F.; Chibout, S.-D.D.; Merz, M.; Kullak-Ublick, G.A. Bile acids in drug induced liver injury: Key players and surrogate markers. *Clin. Res. Hepatol. Gastroenterol.* **2016**, *40*, 257–266. [CrossRef] [PubMed]
6. Russell, D.W. The Enzymes, Regulation, and Genetics of Bile Acid Synthesis. *Annu. Rev. Biochem.* **2003**, *72*, 137–174. [CrossRef]
7. Russell, D.W.; Setchell, K.D.R. Bile Acid Biosynthesis. *Biochemistry* **1992**, *31*, 4737–4749. [CrossRef]
8. Takahashi, S.; Fukami, T.; Masuo, Y.; Brocker, C.N.; Xie, C.; Krausz, K.W.; Wolf, C.R.; Henderson, C.J.; Gonzalez, F.J. Cyp2c70 is responsible for the species difference in bile acid metabolism between mice and humans. *J. Lipid Res.* **2016**, *57*, 2130–2137. [CrossRef]
9. Tint, G.S.; Xu, G.; Batta, A.K.; Shefer, S.; Niemann, W.; Salen, G. Ursodeoxycholic acid, chenodeoxycholic acid, and 7-ketolithocholic acid are primary bile acids of the guinea pig. *J. Lipid Res.* **1990**, *31*, 1301–1306.
10. Hofmann, A.F.; Hagey, L.R.; Krasowski, M.D. Bile salts of vertebrates: Structural variation and possible evolutionary significance. *J. Lipid Res.* **2010**, *51*, 226–246. [CrossRef]
11. Monte, M.J.; Marin, J.J.; Antelo, A.; Vazquez-Tato Maria Monte, J.J.; Vazquez-Tato, J.; Chiang, J.Y.; Jjg, M. Bile acids: Chemistry, physiology, and pathophysiology. *World J. Gastroenterol.* **2009**, *15*. [CrossRef]
12. Hofmann, A.F.; Mosbach, E.H. Identification of Allodeoxycholic Acid as the Major Component of Gallstones Induced in the Rabbit by 5-alpha-cholestan-3-beta-ol. *J. Biol. Chem.* **1964**, *239*, 2813–2821.
13. Chiang, J.Y.L.L. Bile acids: Regulation of synthesis. *J. Lipid Res.* **2009**, *50*, 1955–1966. [CrossRef] [PubMed]
14. Chiang, J.Y.L. Bile acid metabolism and signaling. *Compr. Physiol.* **2013**. [CrossRef]
15. Dawson, P.A.; Karpen, S.J. Intestinal transport and metabolism of bile acids. *J. Lipid Res.* **2015**, *56*, 1085–1099. [CrossRef] [PubMed]
16. Dawson, P.A. Role of the Intestinal Bile Acid Transporters in Bile Acid and Drug Disposition. In *Handbook of Experimental Pharmacology*; Springer: Berlin, Heidelberg, 2011; Volume 201, pp. 169–203, ISBN 9783642145407.
17. Luo, L.; Aubrecht, J.; Li, D.; Warner, R.L.; Johnson, K.J.; Kenny, J.; Colangelo, J.L. Assessment of serum bile acid profiles as biomarkers of liver injury and liver disease in humans. *PLoS ONE* **2018**, *13*, e0193824. [CrossRef] [PubMed]

18. Staley, C.; Weingarden, A.R.; Khoruts, A.; Sadowsky, M.J. Interaction of gut microbiota with bile acid metabolism and its influence on disease states. *Appl. Microbiol. Biotechnol.* **2017**, *101*, 47–64. [CrossRef]
19. Urdaneta, V.; Casadesús, J. Interactions between Bacteria and Bile Salts in the Gastrointestinal and Hepatobiliary Tracts. *Front. Med.* **2017**, *4*, 1–13. [CrossRef]
20. Li, T.; Apte, U. Bile Acid Metabolism and Signaling in Cholestasis, Inflammation, and Cancer. *Adv. Pharmacol.* **2015**, *74*, 263–302.
21. Perez, M.J.; Britz, O. Bile-acid-induced cell injury and protection. *World J. Gastroenterol.* **2009**, *15*, 1677–1689. [CrossRef]
22. Aleo, M.D.; Aubrecht, J.D.; Bonin, P.; Burt, D.A.; Colangelo, J.; Luo, L.; Schomaker, S.; Swiss, R.; Kirby, S.C.; Rigdon, G.; et al. Phase I study of PF-04895162, a Kv7 channel inhibitor, reveals unexpected hepatotoxicity in healthy subjects, but not rats or monkeys: Clinical evidence of disrupted bile acid homeostasis. *Pharm. Res. Perspect.* **2019**, *7*, 1–12. [CrossRef] [PubMed]
23. Penno, C.A.; Morgan, S.A.; Vuorinen, A.; Schuster, D.; Lavery, G.G.; Odermatt, A. Impaired oxidoreduction by 11β-hydroxysteroid dehydrogenase 1 results in the accumulation of 7-oxolithocholic acid. *J. Lipid Res.* **2013**, *54*, 2874–2883. [CrossRef] [PubMed]
24. Chen, S.-M.; Liao, Y.-Y.; Lin, C.-P. Inspissated Bile Syndrome: A Rare Cause of Neonatal Cholestasis. *Pediatr. Neonatol.* **2020**, 2–3. [CrossRef] [PubMed]
25. Clayton, P.T.; Mills, K.A.; Johnson, A.W.; Barabino, A.; Marazzi, M.G. Δ4-3-Oxosteroid 5β-reductase deficiency: Failure of ursodeoxycholic acid treatment and response to chenodeoxycholic acid plus cholic acid. *Gut* **1996**, *38*, 623–628. [CrossRef]
26. Lemonde, H.A.; Custard, E.J.; Bouquet, J.; Duran, M.; Overmars, H.; Scambler, P.J.; Clayton, P.T. Mutations in SRD5B1 (AKR1D1), the gene encoding δ 4-3-oxosteroid 5β-reductase, in hepatitis and liver failure in infancy. *Gut* **2003**, *52*, 1494–1499. [CrossRef]
27. Huang, J.; Bathena, S.P.R.; Csanaky, I.L.; Alnouti, Y. Simultaneous characterization of bile acids and their sulfate metabolites in mouse liver, plasma, bile, and urine using LC–MS/MS. *J. Pharm. Biomed. Anal.* **2011**, *55*, 1111–1119. [CrossRef]
28. Penno, C.A.; Arsenijevic, D.; Da Cunha, T.; Kullak-Ublick, G.A.; Montani, J.-P.; Odermatt, A. Quantification of multiple bile acids in uninephrectomized rats using ultra-performance liquid chromatography-tandem mass spectrometry. *Anal. Methods* **2013**, *5*, 1155. [CrossRef]
29. Qiao, X.; Ye, M.; Liu, C.; Yang, W.; Miao, W.; Dong, J.; Guo, D. A tandem mass spectrometric study of bile acids: Interpretation of fragmentation pathways and differentiation of steroid isomers. *Steroids* **2012**, *77*, 204–211. [CrossRef]
30. Lan, K.; Su, M.; Xie, G.; Ferslew, B.C.; Brouwer, K.L.R.; Rajani, C.; Liu, C.; Jia, W. Key Role for the 12-Hydroxy Group in the Negative Ion Fragmentation of Unconjugated C24 Bile Acids. *Anal. Chem.* **2016**, *88*, 7041–7048. [CrossRef]
31. Reinicke, M.; Schröter, J.; Müller-Klieser, D.; Helmschrodt, C.; Ceglarek, U. Free oxysterols and bile acids including conjugates—Simultaneous quantification in human plasma and cerebrospinal fluid by liquid chromatography-tandem mass spectrometry. *Anal. Chim. Acta* **2018**, *1037*, 245–255. [CrossRef]
32. Perwaiz, S.; Tuchweber, B.; Mignault, D.; Gilat, T.; Yousef, I.M. Determination of bile acids in biological fluids by liquid chromatography-electrospray tandem mass spectrometry. *J. Lipid Res.* **2001**, *42*, 114–119. [PubMed]
33. Sarafian, M.H.; Lewis, M.R.; Pechlivanis, A.; Ralphs, S.; McPhail, M.J.W.; Patel, V.C.; Dumas, M.-E.; Holmes, E.; Nicholson, J.K. Bile Acid Profiling and Quantification in Biofluids Using Ultra-Performance Liquid Chromatography Tandem Mass Spectrometry. *Anal. Chem.* **2015**, *87*, 9662–9670. [CrossRef]
34. García-Cañaveras, J.C.; Donato, M.T.; Castell, J.V.; Lahoz, A. Targeted profiling of circulating and hepatic bile acids in human, mouse, and rat using a UPLC-MRM-MS-validated method. *J. Lipid Res.* **2012**, *53*, 2231–2241. [CrossRef] [PubMed]
35. Tagliacozzi, D.; Mozzi, A.F.; Casetta, B.; Bertucci, P.; Bernardini, S.; Di Illio, C.; Urbani, A.; Federici, G. Quantitative analysis of bile acids in human plasma by liquid chromatography-electrospray tandem mass spectrometry: A simple and rapid one-step method. *Clin. Chem. Lab. Med.* **2003**, *41*, 1633–1641. [CrossRef] [PubMed]
36. Dutta, M.; Cai, J.; Gui, W.; Patterson, A.D. A review of analytical platforms for accurate bile acid measurement. *Anal. Bioanal. Chem.* **2019**, *411*, 4541–4549. [CrossRef] [PubMed]

37. Ward, N.C.; Watts, G.F.; Eckel, R.H. Statin Toxicity: Mechanistic Insights and Clinical Implications. *Circ. Res.* **2019**, *124*, 328–350. [CrossRef]
38. Bouitbir, J.; Sanvee, G.M.; Panajatovic, M.V.; Singh, F.; Krähenbühl, S. Mechanisms of statin-associated skeletal muscle-associated symptoms. *Pharm. Res.* **2020**, *154*, 104201. [CrossRef]
39. Sanvee, G.M.; Panajatovic, M.V.; Bouitbir, J.; Krähenbühl, S. Mechanisms of insulin resistance by simvastatin in C2C12 myotubes and in mouse skeletal muscle. *Biochem. Pharm.* **2019**, *164*, 23–33. [CrossRef]
40. Panajatovic, M.V.; Singh, F.; Roos, N.J.; Duthaler, U.; Handschin, C.; Krähenbühl, S.; Bouitbir, J. PGC-1α plays a pivotal role in simvastatin-induced exercise impairment in mice. *Acta Physiol.* **2020**, *228*, 1–15. [CrossRef]
41. Ramesh, M.; Campos, J.C.; Lee, P.; Song, Y.; Hernandez, G.; Sin, J.; Tucker, K.C.; Saadaeijahromi, H.; Gurney, M.; Ferreira, J.C.B.; et al. Mitophagy protects against statin-mediated skeletal muscle toxicity. *Faseb J.* **2019**, *33*, 11857–11869. [CrossRef]
42. Istvan, E.S.; Deisenhofer, J. Structural mechanism for statin inhibition of HMG-CoA reductase. *Science* **2001**, *292*, 1160–1164. [CrossRef] [PubMed]
43. Committee for Medicinal Products for Human Use Guideline on bioanalytical method validation. *Eur. Med. Agency* **2011**, 1–23.
44. Penno, C.A.; Morgan, S.A.; Rose, A.J.; Herzig, S.; Lavery, G.G.; Odermatt, A. 11β-Hydroxysteroid dehydrogenase-1 is involved in bile acid homeostasis by modulating fatty acid transport protein-5 in the liver of mice. *Mol. Metab.* **2014**, *3*, 554–564. [CrossRef] [PubMed]
45. Taylor, F.C.; Huffman, M.; Ebrahim, S. Statin Therapy for Primary Prevention of Cardiovascular Disease. *JAMA* **2013**, *310*, 2451. [CrossRef]
46. Yin, W.; Carballo-jane, E.; Mclaren, D.G.; Mendoza, V.H.; Gagen, K.; Geoghagen, N.S.; Mcnamara, L.A.; Gorski, J.N.; Eiermann, G.J.; Petrov, A.; et al. Plasma lipid profi ling across species for the identifi cation of optimal animal models of human dyslipidemia. *J. Lipid Res.* **2012**, *53*, 51–65. [CrossRef]
47. Fu, Z.D.; Cui, J.Y.; Klaassen, C.D. Atorvastatin induces bile acid-synthetic enzyme Cyp7a1 by suppressing FXR signaling in both liver and intestine in mice. *J. Lipid Res.* **2014**, *55*, 2576–2586. [CrossRef]
48. Fumiaki, I.; Yuri, I.; Kyoko, K.; Yutaka, K.; Yoshio, S.; Toshio, K. Effect of Simvastatin (MK-733) on Sterol and Bile Acid Excretion in Rabbits. *Jpn. J. Pharm.* **1990**, *53*, 35–45. [CrossRef]
49. Lanzarotto, F.; Panarotto, B.; Sorbara, R.; Panteghini, M.; Pagani, F.; Sosta, S.; Lanzini, A. Effect of long term simvastatin administration as an adjunct to ursodeoxycholic acid: Evidence for a synergistic effect on biliary bile acid composition but not on serum lipids in humans. *Gut* **1999**, *44*, 552–556. [CrossRef]
50. Seibert, J.; Hysek, C.M.; Penno, C.A.; Schmid, Y.; Kratschmar, D.V.; Liechti, M.E.; Odermatt, A. Acute Effects of 3,4-Methylenedioxymethamphetamine and Methylphenidate on Circulating Steroid Levels in Healthy Subjects. *Neuroendocrinology* **2014**, *100*, 17–25. [CrossRef]

6.4 Impact on Bile Acid Concentrations by Alveolar Echinococcosis and Treatment with Albendazole in Mice

Published Article

Cristina Gómez[1], Fadi Jebbawi[1], Michael Weingartner[1], Junhua Wang[2,3], Simon Stücheli[1], Bruno Stieger[4], Bruno Gottstein[2,3], Guido Beldi[5], Britta Lundström-Stadelmann[2], and Alex Odermatt[1]

[1] Division of Molecular and Systems Toxicology, Department of Pharmaceutical Sciences, University of Basel, 4056 Basel, Switzerland.

[2] Department of Infectious Diseases and Pathobiology, Vetsuisse Faculty, Institute of Parasitology, University of Berne, 3012 Berne, Switzerland.

[3] Faculty of Medicine, Institute for Infectious Diseases, University of Bern, 3010 Bern, Switzerland.

[4] Department of Clinical Pharmacology and Toxicology, University hospital Zurich, University of Zurich, 8091 Zurich, Switzerland.

[5] Department of Visceral Surgery and Medicine, University Hospital of Bern, 3010 Bern, Switzerland.

Contribution to the project:

Experimental work

Analysis and interpretation of data

Revising the manuscript

metabolites

MDPI

Article

Impact on Bile Acid Concentrations by Alveolar Echinococcosis and Treatment with Albendazole in Mice

Cristina Gómez [1], Fadi Jebbawi [1], Michael Weingartner [1], Junhua Wang [2,3], Simon Stücheli [1], Bruno Stieger [4], Bruno Gottstein [2,3], Guido Beldi [5], Britta Lundström-Stadelmann [2] and Alex Odermatt [1,*]

1 Division of Molecular and Systems Toxicology, Department of Pharmaceutical Sciences, University of Basel, 4056 Basel, Switzerland; cristina.gomezcastella@unibas.ch (C.G.); fadi.jebbawi@unibas.ch (F.J.); michael.weingartner@unibas.ch (M.W.); simon.stuecheli@unibas.ch (S.S.)
2 Department of Infectious Diseases and Pathobiology, Vetsuisse Faculty, Institute of Parasitology, University of Bern, 3012 Berne, Switzerland; junhua.wang@ifik.unibe.ch (J.W.); bruno.gottstein@ifik.unibe.ch (B.G.); britta.lundstroem@vetsuisse.unibe.ch (B.L.-S.)
3 Faculty of Medicine, Institute for Infectious Diseases, University of Berne, 3010 Berne, Switzerland
4 Department of Clinical Pharmacology and Toxicology, University Hospital Zurich, University of Zurich, 8091 Zurich, Switzerland; bstieger@ethz.ch
5 Department of Visceral Surgery and Medicine, University Hospital of Berne, 3010 Berne, Switzerland; Guido.Beldi@insel.ch
* Correspondence: alex.odermatt@unibas.ch

Abstract: Alveolar echinococcosis (AE) caused by *Echinococcus multilocularis* is a chronic, progressive liver disease widely distributed in the Northern Hemisphere. The main treatment options include surgical interventions and chemotherapy with benzimidazole albendazole (ABZ). To improve the current diagnosis and therapy of AE, further investigations into parasite–host interactions are needed. This study used liquid chromatography–tandem mass spectrometry (LC-MS/MS) to assess serum and liver tissue bile acid profiles in the *i.p.* chronic *E. multilocularis*-infected mouse model and evaluated the effects of the anthelmintic drug ABZ. Additionally, hepatic mRNA and protein expression of enzymes and transporters regulating bile acid concentrations were analyzed. AE significantly decreased unconjugated bile acids in serum and liver tissue. Taurine-conjugated bile salts were unchanged or increased in the serum and unchanged or decreased in the liver. Ratios of unconjugated to taurine-conjugated metabolites are proposed as useful serum markers of AE. The expression of the bile acid synthesis enzymes cytochrome P450 (CYP) 7A1 and aldo-keto reductase (AKR) 1D1 tended to decrease or were decreased in mice with AE, along with decreased expression of the bile acid transporters Na+/taurocholate cotransporting polypeptide (NTCP) and bile salt efflux pump (BSEP). Importantly, treatment with ABZ partially or completely reversed the effects induced by *E. multilocularis* infection. ABZ itself had no effect on the bile acid profiles and the expression of relevant enzymes and transporters. Further research is needed to uncover the exact mechanism of the AE-induced changes in bile acid homeostasis and to test whether serum bile acids and ratios thereof can serve as biomarkers of AE and for monitoring therapeutic efficacy.

Keywords: bile acid; BSEP; NTCP; alveolar echinococcosis; *Echinococcus multilocularis*; albendazole; LC-MS/MS

Citation: Gómez, C.; Jebbawi, F.; Weingartner, M.; Wang, J.; Stücheli, S.; Stieger, B.; Gottstein, B.; Beldi, G.; Lundström-Stadelmann, B.; Odermatt, A. Impact on Bile Acid Concentrations by Alveolar Echinococcosis and Treatment with Albendazole in Mice. *Metabolites* **2021**, *11*, 442. https://doi.org/10.3390/metabo11070442

Academic Editor: Shozo Tomonaga

Received: 15 June 2021
Accepted: 3 July 2021
Published: 6 July 2021

1. Introduction

Human alveolar echinococcosis (AE) caused by *Echinococcus multilocularis* is a severe liver disease with high morbidity and poor prognosis when handled inappropriately [1,2]. In the Northern Hemisphere, 0.3 to 3 per 1,000,000 inhabitants get infected with *E. multilocularis* annually, with the numbers increasing [1–3]. Adult stages of the tapeworm are mainly noted in the intestine of red and arctic foxes, although domestic dogs and cats can also act as definitive hosts [3,4]. A prevalence of <1.5% was found in privately owned rural and urban pet dogs, whereas it was between 3% and 8% in dogs with free access

to rodent habitats, such as farm dogs and hunting dogs. The course of the infection is characterized by a long-term, primarily intrahepatic growth of the metacestode (larval stage) in the intermediate host, including small mammals such as mice [5]. In humans, invasion of the bile ducts by *E. multilocularis* leads to cholangitis and portal hypertension, and the disease can progress to liver cirrhosis after a long latent, asymptomatic period [5,6].

A characteristic feature of AE is the tumor-like growth of the metacestode, which may lead to infiltration of neighboring organs. The only curative treatment is surgical resection of the metacestode tissue, supported by pre- and post-operative chemotherapy [2]. Treatment in inoperable AE cases consists of a long-term and often life-long administration of benzimidazoles albendazole (ABZ) or mebendazole. Long-term treatment with benzimidazoles is required because these drugs are parasitostatic but not parasiticidal, and adverse reactions, including severe hepatotoxicity, are frequently observed [2,7,8].

Although it is well known that impaired liver function in situations such as cholestasis and cirrhosis or in drug-induced liver injury can have profound effects on bile salt homeostasis, little is known whether serum or intrahepatic bile salts are altered during *E. multilocularis* infection and whether this is influenced by the ABZ treatment.

Primary bile acids are synthesized from cholesterol by a complex multistep pathway in hepatocytes [9,10]. The so-called classic (or neutral) pathway starts by introducing a hydroxy-group at the 7α-position of cholesterol, catalyzed by CYP7A1, which constitutes the rate-limiting step of hepatic bile acid biosynthesis. CYP7A1 expression and activity is controlled by various transcription factors and feedback mechanisms. The alternative (or acidic) pathway is initiated by the side chain hydroxylation of cholesterol through sterol 27-hydroxylase (CYP27A1) and is primarily extrahepatic. The primary di- and trihydroxy bile acids are conjugated with taurine or glycine and exported from hepatocytes across the canalicular membrane by the bile salt export pump (BSEP) into the canaliculi, from where they drain with bile into the upper small intestine. The ratio of dihydroxy to trihydroxy bile acids as well as the ratio of glycine to taurine conjugates are different between species and hence result in species-specific bile salt pool compositions [11]. Bile salts are the main organic component of bile [12,13].

Most of the bile acids are absorbed by active transport in the distal ileum and transported back to the liver via the portal vein, while some part is metabolized by the gut flora into secondary bile acids [9,10,14]. In the liver, bile salts are transported from the portal blood plasma across the basolateral membrane on hepatocytes by numerous transport proteins. While Na^+-taurocholate cotransporting polypeptide (NTCP) predominantly transports bile salts and organic anion transporters (OATPs) predominantly mediate the uptake of bile acids from the blood plasma through the basolateral membrane into the hepatocytes [15–19], BSEP represents the rate-limiting step in the secretion of bile salts into the bile fluid. Inherited and acquired forms of liver diseases, which impair proper BSEP function, can lead to intracellular accumulation of bile acids in hepatocytes, i.e., cholestasis. If persistent, cholestasis can cause hepatocellular damage or even cell death [16,17,19]. Elevated hepatocellular levels of bile acids lead to the activation of the farnesoid X receptor (FXR), which directly downregulates CYP7A1 expression and indirectly the sinusoidal uptake transporter NTCP, but upregulates the efflux transporter BSEP to reduce the concentration of intracellular bile salts [16,17,19]. FXR activation upon hepatic bile acid accumulation also increases sinusoidal bile acid efflux by inducing the expression of multidrug resistance-associated protein (MRP)4 and heterodimeric organic solute transporters (OST)α/OSTβ (SLC51A/SLC51B) [14,15,18,20,21].

In many hepatic and intestinal diseases, serum bile acid concentrations are altered due to impaired hepatic synthesis and metabolism and/or intestinal absorption. Thus, serum bile acid concentrations may serve as prognostic and diagnostic markers of liver dysfunctions and diseases [22–26]. Consequently, the present study assessed changes in serum and liver tissue bile acid profiles in mice infected *i.p.* with metacestodes of *E. multilocularis* using ultra-high performance liquid chromatography–tandem mass spectrometry (LC-MS/MS). Furthermore, the effect of the currently most frequently used treatment,

i.e., ABZ, on the serum and intrahepatic bile acid profiles was assessed. Additionally, the mRNA and protein expression levels of key bile salt transporters and enzymes involved in bile acid synthesis were studied in liver tissues.

2. Results

2.1. Murine Model of Alveolar Echinococcosis

In the present investigation, we analyzed serum and liver tissue samples from a previous study on innate and adaptive immune responses in mice infected *i.p.* with metacestodes of *E. multilocularis* and treated with vehicle or ABZ [27]. The natural mode of infection (or primary infection) of intermediate hosts with *E. multilocularis* represents peroral uptake of infectious eggs, which also includes the first phase of intrahepatic parasite development. However, such a model is rarely applied in experimental infection due to the limited availability of infectious eggs for experimental infection, the high risk for the experimenter, and the necessity of high biosafety precautions. The most commonly applied, secondary murine AE infection model includes *i.p.* inoculation of *E. multilocularis* metacestode tissue suspension, mimicking a chronic infection. In this model, the parasite mostly grows in the peritoneal cavity. A macroscopic and histological assessment in an earlier study [27] thus did not detect any visible parasitic structures within the livers of any mouse, but inflammatory cell infiltrates with elevated levels of pro-inflammatory cytokines were observed in infected mice. Furthermore, the treatment efficacy of ABZ was demonstrated in the previous study by a significantly reduced parasite weight (isolated from the peritoneal cavity), the histopathology (immune cell infiltration), and reduced liver tissue cytokine levels.

2.2. Bile Acid Profiles

To assess the potential effects of *E. multilocularis* infection and its main treatment ABZ on the serum bile acid profiles in mice, a recently established LC-MS/MS-based method was applied to quantify a series of conjugated and unconjugated bile acids [28]. Glycine-conjugated bile acids were at or below the lower limit of detection of the quantification method and are not listed in Table 1. The mean concentrations of each individual bile acid as well as the sums of taurine-conjugated, unconjugated, and total bile acids analyzed for the four treatment groups are listed in Table 1, and data for individual bile acids are shown in Supplementary Figure S1. The concentrations of all unconjugated primary (CA, CDCA, αMCA, βMCA, and ωMCA) and secondary (UDCA, DCA, HDCA, 7oxoDCA, and 12oxoLCA) bile acids were 4.6-fold lower in the AE group compared with the control group. In contrast, the taurine-conjugated bile salts (TCDCA, TUDCA, TDCA, TαMCA, and TωMCA) were either not altered or significantly increased (TCA and TβMCA) in AE compared to non-infected control (CTRL) mice, with 1.5-fold higher levels of total taurine-conjugated bile acids in the AE group. The total circulating bile acids were 2.5-fold lower in the AE compared to CTRL mice.

In addition, bile acids were quantified in the liver tissue using the previously described LC-MS/MS method [28]. The mean concentrations of each individual bile acid in addition to the sums of unconjugated, conjugated, and total bile acids analyzed for the four treatment groups are listed in Table 2, and the data for individual bile acids are depicted in Supplementary Figure S2. The concentrations of all unconjugated bile acids were decreased from 2- to 60-fold in the AE group compared with the control group. CDCA, UDCA, HDCA, and 7oxoDCA had lower values than the limit of detection of the method. The taurine-conjugated bile salts were either not altered or significantly decreased (TUDCA and TαMCA) in AE compared to AE-ABZ mice.

ABZ is the drug of choice to treat AE in humans [1,2]. In this mouse model of AE, ABZ treatment was well tolerated. No significant changes in any of the serum or liver tissue bile acids analyzed were detected in the CTRL-ABZ compared to the CTRL group (Tables 1 and 2, Supplementary Figures S1 and S2), although there was a trend to decreased total unconjugated bile acids and taurine-conjugated bile salts in liver tissues of CTRL-ABZ

mice. Importantly, ABZ treatment of *E. multilocularis*-infected mice partially or completely reversed the changes in serum and liver tissue bile acid concentrations observed in AE mice (compared to AE-ABZ), and the bile acid concentrations of all analyzed metabolites in the AE-ABZ group were comparable to those of the non-infected CTRL group. A comparison of the relative abundance of each individual bile acid in percentage shows highly similar profiles for CTRL, CTRL-ABZ, and AE-ABZ but a clearly distinct profile for the AE group (Figure 1). The graphical representation of the profiling facilitates distinguishing the different treatment groups (Figure 1A for serum profiles and Figure 1B for liver tissue profiles).

Table 1. Effects of *E. multilocularis* infection and ABZ treatment on bile acids in the serum of mice. The serum was collected from non-infected control (CTRL, n = 6), *E. multilocularis*-infected (AE, n = 6), *E. multilocularis*-infected and ABZ-treated (AE-ABZ, n = 5, one outlier with aberrant concentrations was removed), and non-infected and ABZ-treated control mice (CTRL-ABZ, n = 6). * $p < 0.05$ AE vs. CRTL, † $p < 0.05$ AE vs. CTRL-ABZ, and ‡ $p < 0.05$ AE vs. AE-ABZ. Values are expressed as mean ± SD (nM).

Compound	CTRL (n = 6) (nM Mean ± SD)	AE (n = 6) (nM Mean ± SD)	AE-ABZ (n = 5) (nM Mean ± SD)	CTRL-ABZ (n = 6) (nM Mean ± SD)
Unconjugated				
CA	2960 ± 1586	753 ± 761 *,†	2218 ± 2861	2760 ± 1521
CDCA	305 ± 148	70 ± 34 *,†	237 ± 200	365 ± 346
ωMCA	3074 ± 1654	489 ± 192 *,†	1744 ± 1467	2522 ± 741
αMCA	554 ± 385	44 ± 37 *,†	287 ± 308	463 ± 399
βMCA	4747 ± 3497	1080 ± 899 *,†	4452 ± 4387	4131 ± 2559
UDCA	590 ± 358	122 ±81 *,†	784 ± 811	686 ± 549
HDCA	245 ± 95	29 ± 18 *,†	174 ± 137	263 ± 91
DCA	917 ± 261	374 ± 146 *,†	1217 ± 939	1176 ± 654
12oxoLCA	15 ± 6	5 ± 1 *,‡	17 ± 13	14 ± 7
7oxoDCA	686 ± 441	93 ± 74 *,†	443 ± 430	609 ± 305
AlloCA	122 ± 45	18 ± 13 *,†	63 ± 73	119 ± 52
Total unconjugated	**14,215 ± 7740**	**3078 ± 2082 ***	**11,636 ± 11,085**	**13,107 ± 6512**
Taurine-conjugated				
TCA	345 ± 173	920 ± 620 †	305 ± 282	232 ± 110
TCDCA	27 ± 29	40 ± 23	19 ± 8	22 ± 19
TωMCA	970 ± 228	642 ± 208	607 ±446	822 ± 236
TαMCA	253 ± 104	325 ± 188	329 ± 372	244 ± 158
TβMCA	606 ± 285	1396 ± 916 †	578 ± 596	398 ± 187
TUDCA	110 ± 37	120 ± 33	132 ± 80	125 ± 36
TDCA	81 ± 43	137 ± 69	108 ± 72	80 ± 39
Total taurine-conjugated	**2392 ± 755**	**3578 ± 1820**	**2078 ± 1787**	**1924 ± 685**
Total bile acids	**16,607 ± 8135**	**6656 ± 3172**	**13,714 ± 12,722**	**15,031 ± 6963**

Table 2. Effects of *E. multilocularis* infection and ABZ treatment on bile acids in liver tissue of mice. The liver samples were collected from non-infected control (CTRL, n = 6), *E. multilocularis*-infected (AE, n = 6), *E. multilocularis*-infected and ABZ-treated (AE-ABZ, n = 5, one outlier with aberrant concentrations was removed), and non-infected and ABZ-treated control mice (CTRL-ABZ, n = 5, one outlier with aberrant concentrations was removed),). * $p < 0.05$ AE vs. CRTL, † $p < 0.05$ AE vs. CTRL-ABZ, and ‡ $p < 0.05$ AE vs. AE-ABZ. Values are expressed as mean ± SD (pg/mg tissue). ND: Not-detected.

Compound	CTRL (n = 6) (pg/mg Tissue Mean ± SD)	AE (n = 6) (pg/mg Tissue Mean ± SD)	AE-ABZ (n = 5) (pg/mg Tissue Mean ± SD)	CTRL-ABZ (n = 5) (pg/mg Tissue Mean ± SD)
Unconjugated				
CA	8520 ± 9256	151 ± 33 †	2464 ± 3418	1615 ± 631
CDCA	42 ± 31	ND ‡	74 ± 63	43 ± 19
ωMCA	1893 ± 1839	182 ± 43 †	964 ± 1010	768 ± 260
αMCA	1627 ± 1627	79 ± 33 ‡	1466 ± 2108	542 ± 122
βMCA	4583 ± 3791	2312 ± 1080	6533 ± 5483	3748 ± 1778
UDCA	88± 74	ND †,‡	127 ± 90	107 ± 46
HDCA	50 ± 42	ND †,‡	46 ± 9	43 ± 9
DCA	40 ± 22	14 ± 2 *	26 ± 8	30 ± 11
7oxoDCA	1887 ± 2131	ND *,†	519 ± 1041	120 ± 43
Total unconjugated	**18,734 ± 18,314**	**2770 ± 1142**	**12,220 ± 13,172**	**7016 ± 1726**
Conjugated				
TCA	93,465 ± 58,895	53,864 ± 22,985	91,956 ± 95,949	47,978 ± 8176
TCDCA	8584 ± 7344	1980 ± 567	12,736 ± 16,372	5275 ± 2482
TωMCA	43,450 ± 33,129	15,090 ± 5925	23,250 ± 8736	25,676 ± 6107
TαMCA	26,984 ± 21,698	7092 ± 2735 ‡	25,708 ± 21,439	14,464 ± 5161
TβMCA	102,187 ± 65,883	84,403 ± 38,111	93,075 ± 51,320	67,780 ± 20,851
TUDCA	12,737 ± 10,579	2449 ± 815 ‡	15,399 ± 18621	6981 ± 1806
TDCA	8091 ± 5150	2602 ± 1044	6989 ± 6001	4148 ± 1787
TLCA	319 ± 188	83 ± 35	406 ± 353	275 ± 116
T7oxoLCA	316 ± 377	256 ± 273	462 ± 974	63 ± 61
GCA	264 ± 225	112 ± 27	387 ± 427	157 ± 30
Total conjugated	**296,395 ± 198,074**	**167,929 ± 67,355**	**270,370 ± 216,375**	**172,798 ± 39,994**
Total bile acids	**314,865 ± 216,097**	**170,587 ± 67,462**	**282,203 ± 229,000**	**179,657 ± 39,812**

As ratios often show lower inter-individual variations than single analytes, they may represent more robust markers to detect changes in bile acid homeostasis. The ratio of total taurine-conjugated to unconjugated bile acids as well as the ratios of TCA/CA, TαMCA/αMCA, and TβMCA/βMCA were all approximately 10-fold higher compared to the CTRL group in AE mice, followed by complete reversal upon ABZ treatment in the serum samples (Figure 2A and Figure S3, Table 3). The intrahepatic ratios tended to be higher in the AE group compared to the CTRL and the AE-ABZ groups (Figure 2B and Figure S4, Table 3).

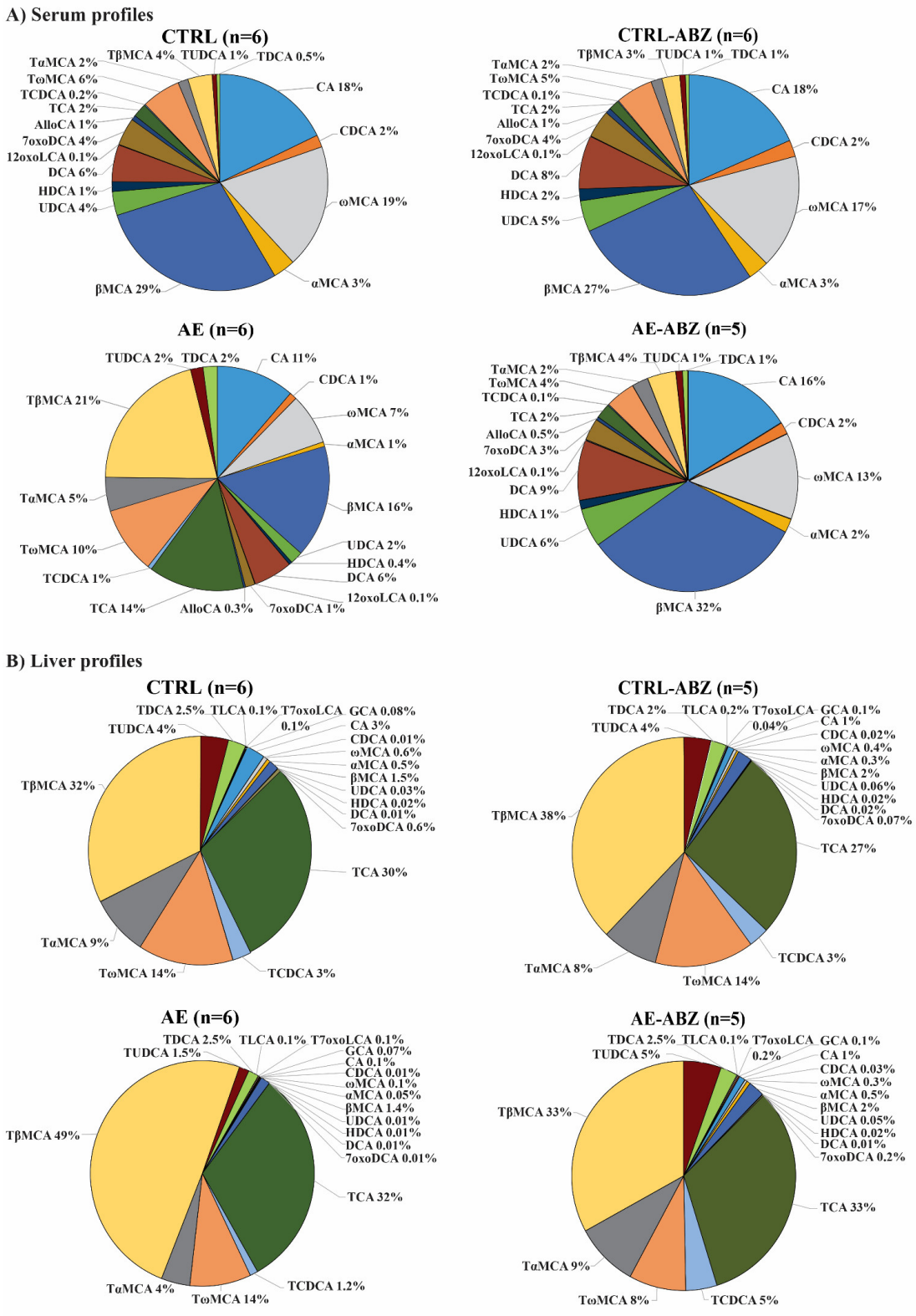

Figure 1. Bile acid profiles of the four different mouse groups in serum (**A**) and in liver tissue (**B**). The relative amounts of individual bile acids, indicated by different colors, are shown for the four different groups: non-infected control (CTRL, n = 6), *E. multilocularis*-infected (AE, n = 6), non-infected and ABZ-treated control (CTRL-ABZ, n = 6 for serum, n = 5 for liver tissue due to exclusion of an outlier), and *E. multilocularis*-infected and ABZ-treated mice (AE-ABZ, n = 5, one outlier with aberrant concentrations was removed). Data represent relative abundances (%) of individual bile acids.

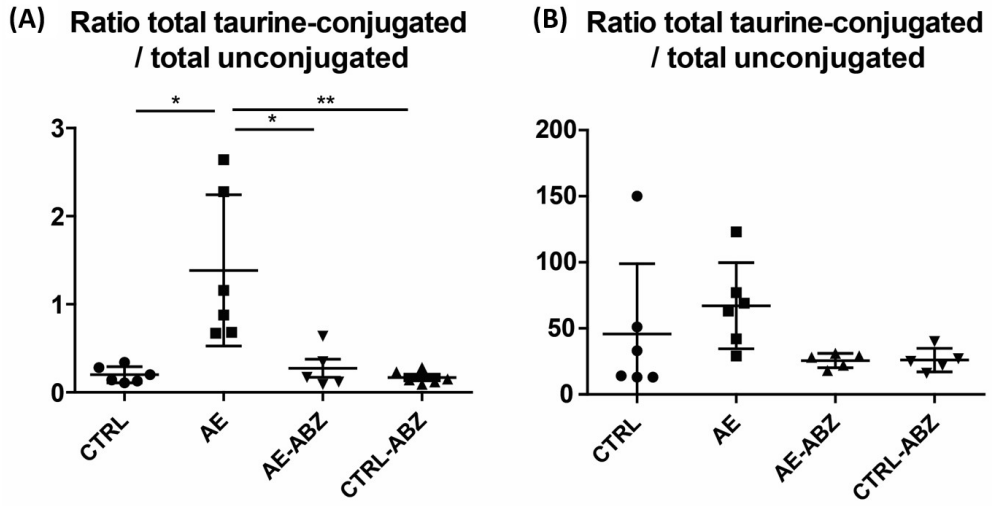

Figure 2. Increased ratio of taurine-conjugated to unconjugated bile acids in AE. The sum of the taurine-conjugated bile acids divided by the sum of unconjugated bile acids was determined in the four different treatment groups, in serum samples (**A**) and liver tissues (**B**). Non-infected control (CTRL, n = 6), *E. multilocularis*-infected (AE, n = 6), *E. multilocularis*-infected and ABZ-treated (AE-ABZ, n = 5, one outlier with aberrant concentrations was removed), and non-infected and ABZ-treated control mice (CTRL-ABZ, n = 6 in serum and n = 5 in liver tissue due to exclusion of an outlier). Values are expressed as mean ± SD. * $p < 0.05$ and ** $p < 0.01$.

Table 3. Increased ratio of taurine-conjugated to unconjugated bile acids in AE. The ratio of total taurine-conjugated to total unconjugated bile acids as well as the ratios of TCA/CA, TαMCA/αMCA, and TβMCA/βMCA were calculated for the four different treatment groups in the serum and liver tissue samples. Non-infected control (CTRL, n = 6), *E. multilocularis*-infected (AE, n = 6), *E. multilocularis*-infected and ABZ-treated (AE-ABZ, n = 5, one outlier with aberrant concentrations was removed), and non-infected and ABZ-treated control mice (CTRL-ABZ, n = 6 in serum and n = 5 in liver tissue due to exclusion of an outlier). Values are expressed as mean ± SD. * $p < 0.05$ AE vs. CTRL, † $p < 0.05$ AE vs. CTRL-ABZ, and ‡ $p < 0.05$ AE vs. AE-ABZ.

Serum	**CTRL (n = 6) (mean ± SD)**	**AE (n = 6) (mean ± SD)**	**AE-ABZ (n = 5) (mean ± SD)**	**CTRL-ABZ (n = 6) (mean ± SD)**
Total taurine-conjugated/total unconjugated	0.20 ± 0.09	1.38 ± 0.86 *,†,‡	0.17 ± 0.07	0.27 ± 0.23
TCA/CA	0.15 ± 0.14	1.63 ± 1.33 *,†,‡	0.25 ± 0.26	0.09 ± 0.02
TαMCA/αMCA	0.72 ± 0.63	9.17 ± 5.74 *,†,‡	1.50 ± 1.04	0.58 ± 0.17
TβMCA/βMCA	0.17 ± 0.10	1.63 ± 1.18 *,†,‡	0.21 ± 0.19	0.12 ± 0.09
Liver tissue	**CTRL (n = 6)** (mean ± SD)	**AE (n = 6)** (mean ± SD)	**AE-ABZ (n = 5)** (mean ± SD)	**CTRL-ABZ (n = 5)** (mean ± SD)
Total taurine-conjugated/total unconjugated	46 ± 53	67 ± 33	26 ± 5	26 ± 9
TCA/CA	156 ± 312	359 ± 146 †	50 ± 14	33 ± 13
TαMCA/αMCA	47 ± 53	104 ± 55	27 ± 9	29 ± 15
TβMCA/βMCA	33 ± 23	41 ± 22	16 ± 4	21 ± 11

2.3. Effect of AE and ABZ Treatment on Enzymes Involved in Bile Acid Synthesis

To assess whether AE and/or the treatment with ABZ affect bile acid synthesis, the mRNA levels of the rate-limiting enzyme Cyp7a1, the sterol 27-hydroxylase Cyp27a1,

which initiates the acidic pathway or alternative pathway for bile acid synthesis, and of the 5β-reductase Akr1d1 were analyzed by quantitative PCR (qPCR). The expression of Cyp7a1, and to a lesser extent that of Cyp27a1, tended to be decreased in the liver tissues of *E. multilocularis*-infected mice (Figure 3). These trends were reversed by treatment with ABZ. Attempts to determine the protein expression of these enzymes in mouse liver tissues failed as no suitable antibodies and conditions could be identified. Regarding the 5β-reductase Akr1d1, significantly lower mRNA levels along with reduced protein levels were observed in liver tissues from AE mice compared to CTRL, and ABZ treatment reversed the decreased mRNA and protein expression.

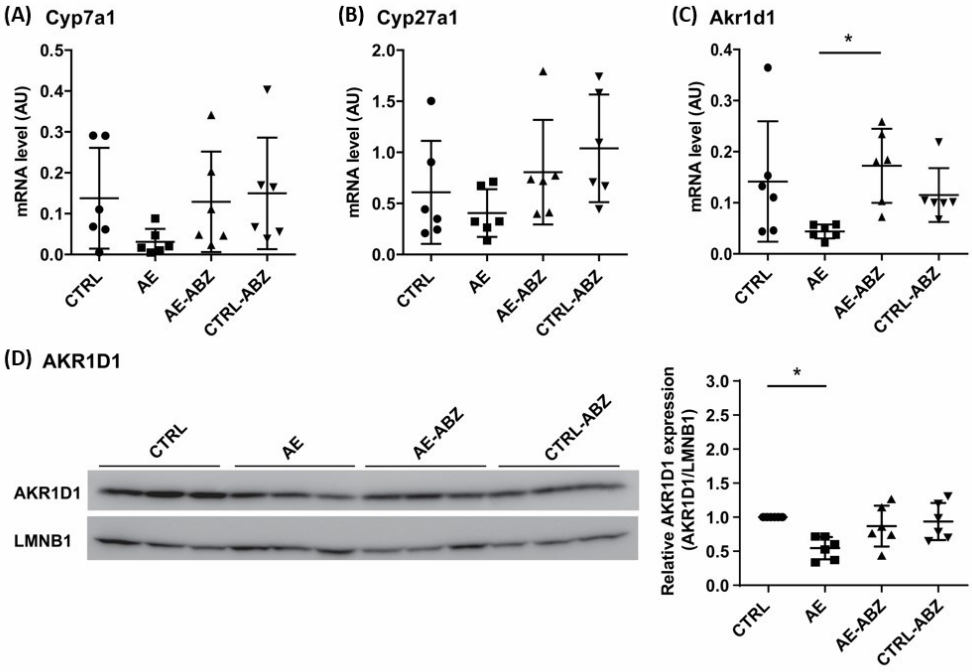

Figure 3. Expression levels of enzymes involved in bile acid synthesis. The mRNA levels of Cyp7a1 (**A**), Cyp27a1 (**B**), and Akr1d1 (**C**) and the protein levels of AKR1D1 (**D**) were determined in the liver tissues of non-infected control (CTRL, n = 6), *E. multilocularis*-infected (AE, n = 6), *E. multilocularis*-infected and ABZ-treated (AE-ABZ, n = 6), and non-infected and ABZ-treated control mice (CTRL-ABZ, n = 6). One representative blot (of two) containing samples from three different mice is shown in (**D**) on the left and densitometry results are shown on the right, representing data from the two blots on samples from six mice, normalized to lamin B1 (LMNB1) control and with CTRL set as 1. Values are expressed as mean ± SD. * $p < 0.05$.

2.4. Influence of AE and ABZ Treatment on the Expression of Bile Acid Transporters

Besides enzymes involved in bile acid synthesis and metabolism, several transport proteins regulate the composition and concentrations of bile acids in the blood, liver tissue, and bile fluid. To investigate a possible involvement of bile acid transporters in the observed alteration of the bile acid profile upon *E. multilocularis* infection, the mRNA levels of Bsep, Ntcp, Ostα, Ostβ, Mrp2, Mrp4, Oatp1a1, and Oatp1b2 were quantified by qPCR. A trend of decrease in Bsep mRNA levels and significantly lower Ntcp mRNA levels were observed in the liver tissues of *E. multilocularis*-infected mice (Figure 4, lower right panel in A and B). Furthermore, a decrease in Ostα and Oatp1b2 mRNA levels and a trend of decrease in Mrp2 mRNA expression was found in the AE group (Supplementary Figure S5). These effects were fully reversed by ABZ treatment, and ABZ itself had no direct effect on any of the genes of bile acid transporters measured. The mRNA levels of Oatp1a1, Mrp4, and Ostβ were not different between the treatment groups.

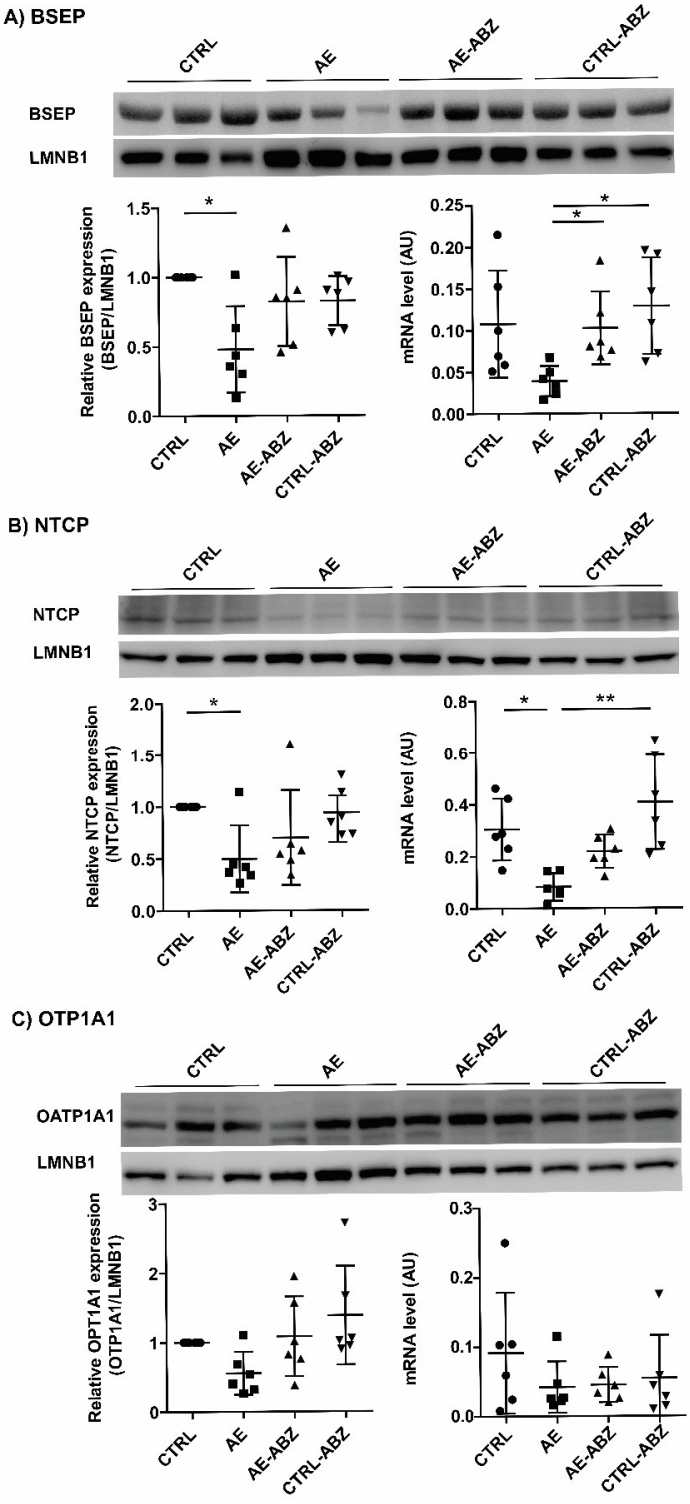

Figure 4. Hepatic mRNA and protein expression levels of BSEP, NTCP, and OATP1A1 in the four treatment groups. Western blot and semi-quantitative analysis by densitometry of protein levels of transporters BSEP (**A**), NTCP (**B**), and OATP1A1 (**C**) in the liver tissues of non-infected control (CTRL, n = 6), *E. multilocularis*-infected (AE, n = 6), *E. multilocularis*-infected and ABZ-treated (AE-ABZ, n = 6), and non-infected and ABZ-treated control mice (CTRL-ABZ, n = 6). One representative blot (of two) containing samples from three different mice is shown in the top panel. Densitometry results represent data from the two blots on samples from six mice (mean ± SD), normalized to lamin B1 (LMNB1) control, and with CTRL set as 1. * $p < 0.05$ and ** $p < 0.01$.

For the assessment of protein expression using western blot analysis, antibodies suitable for BSEP, NTCP, and OATP1A1 were available. Protein expression was analyzed by densitometry and normalized to the house-keeping protein LMNB1. The protein expression levels of the bile acid transporters BSEP and NTCP were both significantly lower in the *E. multilocularis*-infected mice (AE group) compared to the CTRL mice (Figure 4A,B). In contrast, OATP1A1 expression was not significantly altered in any of the four treatment groups (Figure 4C).

3. Discussion

In humans, AE affects the liver as the primary site and progresses by continuous infiltrative proliferation, thereby destroying liver tissue, invading the adjacent organs, and metastasizing to the lungs and the brain [1,6]. The disease progression of AE is usually slow accompanied with underlying inflammation and often not diagnosed until it is well advanced [6,29]. The evaluation of serum bile acid concentrations, including the determination of bile acid profiles as well as ratios of certain bile acids (e.g., taurine-conjugated/unconjugated, CA/CDCA) have the potential as diagnostic markers to distinguish different liver diseases and monitor disease progression and therapeutic efficacy [22–24,26].

For the present study, we used an animal model for chronic infection with an *i.p.* application of metacestodes of *E. multilocularis* to mice. While this model does not show macroscopic changes in livers of infected animals, a diffuse infiltration of immune cells in livers and elevated pro-inflammatory cytokines in the plasma of treated animals is found [27]. Hence, while the animal model does not reproduce completely, the human pathology of AE infection and an oral infection model would more accurately represent it. Our *i.p.* model clearly reproduces the inflammatory component of this disease while avoiding the higher biosafety considerations and limited availability of infections eggs of an oral infection model. The decreased unconjugated bile acids together with unaltered or slightly elevated taurine-conjugated bile salts in plasma and decreased intrahepatic unconjugated bile acid levels and mildly reduced intrahepatic taurine-conjugated bile salts exclude cholestasis in our diseased animals but support a decreased bile salt pool. We can, therefore, not completely rule out that the systemic inflammatory mediators (also seen in other forms of liver disease) contribute on top of inflammatory processes in liver to the alterations in bile acid and bile salt homeostasis in infected mice. This question needs further investigation, including the determination of bile salt pools in the different groups. The ratio of total unconjugated to total taurine-conjugated metabolites as well as that of TCA/CA and TβMCA/βMCA in serum are proposed as useful markers to detect the effect of AE and monitor the efficacy of ABZ treatment in the murine chronic infection model applied. It needs to be noted that in this model of secondary infection, histological analysis did not show any macroscopic changes in the liver, but infiltration of immune cells and elevated pro-inflammatory cytokines were observed [27].

Common symptoms observed in AE patients at a late stage of disease, where hepatic lesions are seen in histological analysis, include jaundice, abdominal pain, and weight loss [6,29,30]. Studies in patients with jaundice showed an altered bile acid metabolism, with an increase in the circulating levels of conjugated bile salts and an elevated ratio of taurine-conjugated to unconjugated bile acids in symptomatic patients [26,31]. The utility of the serum bile acid ratio markers mentioned above should be further studied in animal models, i.e., in mice perorally infected with *E. multilocularis* eggs and at different time points following infection, as well as in humans.

Gene expression analyses of the present study indicated a decreased hepatic bile acid synthesis by lower CYP7A1 and AKR1D1 expression levels, along with decreased canalicular biliary secretion via BSEP, reduced bile acid and bile salt uptake from the portal circulation by NTCP and OATP1B2, and reduced efflux to the general circulation by OSTα and MRP4 (Figure 5). An inhibition of the above-mentioned bile acid transporters may be a result of the hepatic inflammation, shown in the previous study [27], leading to reduced

FXR-mediated activation of SHP and PPARα that are involved in the regulation of the expression of these bile acid transporters [14]. A rapid reduction of bile formation via downregulation of both basolateral bile acids uptake (NTCP) and canalicular efflux system (BSEP) have been observed in response to inflammation [16,20]. A decreased activity of BSEP and OSTα-OSTβ directly relates to decreased bile acid-dependent activation of FXR signaling, which can lead to liver injury [14,18]. The role of inflammation on the bile acid pool in the AE model applied needs further investigations, including analysis of bile flow and bile acid excretion by the kidney and feces.

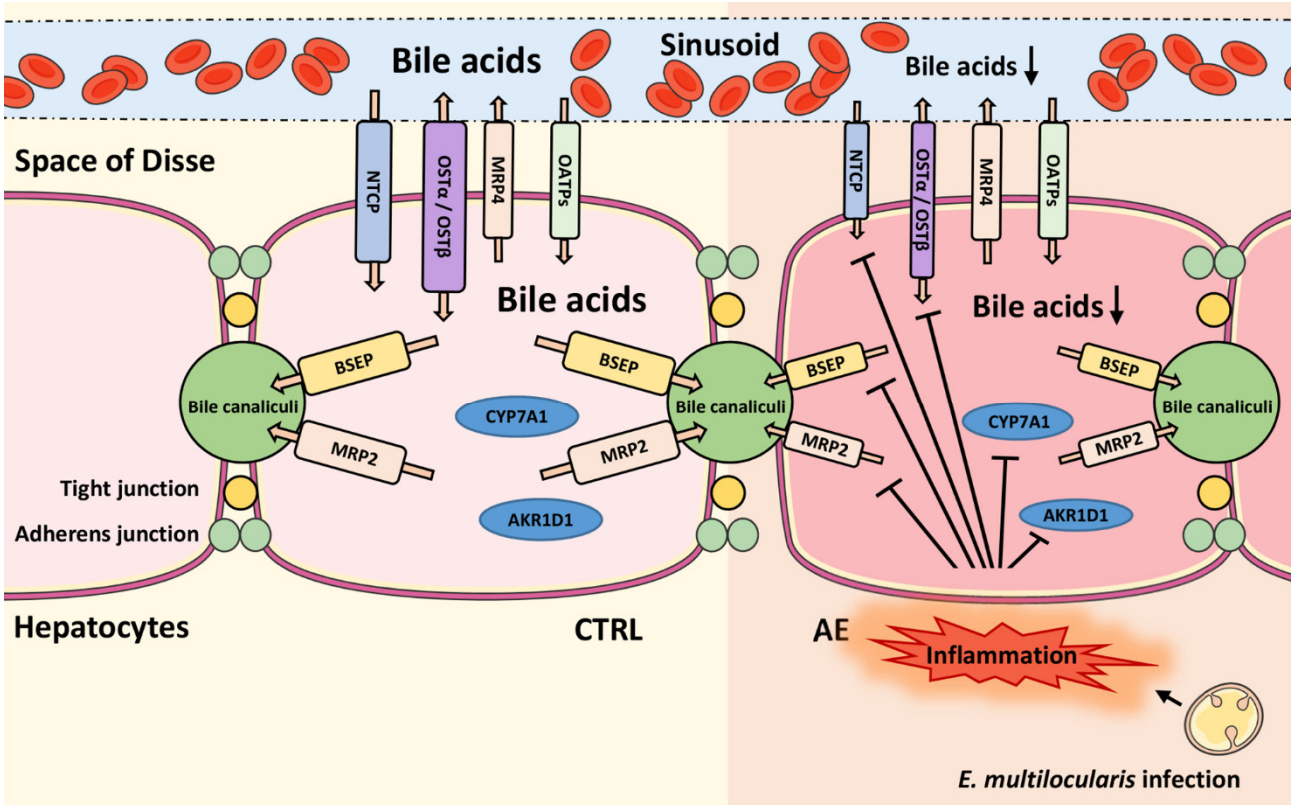

Figure 5. Schematic overview of key transport proteins involved in hepatic bile acid homeostasis. Left panel: situation in hepatocytes of control mice; right panel: model of the situation in hepatocytes in experimental murine alveolar echinococcosis (AE). The *i.p.* infection results in hepatic inflammation, suppressing the expression of the bile acid biosynthesis enzyme cytochrome P450 (CYP) 7A1 and aldo-keto reductase (AKR) 1D1 and of the bile salt transporters bile salt efflux mump (BSEP), multidrug resistance-associated protein (MRP) 2, Na+/taurocholate cotransporting polypeptide (NTCP), and organic solute transporters (OST)α (SLC51A) and OSTβ (SLC51B). OATPs, organic anion transporters; CTRL, control.

In other conditions, such as chronic forms of cholestasis, downregulation of NTCP and upregulation of basolateral bile acid export systems were observed (MRP4 and OSTα-OSTβ) [15,16]. This contrasts the present study on AE, where OSTα and MRP4 were decreased. Moreover, if FXR activity is compromised, one would expect an elevated expression of the rate-limiting bile acid synthesis enzyme CYP7A1. In the liver, TCA, acting as FXR agonist, tended to be lower, while TβMCA, an FXR antagonist [32], was not altered, not supporting profound effects through altered presence of FXR ligands. Unfortunately, bile fluid was not collected, which may provide further mechanistic insight in a follow-on study. Further studies are needed to uncover the mechanism underlying the altered bile acid homeostasis in AE and to elucidate its consequences for AE progression.

Evidence from earlier studies of helminth infections with the liver as the primary affected site indicates an important role of bile acids in the modulation of helminth–host interactions. The liver fluke *Opisthorchis viverrini*, for example, resides in the biliary tree

in an environment of very high bile acid concentrations, and a study in infected hamsters found elevated levels of the secondary bile acid DCA [33], suggesting disturbed activity of the microbiome and/or altered intestinal reuptake of bile acids. Another example includes *Echinococcus granulosus*, where the development of the larvae into secondary hydatid cysts is promoted by bile acids and high levels of bile acids are needed for the development of adult worms [34]. Interestingly, a serum metabolome analysis in Beagle dogs infected with *Toxocara canis* showed that the bile acid CA was increased 24 h post-infection but decreased 10 days after infection, along with a pronounced increase in TCA and TCDCA, thus indicating a shift from unconjugated bile acids to taurine-conjugated bile salts [35], similar to the observed effect in the present study in AE. Furthermore, a study in mice infected with cysticerci of *Taenia crassiceps* showed altered hepatic metabolism with enhanced production of taurine and glycine [36]. Although that study did not assess serum bile acids and salts, the enhanced production of these amino acids suggests an increased capacity for bile acid conjugation. These observations may provide an explanation for the observed shift from conjugated to taurine-conjugated bile acids in AE in the present study, with a potentially higher rate of taurine-conjugation in infected livers. Besides an altered hepatic bile acid metabolism and transport, parasite infections can also disturb intestinal activity and bile acid transport. For example, mice infected with *Trichinella spiralis* displayed gut dysfunction with a decreased bile acid reuptake in the ileum, suggesting an enhanced fecal loss of bile acids [37]. Thus, follow-on experiments should investigate the role of inflammation, microbial bile acid metabolism, bile flow, and intestinal bile acid transport in AE models. Furthermore, it will be important to study the role of FXR, as agonists of this receptor were found to exert protective effects on microbial infections [38–40].

Additionally, the present work showed that ABZ treatment ameliorates *E. multilocularis* infection and almost completely reverses the effects on serum bile acids and gene expression. This further demonstrates the efficacy of ABZ, mainly due to inhibition of parasite proliferation and immune cell infiltration as reported previously [27]. ABZ treatment itself tended to decrease hepatic bile acid concentrations. Whether this may contribute to the hepatotoxic effects seen upon long-term treatment with this drug [41] remains to be investigated. Ultimately, an improved understanding of the pathways involved in the disturbed bile acid homeostasis may help designing novel therapeutic strategies to combat AE in humans, either alone or in combination with benzimidazoles such as ABZ.

4. Materials and Methods

4.1. Chemicals and Reagents

Ultrapure water was obtained using a Milli-Q® Integral 3 purification system equipped with an EDS-Pak® Endfilter for the removal of endocrine active substances (Merck Millipore, Burlington, MA, USA). Acetonitrile (HPLC-S Grade) was purchased from Biosolve (Dieuze, France), methanol (CHROMASOLV™ LC-MS grade) from Honeywell (Charlotte, NC, USA), isopropanol (EMSURE® for analysis) from Merck Millipore, and formic acid (Puriss. p.a. $\geq$ 98%) from Sigma-Aldrich (St. Louis, MO, USA). Bile acids and internal standards were purchased from Sigma-Aldrich or Steraloids (Newport, RI, USA) as described recently [28].

4.2. Mice

Female C57BL/6 mice (8 weeks old, n = 24) were housed under standard conditions in a conventional daylight/night cycle room. The mice were fed a standard pellet chow and water ad libitum. All experiments were performed in accordance with the Federation of European Laboratory Animal Science Association (FELASA) guidelines. The experiments performed in this animal study were reviewed and accepted by the cantonal veterinary authority of the Canton of Bern, Switzerland, and were performed in agreement with the guidelines for care and use of laboratory animals (license BE-112/17).

The mice were randomly divided into four groups: (1) non-infected control (CTRL, n = 6), (2) *E. multilocularis* infected (AE, n = 6), *E. multilocularis* infected treated with

albendazole (AE-ABZ, n = 6), and (4) non-infected treated with ABZ (CTRL-ABZ, n = 6). The animals were examined daily for their health status and changes in weight during the experimental period. All animal experiments were conducted within a laminar flow safety hood. At the end of the experimental part, the mice were euthanized using CO_2. The blood was collected and the serum was separated by centrifugation at 3000× *g* for 15 min. The serum samples were kept at −80 °C for later analysis. Liver tissue was immediately collected, frozen in liquid nitrogen, and stored at −80 °C for later analysis.

Infection with *E. multilocularis* metacestodes was performed by *i.p.* injection [27]. Briefly, *E. multilocularis* (isolate H95) was extracted and maintained by serial passages in C57BL/6 mice. Aseptic removal of infectious material from the abdominal cavity of previously infected animals was used for propagation of AE in mice. The collected tissue was grinded through a sterile 50 µm filter, roughly 100 vesicular cysts were suspended in 100 µL sterile PBS and administrated via *i.p.* injection to groups 2 (AE) and 3 (AE-ABZ). The mice of control groups 1 (CTRL) and 4 (CTRL-ABZ) received 100 µL of sterile PBS. The ABZ treatment started after 6 weeks of initial infection. The mice of groups 1 (CTRL) and 2 (AE) were administered 100 µL corn oil and those of groups 3 (AE-ABZ) and 4 (CTRL-ABZ) received 100 µL ABZ in corn oil (200 mg/kg mouse/injection) orally five times per week. The treatment was terminated after 8 weeks by euthanizing the examined animals. The serum and liver tissue samples were used from a previous study [27].

4.3. Quantification of Bile Acids in Serum

Bile acids were quantified as described recently [28]. Briefly, 10 µL of serum were diluted 1:4 with water, followed by adding 900 µL of 2-propanol for protein precipitation and a mixture of deuterated internal standards. Extraction was performed by continuous shaking for 30 min at 4 °C and centrifugation at 16,000× *g* for 10 min. Supernatants were transferred to new tubes, evaporated to dryness, and reconstituted with 100 µL of methanol to water (1:1, *v*/*v*). Samples were analyzed by LC-MS/MS, consisting of an Agilent 1290 UPLC coupled to an Agilent 6490 triple quadrupole mass spectrometer equipped with an electrospray ionization (ESI) source (Agilent Technologies, Basel, Switzerland). Chromatographic separation of the bile acids was achieved using reversed-phase column (ACQUITY UPLC BEH C18, 1.7 mm, 2.1 µm, 150 mm, Waters, Wexford, Ireland).

4.4. Quantification of Bile Acids in Liver Tissue

Bile acid extraction from liver tissue samples has been described previously [28]. Briefly, liver tissue (20 ± 5 mg) was homogenized in 900 µL of chloroform:methanol:water (1:3:1, *v*/*v*/*v*) and 100 µL internal standard mixture using a Precellys tissue homogenizer (Bertin Instruments, Montigny-le-Bretonneux, France) with three cycles of 30 s at 6500 rpm with 30 s break between cycles. The samples were centrifuged (10 min, 20 °C, 16,000× *g*) and supernatant was transferred to a new tube. Another 800 µL of extraction solvent were added to the samples and the process was repeated. Combined supernatant (1600 µL) was evaporated using a Genevac EZ-2 (SP Scientific, Warminster, PA, USA) and the dried samples resuspended in 200 µL methanol:water (1:1, *v*/*v*). Then, 3 µL was injected into a liquid chromatrography–tandem mass spectrometry system, consisting of an Agilent 1290 UPLC coupled to an Agilent 6490 triple quadrupole mass spectrometer with an electrospray ionization source (Agilent Technologies, Basel, Switzerland). The bile acid analytes were separated using a reversed-phase column (Acquity UPLC BEH C18, 1.7 mm, 2.1 mm, 150 mm; Waters, Wexford, Ireland).

4.5. Total RNA Extraction and qPCR

Total RNA was isolated from the liver tissues using the Qiagen RNeasy MiniKit and QIAcube instrument according to the manufacturer's protocol (SABioscience, Frederick, MD, USA). The quality and concentration of RNA was determined using a Nanodrop™ one C (Cat#13-400-519, Thermo Fisher Scientific, Waltham, MA, USA). Only samples with a 260 nm to 280 nm ratio between 1.9 and 2.1 and a 260 nm to 230 nm ratio between 1.5 and

2.0 were further processed. cDNA was synthesized using GoScript Reverse Transcriptase (Cat#A5003, Promega, Madison, WI, USA). The KAPA SYBR Fast Kit (Cat# SFUKB, Merck, Darmstadt, Germany) was used for qPCR analysis, and the reactions were performed on a Rotor Gene real-time cycler (Corbett Research, Sydney, New South Wales, Australia). The data were normalized to the expression levels of the endogenous control gene β-actin. The primers are listed in Supplementary Table S1.

4.6. Protein Expression/Western Blot

Approximately 7 mg of frozen liver tissues were homogenized (6500 rpm, 30 s, 4 °C, Precellys 24 tissue homogenizer) in 450 µL RIPA buffer (50 mM Tris-HCl, pH 8.0, with 150 mM sodium chloride, 1.0% NP-40, 0.5% sodium deoxycholate, and 0.1% sodium dodecyl sulfate) containing protease inhibitor cocktail (Cat#11836153001, Merck, Darmstadt, Germany) and centrifuged (4 min, 4 °C, 16,000× *g*). Protein concentration in supernatants was measured using standard bicinchoninic acid assay (Pierce BCA Protein Assay Kit, Thermo Fisher Scientific). The samples were heated (5 min at 95 °C) in Laemmli solubilization buffer (LSB; 60 mM Tris-HCl, 10% glycerol, 0.01% bromophenol blue, 2% sodium dodecyl sulfate, pH 6.8, and 5% β-mercaptoethanol) and 20 µg of total protein were separated by 8–14% SDS-PAGE and transferred to PVDF membranes (Immobilon-P Membran, PVDF, pore size: 0.45 µm). The membranes were blocked (1 h, 25 °C) in TBST containing 5% nonfat dry milk (5% nonfat dry milk powder in 20 mM Tris-HCl with 0.1% Tween-20) or 1% bovine serum albumin (in 20 mM Tris-HCl with 0.1% Tween-20). AKR1D1 protein expression was determined using mouse monoclonal anti-AKR1D1 antibody (1:1000, 4 °C, overnight). The washed membranes were incubated with HRP-conjugated secondary goat anti-mouse antibody (1:4000, 25 °C, 1 h). BSEP protein expression was analyzed using a rabbit polyclonal anti-BSEP antibody [42] (1:4000, 4 °C, overnight). The membrane was washed and incubated with HRP-conjugated secondary goat anti-rabbit antibody (1:4000, 25 °C, 1 h). OATP1A1 protein expression was determined using a rabbit polyclonal anti-OATP1A1 antibody [43] (1:1000, 4 °C, overnight) and HRP-conjugated secondary goat anti-rabbit antibody (1:4000, 25 °C, 1 h). Protein levels of NTCP were measured using rabbit polyclonal anti-NTCP antibody [44] (1:1000, 4 °C overnight) and HRP-conjugated secondary goat anti-rabbit antibody (1:4000). LMNB1 served as loading control and was detected using rabbit monoclonal anti-LMNB1 antibody (1:1000, 4 °C, overnight) followed by HRP-conjugated secondary goat anti-rabbit antibody (1:2000, 25 °C, 1 h). Protein bands were visualized by Immobilon Western Chemiluminescence HRP substrate and semi-quantitatively analyzed by densitometry, normalized to LMNB1 protein levels, using Image J software (RRID:SCR_003070, version 1.53n).

4.7. Data Analysis and Statistics

For LC-MS/MS data, MassHunter Acquisition Software (Agilent Technologies, Inc., Santa Clara, CA, USA) and MassHunter Quantitative Analysis vB.07.01 (Agilent Technologies, Inc., Santa Clara, CA, USA) were used for quantification. The Kruskal–Wallis test and Dunn's multiple comparison were used to analyze significance of differences between groups. Grubbs' test was performed to determine outliers. Statistical significance was established at $p < 0.05$. Statistical analysis and graphs were performed using GraphPad Prism v5.02 (GraphPad Software, Inc., San Diego, CA, USA).

5. Conclusions

This work applied LC-MS/MS to quantify bile acids in serum and liver tissue samples of mice infected with *E. multilocularis* in the absence or presence of the parasitostatic drug ABZ. The results revealed decreased unconjugated bile acids and unchanged or increased taurine-conjugated bile salts in the serum, suggesting the use of ratios of unconjugated to taurine-conjugated metabolites as markers for AE and to monitor therapeutic efficacy. Gene expression analyses showed decreases in bile acid synthesis enzymes and in key transport proteins. ABZ, which did not substantially affect bile acid homeostasis itself,

reversed the observed effects on serum and liver tissue bile acids and on gene expression. Follow-on studies need to uncover the exact mechanism underlying the observed effects and to evaluate the bile acid ratio markers in AE and its treatment.

Supplementary Materials: The following are available online at https://www.mdpi.com/article/10.3390/metabo11070442/s1: Table S1: Optimized MRM transitions used as quantifiers and qualifiers, electrospray ionization (ESI) mode (positive (+) or negative (-)), and collision energies (CE); Table S2: Oligonucleotide primers for mRNA quantification by qPCR; Figure S1: Concentrations of individual bile acids quantified in serum of mice from the four treatment groups; Figure S2: Concentrations of individual bile acids quantified in liver tissue of mice from the four treatment groups; Figure S3: Increased ratios of taurine-conjugated to unconjugated bile acids in AE in serum; Figure S4: Increased ratios of taurine-conjugated to unconjugated bile acids in AE in liver tissue; Figure S5: Effect of AE on mRNA expression levels of additional bile acid transporters.

Author Contributions: Conceptualization and methodology, M.W., F.J., C.G. and J.W.; data acquisition and analysis, M.W., F.J., S.S., J.W. and C.G; writing—original draft preparation, C.G., M.W., F.J., J.W., B.S., B.G., G.B., B.L.-S. and A.O.; writing—review and editing, M.W., F.J., C.G., S.S., J.W., B.S., B.G., G.B., B.L.-S. and A.O.; supervision, A.O.; project administration, A.O.; funding acquisition, A.O. and B.L.-S. All authors have read and agreed to the published version of the manuscript.

Funding: The Swiss National Science Foundation, grant number 31003A-179400 (to A.O.) and 31003A-179439 (to B.L.-S.) funded this research.

Institutional Review Board Statement: The study was conducted according to the guidelines of the Declaration of Helsinki. All experiments were performed in accordance with the Federation of European Laboratory Animal Science Association (FELASA) guidelines and approved by the cantonal veterinary authority of the Canton of Bern, Switzerland (license BE-112/17).

Informed Consent Statement: Not applicable.

Data Availability Statement: All raw data files to the presented experiments will be available at https://zenodo.org/, accessed on 15 June 2021.

Acknowledgments: This study was supported by the Swiss National Science Foundation, Grant number 31003A-179400 (to A.O.) and 31003A-179439 (to B.L.-S.).

Conflicts of Interest: The authors declare no conflict of interest.

References

1. Craig, P. Echinococcus multilocularis. *Curr. Opin. Infect. Dis.* **2003**, *16*, 437–444. [CrossRef] [PubMed]
2. Hemphill, A.; Stadelmann, B.; Rufener, R.; Spiliotis, M.; Boubaker, G.; Müller, J.; Müller, N.; Gorgas, D.; Gottstein, B. Treatment of echinococcosis: Albendazole and mebendazole-what else? *Parasite* **2014**, *21*, 70. [CrossRef] [PubMed]
3. Deplazes, P.; Rinaldi, L.; Alvarez Rojas, C.A.; Torgerson, P.R.; Harandi, M.F.; Romig, T.; Antolova, D.; Schurer, J.M.; Lahmar, S.; Cringoli, G.; et al. *Global Distribution of Alveolar and Cystic Echinococcosis*; Elsevier Ltd.: Amsterdam, The Netherlands, 2017; Volume 95, pp. 315–493.
4. Kato, N.; Nonaka, N.; Oku, Y.; Kamiya, M. Modified cellular immune responses in dogs infected with Echinococcus multilocularis. *Parasitol. Res.* **2005**, *95*, 339–345. [CrossRef] [PubMed]
5. Gottstein, B.; Hemphill, A. Echinococcus multilocularis: The parasite-host interplay. *Exp. Parasitol.* **2008**, *119*, 447–452. [CrossRef] [PubMed]
6. Graeter, T.; Ehing, F.; Oeztuerk, S.; Mason, R.A.; Haenle, M.M.; Kratzer, W.; Seufferlein, T.; Gruener, B. Hepatobiliary complications of alveolar echinococcosis: A long-term follow-up study. *World J. Gastroenterol.* **2015**, *21*, 4925–4932. [CrossRef] [PubMed]
7. Lundström-Stadelmann, B.; Rufener, R.; Ritler, D.; Zurbriggen, R.; Hemphill, A. The importance of being parasiticidal . . . an update on drug development for the treatment of alveolar echinococcosis. *Food Waterborne Parasitol.* **2019**, *15*, e00040. [CrossRef] [PubMed]
8. Wen, H.; Vuitton, L.; Tuxun, T.; Li, J.; Vuitton, D.A.; Zhang, W.; McManus, D.P. Echinococcosis: Advances in the 21st century. *Clin. Microbiol. Rev.* **2019**, *32*, 1–39. [CrossRef]
9. Chiang, J.Y.L.L. Bile acids: Regulation of synthesis. *J. Lipid Res.* **2009**, *50*, 1955–1966. [CrossRef]
10. Russell, D.W.; Setchell, K.D.R. Bile Acid Biosynthesis. *Biochemistry* **1992**, *31*, 4737–4749. [CrossRef]
11. Thakare, R.; Alamoudi, J.A.; Gautam, N.; Rodrigues, A.D.; Alnouti, Y. Species differences in bile acids I. Plasma and urine bile acid composition. *J. Appl. Toxicol.* **2018**, *38*, 1323–1335. [CrossRef]
12. Esteller, A. Physiology of bile secretion. *World J. Gastroenterol.* **2008**, *14*, 5641–5649. [CrossRef] [PubMed]
13. Boyer, J.L. Bile formation and secretion. *Compr. Physiol.* **2013**, *3*, 1035–1078. [CrossRef] [PubMed]

14. Jia, W.; Xie, G.; Jia, W. Bile acid–microbiota crosstalk in gastrointestinal inflammation and carcinogenesis. *Nat. Rev. Gastroenterol. Hepatol.* **2018**, *15*, 111–128. [CrossRef] [PubMed]
15. Dawson, P.A.; Lan, T.; Rao, A. Bile acid transporters. *J. Lipid Res.* **2009**, *50*, 2340–2357. [CrossRef] [PubMed]
16. Stieger, B. The Role of the Sodium-taurocholate cotransporting polypeptide (NTCP) and of the bile salt export pump (BSEP) in physiology and pathophysiology of bile Formation. In *Drug Transporters*; Springer: Berlin/Heidelberg, Germany, 2011; Volume 201, ISBN 9783642145407.
17. Cheng, X.; Buckley, D.; Klaassen, C.D. Regulation of hepatic bile acid transporters Ntcp and Bsep expression. *Biochem. Pharmacol.* **2007**, *74*, 1665–1676. [CrossRef] [PubMed]
18. Alrefai, W.A.; Gill, R.K. Bile Acid Transporters: Structure, Function, Regulation and Pathophysiological Implications. *Pharm. Res.* **2007**, *24*, 1803–1823. [CrossRef]
19. Slijepcevic, D.; Van De Graaf, S.F.J. Bile Acid Uptake Transporters as Targets for Therapy. *Dig. Dis.* **2017**, *35*, 251–258. [CrossRef]
20. Halilbasic, E.; Claudel, T.; Trauner, M. Bile acid transporters and regulatory nuclear receptors in the liver and beyond. *J. Hepatol.* **2013**, *58*, 155–168. [CrossRef]
21. Mennone, A.; Soroka, C.J.; Cai, S.-Y.; Harry, K.; Adachi, M.; Hagey, L.; Schuetz, J.D.; Boyer, J.L. Mrp4−/− mice have an impaired cytoprotective response in obstructive cholestasis. *Hepatology* **2006**, *43*, 1013–1021. [CrossRef]
22. Sugita, T.; Amano, K.; Nakano, M.; Masubuchi, N.; Sugihara, M.; Matsuura, T. Analysis of the serum bile acid composition for differential diagnosis in patients with liver disease. *Gastroenterol. Res. Pract.* **2015**, *2015*, 717431. [CrossRef]
23. Luo, L.; Aubrecht, J.; Li, D.; Warner, R.L.; Johnson, K.J.; Kenny, J.; Colangelo, J.L. Assessment of serum bile acid profiles as biomarkers of liver injury and liver disease in humans. *PLoS ONE* **2018**, *13*, e0193824. [CrossRef]
24. Manzotti, C.; Casazza, G.; Stimac, T.; Nikolova, D.; Gluud, C. Total serum bile acids or serum bile acid profile, or both, for the diagnosis of intrahepatic cholestasis of pregnancy. *Cochrane Database Syst. Rev.* **2019**, *2019*, CD012546. [CrossRef] [PubMed]
25. Cepa, S.; Potter, D.; Wong, L.; Schutt, L.; Tarrant, J.; Pang, J.; Zhang, X.; Andaya, R.; Salphati, L.; Ran, Y.; et al. Individual serum bile acid profiling in rats aids in human risk assessment of drug-induced liver injury due to BSEP inhibition. *Toxicol. Appl. Pharmacol.* **2018**, *338*, 204–213. [CrossRef] [PubMed]
26. Makino, I.; Nakagawa, S.; Mashimo, K. Conjugated and Unconjugated Serum Bile Acid Levels in Patients with Hepatobiliary Diseases. *Gastroenterology* **1969**, *56*, 1033–1039. [CrossRef]
27. Jebbawi, F.; Bellanger, A.; Lunström-Stadelmann, B.; Rufener, R.; Dosch, M.; Goepfert, C.; Gottstein, B.; Millon, L.; Grandgirard, D.; Leib, S.L.; et al. Innate and adaptive immune responses following PD-L1 blockade in treating chronic murine alveolar echinococcosis. *Parasite Immunol.* **2021**, e12834. [CrossRef]
28. Gómez, C.; Stücheli, S.; Kratschmar, D.V.; Bouitbir, J.; Odermatt, A. Development and Validation of a Highly Sensitive LC-MS/MS Method for the Analysis of Bile Acids in Serum, Plasma, and Liver Tissue Samples. *Metabolites* **2020**, *10*, 282. [CrossRef] [PubMed]
29. Liu, Y.H.; Wang, X.G.; Chen, Y.T. Computerized tomography of liver in alveolar echinococcosis treated with albendazole. *Zhonghua Nei Ke Za Zhi* **1993**, *32*, 733–735. [PubMed]
30. Rosenfeld, G.; Nimmo, M.; Hague, C.; Buczkowski, A.; Yoshida, E.M. Echinococcus presenting as painless jaundice. *Can. J. Gastroenterol.* **2012**, *26*, 684–685. [CrossRef] [PubMed]
31. Jenniskens, M.; Langouche, L.; Vanwijngaerden, Y.M.; Mesotten, D.; Van den Berghe, G. Cholestatic liver (dys)function during sepsis and other critical illnesses. *Intensive Care Med.* **2016**, *42*, 16–27. [CrossRef]
32. Sayin, S.I.; Wahlström, A.; Felin, J.; Jäntti, S.; Marschall, H.U.; Bamberg, K.; Angelin, B.; Hyötyläinen, T.; Orešič, M.; Bäckhed, F. Gut microbiota regulates bile acid metabolism by reducing the levels of tauro-beta-muricholic acid, a naturally occurring FXR antagonist. *Cell Metab.* **2013**, *17*, 225–235. [CrossRef]
33. Vale, N.; Gouveia, M.J.; Botelho, M.; Sripa, B.; Suttiprapa, S.; Rinaldi, G.; Gomes, P.; Brindley, P.J.; Correia da Costa, J.M. Carcinogenic liver fluke Opisthorchis viverrini oxysterols detected by LC-MS/MS survey of soluble fraction parasite extract. *Parasitol. Int.* **2013**, *62*, 535–542. [CrossRef] [PubMed]
34. Zheng, H.; Zhang, W.; Zhang, L.; Zhang, Z.; Li, J.; Lu, G.; Zhu, Y.; Wang, Y.; Huang, Y.; Liu, J.; et al. The genome of the hydatid tapeworm Echinococcus granulosus. *Nat. Genet.* **2013**, *45*, 1168–1175. [CrossRef] [PubMed]
35. Zheng, W.B.; Zou, Y.; Elsheikha, H.M.; Liu, G.H.; Hu, M.H.; Wang, S.L.; Zhu, X.Q. Serum metabolomic alterations in Beagle dogs experimentally infected with Toxocara canis. *Parasites Vectors* **2019**, *12*, 1–10. [CrossRef]
36. Corbin, I.; Blackburn, B.J.; Wolowiec, T.; Novak, M. Metabolic profile of the liver of mice infected with cysticerci of *Taenia crassiceps*. *Parasitol. Int.* **1996**, *82*, 273–275. [CrossRef] [PubMed]
37. Kalia, N.; Hardcastle, J.; Keating, C.; Pelegrin, P.; Grundy, D.; Grasa, L.; Bardhan, K.D. Intestinal secretory and absorptive function in Trichinella spiralis mouse model of postinfective gut dysfunction: Role of bile acids. *Gut* **2008**, *57*, 41–48. [CrossRef] [PubMed]
38. Zhang, C.; Gan, Y.; Lv, J.W.; Qin, M.Q.; Hu, W.R.; Liu, Z.B.; Ma, L.; Song, B.D.; Li, J.; Jiang, W.Y.; et al. The protective effect of obeticholic acid on lipopolysaccharide-induced disorder of maternal bile acid metabolism in pregnant mice. *Int. Immunopharmacol.* **2020**, *83*, 106442. [CrossRef] [PubMed]
39. Wu, Z.Y.; Li, H.; Li, J.R.; Lv, X.Q.; Jiang, J.D.; Peng, Z.G. Farnesoid X receptor agonist GW4064 indirectly inhibits HCV entry into cells via down-regulating scavenger receptor class B type I. *Eur. J. Pharmacol.* **2019**, *853*, 111–120. [CrossRef] [PubMed]
40. Mouzannar, K.; Fusil, F.; Lacombe, B.; Ollivier, A.; Ménard, C.; Lotteau, V.; Cosset, F.L.; Ramière, C.; André, P. Farnesoid X receptor-α is a proviral host factor for hepatitis B virus that is inhibited by ligands in vitro and in vivo. *FASEB J.* **2019**, *33*, 2472–2483. [CrossRef]

41. Stadelmann, B.; Rufener, R.; Aeschbacher, D.; Spiliotis, M.; Gottstein, B.; Hemphill, A. Screening of the Open Source Malaria Box Reveals an Early Lead Compound for the Treatment of Alveolar Echinococcosis. *PLoS Negl. Trop. Dis.* **2016**, *10*, e0004535. [CrossRef]
42. Gerloff, T.; Stieger, B.; Hagenbuch, B.; Madon, J.; Landmann, L.; Roth, J.; Hofmann, A.F.; Meier, P.J. The sister of P-glycoprotein represents the canalicular bile salt export pump of mammalian liver. *J. Biol. Chem.* **1998**, *273*, 10046–10050. [CrossRef]
43. Eckhardt, U.; Schroeder, A.; Stieger, B.; Höchli, M.; Landmann, L.; Tynes, R.; Meier, P.J.; Hagenbuch, B. Polyspecific substrate uptake by the hepatic organic anion transporter Oatp1 in stably transfected CHO cells. *Am. J. Physiol. Gastrointest. Liver Physiol.* **1999**, *276*, 1037–1042. [CrossRef] [PubMed]
44. Stieger, B.; Hagenbuch, B.; Landmann, L.; Höchli, M.; Schroeder, A.; Meier, P.J. In situ localization of the hepatocytic na+/taurocholate cotransporting polypeptide in rat liver. *Gastroenterology* **1994**, *107*, 1781–1787. [CrossRef]

6.5 Albendazole reduces hepatic inflammation and endoplasmic reticulum-stress in a mouse model of chronic Echinococcus multilocularis infection

Published Article

Michael Weingartner[1#], Simon Stücheli[1#], Fadi Jebbawi[1#], Bruno Gottstein[2,3], Guido Beldi[4], Britta Lundström-Stadelmann[2], Junhua Wang[2,3‡], and Alex Odermatt[1‡]

[1] Division of Molecular and Systems Toxicology, Department of Pharmaceutical Sciences, University of Basel, Basel, Switzerland.

[2] Institute for Infectious Diseases, Faculty of Medicine, University of Bern, Bern, Switzerland.

[3] Institute of Parasitology, Department of Infectious Diseases and Pathobiology, Vetsuisse Faculty, University of Bern, Bern, Switzerland.

[4] Department of Visceral Surgery and Medicine, University Hospital of Bern, Bern, Switzerland.

[#] These authors contributed equally as first author to the present study.

[‡] These authors contributed equally as senior author to the present study.

Contribution to the project:

Experimental work

Analysis, interpretation, and visualization of data

Revising the manuscript

PLOS NEGLECTED TROPICAL DISEASES

RESEARCH ARTICLE

Albendazole reduces hepatic inflammation and endoplasmic reticulum-stress in a mouse model of chronic *Echinococcus multilocularis* infection

Michael Weingartner[1☯], Simon Stücheli[1☯], Fadi Jebbawi[1☯], Bruno Gottstein[2,3], Guido Beldi[4], Britta Lundström-Stadelmann[2], Junhua Wang[2,3]*, Alex Odermatt[1]*

1 Division of Molecular and Systems Toxicology, Department of Pharmaceutical Sciences, University of Basel, Basel, Switzerland, **2** Institute for Infectious Diseases, Faculty of Medicine, University of Bern, Bern, Switzerland, **3** Institute of Parasitology, Department of Infectious Diseases and Pathobiology, Vetsuisse Faculty, University of Bern, Bern, Switzerland, **4** Department of Visceral Surgery and Medicine, University Hospital of Bern, Bern, Switzerland

☯ These authors contributed equally to this work.
* junhua.wang@ifik.unibe.ch (JW); alex.odermatt@unibas.ch (AO)

OPEN ACCESS

Citation: Weingartner M, Stücheli S, Jebbawi F, Gottstein B, Beldi G, Lundström-Stadelmann B, et al. (2022) Albendazole reduces hepatic inflammation and endoplasmic reticulum-stress in a mouse model of chronic *Echinococcus multilocularis* infection. PLoS Negl Trop Dis 16(1): e0009192. https://doi.org/10.1371/journal.pntd.0009192

Editor: Klaus Brehm, University of Würzburg, GERMANY

Received: January 30, 2021

Accepted: December 20, 2021

Published: January 14, 2022

Data Availability Statement: All relevant data are within the manuscript and in its supporting information files. All related data sets are accessible at https://zenodo.org/ under the following DOIs: Fig 1: https://doi.org/10.5281/zenodo.5837948) Fig 2: https://doi.org/10.5281/zenodo.5838107) Fig 3: https://doi.org/10.5281/zenodo.5838117) Fig 4: https://doi.org/10.5281/zenodo.5838137) S1 Fig: https://doi.org/10.5281/zenodo.5838151) S2 Fig: https://doi.org/10.5281/

Abstract

Background

Echinococcus multilocularis causes alveolar echinococcosis (AE), a rising zoonotic disease in the northern hemisphere. Treatment of this fatal disease is limited to chemotherapy using benzimidazoles and surgical intervention, with frequent disease recurrence in cases without radical surgery. Elucidating the molecular mechanisms underlying *E. multilocularis* infections and host-parasite interactions ultimately aids developing novel therapeutic options. This study explored an involvement of unfolded protein response (UPR) and endoplasmic reticulum-stress (ERS) during *E. multilocularis* infection in mice.

Methods

E. multilocularis- and mock-infected C57BL/6 mice were subdivided into vehicle, albendazole (ABZ) and anti-programmed death ligand 1 (αPD-L1) treated groups. To mimic a chronic infection, treatments of mice started six weeks post *i.p.* infection and continued for another eight weeks. Liver tissue was then collected to examine inflammatory cytokines and the expression of UPR- and ERS-related genes.

Results

E. multilocularis infection led to an upregulation of UPR- and ERS-related proteins in the liver, including ATF6, CHOP, GRP78, ERp72, H6PD and calreticulin, whilst PERK and its target eIF2α were not affected, and IRE1α and ATF4 were downregulated. ABZ treatment in *E. multilocularis* infected mice reversed, or at least tended to reverse, these protein expression changes to levels seen in mock-infected mice. Furthermore, ABZ treatment reversed the elevated levels of interleukin (IL)-1β, IL-6, tumor necrosis factor (TNF)-α and interferon

zenodo.5838159) S3 Fig: https://doi.org/10.5281/zenodo.5838170) S4 Fig: https://doi.org/10.5281/zenodo.5838181) S3 Table: https://doi.org/10.5281/zenodo.5838187).

Funding: This study was supported by the Swiss National Science Foundation grant number 31003A-179400 to AO and grant number 31003A-179439 to BLS. http://www.snf.ch. The funders had no role in study design, data collection and analysis, decision to publish, or preparation of the manuscript.

Competing interests: The authors have declared that no competing interests exist.

(IFN)-γ in the liver of infected mice. Similar to ABZ, αPD-L1 immune-treatment tended to reverse the increased CHOP and decreased ATF4 and IRE1α expression levels.

Conclusions and significance

AE caused chronic inflammation, UPR activation and ERS in mice. The *E. multilocularis*-induced inflammation and consecutive ERS was ameliorated by ABZ and αPD-L1 treatment, indicating their effectiveness to inhibit parasite proliferation and downregulate its activity status. Neither ABZ nor αPD-L1 themselves affected UPR in control mice. Further research is needed to elucidate the link between inflammation, UPR and ERS, and if these pathways offer potential for improved therapies of patients with AE.

Author summary

Alveolar echinococcosis (AE) is a zoonotic disease, characterized by chronic progressive hepatic damage caused by the continuous tumor-like proliferation of the larval stage (metacestode) of the fox tapeworm *Echinococcus multilocularis*. Treatment of this fatal disease is limited to surgical intervention, preferably radical curative surgery if possible, and the use of parasitostatic benzimidazoles. It is not yet fully understood how the parasite can remain in the host's tissue for prolonged periods, complicating the development of therapeutic applications. This work investigated an involvement of the unfolded protein response (UPR) and endoplasmic reticulum-stress (ERS) during *E. multilocularis* infection and upon treatment with either albendazole (ABZ) or anti-programmed death ligand-1 (αPD-L1) in mice. The results revealed increased expression levels of the ERS sensor ATF6 and of downstream target genes in liver tissue of *E. multilocularis*- compared to mock-infected mice. Additionally, hexose-6-phosphate dehydrogenase (H6PD), generating NADPH within the endoplasmic reticulum, and the lectin-chaperone calreticulin were increased in *E. multilocularis* infected liver tissue while the expression of the ERS associated genes ATF4 and IRE1α were decreased. The observed gene expression changes were at least partially reversed by ABZ treatment, which also reduced the AE-induced increase of the inflammatory cytokines IL-1β, IL-6, TNF-α and IFN-γ. PD-L1 blockade reversed the AE-induced changes of UPR and ERS associated proteins CHOP, ATF4 and IRE1α. Further investigation is needed to elucidate the link between inflammation and ERS in human patients with AE and whether modulation of these pathways may lead to improved therapy.

Introduction

Alveolar echinococcosis (AE) is a severe helminth disease caused by accidental ingestion of eggs from the fox tapeworm *Echinococcus multilocularis* [1,2]. After an incubation period of 5 up to 15 years without perceivable symptoms, AE has a fatal outcome in up to 90% of cases when left untreated [3–5]. AE is characterized by a slow but progressive tumor-like growth of metacestodes (larval stage) mainly in the liver, with a tendency to spread to various organs like spleen, brain, heart and other tissues such as bile ducts and blood vessels [6–8]. The variable clinical outcomes of AE development depend on the immunological status, and the specific immunological profile with T cell exhaustion seems to play an important role in the established tolerance state in chronic AE [9–11].

Treatment by radical surgical resection is limited by the diffuse infiltrations of AE lesions in liver and other tissues in advanced cases [12,13]. If lesions cannot be completely removed by surgery, a lifelong medication is required, usually using benzimidazoles, which can cause adverse side effects. For example, several cases with hepatotoxic effects due to treatment with the benzimidazole albendazole (ABZ) were reported with various outcomes [14–17]. An inadequate adherence to chemotherapy, due to adverse side effects, and development of resistance can explain the relapsing spread of AE and a worsening general condition of patients with severe *E. multilocularis* infiltrations [11,18,19]. Recent experiments using mice indicated a requirement of functional T cell immunity for efficient treatment of AE with ABZ [20]. Considering these circumstances, the rising number of reported cases of AE especially in Europe and the lack of a curative drug treatment, emphasizes the necessity to further investigate the mechanisms underlying this threat and search for improved therapeutic options [21–26].

Several bacteria and viruses have been described to modulate unfolded protein response (UPR) and endoplasmic reticulum stress (ERS), either by bacterial virulence factors such as toxins (*e.g.* cholera toxin, pore-forming toxins) or by the increased demand of newly synthesized proteins for the production of virions [27–32]. Activation of the UPR via an induction of glucose-regulated protein 78 (GRP78) has previously been shown in cells infected with *Human immunodeficiency virus* (HIV) [31,33], *Dengue virus* (DENV) [34], *West Nile virus* (WNV) [35] or *Human cytomegalovirus* (HCMV) [36]. Moreover, facilitated replication of viruses and immune evasion represent key features following UPR activation by *Mouse hepatitis virus* (MHV) [37] and *Herpes simplex virus 1* (HSV-1) [38]. On the other hand, an ERS-induced upregulation of UPR-related genes was linked with an enhanced production of pro-inflammatory cytokines in monocytes and B-cells [39–41]. A modulation of the UPR pathway was reported not only during viral but also bacterial infections. *Legionella pneumophila* infection led to an inhibition of X-box binding protein 1 (XBP1) splicing in mammalian host cells, thereby suppressing the host UPR pathway [42]. *Mycobacterium tuberculosis* was found to induce ERS, indicated by increased CCAAT/enhancer-binding protein homologous protein (CHOP) and GRP78 protein levels in infected macrophages, leading to host cell apoptosis. Decreased levels of phosphorylated eukaryotic initiation factor 2α (eIF2α) in infected cells were associated with enhanced bacterial survival [43].

However, to date the knowledge of pathogen-induced ERS and UPR activation is incomplete; it is mainly limited to bacterial and viral infections and little is known on extracellular pathogens. A modulation of the host's UPR with an upregulation of CHOP was observed in *Toxoplasma gondii* infected cells, leading to apoptosis of host cells [44]. Another study in a mouse model provided evidence that *Plasmodium berghei* exploits the host's UPR machinery for its survival [45]. However, the involvement of ERS and UPR activation in *E. multilocularis* infection has not been studied in detail to our knowledge.

Several studies revealed a functional interaction between UPR/ERS signaling and the expression of microRNAs (miRs), small non-coding single stranded RNAs (17–24 nucleotides) that regulate the post-transcriptional levels of mRNAs by inhibiting their translation to proteins [46,47]. Silencing of miRs was found to be involved in ERS signaling and miRs act as effectors and modulators of the UPR and ERS pathways [48]. The miRs, isolated from human specimen, including urine, saliva, serum and tissues, are considered as biomarkers of several immune pathologies such as cancer, autoimmune diseases and viral or bacterial infections [49–55]. A recent study revealed miR-125b-5p to be elevated in the plasma of AE patients [56]. Furthermore, recent investigations provided evidence for a role of some miRs in the regulation of UPR signaling, with miR-181a-5p and miR-199a-5p shown to suppress the UPR master regulator GRP78 [48,57,58]. On the other side, UPR pathways also can affect the expression of some miRs, as shown by inositol-requiring enzyme 1α (IRE1α) that cleaves anti-apoptotic

miR-17, miR-34a, miR-96 and miR-125b, preventing them from negatively regulating the expression of caspase 2 and thioredoxin-interacting protein [59,60]. In addition, the activation of protein kinase R (PKR)-like ER kinase (PERK) induces the expression of miR-30c-2-3p, which downregulates XBP1, representing a possible negative crosstalk between PERK and IRE1α [61]. Boubaker *et al.* [62] recently described a murine miR signature in response to early stage, primary *E. multilocularis* egg infection where the expression of several miRs was either decreased or increased in AE-infected compared to mock-infected mice.

The present study addressed how the expression of UPR- and ERS-related genes was affected in liver tissue in a mouse model of chronic *E. multilocularis* infection and whether alterations in miRs might be involved. Moreover, the effect of ABZ and αPD-L1 treatment on UPR and ERS pathways as well as on levels of proinflammatory cytokines in the liver were assessed. A better understanding of a contribution of proteins of the UPR and ERS pathways in the context of infectious diseases is of interest regarding the development of improved therapeutic strategies to cope with parasitic infections [63–65].

Materials and methods

Ethics statement

Animals were housed according to the Federation of European Laboratory Animal Science Association (FELASA) guidelines. The animal studies were performed in compliance with the recommendations of the Swiss Guidelines for the Care and Use of Laboratory Animals. The protocol used for this work was approved by the governmental Commission for Animal Experimentation of the Canton of Bern (approval no. BE112/17).

Chemicals and reagents

Polyvinylidene difluoride (PVDF) membranes (Cat# IPVH00010, pore size: 0.45 μm), Immobilon Western Chemiluminescence horseradish-peroxidase (HRP) substrate kit, radioimmunoprecipitation assay (RIPA) buffer, β-mercaptoethanol, HRP-conjugated goat anti-mouse secondary antibody (Cat# A0168, RRID:AB_257867), rabbit polyclonal anti-hexose-6-phosphate dehydrogenase (H6PD) antibody (Cat# HPA004824, RRID:AB_1079037), protease inhibitor cocktail, dNTPs, and KAPA SYBR FAST qPCR kit (Cat# KK4618) were purchased from Merck (Darmstadt, Germany). RNeasy Mini kit and QIAcube were obtained from Qiagen (Venlo, Netherlands), GoScript reverse transcriptase (Cat# A5003) from Promega (Fitchburg, WI, USA), rabbit monoclonal anti-Lamin B1 antibody (Cat# ab133741, RRID: AB_2616597) and rabbit polyclonal anti-phospho (S724) IRE1α antibody (Cat# ab48187, RRID:AB_873899) from Abcam (Cambridge, UK) and mouse monoclonal anti-GRP78 antibody (Cat# 610978, RRID:AB_398291) from BD Bioscience (Franklin Lakes, NJ, USA). HRP-conjugated goat anti-rabbit secondary antibody (Cat# 7074, RRID:AB_2099233), mouse monoclonal anti-CHOP antibody (Cat# 2895, RRID:AB_2089254), rabbit polyclonal anti-calreticulin (CRT) antibody (Cat# 2891, RRID:AB_2275208), rabbit polyclonal anti-eIF2α antibody (Cat# 9722, RRID:AB_2230924), rabbit monoclonal anti-ATF4 antibody (Cat# 11815, RRID:AB_2616025), rabbit monoclonal anti-ATF6 antibody (Cat# 65880, RRID: AB_2799696), rabbit monoclonal anti-phospho (S51) eIF2α antibody (Cat# 3597, RRID: AB_390740), and rabbit monoclonal anti-XBP1-s antibody (Cat# 12782S, RRID:AB_2687943) were purchased from Cell Signaling (Cambridge, UK). Mouse monoclonal anti-PERK antibody (Cat# sc-377400, RRID:AB_2762850), anti-IRE1α antibody (Cat# sc-390960, RRID: N/A) and anti-ERp72 antibody (Cat# sc-390530, RRID: N/A) were obtained from Santa Cruz Biotechnology (Dallas, TX, USA). Pierce bicinchoninic acid protein assay kit, Nanodrop One C (Cat# 13-400-519), and Trizol total RNA isolation reagent and rabbit monoclonal anti-

phospho (T980) PERK antibody (Cat# MA5-15033, RRID:AB_10980432) were purchased from Thermo Fisher Scientific (Waltham, MA, USA). Precellys-24 tissue homogenizer was purchased from Bertin Instruments (Montigny-le-Bretonneux, France). Primers for real-time quantitative polymerase chain reaction (RT-qPCR) were obtained from Microsynth (Balgach, Switzerland). TaqMan microRNA Assays, snoRNA234, TaqMan microRNA reverse transcription kit (Cat# 4366596), TaqMan fast advanced master mix (Cat# 4444556), TaqMan probes (Cat# 4427975, Assay IDs 000468, 000389, 000398, 000470, 121135_mat, 000416, 000417, and 001234) and ViiA 7 real-time PCR system (Cat# 4453545) were purchased from Applied Biosystems (Foster City, CA, USA). The mouse luminex cytokine kits and the BioPlex-200 platform were purchased from BioRad Labrotories, Cressier, Switzerland. Rat monoclonal anti-PD-L1 antibody (αPD-L1, Cat# BE0101, RRID:AB_10949073) was purchased from BioXCell (Lebanon, NH, USA). Rabbit polyclonal anti-calnexin (CNX) antibody (Cat# SAB4503258, RRID:AB_10746486) and all other reagents were purchased from Sigma-Aldrich (St. Louis, MO, USA).

Animal experimentation and sampling

Animal experimentation, liver tissue extraction and corresponding liver tissue samples were previously described [10]. Briefly, female 8-week-old wild type C57BL/6 mice were randomly distributed into 6 groups with 6 animals per group: 1) mock-infected (corn oil treated) control mice (referred to as "CTRL"); 2) *E. multilocularis* infected, vehicle treated mice (referred to as "AE"); 3) *E. multilocularis* infected, ABZ-treated mice (referred to as "AE-ABZ"); 4) mock-infected, ABZ-treated mice (referred to as "ABZ"); 5) *E. multilocularis* infected, αPD-L1 treated mice (referred to as "AE-αPD-L1"); and 6) mock-infected, αPD-L1-treated mice (referred to as "αPD-L1") (S1 Fig). All animals were housed under standard conditions in a conventional daylight/night cycle room with access to feed and water *ad libitum* and in accordance with the Federation of European Laboratory Animal Science Association (FELASA) guidelines. During the experimental period animals were examined weekly for subjective presence of health status and changes in weight. At the end of the experiment the mice were euthanized by CO_2 and liver tissue was resected followed by immediate freezing in liquid nitrogen and storage at -80˚C until use. Parasitic structures were visible only in the liver of some of the infected mice, and the upper part from the left lobe of the liver (1.5 × 1.5 cm) was collected, irrespective of the presence or absence of parasite lesions.

Parasite preparation and secondary infection of mice by intraperitoneal administration

Infection with *E. multilocularis* by *i.p.* injection was conducted as previously described [10]. Briefly, *E. multilocularis* (isolate H95) was extracted and maintained by serial passages in C57BL/6-mice. Aseptic removal of infectious material from the abdominal cavity of infected animals was used for continuation of AE in mice. Collected tissue was grinded through a sterile 50 μm sieve, roughly 100 vesicular cysts were suspended in 100 μL sterile PBS and administrated *via* intraperitoneal injection to group 2 ("AE"), 3 ("AE-ABZ") and 5 ("AE-αPD-L1"). Mice of the mock-infected groups 1 ("CTRL"), 4 ("ABZ") and 6 ("αPD-L1") received 100 μL of sterile PBS.

Treatment

As described earlier [10], treatment of mice started 6 weeks after initial infection and continued for another 8 weeks (S1 Fig). Mice of the groups 1 and 2 ("CTRL", "AE", respectively) received 100 μL PBS by *i.p.* injection twice/week and 100 μL corn oil orally 5 times/week. Mice

of group 3 and 4 ("AE-ABZ" and "ABZ", respectively) received 100 μL corn oil containing ABZ (200 mg/kg body weight) orally five times/week and 100 μL PBS by *i.p.* injection twice/week. Mice of group 5 and 6 ("AE-αPD-L1" and "αPD-L1", respectively) received αPD-L1 antibody in 100 μL PBS *via i.p.* injection twice/week (200 μg/injection) and 100 μL corn oil orally 5 times/week. At end of treatment all mice were euthanized.

Luminex for quantification of hepatic cytokine levels

Cytokine levels in mouse liver samples were assessed undiluted using microsphere-based multiplex assays according to the manufacturer's instructions; concentrations of the following cytokines were measured: IL-1β, IL-6, TNF-α and INF-γ, using mouse luminex cytokine kits (BioRad Labrotories, Cressier, Switzerland). At least 50 beads per analyte were measured on a Bioplex-200 platform (BioRad). Calibration was performed using BioPlex Manager version 4.1.1 by linear regression analysis using the four lowest standards provided by the manufacturer. If measured cytokine concentrations were below the detection limit, a value corresponding to the detection limit of the assay was used for statistical analysis.

Analysis of protein expression by Western blotting

The procedures for liver sample preparation and Western blotting have been previously described [66]. Briefly, liver samples (approximately 7 mg) were homogenized (30s, 6500 rpm, at 4˚C, using a Precellys-24 tissue homogenizer) in 450 μL RIPA buffer (50 mM Tris-HCl, pH 8.0, with 150 mM NaCl, 1.0% NP-40, 0.5% sodium deoxycholate and 0.1% sodium dodecyl sulfate) containing protease inhibitor cocktail and centrifuged (4 min, 16,000 × g, 4˚C). Protein concentration was measured by a standard bicinchoninic acid assay (Pierce BCA Protein Assay Kit). Samples were boiled (5 min at 95˚C) in Laemmli solubilization buffer (60 mM Tris-HCl, 10% glycerol, 0.01% bromophenol blue, 2% sodium dodecyl sulfate, pH 6.8, 5% β-mercaptoethanol). The protein extract (20 μg) was separated by 7.5–14% SDS-PAGE and blotted on PVDF membranes. The membranes were blocked (1 h, room temperature) in TBST-BSA, (20 mM Tris buffered saline with 0.1% Tween-20, 1% bovine serum albumin). All primary and secondary antibody dilutions and incubations were performed in TBST-BSA. For the detection of primary antibodies raised in rabbit, secondary HRP-conjugated goat anti-rabbit antibody was used. Primary antibodies raised in mouse were detected by HRP-conjugated goat anti-mouse antibody. Primary antibodies were incubated at 4˚C over-night. Secondary antibodies were applied at room temperature for 1 h. Protein content was visualized by Immobilon Western Chemiluminescence HRP substrate. Protein bands were quantified by densitometry normalized to Lamin B1 protein levels using ImageJ software (version 1.53n). The applications of primary and secondary antibodies can be found in S1 Table.

Quantification of mRNA by RT-qPCR

Liver samples were prepared as described recently [10]. Total RNA was isolated from liver tissue (approximately 8 mg) by homogenization (30 s, 6500 rpm, 4˚C; Precellys-24 tissue homogenizer) in 350 μL RLT buffer (RNeasy Mini Kit) supplied with 40 mM dithiothreitol, followed by centrifugation (3 min, 16 000 × g, 4˚C). The supernatant was further processed according to the manufacturer's protocol for RNA isolation from animal tissues and cells using QIAcube. RNA quality and concentration was analyzed using Nanodrop One C. 1000 ng of RNA was transcribed into cDNA using GoScript Reverse Transcriptase. KAPA SYBR FAST Kit was used for RT-qPCR (4 ng of cDNA per reaction in triplicates, 40 cycles) analysis, and reactions were performed using a Rotor Gene Real-Time Cycler (Corbett Research, Sydney, New South Wales, Australia). Data was normalized to the expression levels of the endogenous control

gene β-actin. Comparison of gene expression was performed using the 2-ΔCT-method using β-actin as housekeeping gene [67]. Primers used for RT-qPCR are listed in S2 Table.

Extraction and quantification of miRNA by qPCR

Total RNA was extracted from liver tissues using Trizol total RNA isolation reagent and RNA concentration quantified using Nanodrop One C. TaqMan microRNA assays were used to quantify mature miR expression. SnoRNA234 was used as endogenous control of miR expression. Thus, miR-specific reverse transcription was performed for each miR using 10 ng of purified total RNA and the TaqMan MicroRNA Reverse Transcription kit according to the manufacturer's instructions. Reactions with a volume of 15 μL were incubated for 30 min at 16˚C, 30 min at 42˚C, and 5 min at 85˚C to inactivate the reverse transcriptase. RT-qPCR using the TaqMan Fast Advanced Master Mix and the TaqMan microRNA Assay Mix according to the manufacturer's instructions were run in triplicates at 95˚C for 10 min followed by 40 cycles at 95˚C for 15 s and 60˚C for 1 min. Quantitative miR expression data were acquired and analyzed using the ViiA 7 real-time PCR system.

MicroRNA target predictions

By using the online tools TargetScan Release 7.2 (Whitehead institute, Cambridge, MA, USA, RRID:SCR_010845, [68]), RNA22 Version 2 (Thomas Jefferson University, Philadelphia, PA, USA, RRID:SCR_016507, [69]) and miRDB (MicroRNA Target Prediction Database, RRID: SCR_010848) [70], we screened the 3'-untranslated region (3'UTR) of the genes altered in the AE compared to the control group, *i.e.* ATF4, CHOP, ERp72, IRE1α ATF6, H6PD, GRP78 and calreticulin (S3 Table), for the presence of potential miR binding sites. The selection of the miRs was based on the study by Boubaker *et al.* reporting 28 miRs with significantly altered expression levels in mice after primary *E. multilocularis* infection compared to non-infected mice. Referring to S3 Table, only miRs showing a potential target site in the 3'UTR of our genes of interest were analyzed by qPCR (*i.e.* miR-15a-5p, miR-148a-3p, miR-22-3p, miR-30a-3p, miR-30a-5p, miR-146a-5p, miR-1839-5p).

Statistical analyses

Data are presented as mean ± SD. The significance of the differences between the examined animals were determined by Kruskal-Wallis test followed by Dunn's Multiple Comparison post-test or one-way ANOVA followed by Bonferroni Multiple Comparison post-test, whereby the specific test is indicated in the Figure legend. No outliers were excluded. $^{*}P \leq 0.05$; $^{**}P \leq 0.01$; $^{***}P \leq 0.001$ significantly different as indicated. GaphPad Prism software (version 8.0.2, GraphPad, La Jolla, CA, USA) was used for statistical analysis.

Results

Mouse model of chronic *E. multilocularis* infection

This study employed the secondary murine AE infection model with *i.p.* inoculation of *E. multilocularis* metacestode tissue suspension, mimicking a chronic infection, and used samples from a previous investigation [10]. In this model, parasite proliferation mainly occurs in the peritoneal cavity, and the previous histopathology analysis detected parasitic structures only in some livers of infected mice but revealed immune cell infiltration in all of them [10]. The efficacy of treatment with ABZ and αPD-L1 was shown by a decreased parasite weight in the peritoneum and reduced hepatic immune cell infiltration.

Effects of AE on the expression of proteins related to UPR and ERS pathways

As the present knowledge on the modulation of UPR and ERS pathways by extracellular parasitic infections is limited, this study examined the expression of key proteins related to these pathways in liver tissues of mice *i.p*. infected with *E. multilocularis*. The *E. multilocularis* infection resulted in differential effects on the expression of proteins of the different UPR and ERS branches. GRP78, the master regulator of UPR that is common to all branches, tended to be elevated with 2.7-fold higher levels (Figs 1A, 1G and S2). Among the PERK pathway, ATF4 protein levels were significantly decreased in liver tissue of AE mice compared to mock-infected controls, whereas the expression of PERK itself and its target protein eIF2α were not affected by *E. multilocularis* infection (Fig 1B and 1G). Accordingly, the phosphorylation of eIF2α remained unchanged (Fig 1B–1G) while phosphorylation of PERK could not be detected. However, the most pronounced effects were observed for ERS related proteins of the ATF6 branch of the UPR (Fig 1C–1G). The levels of all three proteins analyzed were elevated in the AE group, whereby the luminal chaperone and protein disulfide isomerase ERp72 and the ERS marker CHOP were 2.0-fold and 4.5-fold increased and ATF6 was 2.2-fold higher than levels in the control group. IRE1α protein expression was decreased by about 3-fold in *E. multilocularis* infected compared to control mouse liver tissues and IRE1α phosphorylation tended to be lower in *E. multilocularis* infected mice (Fig 1D–1G). Since our available antibody was unable to properly detect XBP1 and amount of samples were limited, the expression of XBP1 and its spliced form (XBP1-s) were assessed on the mRNA level instead, which did not reveal significant differences between the treatment groups (S3 Fig).

Additional proteins with a role in ER-redox regulation and ERS include the ER resident lectin chaperones CNX and CRT. Whilst CNX protein levels were unaffected by *E. multilocularis* infection, CRT protein expression was significantly increased in AE mice compared to controls (Fig 1E–1G). Additionally, the expression levels of the luminal NADPH-generating enzyme H6PD were determined, revealing a 2.6-fold higher expression in AE compared to control mice (Fig 1F and 1G).

Treatment with ABZ reverses the effects of AE on proteins involved in UPR and ERS

Treatment of AE mice with 200 mg/kg body weight ABZ (AE-ABZ group), five times per week, has been shown previously to effectively reduce parasite weight without any signs of hepatotoxicity due to drug treatment [10]. In the present study, the same treatment regimen resulted in a reversal of the *E. multilocularis* induced alterations of UPR and ERS related protein expression (Fig 1). Also, the effects on the ER chaperones CNX and the NADPH-generating H6PD were reversed by ABZ treatment. An exception was CHOP that was still upregulated in ABZ treated infected mice. Importantly, ABZ did not cause any significant alterations in the expression of these proteins compared to uninfected, mock-treated control mice (CTRL) (Fig 1). PERK protein levels tended to be increased in ABZ treated but uninfected animals (Fig 1); however, this did not reach significance due to high variance in the detected signals.

Increased miR-146a-5p and miR-1839-5p expression in secondary *E. multilocularis* infection and reversal by ABZ treatment

Boubaker *et al.* [62], using a primary *E. multilocularis* infection mouse model, identified several miRs with altered expression in liver tissues from infected mice. In the present study, the miRs that were significantly altered in the study by Boubaker *et al.* [62] and that possess a

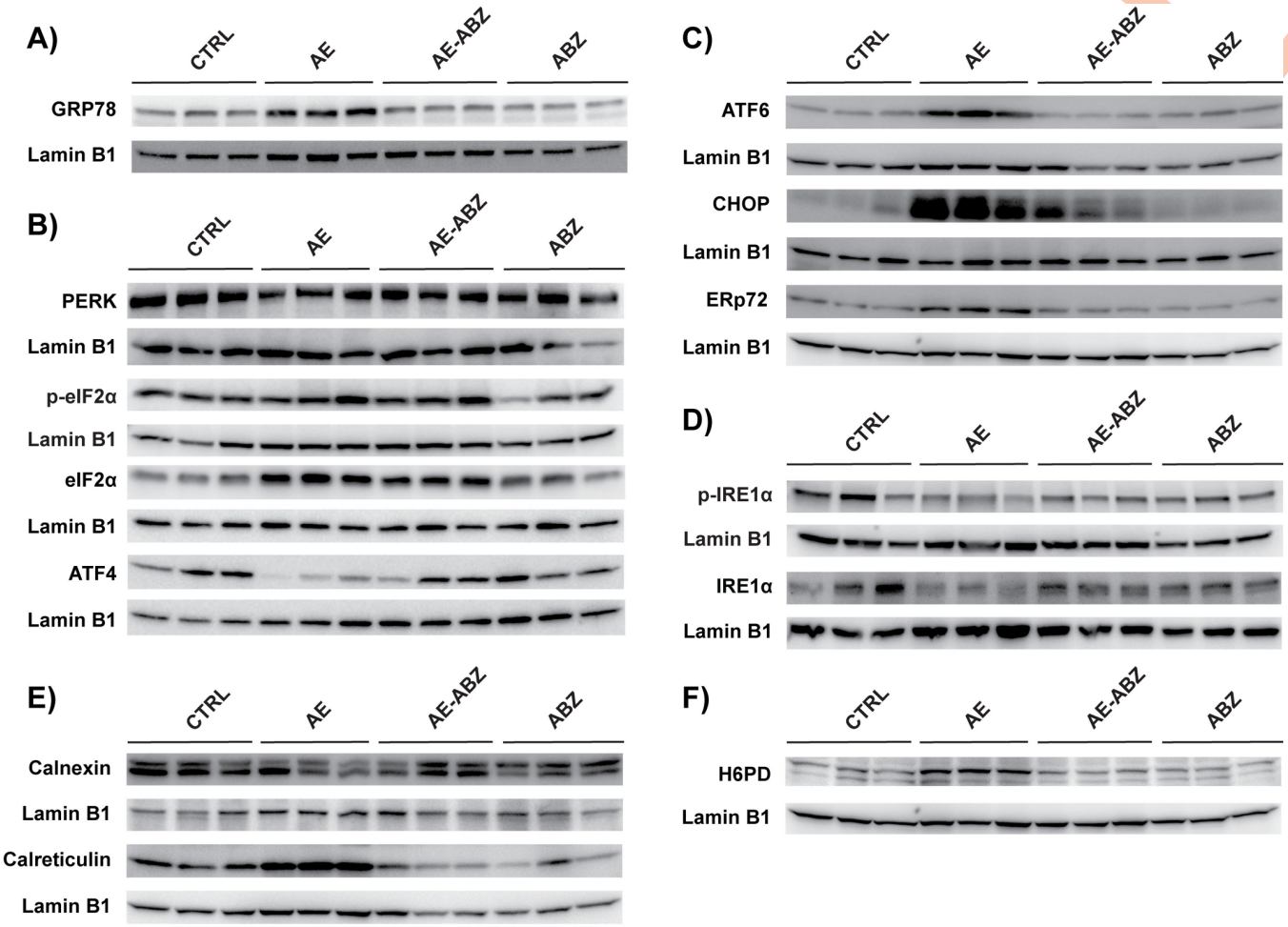

G)

Classification Pathway	Relative protein expression (normalized to CTRL)	Group			
		CTRL (n=6)	AE (n=6)	AE-ABZ (n=6)	ABZ (n=6)
Master regulator	GRP78	1.0	2.7 (±1.5)§	1.3 (±1.1)	1.0 (±0.3)
PERK branch	PERK	1.0	1.1 (±0.8)	1.1 (±0.5)	2.8 (±2.6)
	eIF2α	1.0	1.5 (±0.5)	1.6 (±0.4)	1.1 (±0.4)
	p-eIF2α	1.0	1.5 (±0.5)	0.9 (±0.5)	0.8 (±0.5)
	ATF4	1.0	0.3 (±0.1)*,§	0.8 (±0.2)	1.0 (±0.4)
ATF6 branch	ATF6	1.0	2.2 (±1.0)$^{\#}$	0.6 (±0.2)	1.2 (±0.5)
	CHOP	1.0	4.5 (±2.0)*,§	3.0 (±1.4)§	1.0 (±0.3)
	ERp72	1.0	2.0 (±0.6)*,§	1.3 (±0.6)	0.9 (±0.4)
IRE1 branch	IRE1α	1.0	0.3 (±0.2)*,§	0.8 (±0.4)	1.3 (±0.7)
	p-IRE1α	1.0	0.7 (±0.2)§	0.9 (±0.4)	1.6 (±0.7)
ER chaperones	Calnexin (CNX)	1.0	0.9 (±0.2)	1.2 (±0.6)	1.2 (±0.5)
	Calreticulin (CRT)	1.0	1.6 (±0.5)$^{\#,\S}$	0.9 (±0.3)	0.8 (±0.3)
NADPH generation	H6PD	1.0	2.6 (±1.8)*	1.4 (±0.6)	1.4 (±0.6)

Fig 1. Effect of *E. multilocularis* infection on the expression of proteins involved in UPR and ER redox functions. Western blotting and semi-quantitative analysis by densitometry (graphs of densitometry data are shown in S2 Fig) of protein/phospho-protein levels of **A**) GRP78, **B**) PERK, eIF2α, p-eIF2α and ATF4, **C**) ATF6, CHOP, and ERp72, **D**) IRE1α and p-IRE1α, **E**) CNX and CRT, and **F**) H6PD in mock-infected control mice (CTRL), *E. multilocularis*

infected mice (AE), infected mice treated with ABZ (AE-ABZ) or uninfected mice treated with ABZ (ABZ). One representative blot (of two) containing samples from three different mice is shown. Lamin B1 served as loading control. **G)** Bands corresponding to the respective protein/phospho-protein were analyzed by densitometry (animals per group n = 6). Numbers represent the expression of protein/phospho-protein levels normalized to those of the control (CTRL) group (mean ± SD). Significantly decreased protein/phospho-protein levels are highlighted in red and increased levels in blue. Symbols indicate significant differences ($p \leq 0.05$) between groups: *, compared to CTRL; §, compared to ABZ; #, compared to AE-ABZ. No outliers were detected/excluded. Non-parametric, Kruskal-Wallis test followed by Dunn's Multiple Comparison post-test.

https://doi.org/10.1371/journal.pntd.0009192.g001

potential 3'UTR binding site in at least one of the targets investigated in the present work (S3 Table) were quantified by qPCR in our secondary *E. mulitilocularis* infection model.

The analysis of the seven mouse miRs miR-148a-3p, miR-15a-5p, miR-22-3p, miR-146a-5p, miR-1839-5p, miR-30a-5p and miR-30a-3p revealed significantly higher levels of miR-1839-5p and miR-146a-5p in liver tissue samples of *E. multilocularis* infected mice (AE) compared to control animals (CTRL) (2.2-fold and 2.9 -fold, respectively, AE *vs* CTRL; S3 Fig). The other miRs remained either unchanged or showed a weak trend to be elevated (S4 Fig). Importantly, ABZ treatment reversed the elevated miR-1839-5p levels in AE mice to that seen in CTRL animals or even lower (2.0-fold and 4.1-fold, respectively, AE vs AE-ABZ). ABZ treatment in uninfected mice tended to decrease miR-1839-5p and miR-146a-5p expression levels (S3 Fig). Because miR-1839-5p is significantly increased and its predicted target IRE1α decreased in AE compared to CTRL mice, we highlighted the complementary sequence of miR-1839-5p in the 3'UTR of IRE1α (S3 Fig).

Elevation of inflammatory cytokines due to *E. multilocularis* infection is reversed by ABZ treatment

A previous study has shown that immune modulatory treatment of AE in mice by PD-L1 blockade using antibodies successfully reduces parasite weight and inflammatory markers, such as IL-1β, IL-6, TNF-α and INF-γ [10]. In the same study, ABZ was shown to decrease the parasite weight even more than αPD-L1 treatment did, yet cytokines were not assessed. To potentially link inflammation to our current observations regarding UPR and ERS pathways, we measured the cytokines in liver samples of our present mouse model. Fig 2 shows that IL-1β, IL-6, TNF-α and INF-γ are all elevated in mice infected with *E. multilocularis* compared to non-infected control mice, reaching significance for IL-1β and INF-γ. Treatment with ABZ successfully reduced all the inflammatory markers back to the levels detected in non-infected control mice and itself did not alter the levels of these cytokines.

Antibody-mediated blockade of PD-L1 reverses the effects of AE on key proteins of the UPR branches

To see whether αPD-L1 treatment ameliorates the effects of AE on UPR and ERS, we investigated the expression levels of proteins related to the three UPR branches by Western blotting. Due to the limited amount of samples, we could only investigate selected key proteins, based on the changes shown in Fig 1. The protein levels of ATF4 from the PERK branch and IRE1α from the IRE1 branch were decreased in mice infected with *E. multilocularis* compared to non-infected control mice (Figs 1 and 3), and αPD-L1 treatment reversed both ATF4 and IRE1α expression levels. Similarly, the increased levels of CHOP from the ATF6 branch were reversed back to levels seen in control mice.

Discussion

Recent studies on viral, bacterial and intracellular parasitic infections emphasize the importance of the UPR and ERS pathways in pathogen-induced diseases [27–29,71,72]. Activation of

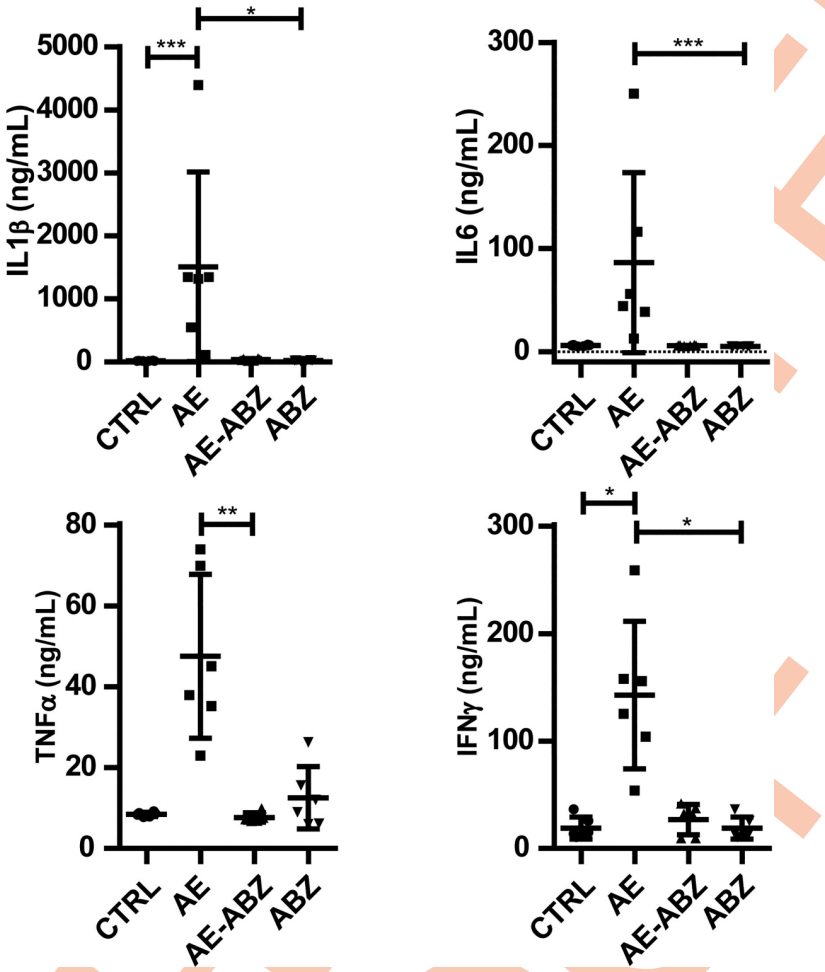

Fig 2. Albendazole decreases proinflammatory cytokine levels in the liver that were elevated by *E. multilocularis* infection. Cytokine levels of IL1β, IL6, TNFα, and IFNγ in liver tissue samples of mock-infected control mice (CTRL), *E. multilocularis* infected mice (AE), infected mice treated with ABZ (AE-ABZ) or uninfected mice treated with ABZ (ABZ) (animals per group n = 6). No outliers were detected/excluded. Non-parametric, Kruskal-Wallis test followed by Dunn's Multiple Comparison post-test. *P≤0.05; **p≤0.01; ***p≤0.001.

https://doi.org/10.1371/journal.pntd.0009192.g002

the UPR, a specific form of ERS triggered by an accumulation of unfolded or misfolded proteins within the ER, can be mediated by three branches, represented by the ER transmembrane stress sensor proteins ATF6, PERK and IRE1α [73–81] (Fig 4). In non-stressed cells, these proteins remain in an inactive state, bound to the luminal chaperone GRP78. Upon activation, GRP78 is released to support luminal protein folding, followed by the activation of ATF6, PERK and IRE1α and their downstream targets such as eIF2α, ATF4, XBP1 and CHOP in order to mediate the stress responses [82–84].

Our current results revealed a pronounced induction of ATF6 in livers of mice infected with *E. multilocularis*. The PERK branch was less active, indicated by the downregulation of ATF4 and the unchanged protein levels of PERK, eIF2α and unchanged eIF2α phosphorylation. A phosphorylation of PERK was not detectable. The IRE1α branch also was less active since IRE1α protein and phosphorylation levels were lower or tended to be lower in *E. multilocularis* infected mice. The decreased ATF4 levels in livers of infected animals suggest that the observed upregulation of CHOP is mainly caused by enhanced ATF6 activity. CHOP, well-known as a mediator of apoptosis, was previously found to play an important role in the

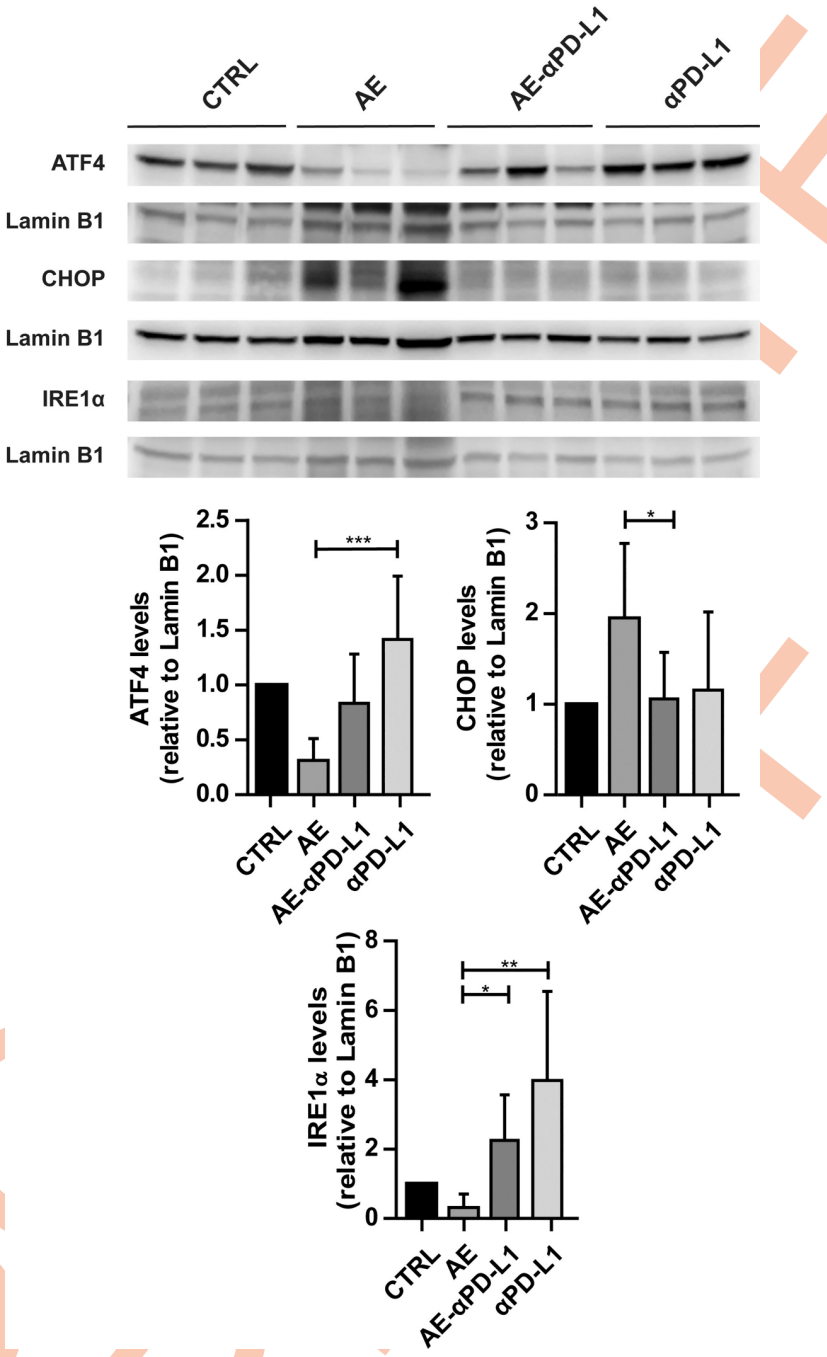

Fig 3. Effect of *E. multilocularis* infection and αPD-L1 treatment on the expression of proteins involved in UPR. Western blotting and semi-quantitative analysis by densitometry of protein levels of ATF4, CHOP, and IRE1α in mock-infected control mice (CTRL), *E. multilocularis* infected mice (AE), infected mice treated with αPD-L1 (AE-αPD-L1) or uninfected mice treated with αPD-L1 (αPD-L1) (animals per group n = 6). One representative blot (of two) containing samples from three different mice is shown. Lamin B1 served as loading control (animals per group n = 6). Densitometry results represent data from the two blots on samples from six mice (mean ± SD), normalized to Lamin B1 control and with CTRL set as 1. No outliers were detected/excluded. Non-parametric, Kruskal-Wallis test followed by Dunn's Multiple Comparison post-test. *P≤0.05; **p≤0.01; ***p≤0.001.

https://doi.org/10.1371/journal.pntd.0009192.g003

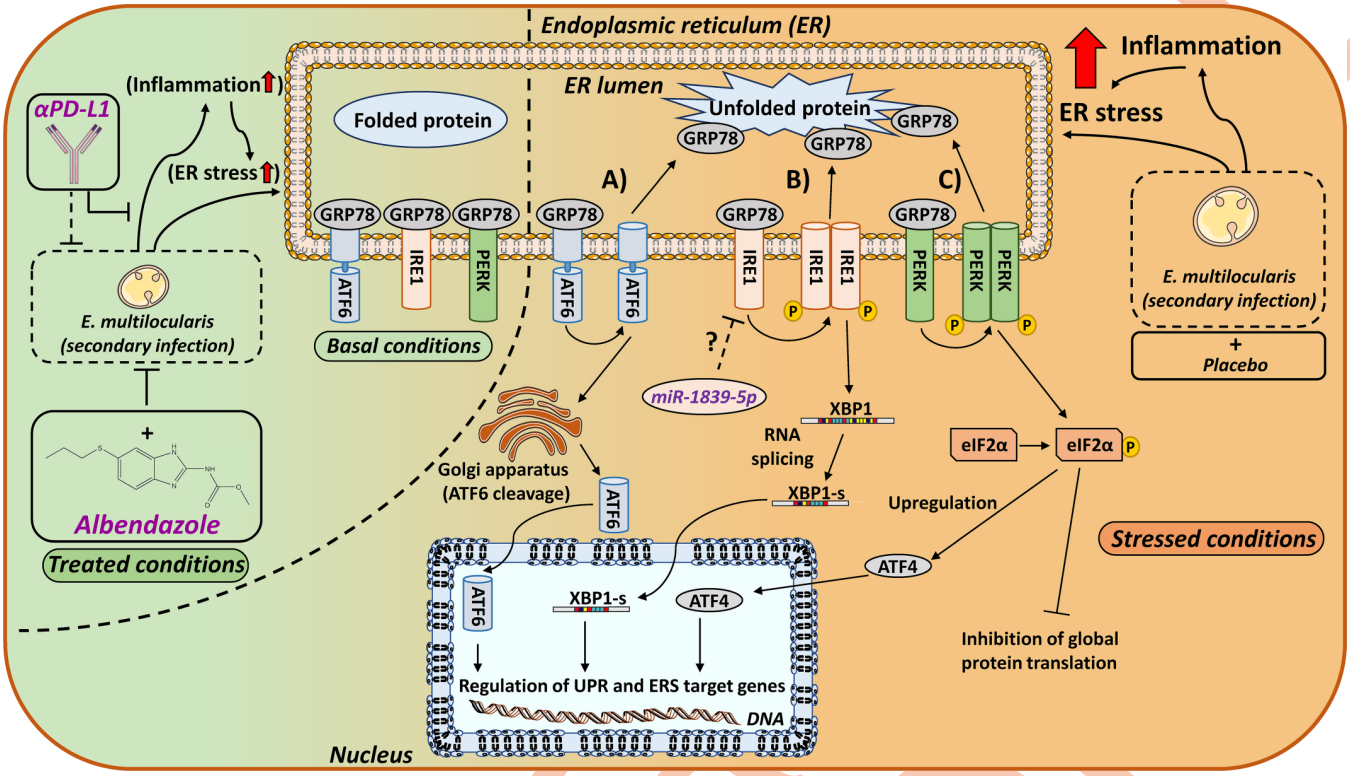

Fig 4. Schematic overview of ERS signaling pathways under basal and *E. multilocularis* infection stressed conditions. The ER chaperone GRP78 binds to unfolded luminal proteins and dissociates from the three major ERS sensors: A) ATF6, B) IRE1α and C) PERK. A) Loss of GRP78 binding leads to the translocation of ATF6 to the Golgi apparatus, where it is cleaved by proteases. The cleaved form of ATF6 translocates into the nucleus to act as a transcription factor for ER chaperons (*e.g.* ERp72) and ERS related genes. B) ERS promotes IRE1α dimerization and autophosphorylation, which activates the endoribonuclease activity resulting in the splicing and thereby activation of XBP1. XBP1-s promotes the expression of ERAD related genes and chaperones (*e.g.* GRP78). C) Activation of PERK is initiated by dimerization and self-phosphorylation. Activated PERK phosphorylates eIF2α, leading to eIF2α-mediated inhibition of global protein translation in order to decrease the luminal protein load. Besides, phosphorylated eIF2α increases the transcription of ATF4, which in turn upregulates expression of genes related to cell homeostasis restoration. If prolonged ERS occurs and pro-adaptive UPR fails, ATF4 induces genes (including CHOP) leading to apoptosis. During ERS, increased levels of miR-1839-5p potentially control the expression of the IRE1α gene, which contains a predicted target site in its 3'-UTR for this miR, thereby affecting the cellular ERS response. By suppressing the propagation of *E. multilocularis* infection, through yet poorly defined molecular mechanisms, ABZ and αPD-L1 treatment decrease inflammation and ERS.

https://doi.org/10.1371/journal.pntd.0009192.g004

efficient expansion of the intracellular fungus *Histoplasma capsulatum* [85]. Following infection, an increase in CHOP levels led to augmented apoptosis of macrophages, thus suppressing the host's defense and contributing to the virulence of this particular pathogen. Another study, using intestinal epithelial cell lines, showed a direct effect of heat-labile enterotoxins of *Escherichia coli* on the induction upregulation of CHOP, which led to an accelerated apoptosis of the host cells [86]. Thus, the upregulation of CHOP in murine hepatocytes during *E. multilocularis* infection might similarly promote parasitic growth.

In contrast to the pro-apoptotic UPR mediator CHOP, the protein levels of the PERK target ATF4 were significantly decreased in livers of *E. multilocularis* infected compared to mock-infected mice. This differs from a previous study on human cutaneous leishmaniasis where both CHOP and ATF4 were found to be upregulated [87]. Decreased ATF4 levels were recently described as a mechanism of acquired resistance to cope with a limited availability of amino acids in cancer cells [88]. Unrestricted tumor growth requires a high demand of nutrients and has been associated with a depletion of essential amino acids in the tumor tissue. Similar metabolic perturbations and adaptive responses may occur in patients with hepatic AE. A recent study summarizing analyses of serum samples from *E. multilocularis* infected and

healthy adults (group size: n = 18) revealed decreased levels of branched-chain amino acids such as leucine, isoleucine and valine along with lowered levels of serine and glutamine in samples from infected patients [89]. In contrast, the aromatic amino acids tyrosine and phenylalanine were increased, together with glutamate. Thus, the observed decrease in ATF4 expression may be a response to adapt the amino acid availability in the situation of parasitic growth.

Similar to ATF4, the IRE1α protein expression and phosphorylation levels were decreased or tended to be lower in liver tissues of AE mice. The reason of the decreased IRE1α expression in *E. multilocularis* infected mice and the underlying mechanism remain unclear. IRE1 enzymes are transmembrane proteins exhibiting Ser/Thr protein kinase and endoribonuclease activities and acting as major ERS sensors [90,91]. There are two IRE1 isoforms in mammals: the ubiquitously expressed IRE1α and IRE1β which is predominantly expressed in the intestine and lung [92]. Further analysis of the liver resident IRE1α showed that the decreased protein expression in *E. multilocularis* infected mouse livers is supported by a trend of lower mRNA levels along with an increased expression of miR-1839-5p that has a target site in the 3'UTR of IRE1α as predicted by the computer-based programs Targetscan [68] and RNA22 [69]. Additionally, we found enhanced miR-146a-5p in livers of infected mice. An earlier study in primary dermal fibroblasts provided evidence for a downregulation of miR-146a-5p by IRE1-dependent cleavage in response to UPR activation [93]. Thus, the elevated miR-146a-5p may be due to decreased IRE1α activity in *E. multilocularis* infected mice. Furthermore, proinflammatory cytokines were found to induce miR-146a-5p [94], suggesting an upregulation of this miR in AE due to the hepatic inflammation.

An extensive analysis of miRs altered in livers of mice after primary infection with *E. multilocularis* by Boubaker *et al.* [62] identified several miRs with altered expression levels, including miR-1839-5p and miR-146a-5p. An increase of miR-1839-5p and miR-146a-5p in the primary as well as in the secondary infection mouse models suggests that these two miRs may represent potential biomarkers of AE; however, for this purpose they will need to be robustly detected and quantified in blood samples. In this respect, a recent study showed elevated miR-125b-5p levels in plasma of patients with AE [56], supporting the potential use of miRs as biomarkers of AE. Furthermore, Luis *et al.* reported an association of several circulating miRs, including miR-146a-5p, with ERS and organ damage in a model of trauma hemorrhagic shock [95]. Moreover, Wilczynski *et al.* reported increased miR-146a expression levels in tumor tissues of patients with ovarian cancer [96]. The advanced AE resembles a tumorigenic situation with alterations in the microenvironment and immune responses. Thus, follow-on research should address whether miR-146a-5p and miR-1839-5p can serve as serum biomarkers of AE and AE-dependent inflammation.

Besides the UPR, the ER-associated degradation (ERAD) is an important quality control machinery to cope with ER stressors. ERAD plays a crucial role in the degradation of terminally misfolded proteins by retro-translocating them from the ER to the cytoplasm for deglycosylation and ubiquitination and subsequent proteasomal degradation [97,98]. Prior to ERAD, misfolded proteins undergo repeated cycles of re-folding by the assistance of several ER-resident chaperones including lectins such as CRT and CNX, protein disulfide isomerase family members like ERp72 and ERp57 as well as members of the heat shock protein 70 family (e.g. GRP78) [99–102]. The elevated expression of CRT together with GRP78 and ERp72 indicates a higher demand for protein folding capacity in the ER in livers from infected mice. This was accompanied by an elevated demand for NADPH redox equivalents in the ER and/or an enhanced need for the products of the ER pentose phosphate pathway as indicated by the elevated H6PD expression. H6PD was found to promote cancer cell proliferation and the modulation of its expression affected GRP78, ATF6 and CHOP, emphasizing its role in ERS regulation [103].

Importantly, treatment with the parasitostatic benzimidazole ABZ and the immune-modulatory αPD-L1, which both were shown to decrease the weight of parasitic cysts in the peritoneal cavity of *i.p. E. multilocularis* infected mice [10], reversed the observed effects on UPR and ERS pathways and on associated ERAD and ER redox genes. Furthermore, these treatments reduced the hepatic inflammation caused by *E. multilocularis* infection as indicated by the reversal of the increased levels of proinflammatory cytokines in the AE-ABZ group. Our previous study, using the same infection model, showed that most mice had infiltrating parasitic structures in their liver [10]. As the concentrations of the four inflammatory cytokines showed considerable inter-individual variation, we comparatively analyzed whether this variation was associated with the presence or absence of parasitic structures in the liver, but found no correlation. Importantly, in the absence of infection, neither ABZ nor αPD-L1 affected any of the investigated ER related targets, emphasizing their favorable safety profile regarding ERS related adverse effects.

ABZ acts as an intracellular tubulin inhibitor, preventing metacestode formation [104], and it leads to a loss of integrity in the germinal layer and a reduction in metacestode mass [105]. Rodents inoculated with *E. multilocularis* material from ABZ treated patients, compared to inoculation with samples from untreated patients, exhibited decreased larval development [106]. At high concentrations, ABZ leads to a collapse of the alveolar architecture of the parasite, partially dissolving the laminated layer, followed by an invasion of the lesion with host inflammatory cells, such as histiocytes, lymphocytes, neutrophils and eosinophils [107]. A reduction of the width of the laminated layer upon ABZ therapy was found both in mice [108] and humans [109]. In the present study, we also observed a reduction of parasite mass.

A degradation of the laminated layer may contribute to the observed increase of small particles of *E. multilocularis* in and around the lesion, such as sinusoids, vessels and lymph follicles, which may influence the immune reaction [110]. Ricken *et al.* [109] showed an overall increase in the number of immune cells during the course of ABZ treatment in human AE patients. This suggests that the non-specific immune reaction is activated at the begin of ABZ treatment, with an increase in macrophages and granulocytes; and this response is shifted towards a specific immune response dominated by B and plasma cells, which does, however, not eliminate the infection. Therefore, ABZ treatment may activate the host immune system by reducing the parasite's immunosuppressive functions. Furthermore, by reducing the metabolism of the metacestode during ABZ treatment and dissolution of the laminated layer, more parasite antigens are exposed and detected by the immune system, and this likely leads to a more specific immune response [109].

Together, this suggests that the mechanisms of ABZ and αPD-L1 are different. Inhibition of the PD-L1 pathway rather contributes to T cell activity by increasing $CD4^+$/$CD8^+$ effector T cells and decreasing regulatory T cells, and it has also the capacity to restore dendritic cells and Kupffer cells/macrophages and to suppresses NKT and NK cells, which leads to an improved control of *E. multilocularis* infection in mice.

In conclusion, the present study showed that *E. multilocularis* infection led to a modulation of the UPR, characterized by an activation of the ATF6-branch with an upregulation of CHOP along with decreased ATF4 and IRE1α protein levels and an increase of miR-1839-5p and miR-146a-5p. Future studies should evaluate whether these miRs can be quantified in blood samples and whether they could act as biomarkers of *E. multilocularis* infection and to report treatment efficacy. ABZ, the most commonly used drug to treat human AE in the clinics, as well as αPD-L1 treatment ameliorated the effects of *E. multilocularis* infection on ER related genes. The fact that ABZ and immune-modulatory αPD-L1 treatment both decreased the elevated levels of proinflammatory cytokines and reversed the effects of *E. multilocularis* infection on UPR and ERS pathways, indicates a correlation between inflammation and UPR/ERS in

AE. How immune therapy and interventions in the UPR/ERS pathways could ameliorate AE warrants further investigations.

Supporting information

S1 Table. Antibodies and corresponding dilutions.
(DOCX)

S2 Table. Primers used for RT-qPCR.
(DOCX)

S3 Table. Prediction of miR target sites.
(DOCX)

S1 Fig. Schematic overview of the experimental setup. Animals were divided into six groups: $CTRL_{(n = 6)}$, $AE_{(n = 6)}$, $AE\text{-}ABZ_{(n = 6)}$, $ABZ_{(n = 6)}$, $AE\text{-}\alpha PD\text{-}L1_{(n = 6)}$ and $\alpha PD\text{-}L1_{(n = 6)}$. CTRL, ABZ and αPD-L1 mice received an intraperitoneal administration of 100 μL PBS. AE, AE-ABZ and AE-αPD-L1 mice were infected intraperitoneally with *E. multilocularis* metacestode suspension containing approximately 100 vesicular cysts resuspended in 100 μL PBS. Treatment started 6 weeks after infection. CTRL and AE mice received 100 μL corn oil orally 5 times per week and 100 μL PBS intraperitoneally twice per week for another 8 weeks. AE-ABZ and ABZ mice received ABZ (200 mg/kg body weight) in 100 μL corn oil orally 5 times per week and 100 μL PBS intraperitoneally twice per week for 8 weeks. AE-αPD-L1 and αPD-L1 mice received αPD-L1 antibody in 100 μL PBS intraperitoneally twice per week (200 μg/injection) and 100 μL corn oil orally 5 times per week. All animals were sacrificed at the end of treatment. Smart Servier Medical Art, **smart.servier.com, was used to draw the figure.**
(TIF)

S2 Fig. Graphs of densitometry data of the effect of *E. multilocularis* infection on the expression of proteins involved in UPR and ER redox functions. Semi-quantitative analysis by densitometry of protein/phospho-protein levels of GRP78, PERK, eIF2α, p-eIF2α, and ATF4, ATF6, CHOP, and ERp72, IRE1α and p-IRE1α, calnexin, calreticulin, and H6pd in mock-infected control mice (CTRL), *E. multilocularis* infected mice (AE), infected mice treated with ABZ (AE-ABZ) or uninfected mice treated with ABZ (ABZ) (animals per group n = 6). Densitometry results represent data from two blots on samples from six mice (mean ± SD), normalized to Lamin B1 control and with CTRL set as 1. No outliers were detected/excluded. Non-parametric, Kruskal-Wallis test followed by Dunn's Multiple Comparison post-test. $^{*}P \leq 0.05$; $^{**}p \leq 0.01$; $^{***}p \leq 0.001$.
(TIF)

S3 Fig. IRE1α, XBP1 and XBP1-s mRNA, as well as miR-1839-5p and miR-146a-5p levels upon *E. multilocularis* infection and ABZ treatment. Top: IRE1α, XBP1 and XBP1-s mRNA and miR-1839-5p and miR-146a-5p levels in mock-infected control mice ($CTRL_{n = 6}$), *E. multilocularis* infected mice ($AE_{n = 6}$), infected mice treated with ABZ ($AE\text{-}ABZ_{n = 6}$) or uninfected mice treated with ABZ ($ABZ_{n = 6}$). mRNA levels were normalized to β-actin and miR levels to Sno234. Results represent mean ± SD. No outliers were detected/excluded. One-way ANOVA test followed by Bonferroni Multiple Comparison post-test was applied to assess significance. Bottom: Nucleotide sequence of the murine IRE1α mRNA including the 3'-UTR. The start and stop codon of the IRE1α CDS are indicated in bold and the miR-1839-5p binding site is highlighted by red and bold letters. $^{*}P \leq 0.05$; $^{**}p \leq 0.01$; $^{***}p \leq 0.001$.
(TIF)

S4 Fig. *E. multilocularis* infection does not affect miR-15a-5p, miR-148a-3p, miR-22-3p, miR-30a-3p and miR-30a-5p expression levels. miR-15a-5p, miR-148a-3p, miR-22-3p, miR-30a-5p and miR-30a-3p levels, in mock-infected, mock-treated mice (CTRL $_{n = 6}$) and *E. multilocularis* infected mock-treated mice (AE $_{n = 6}$). Results represent mean ± SD. No outliers were excluded. Two-tailed unpaired t-test was applied to test significance.
(TIF)

S1 File. Raw data of Western blotting used to produce graphs and figures.
(PDF)

Author Contributions

Conceptualization: Michael Weingartner, Simon Stücheli, Fadi Jebbawi, Junhua Wang, Alex Odermatt.

Data curation: Michael Weingartner, Simon Stücheli, Fadi Jebbawi, Junhua Wang.

Formal analysis: Michael Weingartner, Simon Stücheli, Fadi Jebbawi, Junhua Wang.

Funding acquisition: Britta Lundström-Stadelmann, Alex Odermatt.

Investigation: Michael Weingartner, Simon Stücheli, Fadi Jebbawi, Junhua Wang.

Methodology: Michael Weingartner, Simon Stücheli, Fadi Jebbawi, Britta Lundström-Stadelmann, Junhua Wang.

Project administration: Alex Odermatt.

Resources: Bruno Gottstein, Guido Beldi, Britta Lundström-Stadelmann, Alex Odermatt.

Supervision: Bruno Gottstein, Guido Beldi, Britta Lundström-Stadelmann.

Validation: Alex Odermatt.

Visualization: Michael Weingartner, Simon Stücheli.

Writing – original draft: Michael Weingartner.

Writing – review & editing: Michael Weingartner, Simon Stücheli, Fadi Jebbawi, Bruno Gottstein, Guido Beldi, Britta Lundström-Stadelmann, Junhua Wang, Alex Odermatt.

References

1. Spicher M, Roethlisberger C, Lany C, Stadelmann B, Keiser J, Ortega-Mora LM, et al. In vitro and in vivo treatments of echinococcus protoscoleces and metacestodes with artemisinin and artemisinin derivatives. Antimicrob Agents Chemother. 2008; 52(9):3447–50. Epub 2008/07/16. https://doi.org/10.1128/AAC.00553-08 PMID: 18625777; PubMed Central PMCID: PMC2533465.
2. Conraths FJ, Probst C, Possenti A, Boufana B, Saulle R, Torre GL, et al. Potential risk factors associated with human alveolar echinococcosis: Systematic review and meta-analysis. PLOS Neglected Tropical Diseases. 2017; 11(7):e0005801. https://doi.org/10.1371/journal.pntd.0005801 PMID: 28715408
3. Kowalczyk M, Kurpiewski W, Zieliński E, Zadrożny D, Klepacki Ł, Juśkiewicz W, et al. A rare case of the simultaneous location of Echinococcus multilocularis in the liver and the head of the pancreas: case report analysis and review of literature. BMC Infectious Diseases. 2019; 19(1):661. https://doi.org/10.1186/s12879-019-4274-y PMID: 31340769
4. Ritler D, Rufener R, Li JV, Kämpfer U, Müller J, Bühr C, et al. In vitro metabolomic footprint of the Echinococcus multilocularis metacestode. Sci Rep. 2019; 9(1):1–13. https://doi.org/10.1038/s41598-018-37186-2 PMID: 30626917
5. Schweiger A, Ammann RW, Candinas D, Clavien P-A, Eckert J, Gottstein B, et al. Human Alveolar Echinococcosis after Fox Population Increase, Switzerland. Emerg Infect Dis. 2007; 13(6):878–82. https://doi.org/10.3201/eid1306.061074 PMID: 17553227

6. Kantarci M, Bayraktutan U, Karabulut N, Aydinli B, Ogul H, Yuce I, et al. Alveolar echinococcosis: spectrum of findings at cross-sectional imaging. Radiographics. 2012; 32(7):2053–70. Epub 2012/11/15. https://doi.org/10.1148/rg.327125708 PMID: 23150858.
7. Kayacan SM, Vatansever S, Temiz S, Uslu B, Kayacan D, Akkaya V, et al. Alveolar echinococcosis localized in the liver, lung and brain. Chin Med J (Engl). 2008; 121(1):90–2. Epub 2008/01/23. PMID: 18208675.
8. Niu F, Chong S, Qin M, Li S, Wei R, Zhao Y. Mechanism of Fibrosis Induced by Echinococcus spp. Diseases. 2019; 7(3). https://doi.org/10.3390/diseases7030051 PMID: 31409055
9. Wang J, Jebbawi F, Bellanger A-P, Beldi G, Millon L, Gottstein B. Immunotherapy of alveolar echinococcosis via PD-1/PD-L1 immune checkpoint blockade in mice. Parasite Immunology. 2018; 40(12): e12596. https://doi.org/10.1111/pim.12596 PMID: 30315719
10. Jebbawi F, Bellanger AP, Lunstrom-Stadelmann B, Rufener R, Dosch M, Goepfert C, et al. Innate and adaptive immune responses following PD-L1 blockade in treating chronic murine alveolar echinococcosis. Parasite Immunol. 2021; 43(8):e12834. Epub 2021/03/24. https://doi.org/10.1111/pim.12834 PMID: 33754355.
11. Wen H, Vuitton L, Tuxun T, Li J, Vuitton DA, Zhang W, et al. Echinococcosis: Advances in the 21st Century. Clin Microbiol Rev. 2019; 32(2). Epub 2019/02/15. https://doi.org/10.1128/CMR.00075-18 PMID: 30760475; PubMed Central PMCID: PMC6431127.
12. Bulakçı M, Kartal MG, Yılmaz S, Yılmaz E, Yılmaz R, Şahin D, et al. Multimodality imaging in diagnosis and management of alveolar echinococcosis: an update. Diagn Interv Radiol. 2016; 22(3):247–56. https://doi.org/10.5152/dir.2015.15456 PMID: 27082120
13. Gottstein B, Wang J, Boubaker G, Marinova I, Spiliotis M, Muller N, et al. Susceptibility versus resistance in alveolar echinococcosis (larval infection with Echinococcus multilocularis). Vet Parasitol. 2015; 213(3–4):103–9. Epub 2015/08/12. https://doi.org/10.1016/j.vetpar.2015.07.029 PMID: 26260407.
14. Aasen TD, Nasrollah L, Seetharam A. Acute Liver Failure Secondary to Albendazole: Defining Albendazole's Role in the Management of Echinococcal Infection: 722. American Journal of Gastroenterology. 2015; 110:S316.
15. Hemphill A, Stadelmann B, Rufener R, Spiliotis M, Boubaker G, Muller J, et al. Treatment of echinococcosis: albendazole and mebendazole—what else? Parasite. 2014; 21:70. Epub 2014/12/20. https://doi.org/10.1051/parasite/2014073 PMID: 25526545; PubMed Central PMCID: PMC4271654.
16. Choi GY, Yang HW, Cho SH, Kang DW, Go H, Lee WC, et al. Acute drug-induced hepatitis caused by albendazole. J Korean Med Sci. 2008; 23(5):903–5. Epub 2008/10/29. https://doi.org/10.3346/jkms.2008.23.5.903 PMID: 18955802; PubMed Central PMCID: PMC2580005.
17. Marin Zuluaga JI, Marin Castro AE, Perez Cadavid JC, Restrepo Gutierrez JC. Albendazole-induced granulomatous hepatitis: a case report. J Med Case Rep. 2013; 7:201. Epub 2013/07/31. https://doi.org/10.1186/1752-1947-7-201 PMID: 23889970; PubMed Central PMCID: PMC3750323.
18. Ammann RW, Hirsbrunner R, Cotting J, Steiger U, Jacquier P, Eckert J. Recurrence Rate after Discontinuation of Long-Term Mebendazole Therapy in Alveolar Echinococcosis (Preliminary-Results). Am J Trop Med Hyg. 1990; 43(5):506–15. https://doi.org/10.4269/ajtmh.1990.43.506 WOS: A1990EL12600009. PMID: 2240375
19. Buttenschoen K, Gruener B, Carli Buttenschoen D, Reuter S, Henne-Bruns D, Kern P. Palliative operation for the treatment of alveolar echinococcosis. Langenbecks Arch Surg. 2009; 394(1):199–204. Epub 2008/06/26. https://doi.org/10.1007/s00423-008-0367-6 PMID: 18575882.
20. Wang J, Marreros N, Rufener R, Hemphill A, Gottstein B, Lundstrom-Stadelmann B. Short communication: Efficacy of albendazole in Echinococcus multilocularis-infected mice depends on the functional immunity of the host. Exp Parasitol. 2020; 219:108013. Epub 2020/10/04. https://doi.org/10.1016/j.exppara.2020.108013 PMID: 33010287.
21. Charbonnet P, Bühler L, Sagnak E, Villiger P, Morel P, Mentha G. Devenir à long terme des malades opérés et traités pour échinococcose alvéolaire. Annales de Chirurgie. 2004; 129(6):337–42. https://doi.org/10.1016/j.anchir.2004.01.017 PMID: 15297222
22. Baumann S, Shi R, Liu W, Bao H, Schmidberger J, Kratzer W, et al. Worldwide literature on epidemiology of human alveolar echinococcosis: a systematic review of research published in the twenty-first century. Infection. 2019; 47(5):703–27. Epub 2019/05/31. https://doi.org/10.1007/s15010-019-01325-2 PMID: 31147846.
23. Kuscher S, Kronberger IE, Loizides A, Plaikner M, Ninkovic M, Brunner A, et al. Exploring the limits of hepatic surgery for alveolar echinococcosis—10-years' experience in an endemic area of Austria. Eur Surg. 2019; 51(4):189–96. https://doi.org/10.1007/s10353-019-0596-7

24. Qu B, Guo L, Sheng G, Yu F, Chen G, Wang Y, et al. Management of Advanced Hepatic Alveolar Echinococcosis: Report of 42 Cases. The American Journal of Tropical Medicine and Hygiene. 2017; 96 (3):680–5. https://doi.org/10.4269/ajtmh.16-0557 PMID: 28070011

25. Sréter T, Széll Z, Egyed Z, Varga I. Echinococcus multilocularis: An Emerging Pathogen in Hungary and Central Eastern Europe? Emerg Infect Dis. 2003; 9(3):384–6. https://doi.org/10.3201/eid0903.020320 PMID: 12643838

26. Vuitton DA, Demonmerot F, Knapp J, Richou C, Grenouillet F, Chauchet A, et al. Clinical epidemiology of human AE in Europe. Veterinary Parasitology. 2015; 213(3):110–20. https://doi.org/10.1016/j.vetpar.2015.07.036 PMID: 26346900

27. Galluzzi L, Diotallevi A, Magnani M. Endoplasmic reticulum stress and unfolded protein response in infection by intracellular parasites. Future Sci OA. 2017; 3(3):FSO198. Epub 2017/09/09. https://doi.org/10.4155/fsoa-2017-0020 PMID: 28883998; PubMed Central PMCID: PMC5583660.

28. Pillich H, Loose M, Zimmer KP, Chakraborty T. Diverse roles of endoplasmic reticulum stress sensors in bacterial infection. Mol Cell Pediatr. 2016; 3(1):9. Epub 2016/02/18. https://doi.org/10.1186/s40348-016-0037-7 PMID: 26883353; PubMed Central PMCID: PMC4755955.

29. Zhang L, Wang A. Virus-induced ER stress and the unfolded protein response. Front Plant Sci. 2012; 3:293. Epub 2013/01/08. https://doi.org/10.3389/fpls.2012.00293 PMID: 23293645; PubMed Central PMCID: PMC3531707.

30. Neerukonda SN, Katneni UK, Bott M, Golovan SP, Parcells MS. Induction of the unfolded protein response (UPR) during Marek's disease virus (MDV) infection. Virology. 2018; 522:1–12. Epub 2018/07/07. https://doi.org/10.1016/j.virol.2018.06.016 PMID: 29979959.

31. Mehrbod P, Ande SR, Alizadeh J, Rahimizadeh S, Shariati A, Malek H, et al. The roles of apoptosis, autophagy and unfolded protein response in arbovirus, influenza virus, and HIV infections. Virulence. 2019; 10(SI1):376–413. https://doi.org/10.1080/21505594.2019.1605803 PMID: 30966844

32. Smith JA. A new paradigm: innate immune sensing of viruses via the unfolded protein response. Front Microbiol. 2014; 5. https://doi.org/10.3389/fmicb.2014.00222 PMID: 24904537

33. Borsa M, Ferreira PLC, Petry A, Ferreira LGE, Camargo MM, Bou-Habib DC, et al. HIV infection and antiretroviral therapy lead to unfolded protein response activation. Virol J. 2015; 12:77. https://doi.org/10.1186/s12985-015-0298-0 PMID: 25976933

34. Perera N, Miller JL, Zitzmann N. The role of the unfolded protein response in dengue virus pathogenesis. Cell Microbiol. 2017; 19(5). https://doi.org/10.1111/cmi.12734 PMID: 28207988

35. Ambrose RL, Mackenzie JM. West Nile Virus Differentially Modulates the Unfolded Protein Response To Facilitate Replication and Immune Evasion. J Virol. 2011; 85(6):2723–32. https://doi.org/10.1128/JVI.02050-10 PMID: 21191014

36. Isler JA, Skalet AH, Alwine JC. Human cytomegalovirus infection activates and regulates the unfolded protein response. J Virol. 2005; 79(11):6890–9. Epub 2005/05/14. https://doi.org/10.1128/JVI.79.11.6890-6899.2005 PMID: 15890928; PubMed Central PMCID: PMC1112127.

37. Bechill J, Chen Z, Brewer JW, Baker SC. Coronavirus infection modulates the unfolded protein response and mediates sustained translational repression. J Virol. 2008; 82(9):4492–501. Epub 2008/02/29. https://doi.org/10.1128/JVI.00017-08 PMID: 18305036; PubMed Central PMCID: PMC2293058.

38. Burnett HF, Audas TE, Liang G, Lu RR. Herpes simplex virus-1 disarms the unfolded protein response in the early stages of infection. Cell Stress Chaperones. 2012; 17(4):473–83. Epub 2012/01/25. https://doi.org/10.1007/s12192-012-0324-8 PMID: 22270612; PubMed Central PMCID: PMC3368031.

39. So JS. Roles of Endoplasmic Reticulum Stress in Immune Responses. Mol Cells. 2018; 41(8):705–16. Epub 2018/08/07. https://doi.org/10.14348/molcells.2018.0241 PMID: 30078231; PubMed Central PMCID: PMC6125421.

40. Smith JA. Regulation of Cytokine Production by the Unfolded Protein Response; Implications for Infection and Autoimmunity. Front Immunol. 2018; 9:422. Epub 2018/03/21. https://doi.org/10.3389/fimmu.2018.00422 PMID: 29556237; PubMed Central PMCID: PMC5844972.

41. Romeo MA, Gilardini Montani MS, Benedetti R, Giambelli L, D'Aprile R, Gaeta A, et al. The cross-talk between STAT1/STAT3 and ROS up-regulates PD-L1 and promotes the release of pro-inflammatory/immune suppressive cytokines in primary monocytes infected by HHV-6B. Virus Res. 2021; 292:198231. Epub 2020/11/19. https://doi.org/10.1016/j.virusres.2020.198231 PMID: 33207265.

42. Treacy-Abarca S, Mukherjee S. Legionella suppresses the host unfolded protein response via multiple mechanisms. Nat Commun. 2015; 6. https://doi.org/10.1038/ncomms8887 PMID: 26219498

43. Lim YJ, Choi JA, Choi HH, Cho SN, Kim HJ, Jo EK, et al. Endoplasmic reticulum stress pathway-mediated apoptosis in macrophages contributes to the survival of Mycobacterium tuberculosis. PLoS One.

2011; 6(12):e28531. Epub 2011/12/24. https://doi.org/10.1371/journal.pone.0028531 PMID: 22194844; PubMed Central PMCID: PMC3237454.

44. Wang T, Zhou J, Gan X, Wang H, Ding X, Chen L, et al. Toxoplasma gondii induce apoptosis of neural stem cells via endoplasmic reticulum stress pathway. Parasitology. 2014; 141(7):988–95. https://doi.org/10.1017/S0031182014000183 PMID: 24612639

45. Inácio P, Zuzarte-Luís V, Ruivo MTG, Falkard B, Nagaraj N, Rooijers K, et al. Parasite-induced ER stress response in hepatocytes facilitates Plasmodium liver stage infection. EMBO reports. 2015; 16 (8):955–64. https://doi.org/10.15252/embr.201439979 PMID: 26113366

46. Leung AK, Calabrese JM, Sharp PA. Quantitative analysis of Argonaute protein reveals microRNA-dependent localization to stress granules. Proc Natl Acad Sci U S A. 2006; 103(48):18125–30. Epub 2006/11/23. https://doi.org/10.1073/pnas.0608845103 PMID: 17116888; PubMed Central PMCID: PMC1838717.

47. Geslain R, Cubells L, Bori-Sanz T, Alvarez-Medina R, Rossell D, Marti E, et al. Chimeric tRNAs as tools to induce proteome damage and identify components of stress responses. Nucleic Acids Res. 2010; 38(5):e30. Epub 2009/12/17. https://doi.org/10.1093/nar/gkp1083 PMID: 20007146; PubMed Central PMCID: PMC2836549.

48. Maurel M, Chevet E. Endoplasmic reticulum stress signaling: the microRNA connection. Am J Physiol Cell Physiol. 2013; 304(12):C1117–26. Epub 2013/03/22. https://doi.org/10.1152/ajpcell.00061.2013 PMID: 23515532.

49. Zhou X, Li X, Wu M. miRNAs reshape immunity and inflammatory responses in bacterial infection. Signal Transduct Target Ther. 2018; 3:14. Epub 2018/05/31. https://doi.org/10.1038/s41392-018-0006-9 PMID: 29844933; PubMed Central PMCID: PMC5968033.

50. Drury RE, O'Connor D, Pollard AJ. The Clinical Application of MicroRNAs in Infectious Disease. Front Immunol. 2017; 8:1182. Epub 2017/10/11. https://doi.org/10.3389/fimmu.2017.01182 PMID: 28993774; PubMed Central PMCID: PMC5622146.

51. Tribolet L, Kerr E, Cowled C, Bean AGD, Stewart CR, Dearnley M, et al. MicroRNA Biomarkers for Infectious Diseases: From Basic Research to Biosensing. Front Microbiol. 2020; 11:1197. Epub 2020/06/26. https://doi.org/10.3389/fmicb.2020.01197 PMID: 32582115; PubMed Central PMCID: PMC7286131.

52. Gallo A, Tandon M, Alevizos I, Illei GG. The majority of microRNAs detectable in serum and saliva is concentrated in exosomes. PLoS One. 2012; 7(3):e30679. Epub 2012/03/20. https://doi.org/10.1371/journal.pone.0030679 PMID: 22427800; PubMed Central PMCID: PMC3302865.

53. Wu L, Zheng K, Yan C, Pan X, Liu Y, Liu J, et al. Genome-wide study of salivary microRNAs as potential noninvasive biomarkers for detection of nasopharyngeal carcinoma. BMC Cancer. 2019; 19 (1):843. Epub 2019/08/29. https://doi.org/10.1186/s12885-019-6037-y PMID: 31455274; PubMed Central PMCID: PMC6712819.

54. Ishige F, Hoshino I, Iwatate Y, Chiba S, Arimitsu H, Yanagibashi H, et al. MIR1246 in body fluids as a biomarker for pancreatic cancer. Sci Rep. 2020; 10(1):8723. Epub 2020/05/28. https://doi.org/10.1038/s41598-020-65695-6 PMID: 32457495; PubMed Central PMCID: PMC7250935.

55. Sisto R, Capone P, Cerini L, Sanjust F, Paci E, Pigini D, et al. Circulating microRNAs as potential biomarkers of occupational exposure to low dose organic solvents. Toxicol Rep. 2019; 6:126–35. Epub 2019/01/24. https://doi.org/10.1016/j.toxrep.2019.01.001 PMID: 30671348; PubMed Central PMCID: PMC6330509.

56. Deping C, Bofan J, Yaogang Z, Mingquan P. microRNA-125b-5p is a promising novel plasma biomarker for alveolar echinococcosis in patients from the southern province of Qinghai. BMC Infect Dis. 2021; 21(1):246. Epub 2021/03/09. https://doi.org/10.1186/s12879-021-05940-z PMID: 33678159; PubMed Central PMCID: PMC7938541.

57. Byrd AE, Brewer JW. Micro(RNA)managing endoplasmic reticulum stress. IUBMB Life. 2013; 65 (5):373–81. Epub 2013/04/05. https://doi.org/10.1002/iub.1151 PMID: 23554021; PubMed Central PMCID: PMC3637854.

58. Bartoszewska S, Kochan K, Madanecki P, Piotrowski A, Ochocka R, Collawn JF, et al. Regulation of the unfolded protein response by microRNAs. Cell Mol Biol Lett. 2013; 18(4):555–78. Epub 2013/10/05. https://doi.org/10.2478/s11658-013-0106-z PMID: 24092331; PubMed Central PMCID: PMC3877167.

59. Lerner AG, Upton JP, Praveen PV, Ghosh R, Nakagawa Y, Igbaria A, et al. IRE1alpha induces thioredoxin-interacting protein to activate the NLRP3 inflammasome and promote programmed cell death under irremediable ER stress. Cell Metab. 2012; 16(2):250–64. Epub 2012/08/14. https://doi.org/10.1016/j.cmet.2012.07.007 PMID: 22883233; PubMed Central PMCID: PMC4014071.

60. Upton JP, Wang L, Han D, Wang ES, Huskey NE, Lim L, et al. IRE1alpha cleaves select microRNAs during ER stress to derepress translation of proapoptotic Caspase-2. Science. 2012; 338(6108):818–

22. Epub 2012/10/09. https://doi.org/10.1126/science.1226191 PMID: 23042294; PubMed Central PMCID: PMC3742121.

61. Byrd AE, Aragon IV, Brewer JW. MicroRNA-30c-2* limits expression of proadaptive factor XBP1 in the unfolded protein response. J Cell Biol. 2012; 196(6):689–98. Epub 2012/03/21. https://doi.org/10.1083/jcb.201201077 PMID: 22431749; PubMed Central PMCID: PMC3308703.

62. Boubaker G, Strempel S, Hemphill A, Muller N, Wang J, Gottstein B, et al. Regulation of hepatic microRNAs in response to early stage Echinococcus multilocularis egg infection in C57BL/6 mice. PLoS Negl Trop Dis. 2020; 14(5):e0007640. Epub 2020/05/23. https://doi.org/10.1371/journal.pntd.0007640 PMID: 32442168; PubMed Central PMCID: PMC7244097 following competing interests: Sebastian Strempel is employee of Microsynth AG.

63. Banerjee A, Czinn SJ, Reiter RJ, Blanchard TG. Crosstalk between endoplasmic reticulum stress and anti-viral activities: A novel therapeutic target for COVID-19. Life Sciences. 2020; 255:117842. https://doi.org/10.1016/j.lfs.2020.117842 PMID: 32454157

64. Crunkhorn S. ER stress modulator reverses diabetes. Nat Rev Drug Discov. 2015; 14(8):528–. https://doi.org/10.1038/nrd4693 PMID: 26228756

65. Schögler A, Caliaro O, Brügger M, Oliveira Esteves BI, Nita I, Gazdhar A, et al. Modulation of the unfolded protein response pathway as an antiviral approach in airway epithelial cells. Antiviral Res. 2019; 162:44–50. https://doi.org/10.1016/j.antiviral.2018.12.007 PMID: 30550797

66. Weingartner M, Stücheli S. The ratio of ursodeoxycholyltaurine to 7-oxolithocholyltaurine serves as a biomarker of decreased 11β-hydroxysteroid dehydrogenase 1 activity in mouse.

67. Schmittgen TD, Livak KJ. Analyzing real-time PCR data by the comparative C(T) method. Nat Protoc. 2008; 3(6):1101–8. Epub 2008/06/13. https://doi.org/10.1038/nprot.2008.73 PMID: 18546601.

68. Agarwal V, Bell GW, Nam JW, Bartel DP. Predicting effective microRNA target sites in mammalian mRNAs. Elife. 2015; 4. Epub 2015/08/13. https://doi.org/10.7554/eLife.05005 PMID: 26267216; PubMed Central PMCID: PMC4532895.

69. Miranda KC, Huynh T, Tay Y, Ang YS, Tam WL, Thomson AM, et al. A pattern-based method for the identification of MicroRNA binding sites and their corresponding heteroduplexes. Cell. 2006; 126 (6):1203–17. Epub 2006/09/23. https://doi.org/10.1016/j.cell.2006.07.031 PMID: 16990141.

70. Chen Y, Wang X. miRDB: an online database for prediction of functional microRNA targets. Nucleic Acids Res. 2020; 48(D1):D127–D31. Epub 2019/09/11. https://doi.org/10.1093/nar/gkz757 PMID: 31504780; PubMed Central PMCID: PMC6943051.

71. Celli J, Tsolis RM. Bacteria, the endoplasmic reticulum and the unfolded protein response: friends or foes? Nat Rev Microbiol. 2015; 13(2):71–82. Epub 2014/12/24. https://doi.org/10.1038/nrmicro3393 PMID: 25534809; PubMed Central PMCID: PMC4447104.

72. Pathinayake PS, Hsu ACY, Waters DW, Hansbro PM, Wood LG, Wark PAB. Understanding the Unfolded Protein Response in the Pathogenesis of Asthma. Front Immunol. 2018; 9. https://doi.org/10.3389/fimmu.2018.00175 PMID: 29472925

73. Abhishek K, Das S, Kumar A, Kumar A, Kumar V, Saini S, et al. Leishmania donovani induced Unfolded Protein Response delays host cell apoptosis in PERK dependent manner. PLOS Neglected Tropical Diseases. 2018; 12(7). https://doi.org/10.1371/journal.pntd.0006646 PMID: 30036391

74. Adams CJ, Kopp MC, Larburu N, Nowak PR, Ali MMU. Structure and Molecular Mechanism of ER Stress Signaling by the Unfolded Protein Response Signal Activator IRE1. Front Mol Biosci. 2019; 6. https://doi.org/10.3389/fmolb.2019.00011 PMID: 30931312

75. Amen OM, Sarker SD, Ghildyal R, Arya A. Endoplasmic Reticulum Stress Activates Unfolded Protein Response Signaling and Mediates Inflammation, Obesity, and Cardiac Dysfunction: Therapeutic and Molecular Approach. Front Pharmacol. 2019; 10. https://doi.org/10.3389/fphar.2019.00977 PMID: 31551782

76. Bergmann TJ, Molinari M. Three branches to rule them all? UPR signalling in response to chemically versus misfolded proteins-induced ER stress. Biol Cell. 2018; 110(9):197–204. https://doi.org/10.1111/boc.201800029 PMID: 29979817

77. Bravo R, Parra V, Gatica D, Rodriguez AE, Torrealba N, Paredes F, et al. Endoplasmic reticulum and the unfolded protein response: dynamics and metabolic integration. Int Rev Cell Mol Biol. 2013; 301:215–90. Epub 2013/01/16. https://doi.org/10.1016/B978-0-12-407704-1.00005-1 PMID: 23317820; PubMed Central PMCID: PMC3666557.

78. Hollien J. Evolution of the unfolded protein response. Biochimica et Biophysica Acta (BBA)—Molecular Cell Research. 2013; 1833(11):2458–63. https://doi.org/10.1016/j.bbamcr.2013.01.016 PMID: 23369734

79. Clark EM, Nonarath HJT, Bostrom JR, Link BA. Establishment and validation of an endoplasmic reticulum stress reporter to monitor zebrafish ATF6 activity in development and disease. Dis Model Mech. 2020; 13(1). https://doi.org/10.1242/dmm.041426 PMID: 31852729

80. Oslowski CM, Urano F. Measuring ER stress and the unfolded protein response using mammalian tissue culture system. Methods Enzymol. 2011; 490:71–92. https://doi.org/10.1016/B978-0-12-385114-7.00004-0 PMID: 21266244

81. Sundaram A, Appathurai S, Plumb R, Mariappan M. Dynamic changes in complexes of IRE1α, PERK, and ATF6α during endoplasmic reticulum stress. Mol Biol Cell. 2018; 29(11):1376–88. https://doi.org/10.1091/mbc.E17-10-0594 PMID: 29851562

82. Walter P, Ron D. The Unfolded Protein Response: From Stress Pathway to Homeostatic Regulation. Science. 2011; 334(6059):1081–6. https://doi.org/10.1126/science.1209038 PMID: 22116877

83. Shaheen A. Effect of the unfolded protein response on ER protein export: a potential new mechanism to relieve ER stress. Cell Stress & Chaperones. 2018; 23(5):797–806. https://doi.org/10.1007/s12192-018-0905-2 PMID: 29730847

84. Almanza A, Carlesso A, Chintha C, Creedican S, Doultsinos D, Leuzzi B, et al. Endoplasmic reticulum stress signalling–from basic mechanisms to clinical applications. The FEBS Journal. 2019; 286 (2):241–78. https://doi.org/10.1111/febs.14608 PMID: 30027602

85. English BC, Van Prooyen N, Ord T, Ord T, Sil A. The transcription factor CHOP, an effector of the integrated stress response, is required for host sensitivity to the fungal intracellular pathogen Histoplasma capsulatum. PLoS Pathog. 2017; 13(9):e1006589. Epub 2017/09/28. https://doi.org/10.1371/journal.ppat.1006589 PMID: 28953979; PubMed Central PMCID: PMC5633207.

86. Lu X, Li C, Li C, Li P, Fu E, Xie Y, et al. Heat-Labile Enterotoxin-Induced PERK-CHOP Pathway Activation Causes Intestinal Epithelial Cell Apoptosis. Front Cell Infect Microbiol. 2017; 7:244. Epub 2017/06/24. https://doi.org/10.3389/fcimb.2017.00244 PMID: 28642847; PubMed Central PMCID: PMC5463185.

87. Dias-Teixeira KL, Calegari-Silva TC, Medina JM, Vivarini AC, Cavalcanti A, Teteo N, et al. Emerging Role for the PERK/eIF2alpha/ATF4 in Human Cutaneous Leishmaniasis. Sci Rep. 2017; 7(1):17074. Epub 2017/12/08. https://doi.org/10.1038/s41598-017-17252-x PMID: 29213084; PubMed Central PMCID: PMC5719050.

88. Mesclon F, Lambert-Langlais S, Carraro V, Parry L, Hainault I, Jousse C, et al. Decreased ATF4 expression as a mechanism of acquired resistance to long-term amino acid limitation in cancer cells. Oncotarget. 2017; 8(16):27440–53. Epub 2017/05/04. https://doi.org/10.18632/oncotarget.15828 PMID: 28460466; PubMed Central PMCID: PMC5432347.

89. Lin C, Chen Z, Zhang L, Wei Z, Cheng KK, Liu Y, et al. Deciphering the metabolic perturbation in hepatic alveolar echinococcosis: a (1)H NMR-based metabolomics study. Parasit Vectors. 2019; 12 (1):300. Epub 2019/06/15. https://doi.org/10.1186/s13071-019-3554-0 PMID: 31196218; PubMed Central PMCID: PMC6567409.

90. Paschen W, Mengesdorf T. Endoplasmic reticulum stress response and neurodegeneration. Cell Calcium. 2005; 38(3–4):409–15. Epub 2005/08/10. https://doi.org/10.1016/j.ceca.2005.06.019 PMID: 16087231.

91. Chen Y, Brandizzi F. IRE1: ER stress sensor and cell fate executor. Trends Cell Biol. 2013; 23 (11):547–55. Epub 2013/07/25. https://doi.org/10.1016/j.tcb.2013.06.005 PMID: 23880584; PubMed Central PMCID: PMC3818365.

92. Akhter MS, Uddin MA, Kubra KT, Barabutis N. Autophagy, Unfolded Protein Response and Lung Disease. Curr Res Cell Biol. 2020; 1. Epub 2020/11/10. https://doi.org/10.1016/j.crcbio.2020.100003 PMID: 33163960; PubMed Central PMCID: PMC7643908.

93. Harrison SR, Scambler T, Oubussad L, Wong C, Wittmann M, McDermott MF, et al. Inositol-Requiring Enzyme 1-Mediated Downregulation of MicroRNA (miR)-146a and miR-155 in Primary Dermal Fibroblasts across Three TNFRSF1A Mutations Results in Hyperresponsiveness to Lipopolysaccharide. Front Immunol. 2018; 9:173. Epub 2018/02/23. https://doi.org/10.3389/fimmu.2018.00173 PMID: 29467762; PubMed Central PMCID: PMC5808292.

94. Zhao G, Gu W. Effects of miR-146a-5p on chondrocyte interleukin-1beta-induced inflammation and apoptosis involving thioredoxin interacting protein regulation. J Int Med Res. 2020; 48 (11):300060520969550. Epub 2020/11/10. https://doi.org/10.1177/0300060520969550 PMID: 33161770; PubMed Central PMCID: PMC7658527.

95. Luis A, Hackl M, Jafarmadar M, Keibl C, Jilge JM, Grillari J, et al. Circulating miRNAs Associated With ER Stress and Organ Damage in a Preclinical Model of Trauma Hemorrhagic Shock. Front Med (Lausanne). 2020; 7:568096. Epub 2020/10/20. https://doi.org/10.3389/fmed.2020.568096 PMID: 33072784; PubMed Central PMCID: PMC7542230.

96. Wilczynski M, Zytko E, Szymanska B, Dzieniecka M, Nowak M, Danielska J, et al. Expression of miR-146a in patients with ovarian cancer and its clinical significance. Oncol Lett. 2017; 14(3):3207–14. Epub 2017/09/21. https://doi.org/10.3892/ol.2017.6477 PMID: 28927067; PubMed Central PMCID: PMC5588008.

97. Halperin L, Jung J, Michalak M. The many functions of the endoplasmic reticulum chaperones and folding enzymes. IUBMB Life. 2014; 66(5):318–26. https://doi.org/10.1002/iub.1272 PMID: 24839203

98. Ruggiano A, Foresti O, Carvalho P. ER-associated degradation: Protein quality control and beyond. J Cell Biol. 2014; 204(6):869–79. https://doi.org/10.1083/jcb.201312042 PMID: 24637321

99. Danilczyk UG, Cohen-Doyle MF, Williams DB. Functional Relationship between Calreticulin, Calnexin, and the Endoplasmic Reticulum Luminal Domain of Calnexin. J Biol Chem. 2000; 275(17):13089–97. https://doi.org/10.1074/jbc.275.17.13089 PMID: 10777614

100. Radons J. The human HSP70 family of chaperones: where do we stand? Cell Stress & Chaperones. 2016; 21(3):379–404. https://doi.org/10.1007/s12192-016-0676-6 PMID: 26865365

101. Williams DB. Beyond lectins: the calnexin/calreticulin chaperone system of the endoplasmic reticulum. J Cell Sci. 2006; 119(4):615–23. https://doi.org/10.1242/jcs.02856 PMID: 16467570

102. Ni M, Lee AS. ER chaperones in mammalian development and human diseases. FEBS Lett. 2007; 581(19):3641–51. https://doi.org/10.1016/j.febslet.2007.04.045 PMID: 17481612

103. Tsachaki M, Mladenovic N, Stambergova H, Birk J, Odermatt A. Hexose-6-phosphate dehydrogenase controls cancer cell proliferation and migration through pleiotropic effects on the unfolded-protein response, calcium homeostasis, and redox balance. FASEB J. 2018; 32(5):2690–705. Epub 2018/01/04. https://doi.org/10.1096/fj.201700870RR PMID: 29295867; PubMed Central PMCID: PMC5901385.

104. Dayan AD. Albendazole, mebendazole and praziquantel. Review of non-clinical toxicity and pharmacokinetics. Acta Trop. 2003; 86(2–3):141–59. Epub 2003/05/15. https://doi.org/10.1016/s0001-706x(03)00031-7 PMID: 12745134.

105. Taylor DH, Morris DL, Reffin D, Richards KS. Comparison of albendazole, mebendazole and praziquantel chemotherapy of Echinococcus multilocularis in a gerbil model. Gut. 1989; 30(10):1401–5. Epub 1989/10/01. https://doi.org/10.1136/gut.30.10.1401 PubMed Central PMCID: PMC1434421. PMID: 2583567

106. Liance M, Bresson-Hadni S, Vuitton D, Bretagne S, Houin R. Comparison of the viability and developmental characteristics of Echinococcus multilocularis isolates from human patients in France. Int J Parasitol. 1990; 20(1):83–6. Epub 1990/02/01. https://doi.org/10.1016/0020-7519(90)90177-o PMID: 2312231

107. Abulaihaiti M, Wu XW, Qiao L, Lv HL, Zhang HW, Aduwayi N, et al. Efficacy of Albendazole-Chitosan Microsphere-based Treatment for Alveolar Echinococcosis in Mice. PLoS Negl Trop Dis. 2015; 9(9): e0003950. Epub 2015/09/10. https://doi.org/10.1371/journal.pntd.0003950 PMID: 26352932; PubMed Central PMCID: PMC4564103.

108. Kuster T, Hermann C, Hemphill A, Gottstein B, Spiliotis M. Subcutaneous infection model facilitates treatment assessment of secondary Alveolar echinococcosis in mice. PLoS Negl Trop Dis. 2013; 7(5): e2235. Epub 2013/05/30. https://doi.org/10.1371/journal.pntd.0002235 PMID: 23717701; PubMed Central PMCID: PMC3662659.

109. Ricken FJ, Nell J, Gruner B, Schmidberger J, Kaltenbach T, Kratzer W, et al. Albendazole increases the inflammatory response and the amount of Em2-positive small particles of Echinococcus multilocularis (spems) in human hepatic alveolar echinococcosis lesions. PLoS Negl Trop Dis. 2017; 11(5): e0005636. Epub 2017/05/26. https://doi.org/10.1371/journal.pntd.0005636 PMID: 28542546; PubMed Central PMCID: PMC5462468.

110. Barth TF, Herrmann TS, Tappe D, Stark L, Gruner B, Buttenschoen K, et al. Sensitive and specific immunohistochemical diagnosis of human alveolar echinococcosis with the monoclonal antibody Em2G11. PLoS Negl Trop Dis. 2012; 6(10):e1877. Epub 2012/11/13. https://doi.org/10.1371/journal.pntd.0001877 PMID: 23145198; PubMed Central PMCID: PMC3493387.

7 ACKNOWLEDGEMENTS

First and foremost I would like to thank Prof. Dr. Alex Odermatt for giving me the opportunity to conduct my PhD in his laboratory after my Master's Thesis. He was always open for discussion and I want to thank him for his support, ideas, scientific input, and especially for the uncomplicated extension of my PhD.

I want to thank Prof. Dr. Henriette E. Meyer zu Schwabedissen of the Biopharmacy group, my second supervisor, for her support, scientific input, and our interesting discussions throughout the years and Prof. Dr. Didier Picard of the University of Geneva for agreeing to be my assigned external expert.

To Dr. Selene Araya, my previous supervisor during my Master's Thesis, I want to say thank you for having introduced me to many techniques and taught me much. Also for her early work on which a large part of my thesis is based on and for patiently taking her time to respond to my inquiries.

I want to say thank you to all my collaborators, both of the Molecular & Systems Toxicology group and external ones, but especially to my co-first authors Dr. Michael Weingartner and Dr. Fadi Jebbawi. I also want to mention Dr. André Fischer for his contribution to the HSD17B6 project, Caner Ercan, and Dr. John Gallon for their analysis of the TMA and TCGA data, respectively.

Further gratitude goes to Dr. Danilo Ritz, Dr. Thomas Hammond, and Dr. Paul Jenö for their kind help in analyzing the proteomics data and to Rebecca Warmers for diligently performing some of the experiments as an intern under my supervision. I also want to thank Dr. Cristina Gómez Castellà for proof reading the thesis and the related feedback and Dr. Miljenko Panajatović for all our discussions.

A big thanks goes to all the members, past and present, of the Molecular & Systems Toxicology group, not only for all the help and feedback anyone ever provided, but especially for creating a wonderful atmosphere with many laughs.

Finally, I want to thank friends and family members for their support.

8 SUPPLEMENTARY INFORMATION

Table S1. Steroids mentioned in this thesis in the context of androgen synthesis [5, 280].

Name in this thesis	Other name	Chemical name	CAS Nr.
17OH-Allopregnanolone	17β-Hydroxyallopregnanolone	5α-pregnane-3α,17α-diol-20-one	6890-65-9
17OH-Dihydroprogesterone	17β-Hydroxydihydroprogesterone	5α-pregnane-17α-ol-3,20-dione	570-59-2
17OH-Pregnenolone	17β-Hydroxypregnenolone	5-pregnen-3β,17α-diol-20-one	387-79-1
17OH-Progesterone	17β-Hydroxyprogesterone	4-pregnen-17α-ol-3,20-dione	68-96-2
3α-Adiol	3α-Androstanediol	5α-androstane-3α,17β-diol	1852-53-5
3α-ADT	(3α-)Androsterone	3α-hydroxy-5α-androstan-17-one	53-41-8
3β-Adiol	3β-Androstanediol	5α-androstane-3β,17β-diol	571-20-0
3β-ADT	(3β-)Epiandrosterone	3β-hydroxy-5α-androstan-17-one	481-29-8
5α-Androstanedione		5a-androstane-3,17-dione	846-46-8
5α-DHT	(5α-)Dihydrotestosterone	5α-androstan-17β-ol-3-one	521-18-6
Allopregnanolone		5α-pregnane-3α-ol-20-one	516-54-1
Androstenediol		5-androsten-3β,17β-diol	521-17-5
Androstenedione		4-androsten-3,17-dione	63-05-8
Cholesterol		Cholest-5-en-3β-ol	57-88-5
DHEA	Dehydroepiandrosterone	5-androsten-3β-ol-17-one	53-43-0
Dihydroprogesterone		5α-pregnane-3,20-dione	566-65-4
Isopregnanolone		5α-pregnane-3β-ol-20-one	516-55-2
Pregnenolone		5-pregnen-3β-ol-20-one	145-13-1
Progesterone		4-pregnen-3,20-dione	57-83-0
Testosterone		4-androsten-17β-ol-3-one	58-22-0

Table S2. Primers used for site directed mutagenesis and cloning.

Use	Direction	Sequence (5' - 3')
Inactivating mutation (Y176F)	Forward	CCA TAC TTG GAG ACA CAG AAG CCT CCT ACA AAG AAA G
Inactivating mutation (Y176F)	Reverse	CTT TCT TTG TAG GAG GCT TCT GTG TCT CCA AGT ATG G
Silent mutation to remove restriction site (g234a)	Forward	AGA CGT CTG ACA GGC TGG AAA CGG TGA CCC TGG AT
Silent mutation to remove restriction site (g234a)	Reverse	ATC CAG GGT CAC CGT TTC CAG CCT GTC AGA CGT CT
Cloning into pDSG-IBA103:	Forward	AGC GCG TCT CCA ATG TGG CTC TAC CTG GC
Cloning into pDSG-IBA103:	Reverse	AGC GCG TCT CCT CCC GAC TGC CTG GGC TGG
Cloning into pDSG-IBA103 with stop in front of the Twin-Strep-tag:	Reverse	AGC GCG TCT CCT CCC CTA GAC TGC CTG GGC TGG

Table S3. Proposed hits of the virtual screening.

ZINC_ID	*2D Structure*	*Consensus score (kcal/mol) 17B6*	*Consensus score (kcal/mol) 17B1*
ZINC000072320548	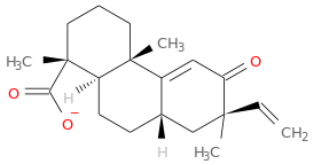	-20.4	-17.0
ZINC000899435119	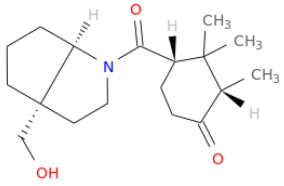	-19	-18.1
ZINC000003849669	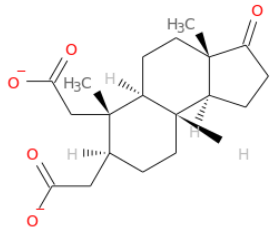	-18.9	-18.0
ZINC000790527981	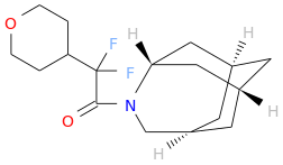	-18.7	-18.2
ZINC000004061141	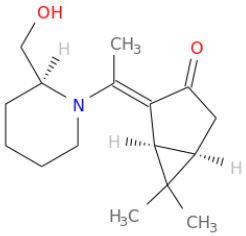	-18	-15.5
ZINC000846581806	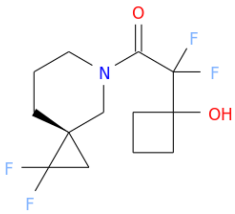	-17.9	-16.7
ZINC000349031459	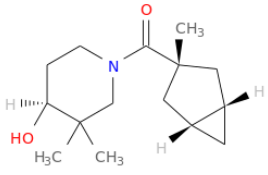	-17.8	-16.0

ZINC000617818752	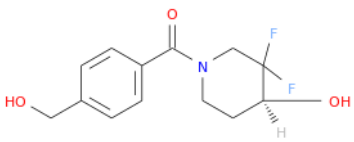	-17.7	-17.9
ZINC000617804938	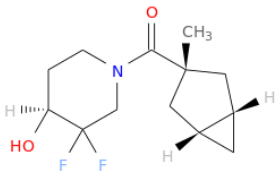	-17.2	-16.6
ZINC001361460958	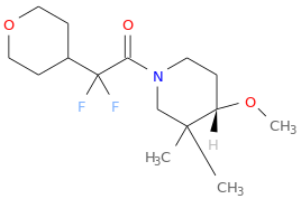	-17.1	-16.5
ZINC000613799024	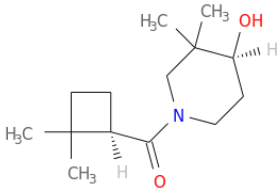	-17.1	-15.3
ZINC000169294805	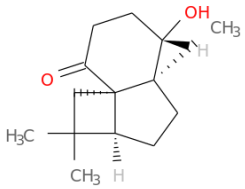	-17.0	-15.1
ZINC000664468770	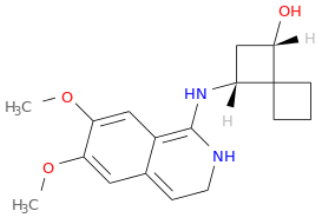	-17.0	-15.1
ZINC000615350795	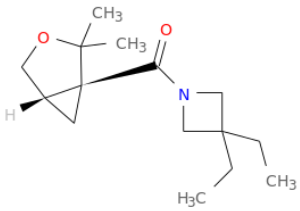	-17.0	-14.4
ZINC000701499841	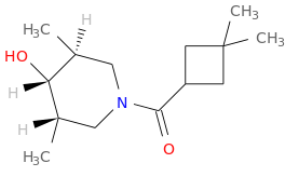	-17.0	-15.8

ZINC_ID	*2D Structure*	*Consensus score (kcal/mol) 17B6*	*Consensus score (kcal/mol) 17B1*
ZINC000008615740	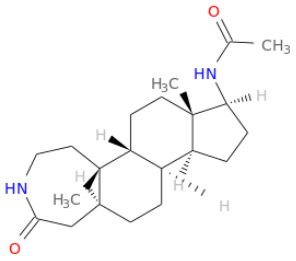	-21.5	-18.3
ZINC000004983567	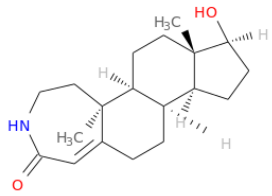	-21.3	-17.7
ZINC000006468568	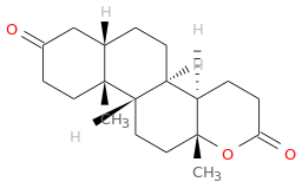	-21.3	-18.1
ZINC000006175885	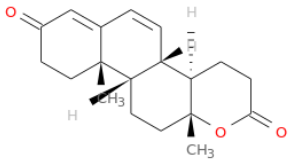	-21.2	-19.3
ZINC000005029545	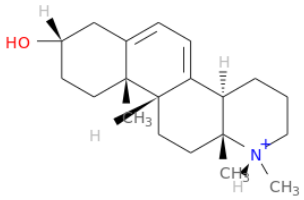	-21.1	-17.9
ZINC000004983563	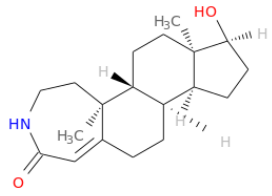	-21.1	-18.5
ZINC000006200052	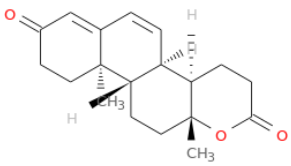	-21.1	-19.2

ZINC000006469390	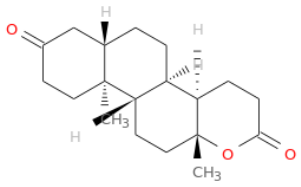	-21.1	-18.6
ZINC000104366884	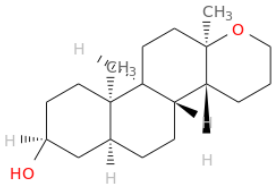	-21.1	-18.4
ZINC000104115404	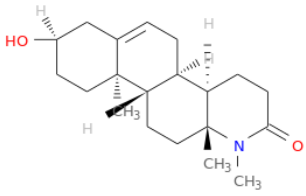	-21.0	-19.5

Correlation of consensus score of HSD17B6 and HSD17B1

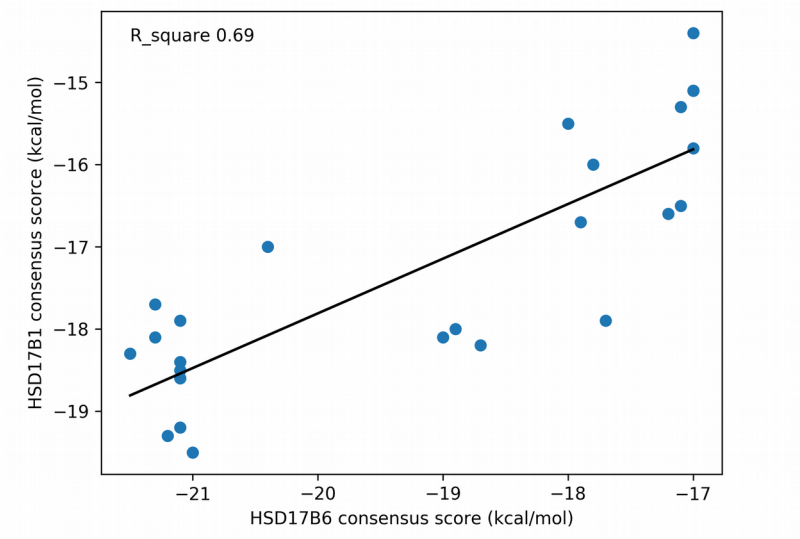

9 REFERENCES

1. Evans, R.M., *The steroid and thyroid hormone receptor superfamily.* Science, 1988. **240**(4854): p. 889-95.
2. Mangelsdorf, D.J., et al., *The nuclear receptor superfamily: the second decade.* Cell, 1995. **83**(6): p. 835-9.
3. Miller, W.L. and R.J. Auchus, *The molecular biology, biochemistry, and physiology of human steroidogenesis and its disorders.* Endocr Rev, 2011. **32**(1): p. 81-151.
4. Biason-Lauber, A., et al., *Of marsupials and men: "Backdoor" dihydrotestosterone synthesis in male sexual differentiation.* Mol Cell Endocrinol, 2013. **371**(1-2): p. 124-32.
5. Fukami, M., et al., *Backdoor pathway for dihydrotestosterone biosynthesis: implications for normal and abnormal human sex development.* Dev Dyn, 2013. **242**(4): p. 320-9.
6. Keller, E.T., W.B. Ershler, and C. Chang, *The androgen receptor: a mediator of diverse responses.* Front Biosci, 1996. **1**: p. d59-71.
7. Smith, L.B. and W.H. Walker, *The regulation of spermatogenesis by androgens.* Semin Cell Dev Biol, 2014. **30**: p. 2-13.
8. Penning, T.M., *New frontiers in androgen biosynthesis and metabolism.* Curr Opin Endocrinol Diabetes Obes, 2010. **17**(3): p. 233-9.
9. Bennett, N.C., et al., *Molecular cell biology of androgen receptor signalling.* Int J Biochem Cell Biol, 2010. **42**(6): p. 813-27.
10. Bauman, D.R., et al., *Identification of the major oxidative 3alpha-hydroxysteroid dehydrogenase in human prostate that converts 5alpha-androstane-3alpha,17beta-diol to 5alpha-dihydrotestosterone: a potential therapeutic target for androgen-dependent disease.* Mol Endocrinol, 2006. **20**(2): p. 444-58.
11. Vaupel, P., E. Mutschler, and H. Schaible, *Anatomie, Physiologie, Pathophysiologie des Menschen. Kapitel 16, Hormonelles System, Seiten 565 - 626*. 2015, Stuttgart: Wiss. Verl.-Ges.
12. Standring, S. and H. Gray, *Gray's Anatomy: The Anatomical Basis of Clinical Practice. Section 3, Chapter 23, Diencephalon, pages 350 - 363 & Section 8, Chapter 71, Suprarenal (adrenal) gland, pages 1194 - 1198*. 2016, Amsterdam: Elsevier.
13. Denmeade, S.R. and J.T. Isaacs, *A history of prostate cancer treatment.* Nat Rev Cancer, 2002. **2**(5): p. 389-96.
14. Gupta, M.K., O.L. Guryev, and R.J. Auchus, *5alpha-reduced C21 steroids are substrates for human cytochrome P450c17.* Arch Biochem Biophys, 2003. **418**(2): p. 151-60.
15. Geissler, W.M., et al., *Male pseudohermaphroditism caused by mutations of testicular 17 beta-hydroxysteroid dehydrogenase 3.* Nat Genet, 1994. **7**(1): p. 34-9.
16. Fluck, C.E., et al., *Why boys will be boys: two pathways of fetal testicular androgen biosynthesis are needed for male sexual differentiation.* Am J Hum Genet, 2011. **89**(2): p. 201-18.
17. Fiandalo, M.V., J. Wilton, and J.L. Mohler, *Roles for the backdoor pathway of androgen metabolism in prostate cancer response to castration and drug treatment.* Int J Biol Sci, 2014. **10**(6): p. 596-601.
18. Chang, K.H. and N. Sharifi, *Prostate cancer-from steroid transformations to clinical translation.* Nat Rev Urol, 2012. **9**(12): p. 721-4.
19. Chang, K.H., et al., *Dihydrotestosterone synthesis bypasses testosterone to drive castration-resistant prostate cancer.* Proc Natl Acad Sci U S A, 2011. **108**(33): p. 13728-33.
20. Steckelbroeck, S., et al., *Human cytosolic 3alpha-hydroxysteroid dehydrogenases of the aldo-keto reductase superfamily display significant 3beta-hydroxysteroid dehydrogenase activity: implications for steroid hormone metabolism and action.* J Biol Chem, 2004. **279**(11): p. 10784-95.
21. Belanger, A., et al., *Inactivation of androgens by UDP-glucuronosyltransferase enzymes in humans.* Trends Endocrinol Metab, 2003. **14**(10): p. 473-9.
22. Barbier, O. and A. Belanger, *Inactivation of androgens by UDP-glucuronosyltransferases in the human prostate.* Best Pract Res Clin Endocrinol Metab, 2008. **22**(2): p. 259-70.
23. Bhatia, C., et al., *Towards a systematic analysis of human short-chain dehydrogenases/reductases (SDR): Ligand identification and structure-activity relationships.* Chem Biol Interact, 2015. **234**: p. 114-25.
24. Filling, C., et al., *Critical residues for structure and catalysis in short-chain dehydrogenases/reductases.* J Biol Chem, 2002. **277**(28): p. 25677-84.
25. Oppermann, U., et al., *Short-chain dehydrogenases/reductases (SDR): the 2002 update.* Chem Biol Interact, 2003. **143-144**: p. 247-53.

26. Kavanagh, K.L., et al., *Medium- and short-chain dehydrogenase/reductase gene and protein families : the SDR superfamily: functional and structural diversity within a family of metabolic and regulatory enzymes.* Cell Mol Life Sci, 2008. **65**(24): p. 3895-906.
27. Araya, S., et al., *DHRS7 (SDR34C1) - A new player in the regulation of androgen receptor function by inactivation of 5alpha-dihydrotestosterone?* J Steroid Biochem Mol Biol, 2017. **171**: p. 288-295.
28. Persson, B., et al., *The SDR (short-chain dehydrogenase/reductase and related enzymes) nomenclature initiative.* Chem Biol Interact, 2009. **178**(1-3): p. 94-8.
29. Penning, T.M., et al., *Identification of the molecular switch that regulates access of 5alpha-DHT to the androgen receptor.* Mol Cell Endocrinol, 2007. **265-266**: p. 77-82.
30. Mohler, J.L., et al., *Activation of the androgen receptor by intratumoral bioconversion of androstanediol to dihydrotestosterone in prostate cancer.* Cancer Res, 2011. **71**(4): p. 1486-96.
31. Bray, J.E., B.D. Marsden, and U. Oppermann, *The human short-chain dehydrogenase/reductase (SDR) superfamily: a bioinformatics summary.* Chem Biol Interact, 2009. **178**(1-3): p. 99-109.
32. Chetyrkin, S.V., et al., *Characterization of a novel type of human microsomal 3alpha -hydroxysteroid dehydrogenase: unique tissue distribution and catalytic properties.* J Biol Chem, 2001. **276**(25): p. 22278-86.
33. Markova, N.G., et al., *Expression pattern and biochemical characteristics of a major epidermal retinol dehydrogenase.* Mol Genet Metab, 2003. **78**(2): p. 119-35.
34. Hu, L., et al., *Downregulation of DHRS9 expression in colorectal cancer tissues and its prognostic significance.* Tumour Biol, 2016. **37**(1): p. 837-45.
35. Khalid, M., et al., *Gene Regulation by Antitumor miR-204-5p in Pancreatic Ductal Adenocarcinoma: The Clinical Significance of Direct RACGAP1 Regulation.* Cancers (Basel), 2019. **11**(3).
36. Li, H.B., et al., *Prognostic Impact of DHRS9 Overexpression in Pancreatic Cancer.* Cancer Manag Res, 2020. **12**: p. 5997-6006.
37. Mertz, J.R., et al., *Identification and characterization of a stereospecific human enzyme that catalyzes 9-cis-retinol oxidation. A possible role in 9-cis-retinoic acid formation.* J Biol Chem, 1997. **272**(18): p. 11744-9.
38. Wang, J., et al., *Activity of human 11-cis-retinol dehydrogenase (Rdh5) with steroids and retinoids and expression of its mRNA in extra-ocular human tissue.* Biochem J, 1999. **338 (Pt 1)**: p. 23-7.
39. Simon, A., et al., *The retinal pigment epithelial-specific 11-cis retinol dehydrogenase belongs to the family of short chain alcohol dehydrogenases.* J Biol Chem, 1995. **270**(3): p. 1107-12.
40. Hu, H., et al., *Retinal dehydrogenase 5 (RHD5) attenuates metastasis via regulating HIPPO/YAP signaling pathway in Hepatocellular Carcinoma.* Int J Med Sci, 2020. **17**(13): p. 1897-1908.
41. Ashla, A.A., et al., *Genetic analysis of expression profile involved in retinoid metabolism in non-alcoholic fatty liver disease.* Hepatol Res, 2010. **40**(6): p. 594-604.
42. Gough, W.H., et al., *cDNA cloning and characterization of a new human microsomal NAD+-dependent dehydrogenase that oxidizes all-trans-retinol and 3alpha-hydroxysteroids.* J Biol Chem, 1998. **273**(31): p. 19778-85.
43. Jurukovski, V., et al., *Cloning and characterization of retinol dehydrogenase transcripts expressed in human epidermal keratinocytes.* Mol Genet Metab, 1999. **67**(1): p. 62-73.
44. Udali, S., et al., *DNA methylation and gene expression profiles show novel regulatory pathways in hepatocellular carcinoma.* Clin Epigenetics, 2015. **7**: p. 43.
45. Ouyang, G., et al., *A robust twelve-gene signature for prognosis prediction of hepatocellular carcinoma.* Cancer Cell Int, 2020. **20**: p. 207.
46. Zhu, Y.H., et al., *Clinical significance and function of RDH16 as a tumor-suppressing gene in hepatocellular carcinoma.* Hepatol Res, 2020. **50**(1): p. 110-120.
47. Tsachaki, M. and A. Odermatt, *Subcellular localization and membrane topology of 17beta-hydroxysteroid dehydrogenases.* Mol Cell Endocrinol, 2019. **489**: p. 98-106.
48. Yang, S.Y., X.Y. He, and D. Miller, *Hydroxysteroid (17beta) dehydrogenase X in human health and disease.* Mol Cell Endocrinol, 2011. **343**(1-2): p. 1-6.
49. He, X.Y., et al., *Oxidative 3alpha-hydroxysteroid dehydrogenase activity of human type 10 17beta-hydroxysteroid dehydrogenase.* J Steroid Biochem Mol Biol, 2003. **87**(2-3): p. 191-8.
50. He, X.Y., et al., *Function of human brain short chain L-3-hydroxyacyl coenzyme A dehydrogenase in androgen metabolism.* Biochim Biophys Acta, 2000. **1484**(2-3): p. 267-77.
51. He, X.Y., et al., *Type 10 17beta-hydroxysteroid dehydrogenase catalyzing the oxidation of steroid modulators of gamma-aminobutyric acid type A receptors.* Mol Cell Endocrinol, 2005. **229**(1-2): p. 111-7.

52. Salas, S., et al., *Molecular characterization of the response to chemotherapy in conventional osteosarcomas: predictive value of HSD17B10 and IFITM2.* Int J Cancer, 2009. **125**(4): p. 851-60.
53. Biswas, M.G. and D.W. Russell, *Expression cloning and characterization of oxidative 17beta- and 3alpha-hydroxysteroid dehydrogenases from rat and human prostate.* J Biol Chem, 1997. **272**(25): p. 15959-66.
54. Huang, X.F. and V. Luu-The, *Molecular characterization of a first human 3(alpha-->beta)-hydroxysteroid epimerase.* J Biol Chem, 2000. **275**(38): p. 29452-7.
55. Lv, L., et al., *Downexpression of HSD17B6 correlates with clinical prognosis and tumor immune infiltrates in hepatocellular carcinoma.* Cancer Cell Int, 2020. **20**: p. 210.
56. Chetyrkin, S.V., et al., *Further characterization of human microsomal 3alpha-hydroxysteroid dehydrogenase.* Arch Biochem Biophys, 2001. **386**(1): p. 1-10.
57. Muthusamy, S., et al., *Estrogen receptor beta and 17beta-hydroxysteroid dehydrogenase type 6, a growth regulatory pathway that is lost in prostate cancer.* Proc Natl Acad Sci U S A, 2011. **108**(50): p. 20090-4.
58. Huang, X.F. and V. Luu-The, *Gene structure, chromosomal localization and analysis of 3-ketosteroid reductase activity of the human 3(alpha-->beta)-hydroxysteroid epimerase.* Biochim Biophys Acta, 2001. **1520**(2): p. 124-30.
59. Mohler, J.L., M.A. Titus, and E.M. Wilson, *Potential prostate cancer drug target: bioactivation of androstanediol by conversion to dihydrotestosterone.* Clin Cancer Res, 2011. **17**(18): p. 5844-9.
60. Wu, M. and L. Jiang, *Hydroxysteroid 17-Beta Dehydrogenase 6 Is a Prognostic Biomarker and Correlates with Immune Infiltrates in Hepatocellular Carcinoma.* Dig Dis Sci, 2021.
61. Hu, J., et al., *Identification of an Individualized Metabolism Prognostic Signature and Related Therapy Regimens in Early Stage Lung Adenocarcinoma.* Front Oncol, 2021. **11**: p. 650853.
62. Ju, R., et al., *Association analysis between the polymorphisms of HSD17B5 and HSD17B6 and risk of polycystic ovary syndrome in Chinese population.* Eur J Endocrinol, 2015. **172**(3): p. 227-33.
63. Seibert, J.K., et al., *A role for the dehydrogenase DHRS7 (SDR34C1) in prostate cancer.* Cancer Med, 2015. **4**(11): p. 1717-29.
64. Stambergova, H., et al., *Human DHRS7, promising enzyme in metabolism of steroids and retinoids?* J Steroid Biochem Mol Biol, 2016. **155**(Pt A): p. 112-9.
65. Haeseleer, F. and K. Palczewski, *Short-chain dehydrogenases/reductases in retina.* Methods Enzymol, 2000. **316**: p. 372-83.
66. Keildson, S., et al., *Expression of phosphofructokinase in skeletal muscle is influenced by genetic variation and associated with insulin sensitivity.* Diabetes, 2014. **63**(3): p. 1154-65.
67. Stambergova, H., et al., *Biochemical properties of human dehydrogenase/reductase (SDR family) member 7.* Chem Biol Interact, 2014. **207**: p. 52-7.
68. Skarka, A., et al., *Purification and reconstitution of human membrane-bound DHRS7 (SDR34C1) from Sf9 cells.* Protein Expr Purif, 2014. **95**: p. 44-9.
69. Zemanova, L., et al., *The identification of new substrates of human DHRS7 by molecular modeling and in vitro testing.* Int J Biol Macromol, 2017. **105**(Pt 1): p. 171-182.
70. Lathe, R. and Y. Kotelevtsev, *Steroid signaling: ligand-binding promiscuity, molecular symmetry, and the need for gating.* Steroids, 2014. **82**: p. 14-22.
71. Stanbrough, M., et al., *Increased expression of genes converting adrenal androgens to testosterone in androgen-independent prostate cancer.* Cancer Res, 2006. **66**(5): p. 2815-25.
72. Romanuik, T.L., et al., *LNCaP Atlas: gene expression associated with in vivo progression to castration-recurrent prostate cancer.* BMC Med Genomics, 2010. **3**: p. 43.
73. McNeal, J.E., *The zonal anatomy of the prostate.* Prostate, 1981. **2**(1): p. 35-49.
74. Young, B., P. Woodford, and G. O'Dowd, *Wheater's Functional Histology: A Text and Colour Atlas. Part III, Organ Systems, 18, Male Reproductive System, pages 347 - 348*. Sixth edition / ed. 2014, Philadelphia, PA: Churchill Livingston/Elsevier.
75. Rebello, R.J., et al., *Prostate cancer.* Nat Rev Dis Primers, 2021. **7**(1): p. 9.
76. Foster, C.S., et al., *Prostatic stem cells.* J Pathol, 2002. **197**(4): p. 551-65.
77. Parimi, V., et al., *Neuroendocrine differentiation of prostate cancer: a review.* Am J Clin Exp Urol, 2014. **2**(4): p. 273-85.
78. Puca, L., P.J. Vlachostergios, and H. Beltran, *Neuroendocrine Differentiation in Prostate Cancer: Emerging Biology, Models, and Therapies.* Cold Spring Harb Perspect Med, 2019. **9**(2).
79. Krijnen, J.L., et al., *Do neuroendocrine cells in human prostate cancer express androgen receptor?* Histochemistry, 1993. **100**(5): p. 393-8.

80. Bonkhoff, H., U. Stein, and K. Remberger, *Androgen receptor status in endocrine-paracrine cell types of the normal, hyperplastic, and neoplastic human prostate.* Virchows Arch A Pathol Anat Histopathol, 1993. **423**(4): p. 291-4.
81. Henry, G.H., et al., *A Cellular Anatomy of the Normal Adult Human Prostate and Prostatic Urethra.* Cell Rep, 2018. **25**(12): p. 3530-3542 e5.
82. Bray, F., et al., *Global cancer statistics 2018: GLOBOCAN estimates of incidence and mortality worldwide for 36 cancers in 185 countries.* CA Cancer J Clin, 2018. **68**(6): p. 394-424.
83. Office, F.S., *Swiss Cancer Report 2015 - Current situation and developments.* 2016.
84. Gann, P.H., *Risk factors for prostate cancer.* Rev Urol, 2002. **4 Suppl 5**: p. S3-S10.
85. Gronberg, H., *Prostate cancer epidemiology.* Lancet, 2003. **361**(9360): p. 859-64.
86. Rebbeck, T.R. and G.P. Haas, *Temporal trends and racial disparities in global prostate cancer prevalence.* Can J Urol, 2014. **21**(5): p. 7496-506.
87. Jahn, J.L., E.L. Giovannucci, and M.J. Stampfer, *The high prevalence of undiagnosed prostate cancer at autopsy: implications for epidemiology and treatment of prostate cancer in the Prostate-specific Antigen-era.* Int J Cancer, 2015. **137**(12): p. 2795-802.
88. Chu, K.C., R.E. Tarone, and H.P. Freeman, *Trends in prostate cancer mortality among black men and white men in the United States.* Cancer, 2003. **97**(6): p. 1507-16.
89. Siegel, R.L., K.D. Miller, and A. Jemal, *Cancer statistics, 2020.* CA Cancer J Clin, 2020. **70**(1): p. 7-30.
90. Chornokur, G., et al., *Disparities at presentation, diagnosis, treatment, and survival in African American men, affected by prostate cancer.* Prostate, 2011. **71**(9): p. 985-97.
91. Rebbeck, T.R., *Prostate Cancer Disparities by Race and Ethnicity: From Nucleotide to Neighborhood.* Cold Spring Harb Perspect Med, 2018. **8**(9).
92. Barber, L., et al., *Family History of Breast or Prostate Cancer and Prostate Cancer Risk.* Clin Cancer Res, 2018. **24**(23): p. 5910-5917.
93. Chen, Y.C., et al., *Family history of prostate and breast cancer and the risk of prostate cancer in the PSA era.* Prostate, 2008. **68**(14): p. 1582-91.
94. Cerhan, J.R., et al., *Family history and prostate cancer risk in a population-based cohort of Iowa men.* Cancer Epidemiol Biomarkers Prev, 1999. **8**(1): p. 53-60.
95. Stanford, J.L. and E.A. Ostrander, *Familial prostate cancer.* Epidemiol Rev, 2001. **23**(1): p. 19-23.
96. Whittemore, A.S., et al., *Family history and prostate cancer risk in black, white, and Asian men in the United States and Canada.* Am J Epidemiol, 1995. **141**(8): p. 732-40.
97. Strope, S.A. and G.L. Andriole, *Prostate cancer screening: current status and future perspectives.* Nat Rev Urol, 2010. **7**(9): p. 487-93.
98. Descotes, J.L., *Diagnosis of prostate cancer.* Asian J Urol, 2019. **6**(2): p. 129-136.
99. Qaseem, A., et al., *Screening for prostate cancer: a guidance statement from the Clinical Guidelines Committee of the American College of Physicians.* Ann Intern Med, 2013. **158**(10): p. 761-769.
100. Agalliu, I., et al., *Prostate cancer mortality in relation to screening by prostate-specific antigen testing and digital rectal examination: a population-based study in middle-aged men.* Cancer Causes Control, 2007. **18**(9): p. 931-7.
101. Hugosson, J., et al., *A 16-yr Follow-up of the European Randomized study of Screening for Prostate Cancer.* Eur Urol, 2019. **76**(1): p. 43-51.
102. Kopec, J.A., et al., *Screening with prostate specific antigen and metastatic prostate cancer risk: a population based case-control study.* J Urol, 2005. **174**(2): p. 495-9; discussion 499.
103. Hayes, J.H. and M.J. Barry, *Screening for prostate cancer with the prostate-specific antigen test: a review of current evidence.* JAMA, 2014. **311**(11): p. 1143-9.
104. Chou, R., et al., *Screening for prostate cancer: a review of the evidence for the U.S. Preventive Services Task Force.* Ann Intern Med, 2011. **155**(11): p. 762-71.
105. Schroder, F.H., et al., *Prostate-cancer mortality at 11 years of follow-up.* N Engl J Med, 2012. **366**(11): p. 981-90.
106. Shao, Y.H., et al., *Contemporary risk profile of prostate cancer in the United States.* J Natl Cancer Inst, 2009. **101**(18): p. 1280-3.
107. Andriole, G.L., et al., *Prostate cancer screening in the randomized Prostate, Lung, Colorectal, and Ovarian Cancer Screening Trial: mortality results after 13 years of follow-up.* J Natl Cancer Inst, 2012. **104**(2): p. 125-32.
108. Abrahamsson, P.A., et al., *European Association of Urology position statement on screening for prostate cancer.* Eur Urol, 2009. **56**(2): p. 270-1.
109. Epstein, J.I., et al., *A Contemporary Prostate Cancer Grading System: A Validated Alternative to the Gleason Score.* Eur Urol, 2016. **69**(3): p. 428-35.

110. Mottet, N., et al., *EAU-ESTRO-SIOG Guidelines on Prostate Cancer. Part 1: Screening, Diagnosis, and Local Treatment with Curative Intent.* Eur Urol, 2017. **71**(4): p. 618-629.
111. Kweldam, C.F., G.J. van Leenders, and T. van der Kwast, *Grading of prostate cancer: a work in progress.* Histopathology, 2019. **74**(1): p. 146-160.
112. Gleason, D.F., *Classification of prostatic carcinomas.* Cancer Chemother Rep, 1966. **50**(3): p. 125-8.
113. Berney, D.M., *The case for modifying the Gleason grading system.* BJU Int, 2007. **100**(4): p. 725-6.
114. Stark, J.R., et al., *Gleason score and lethal prostate cancer: does 3 + 4 = 4 + 3?* J Clin Oncol, 2009. **27**(21): p. 3459-64.
115. Humphrey, P.A., et al., *The 2016 WHO Classification of Tumours of the Urinary System and Male Genital Organs-Part B: Prostate and Bladder Tumours.* Eur Urol, 2016. **70**(1): p. 106-119.
116. Edge, S.B., et al., eds. *AJCC cancer staging manual. Part IX, Section 41, pages 457 - 468*. 7th ed. 2009, Springer.
117. Cornford, P., et al., *EAU-ESTRO-SIOG Guidelines on Prostate Cancer. Part II: Treatment of Relapsing, Metastatic, and Castration-Resistant Prostate Cancer.* Eur Urol, 2017. **71**(4): p. 630-642.
118. *Charles B. Huggins – Facts. NobelPrize.org. Nobel Prize Outreach AB 2021.* 2021 [cited 2021 15.11.2021]; Available from: https://www.nobelprize.org/prizes/medicine/1966/huggins/facts/.
119. Huggins, C. and C.V. Hodges, *Studies on prostatic cancer. I. The effect of castration, of estrogen and androgen injection on serum phosphatases in metastatic carcinoma of the prostate.* CA Cancer J Clin, 1972. **22**(4): p. 232-40.
120. Morote, J., et al., *Redefining clinically significant castration levels in patients with prostate cancer receiving continuous androgen deprivation therapy.* J Urol, 2007. **178**(4 Pt 1): p. 1290-5.
121. Oefelein, M.G., et al., *Reassessment of the definition of castrate levels of testosterone: implications for clinical decision making.* Urology, 2000. **56**(6): p. 1021-4.
122. Garje, R., et al., *Utilization and Outcomes of Surgical Castration in Comparison to Medical Castration in Metastatic Prostate Cancer.* Clin Genitourin Cancer, 2020. **18**(2): p. e157-e166.
123. Schally, A.V., N.L. Block, and F.G. Rick, *Discovery of LHRH and development of LHRH analogs for prostate cancer treatment.* Prostate, 2017. **77**(9): p. 1036-1054.
124. Weckermann, D. and R. Harzmann, *Hormone therapy in prostate cancer: LHRH antagonists versus LHRH analogues.* Eur Urol, 2004. **46**(3): p. 279-83; discussion 283-4.
125. Tsushima, T., et al., *Optimal starting time for flutamide to prevent disease flare in prostate cancer patients treated with a gonadotropin-releasing hormone agonist.* Urol Int, 2001. **66**(3): p. 135-9.
126. Kunath, F., et al., *Non-steroidal antiandrogen monotherapy compared with luteinising hormone-releasing hormone agonists or surgical castration monotherapy for advanced prostate cancer.* Cochrane Database Syst Rev, 2014(6): p. CD009266.
127. Seidenfeld, J., et al., *Single-therapy androgen suppression in men with advanced prostate cancer: a systematic review and meta-analysis.* Ann Intern Med, 2000. **132**(7): p. 566-77.
128. Schmitt, B., et al., *Maximal androgen blockade for advanced prostate cancer.* Cochrane Database Syst Rev, 2000(2): p. CD001526.
129. Akaza, H., et al., *Combined androgen blockade with bicalutamide for advanced prostate cancer: long-term follow-up of a phase 3, double-blind, randomized study for survival.* Cancer, 2009. **115**(15): p. 3437-45.
130. Rydzewska, L.H.M., et al., *Adding abiraterone to androgen deprivation therapy in men with metastatic hormone-sensitive prostate cancer: A systematic review and meta-analysis.* Eur J Cancer, 2017. **84**: p. 88-101.
131. Li, Z., et al., *Conversion of abiraterone to D4A drives anti-tumour activity in prostate cancer.* Nature, 2015. **523**(7560): p. 347-51.
132. McKay, R.R., et al., *A phase 2 trial of abiraterone acetate without glucocorticoids for men with metastatic castration-resistant prostate cancer.* Cancer, 2019. **125**(4): p. 524-532.
133. Clarke, N.W., et al., *Addition of docetaxel to hormonal therapy in low- and high-burden metastatic hormone sensitive prostate cancer: long-term survival results from the STAMPEDE trial.* Ann Oncol, 2019. **30**(12): p. 1992-2003.
134. Parker, C., et al., *Prostate cancer: ESMO Clinical Practice Guidelines for diagnosis, treatment and follow-up.* Ann Oncol, 2020. **31**(9): p. 1119-1134.
135. Taylor, C.D., P. Elson, and D.L. Trump, *Importance of continued testicular suppression in hormone-refractory prostate cancer.* J Clin Oncol, 1993. **11**(11): p. 2167-72.
136. Massard, C. and K. Fizazi, *Targeting continued androgen receptor signaling in prostate cancer.* Clin Cancer Res, 2011. **17**(12): p. 3876-83.
137. Lee, S.H. and M.M. Shen, *Cell types of origin for prostate cancer.* Curr Opin Cell Biol, 2015. **37**: p. 35-41.

138. Beltran, H., et al., *Aggressive variants of castration-resistant prostate cancer.* Clin Cancer Res, 2014. **20**(11): p. 2846-50.
139. Ku, S.Y., et al., *Rb1 and Trp53 cooperate to suppress prostate cancer lineage plasticity, metastasis, and antiandrogen resistance.* Science, 2017. **355**(6320): p. 78-83.
140. Mu, P., et al., *SOX2 promotes lineage plasticity and antiandrogen resistance in TP53- and RB1-deficient prostate cancer.* Science, 2017. **355**(6320): p. 84-88.
141. Berish, R.B., et al., *Translational models of prostate cancer bone metastasis.* Nat Rev Urol, 2018. **15**(7): p. 403-421.
142. Clarke, N.W., C.A. Hart, and M.D. Brown, *Molecular mechanisms of metastasis in prostate cancer.* Asian J Androl, 2009. **11**(1): p. 57-67.
143. Feldman, B.J. and D. Feldman, *The development of androgen-independent prostate cancer.* Nat Rev Cancer, 2001. **1**(1): p. 34-45.
144. Han, M., et al., *Long-term biochemical disease-free and cancer-specific survival following anatomic radical retropubic prostatectomy. The 15-year Johns Hopkins experience.* Urol Clin North Am, 2001. **28**(3): p. 555-65.
145. Yuan, X., et al., *Androgen receptor remains critical for cell-cycle progression in androgen-independent CWR22 prostate cancer cells.* Am J Pathol, 2006. **169**(2): p. 682-96.
146. Chen, C.D., et al., *Molecular determinants of resistance to antiandrogen therapy.* Nat Med, 2004. **10**(1): p. 33-9.
147. Arora, V.K., et al., *Glucocorticoid receptor confers resistance to antiandrogens by bypassing androgen receptor blockade.* Cell, 2013. **155**(6): p. 1309-22.
148. Watson, P.A., V.K. Arora, and C.L. Sawyers, *Emerging mechanisms of resistance to androgen receptor inhibitors in prostate cancer.* Nat Rev Cancer, 2015. **15**(12): p. 701-11.
149. Barnard, M., et al., *The role of adrenal derived androgens in castration resistant prostate cancer.* J Steroid Biochem Mol Biol, 2020. **197**: p. 105506.
150. Chang, K.H., et al., *A gain-of-function mutation in DHT synthesis in castration-resistant prostate cancer.* Cell, 2013. **154**(5): p. 1074-1084.
151. Mostaghel, E.A., et al., *Resistance to CYP17A1 inhibition with abiraterone in castration-resistant prostate cancer: induction of steroidogenesis and androgen receptor splice variants.* Clin Cancer Res, 2011. **17**(18): p. 5913-25.
152. Cai, C., et al., *Intratumoral de novo steroid synthesis activates androgen receptor in castration-resistant prostate cancer and is upregulated by treatment with CYP17A1 inhibitors.* Cancer Res, 2011. **71**(20): p. 6503-13.
153. Locke, J.A., et al., *Androgen levels increase by intratumoral de novo steroidogenesis during progression of castration-resistant prostate cancer.* Cancer Res, 2008. **68**(15): p. 6407-15.
154. Montgomery, R.B., et al., *Maintenance of intratumoral androgens in metastatic prostate cancer: a mechanism for castration-resistant tumor growth.* Cancer Res, 2008. **68**(11): p. 4447-54.
155. Visakorpi, T., et al., *In vivo amplification of the androgen receptor gene and progression of human prostate cancer.* Nat Genet, 1995. **9**(4): p. 401-6.
156. Cancer Genome Atlas Research, N., *The Molecular Taxonomy of Primary Prostate Cancer.* Cell, 2015. **163**(4): p. 1011-25.
157. Edwards, J., et al., *Androgen receptor gene amplification and protein expression in hormone refractory prostate cancer.* Br J Cancer, 2003. **89**(3): p. 552-6.
158. Taylor, B.S., et al., *Integrative genomic profiling of human prostate cancer.* Cancer Cell, 2010. **18**(1): p. 11-22.
159. Yeh, S., et al., *From HER2/Neu signal cascade to androgen receptor and its coactivators: a novel pathway by induction of androgen target genes through MAP kinase in prostate cancer cells.* Proc Natl Acad Sci U S A, 1999. **96**(10): p. 5458-63.
160. Veldscholte, J., et al., *The androgen receptor in LNCaP cells contains a mutation in the ligand binding domain which affects steroid binding characteristics and response to antiandrogens.* J Steroid Biochem Mol Biol, 1992. **41**(3-8): p. 665-9.
161. Veldscholte, J., et al., *A mutation in the ligand binding domain of the androgen receptor of human LNCaP cells affects steroid binding characteristics and response to anti-androgens.* Biochem Biophys Res Commun, 1990. **173**(2): p. 534-40.
162. Korpal, M., et al., *An F876L mutation in androgen receptor confers genetic and phenotypic resistance to MDV3100 (enzalutamide).* Cancer Discov, 2013. **3**(9): p. 1030-43.

163. Small, E.J., et al., *Antiandrogen withdrawal alone or in combination with ketoconazole in androgen-independent prostate cancer patients: a phase III trial (CALGB 9583).* J Clin Oncol, 2004. **22**(6): p. 1025-33.
164. Leone, G., et al., *Antiandrogen withdrawal syndrome (AAWS) in the treatment of patients with prostate cancer.* Endocr Relat Cancer, 2018. **25**(1): p. R1-R9.
165. Watson, P.A., et al., *Constitutively active androgen receptor splice variants expressed in castration-resistant prostate cancer require full-length androgen receptor.* Proc Natl Acad Sci U S A, 2010. **107**(39): p. 16759-65.
166. Hu, R., et al., *Ligand-independent androgen receptor variants derived from splicing of cryptic exons signify hormone-refractory prostate cancer.* Cancer Res, 2009. **69**(1): p. 16-22.
167. Antonarakis, E.S., et al., *Androgen receptor variant-driven prostate cancer: clinical implications and therapeutic targeting.* Prostate Cancer Prostatic Dis, 2016. **19**(3): p. 231-41.
168. Culig, Z., et al., *Androgen receptor activation in prostatic tumor cell lines by insulin-like growth factor-I, keratinocyte growth factor, and epidermal growth factor.* Cancer Res, 1994. **54**(20): p. 5474-8.
169. Hobisch, A., et al., *Interleukin-6 regulates prostate-specific protein expression in prostate carcinoma cells by activation of the androgen receptor.* Cancer Res, 1998. **58**(20): p. 4640-5.
170. Lin, H.P., et al., *DUSP22 suppresses prostate cancer proliferation by targeting the EGFR-AR axis.* FASEB J, 2019. **33**(12): p. 14653-14667.
171. Guo, Z., et al., *Regulation of androgen receptor activity by tyrosine phosphorylation.* Cancer Cell, 2006. **10**(4): p. 309-19.
172. Hernes, E., et al., *Expression of the epidermal growth factor receptor family in prostate carcinoma before and during androgen-independence.* Br J Cancer, 2004. **90**(2): p. 449-54.
173. Schlomm, T., et al., *Clinical significance of epidermal growth factor receptor protein overexpression and gene copy number gains in prostate cancer.* Clin Cancer Res, 2007. **13**(22 Pt 1): p. 6579-84.
174. Sadar, M.D., *Androgen-independent induction of prostate-specific antigen gene expression via cross-talk between the androgen receptor and protein kinase A signal transduction pathways.* J Biol Chem, 1999. **274**(12): p. 7777-83.
175. Nazareth, L.V. and N.L. Weigel, *Activation of the human androgen receptor through a protein kinase A signaling pathway.* J Biol Chem, 1996. **271**(33): p. 19900-7.
176. Bluemn, E.G., et al., *Androgen Receptor Pathway-Independent Prostate Cancer Is Sustained through FGF Signaling.* Cancer Cell, 2017. **32**(4): p. 474-489 e6.
177. Quintanal-Villalonga, A., et al., *Lineage plasticity in cancer: a shared pathway of therapeutic resistance.* Nat Rev Clin Oncol, 2020. **17**(6): p. 360-371.
178. Aggarwal, R., et al., *Clinical and Genomic Characterization of Treatment-Emergent Small-Cell Neuroendocrine Prostate Cancer: A Multi-institutional Prospective Study.* J Clin Oncol, 2018. **36**(24): p. 2492-2503.
179. Sterling, T. and J.J. Irwin, *ZINC 15--Ligand Discovery for Everyone.* J Chem Inf Model, 2015. **55**(11): p. 2324-37.
180. Tsachaki, M., et al., *Determination of the topology of endoplasmic reticulum membrane proteins using redox-sensitive green-fluorescence protein fusions.* Biochim Biophys Acta, 2015. **1853**(7): p. 1672-82.
181. Weihua, Z., et al., *An endocrine pathway in the prostate, ERbeta, AR, 5alpha-androstane-3beta,17beta-diol, and CYP7B1, regulates prostate growth.* Proc Natl Acad Sci U S A, 2002. **99**(21): p. 13589-94.
182. Pettersson, H., et al., *CYP7B1-mediated metabolism of dehydroepiandrosterone and 5alpha-androstane-3beta,17beta-diol--potential role(s) for estrogen signaling.* FEBS J, 2008. **275**(8): p. 1778-89.
183. Pettersson, H., et al., *CYP7B1-mediated metabolism of 5alpha-androstane-3alpha,17beta-diol (3alpha-Adiol): a novel pathway for potential regulation of the cellular levels of androgens and neurosteroids.* Biochim Biophys Acta, 2009. **1791**(12): p. 1206-15.
184. Nelson, A.W., et al., *Estrogen receptor beta in prostate cancer: friend or foe?* Endocr Relat Cancer, 2014. **21**(4): p. T219-34.
185. Mitsiades, N., et al., *Distinct patterns of dysregulated expression of enzymes involved in androgen synthesis and metabolism in metastatic prostate cancer tumors.* Cancer Res, 2012. **72**(23): p. 6142-52.
186. Beck, K.R., et al., *Virtual screening applications in short-chain dehydrogenase/reductase research.* J Steroid Biochem Mol Biol, 2017. **171**: p. 157-177.
187. Vuorinen, A., et al., *Ligand-based pharmacophore modeling and virtual screening for the discovery of novel 17beta-hydroxysteroid dehydrogenase 2 inhibitors.* J Med Chem, 2014. **57**(14): p. 5995-6007.

188. Aka, J.A., et al., *17beta-hydroxysteroid dehydrogenase type 1 stimulates breast cancer by dihydrotestosterone inactivation in addition to estradiol production.* Mol Endocrinol, 2010. **24**(4): p. 832-45.
189. He, W., et al., *Current knowledge of the multifunctional 17beta-hydroxysteroid dehydrogenase type 1 (HSD17B1).* Gene, 2016. **588**(1): p. 54-61.
190. Penning, T.M., *Aldo-Keto Reductase (AKR) 1C3 inhibitors: a patent review.* Expert Opin Ther Pat, 2017. **27**(12): p. 1329-1340.
191. Hamid, A.R., et al., *Aldo-keto reductase family 1 member C3 (AKR1C3) is a biomarker and therapeutic target for castration-resistant prostate cancer.* Mol Med, 2013. **18**: p. 1449-55.
192. Liu, C., et al., *Intracrine Androgens and AKR1C3 Activation Confer Resistance to Enzalutamide in Prostate Cancer.* Cancer Res, 2015. **75**(7): p. 1413-22.
193. Liu, C., et al., *Inhibition of AKR1C3 Activation Overcomes Resistance to Abiraterone in Advanced Prostate Cancer.* Mol Cancer Ther, 2017. **16**(1): p. 35-44.
194. Loriot, Y., et al., *Safety, tolerability and anti-tumour activity of the androgen biosynthesis inhibitor ASP9521 in patients with metastatic castration-resistant prostate cancer: multi-centre phase I/II study.* Invest New Drugs, 2014. **32**(5): p. 995-1004.
195. Jez, J.M., T.G. Flynn, and T.M. Penning, *A new nomenclature for the aldo-keto reductase superfamily.* Biochem Pharmacol, 1997. **54**(6): p. 639-47.
196. Zannas, A.S., et al., *Gene-Stress-Epigenetic Regulation of FKBP5: Clinical and Translational Implications.* Neuropsychopharmacology, 2016. **41**(1): p. 261-74.
197. Cui, X. and G.A. Churchill, *Statistical tests for differential expression in cDNA microarray experiments.* Genome Biol, 2003. **4**(4): p. 210.
198. Kanehisa, M. and S. Goto, *KEGG: kyoto encyclopedia of genes and genomes.* Nucleic Acids Res, 2000. **28**(1): p. 27-30.
199. Huang da, W., B.T. Sherman, and R.A. Lempicki, *Bioinformatics enrichment tools: paths toward the comprehensive functional analysis of large gene lists.* Nucleic Acids Res, 2009. **37**(1): p. 1-13.
200. Huang da, W., B.T. Sherman, and R.A. Lempicki, *Systematic and integrative analysis of large gene lists using DAVID bioinformatics resources.* Nat Protoc, 2009. **4**(1): p. 44-57.
201. Buser, D.P., et al., *Quantitative proteomics reveals reduction of endocytic machinery components in gliomas.* EBioMedicine, 2019. **46**: p. 32-41.
202. Olsen, J.V., et al., *Global, in vivo, and site-specific phosphorylation dynamics in signaling networks.* Cell, 2006. **127**(3): p. 635-48.
203. Abbas, T. and A. Dutta, *p21 in cancer: intricate networks and multiple activities.* Nat Rev Cancer, 2009. **9**(6): p. 400-14.
204. Kim, T.H., et al., *The role of CREB3L4 in the proliferation of prostate cancer cells.* Sci Rep, 2017. **7**: p. 45300.
205. Clevers, H. and R. Nusse, *Wnt/beta-catenin signaling and disease.* Cell, 2012. **149**(6): p. 1192-205.
206. Fang, Y., et al., *Hsp90 regulates androgen receptor hormone binding affinity in vivo.* J Biol Chem, 1996. **271**(45): p. 28697-702.
207. Bohonowych, J.E., et al., *Extracellular Hsp90 mediates an NF-kappaB dependent inflammatory stromal program: implications for the prostate tumor microenvironment.* Prostate, 2014. **74**(4): p. 395-407.
208. Zuehlke, A.D., et al., *Regulation and function of the human HSP90AA1 gene.* Gene, 2015. **570**(1): p. 8-16.
209. Lavoie, H., J. Gagnon, and M. Therrien, *ERK signalling: a master regulator of cell behaviour, life and fate.* Nat Rev Mol Cell Biol, 2020. **21**(10): p. 607-632.
210. Thorpe, L.M., H. Yuzugullu, and J.J. Zhao, *PI3K in cancer: divergent roles of isoforms, modes of activation and therapeutic targeting.* Nat Rev Cancer, 2015. **15**(1): p. 7-24.
211. Wee, S., et al., *PTEN-deficient cancers depend on PIK3CB.* Proc Natl Acad Sci U S A, 2008. **105**(35): p. 13057-62.
212. Song, L., et al., *Activation of Stat3 by receptor tyrosine kinases and cytokines regulates survival in human non-small cell carcinoma cells.* Oncogene, 2003. **22**(27): p. 4150-65.
213. Garcia, R., et al., *Constitutive activation of Stat3 by the Src and JAK tyrosine kinases participates in growth regulation of human breast carcinoma cells.* Oncogene, 2001. **20**(20): p. 2499-513.
214. Leaman, D.W., et al., *Roles of JAKs in activation of STATs and stimulation of c-fos gene expression by epidermal growth factor.* Mol Cell Biol, 1996. **16**(1): p. 369-75.
215. Avraham, R. and Y. Yarden, *Feedback regulation of EGFR signalling: decision making by early and delayed loops.* Nat Rev Mol Cell Biol, 2011. **12**(2): p. 104-17.

216. Hynes, N.E. and G. MacDonald, *ErbB receptors and signaling pathways in cancer.* Curr Opin Cell Biol, 2009. **21**(2): p. 177-84.
217. Yarden, Y. and M.X. Sliwkowski, *Untangling the ErbB signalling network.* Nat Rev Mol Cell Biol, 2001. **2**(2): p. 127-37.
218. Lynch, T.J., et al., *Activating mutations in the epidermal growth factor receptor underlying responsiveness of non-small-cell lung cancer to gefitinib.* N Engl J Med, 2004. **350**(21): p. 2129-39.
219. Engelman, J.A. and P.A. Janne, *Mechanisms of acquired resistance to epidermal growth factor receptor tyrosine kinase inhibitors in non-small cell lung cancer.* Clin Cancer Res, 2008. **14**(10): p. 2895-9.
220. Libermann, T.A., et al., *Amplification, enhanced expression and possible rearrangement of EGF receptor gene in primary human brain tumours of glial origin.* Nature, 1985. **313**(5998): p. 144-7.
221. Martinelli, E., et al., *Implementing anti-epidermal growth factor receptor (EGFR) therapy in metastatic colorectal cancer: challenges and future perspectives.* Ann Oncol, 2020. **31**(1): p. 30-40.
222. Ciardiello, F. and G. Tortora, *EGFR antagonists in cancer treatment.* N Engl J Med, 2008. **358**(11): p. 1160-74.
223. Scher, H.I., et al., *Changing pattern of expression of the epidermal growth factor receptor and transforming growth factor alpha in the progression of prostatic neoplasms.* Clin Cancer Res, 1995. **1**(5): p. 545-50.
224. Douglas, D.A., et al., *Novel mutations of epidermal growth factor receptor in localized prostate cancer.* Front Biosci, 2006. **11**: p. 2518-25.
225. Baek, K.H., et al., *Correlation of AR, EGFR, and HER2 Expression Levels in Prostate Cancer: Immunohistochemical Analysis and Chromogenic In Situ Hybridization.* Cancer Res Treat, 2012. **44**(1): p. 50-6.
226. Canil, C.M., et al., *Randomized phase II study of two doses of gefitinib in hormone-refractory prostate cancer: a trial of the National Cancer Institute of Canada-Clinical Trials Group.* J Clin Oncol, 2005. **23**(3): p. 455-60.
227. Small, E.J., et al., *A phase II trial of gefitinib in patients with non-metastatic hormone-refractory prostate cancer.* BJU Int, 2007. **100**(4): p. 765-9.
228. Gravis, G., et al., *Results from a monocentric phase II trial of erlotinib in patients with metastatic prostate cancer.* Ann Oncol, 2008. **19**(9): p. 1624-8.
229. Nabhan, C., et al., *Erlotinib has moderate single-agent activity in chemotherapy-naive castration-resistant prostate cancer: final results of a phase II trial.* Urology, 2009. **74**(3): p. 665-71.
230. Sridhar, S.S., et al., *A multicenter phase II clinical trial of lapatinib (GW572016) in hormonally untreated advanced prostate cancer.* Am J Clin Oncol, 2010. **33**(6): p. 609-13.
231. Whang, Y.E., et al., *A phase II study of lapatinib, a dual EGFR and HER-2 tyrosine kinase inhibitor, in patients with castration-resistant prostate cancer.* Urol Oncol, 2013. **31**(1): p. 82-6.
232. Cathomas, R., et al., *Efficacy of cetuximab in metastatic castration-resistant prostate cancer might depend on EGFR and PTEN expression: results from a phase II trial (SAKK 08/07).* Clin Cancer Res, 2012. **18**(21): p. 6049-57.
233. Arriza, J.L., et al., *Cloning of human mineralocorticoid receptor complementary DNA: structural and functional kinship with the glucocorticoid receptor.* Science, 1987. **237**(4812): p. 268-75.
234. Krug, A.W., et al., *Aldosterone stimulates epidermal growth factor receptor expression.* J Biol Chem, 2003. **278**(44): p. 43060-6.
235. Grossmann, C., et al., *Aldosterone-induced EGFR expression: interaction between the human mineralocorticoid receptor and the human EGFR promoter.* Am J Physiol Endocrinol Metab, 2007. **292**(6): p. E1790-800.
236. Mackenzie, I.S., et al., *Spironolactone use and risk of incident cancers: a retrospective, matched cohort study.* Br J Clin Pharmacol, 2017. **83**(3): p. 653-663.
237. Hiebert, B.M., et al., *Impact of spironolactone exposure on prostate cancer incidence amongst men with heart failure: A Pharmacoepidemiological study.* Br J Clin Pharmacol, 2021. **87**(4): p. 1801-1813.
238. Yarden, Y. and J. Schlessinger, *The EGF receptor kinase: evidence for allosteric activation and intramolecular self-phosphorylation.* Ciba Found Symp, 1985. **116**: p. 23-45.
239. Derer, S., et al., *Impact of epidermal growth factor receptor (EGFR) cell surface expression levels on effector mechanisms of EGFR antibodies.* J Immunol, 2012. **189**(11): p. 5230-9.
240. Yu, H. and R. Jove, *The STATs of cancer--new molecular targets come of age.* Nat Rev Cancer, 2004. **4**(2): p. 97-105.
241. Campbell, C.L., et al., *Increased expression of the interleukin-11 receptor and evidence of STAT3 activation in prostate carcinoma.* Am J Pathol, 2001. **158**(1): p. 25-32.

242. Mora, L.B., et al., *Constitutive activation of Stat3 in human prostate tumors and cell lines: direct inhibition of Stat3 signaling induces apoptosis of prostate cancer cells.* Cancer Res, 2002. **62**(22): p. 6659-66.
243. Pencik, J., et al., *STAT3 regulated ARF expression suppresses prostate cancer metastasis.* Nat Commun, 2015. **6**: p. 7736.
244. Viswanathan, S.R., et al., *Structural Alterations Driving Castration-Resistant Prostate Cancer Revealed by Linked-Read Genome Sequencing.* Cell, 2018. **174**(2): p. 433-447 e19.
245. Jamaspishvili, T., et al., *Clinical implications of PTEN loss in prostate cancer.* Nat Rev Urol, 2018. **15**(4): p. 222-234.
246. Berns, K., et al., *A functional genetic approach identifies the PI3K pathway as a major determinant of trastuzumab resistance in breast cancer.* Cancer Cell, 2007. **12**(4): p. 395-402.
247. Frattini, M., et al., *PTEN loss of expression predicts cetuximab efficacy in metastatic colorectal cancer patients.* Br J Cancer, 2007. **97**(8): p. 1139-45.
248. Bouali, S., et al., *PTEN expression controls cellular response to cetuximab by mediating PI3K/AKT and RAS/RAF/MAPK downstream signaling in KRAS wild-type, hormone refractory prostate cancer cells.* Oncol Rep, 2009. **21**(3): p. 731-5.
249. Teahan, O., et al., *Metabolic signatures of malignant progression in prostate epithelial cells.* Int J Biochem Cell Biol, 2011. **43**(7): p. 1002-9.
250. Putluri, N., et al., *Metabolomic profiling reveals a role for androgen in activating amino acid metabolism and methylation in prostate cancer cells.* PLoS One, 2011. **6**(7): p. e21417.
251. Halama, A., *Metabolomics in cell culture--a strategy to study crucial metabolic pathways in cancer development and the response to treatment.* Arch Biochem Biophys, 2014. **564**: p. 100-9.
252. Raamsdonk, L.M., et al., *A functional genomics strategy that uses metabolome data to reveal the phenotype of silent mutations.* Nat Biotechnol, 2001. **19**(1): p. 45-50.
253. Wang, D. and R.N. Dubois, *Eicosanoids and cancer.* Nat Rev Cancer, 2010. **10**(3): p. 181-93.
254. Pai, R., et al., *Prostaglandin E2 transactivates EGF receptor: a novel mechanism for promoting colon cancer growth and gastrointestinal hypertrophy.* Nat Med, 2002. **8**(3): p. 289-93.
255. Basu, S., A. Ray, and B.N. Dittel, *Cannabinoid receptor 2 is critical for the homing and retention of marginal zone B lineage cells and for efficient T-independent immune responses.* J Immunol, 2011. **187**(11): p. 5720-32.
256. Sharaf, A., et al., *Systematic Affinity Purification Coupled to Mass Spectrometry Identified p62 as Part of the Cannabinoid Receptor CB2 Interactome.* Front Mol Neurosci, 2019. **12**: p. 224.
257. Miller, M.R., et al., *Unconventional endocannabinoid signaling governs sperm activation via the sex hormone progesterone.* Science, 2016. **352**(6285): p. 555-9.
258. Baggelaar, M.P., et al., *ABHD2 Inhibitor Identified by Activity-Based Protein Profiling Reduces Acrosome Reaction.* ACS Chem Biol, 2019. **14**(10): p. 2295-2304.
259. Konstantinou, E., et al., *Tobacco-specific nitrosamines: A literature review.* Food Chem Toxicol, 2018. **118**: p. 198-203.
260. Landi, M.T., et al., *Gene expression signature of cigarette smoking and its role in lung adenocarcinoma development and survival.* PLoS One, 2008. **3**(2): p. e1651.
261. Pernar, C.H., et al., *The Epidemiology of Prostate Cancer.* Cold Spring Harb Perspect Med, 2018. **8**(12).
262. Weingartner, M., et al., *The ratio of ursodeoxycholyltaurine to 7-oxolithocholyltaurine serves as a biomarker of decreased 11beta-hydroxysteroid dehydrogenase 1 activity in mouse.* Br J Pharmacol, 2021. **178**(16): p. 3309-3326.
263. Gomez, C., et al., *Development and Validation of a Highly Sensitive LC-MS/MS Method for the Analysis of Bile Acids in Serum, Plasma, and Liver Tissue Samples.* Metabolites, 2020. **10**(7).
264. Gomez, C., et al., *Impact on Bile Acid Concentrations by Alveolar Echinococcosis and Treatment with Albendazole in Mice.* Metabolites, 2021. **11**(7).
265. Weingartner, M., et al., *Albendazole reduces hepatic inflammation and endoplasmic reticulum-stress in a mouse model of chronic Echinococcus multilocularis infection.* PLoS Negl Trop Dis, 2022. **16**(1): p. e0009192.
266. Odermatt, A. and D.V. Kratschmar, *Tissue-specific modulation of mineralocorticoid receptor function by 11beta-hydroxysteroid dehydrogenases: an overview.* Mol Cell Endocrinol, 2012. **350**(2): p. 168-86.
267. Quax, R.A., et al., *Glucocorticoid sensitivity in health and disease.* Nat Rev Endocrinol, 2013. **9**(11): p. 670-86.
268. Odermatt, A. and P. Klusonova, *11beta-Hydroxysteroid dehydrogenase 1: Regeneration of active glucocorticoids is only part of the story.* J Steroid Biochem Mol Biol, 2015. **151**: p. 85-92.

269. Snell, K., *Enzymes of serine metabolism in normal and neoplastic rat tissues.* Biochim Biophys Acta, 1985. **843**(3): p. 276-81.
270. Garcia-Canaveras, J.C., et al., *Targeted profiling of circulating and hepatic bile acids in human, mouse, and rat using a UPLC-MRM-MS-validated method.* J Lipid Res, 2012. **53**(10): p. 2231-2241.
271. Penno, C.A., et al., *Quantification of multiple bile acids in uninephrectomized rats using ultra-performance liquid chromatography-tandem mass spectrometry.* Analytical Methods, 2013. **5**(5): p. 1155-1164.
272. Hofmann, A.F., L.R. Hagey, and M.D. Krasowski, *Bile salts of vertebrates: structural variation and possible evolutionary significance.* J Lipid Res, 2010. **51**(2): p. 226-46.
273. Craig, P., *Echinococcus multilocularis.* Curr Opin Infect Dis, 2003. **16**(5): p. 437-44.
274. Hemphill, A., et al., *Treatment of echinococcosis: albendazole and mebendazole--what else?* Parasite, 2014. **21**: p. 70.
275. Kayacan, S.M., et al., *Alveolar echinococcosis localized in the liver, lung and brain.* Chin Med J (Engl), 2008. **121**(1): p. 90-2.
276. Zhang, L. and A. Wang, *Virus-induced ER stress and the unfolded protein response.* Front Plant Sci, 2012. **3**: p. 293.
277. Pillich, H., et al., *Diverse roles of endoplasmic reticulum stress sensors in bacterial infection.* Mol Cell Pediatr, 2016. **3**(1): p. 9.
278. Galluzzi, L., A. Diotallevi, and M. Magnani, *Endoplasmic reticulum stress and unfolded protein response in infection by intracellular parasites.* Future Sci OA, 2017. **3**(3): p. FSO198.
279. Jebbawi, F., et al., *Innate and adaptive immune responses following PD-L1 blockade in treating chronic murine alveolar echinococcosis.* Parasite Immunol, 2021. **43**(8): p. e12834.
280. CAS. *Common Chemistry*. [cited 2021 15.11.2021]; Available from: https://commonchemistry.cas.org/.

10 CURRICULUM VITAE

Simon Stücheli, PhD in Toxicology

Current position: PhD student with a focus on androgen metabolizing enzymes in prostate cancer

Personal Information

Last name:	Stücheli
First name:	Simon
Address:	Schönaustrasse 44
	4058 Basel – CH
Contact:	+41 76 490 23 94
	simon.stuecheli@protonmail.ch
	linkedin.com/in/simon-stücheli-096714196
Date of birth:	29.09.1991
Nationality:	Swiss

Skills & Expertise

Molecular Biology:	Mammalian cell culture (several different cell lines)
	RT-qPCR (SYBR Green & TaqMan, including microRNA)
	Gene silencing using siRNA
	Western blot
	Transactivation / reporter gene assay
	Analyte extraction from cell culture and animal tissue for LC-MS
	Ex vivo activity assay with radiolabeled compound
	Cloning

Analytical:	LC-MS (Agilent Triple Quadrupole 6490/6945)
	Proteomics (data analysis)
	Thin layer chromatography
Computer:	Microsoft Office (Word, Excel, PowerPoint)
	Adobe Photoshop, Illustrator
	GraphPad Prism
	Perseus
	Agilent MassHunter

Education

2017 – Present:	PhD in Toxicology (Molecular & Systems Toxicology, Department of Pharmaceutical Sciences, University of Basel)
2015 – 2017:	Master of Science in Toxicology (Molecular & Systems Toxicology, Department of Pharmaceutical Sciences, University of Basel)
	Master's Thesis: Modulation of Androgen Receptor Activity by DHRS7
2012 – 2015:	Bachelor of Science in Pharmaceutical Sciences, University of Basel
2006 – 2010:	High School (Gymnasium Münchenstein, major in Latin)

Languages

German:	Native speaker
English:	Proficient in writing and speaking
French:	High school level
Finnish:	Personal study and language course participation (3 semesters)

Further Training & Experiences

Project presentation: Annual Research Meeting, Department of Pharmaceutical Sciences, University of Basel, 2020

Supervision of an intern (3 months): Molecular & Systems Toxicology, Department of Pharmaceutical Sciences, University of Basel, 2019

4-Day in house training by Agilent Technologies: Agilent LC-MS 6400 Series Triple Quadrupole System Operation, 2018

CAS/DAS in Translational Nephrology – Module 3: Calcium and Phosphate Homeostasis, Berne, 2018

Membership: Swiss Society of Toxicology

Attendance at various conferences:

Annual Meeting of the Swiss Society of Toxicology (Basel, 2016, 2017, 2019, 2021)

Annual Research Meeting (Department of Pharmaceutical Sciences, University of Basel, 2017, 2018, 2019)

Swiss Steroid Symposium (University Hospital of Berne, 2019)

Previous Positions

2011 – 2012: Civil service at the University Hospital of Basel

2012, April: Assistance (Famulatur) in two pharmacies (Medbase Stedtli Apotheke Laufen & Amavita Schneeberger Apotheke Arlesheim)

Interests & Hobbies

Languages, photography, cars & motorbikes, reading

Driver licenses

Car (Cat. B)
Motorbike (Cat. A1)

References

Prof. Dr. Alex Odermatt
Group Leader
Molecular & Systems Toxicology
Pharmacenter, University of Basel
Klingelbergstrasse 50
4056 Basel, Switzerland
+41 61 207 15 30
alex.odermatt@unibas.ch

Dr. Selene Araya
Managing Toxicologist
Lonza
Münchensteinerstrasse 38
4002 Basel, Switzerland
+41 79 153 11 25
selene.araya@lonza.com

Dr. Cristina Gómez Castellà
PostDoc
Molecular & Systems Toxicology
Pharmacenter, University of Basel
Klingelbergstrasse 50
4056 Basel, Switzerland
+41 61 207 14 89
cristina.gomezcastella@unibas.ch

Dr. Denise Winter
Senior Staff Scientist
Molecular & Systems Toxicology
Pharmacenter, University of Basel
Klingelbergstrasse 50
4056 Basel, Switzerland
+41 61 207 14 86
denise.winter@unibas.ch

Publications

"Albendazole reduces hepatic inflammation and endoplasmic reticulum-stress in a mouse model of chronic *Echinococcus multilocularis* infection"; Weingartner M., **Stücheli S.**, Jebbawi F., Gottstein B., Beldi G., Lundström-Stadelmann B., Wang J., Odermatt A.; PLoS Neglected Tropical Diseases, 2022 Jan 14;16(1):e0009192. (**Co-first authorship**).

"Impact on Bile Acid Concentrations by Alveolar Echinococcosis and Treatment with Albendazole in Mice"; Gómez C., Jebbawi F., Weingartner M., Wang J., **Stücheli S.**, Stieger B., Gottstein B., Beldi G., Lundström-Stadelmann B., Odermatt A.; Metabolites, 2021 Jul 6;11(7):442.

"The ratio of ursodeoxycholyltaurine to 7-oxolithocholyltaurine serves as a biomarker of decreased 11β-hydroxysteroid dehydrogenase 1 activity in mouse"; Weingartner M.; **Stücheli S.**, Kratschmar D.V., Birk J., Klusonova P., Chapman K.E., Lavery G.G., Odermatt A.; British Journal of Pharmacology, 2021 Aug;178(16):3309-3326. (**Co-first authorship**)

"Development and Validation of a Highly Sensitive LC-MS/MS Method for the Analysis of Bile Acids in Serum, Plasma, and Liver Tissue Samples"; Gómez C., **Stücheli S.**, Kratschmar D.V., Bouitbir J., Odermatt A.; Metabolites, 2020, Jul 9;10(7):282.

"DHRS7 (SDR34C1) – A new player in the regulation of androgen receptor function by inactivation of 5α-dihydrotestosterone?"; Araya S., Kratschmar D.V., Tsachaki M., **Stücheli S.**, Beck K.R., Odermatt A.; Journal of Steroid Biochemistry and Molecular Biology, 2017, Jul;171:288-295.

"The Expression of DHRS7 Correlates Negatively with EGFR Expression and Positively with Survival Rate in Prostate Cancer"; **Stücheli S.**, Araya S., Ercan C., Gallon J., Jenö P., Piscuoglio S., Terracciano L., Odermatt A.; manuscript submitted (target journal: Cancers). (**First authorship**)